MILLING FORCE ESTIMATION BASED ON SPINDLE MODEL

A THESIS SUBMITTED TO
THE GRADUATE SCHOOL OF NATURAL AND APPLIED SCIENCES
OF
MIDDLE EAST TECHNICAL UNIVERSITY

BY

BATUHAN ALTINEL

IN PARTIAL FULFILLMENT OF THE REQUIREMENTS
FOR
THE DEGREE OF MASTER OF SCIENCE
IN
MECHANICAL ENGINEERING

NOVEMBER 2024

Approval of the thesis:

MILLING FORCE ESTIMATION BASED ON SPINDLE MODEL

submitted by **BATUHAN ALTINEL** in partial fulfillment of the requirements for the degree of **Master of Science in Mechanical Engineering Department, Middle East Technical University** by,

Prof. Dr. Naci Emre Altun
Dean, Graduate School of **Natural and Applied Sciences** _____

Prof. Dr. Serkan Dağ
Head of Department, **Mechanical Engineering** _____

Assist. Prof. Dr. Hakan Çalışkan
Supervisor, **Mechanical Engineering, METU** _____

Prof. Dr. Umut Orguner
Co-supervisor, **Electrical and Electronics Engineering, METU** _____

Examining Committee Members:

Assoc. Prof. Dr. Ender Yıldırım
Mechanical Engineering, METU _____

Assist. Prof. Dr. Hakan Çalışkan
Mechanical Engineering, METU _____

Prof. Dr. Umut Orguner
Electrical and Electronics Engineering, METU _____

Assist. Prof. Dr. Ramazan Hakkı Namlu
Mechanical Engineering, Atılım University _____

Assist. Prof. Dr. Orkun Özşahin
Mechanical Engineering, METU _____

Date:06.11.2024

I hereby declare that all information in this document has been obtained and presented in accordance with academic rules and ethical conduct. I also declare that, as required by these rules and conduct, I have fully cited and referenced all material and results that are not original to this work.

Name, Surname: Batuhan Altınel

Signature :

ABSTRACT

MILLING FORCE ESTIMATION BASED ON SPINDLE MODEL

Altınel, Batuhan
M.S., Department of Mechanical Engineering
Supervisor: Assist. Prof. Dr. Hakan Çalışkan
Co-Supervisor: Prof. Dr. Umut Orguner

November 2024, 227 pages

This thesis proposes a real-time estimation method for milling cutting forces, using intrinsic signals such as motor currents, voltages, and angular encoder feedback. The approach relies on a spindle model with electrical and mechanical subsystems, where the electrical subsystem includes an AC induction motor and the mechanical subsystem is represented as a two-inertia system. Unknown motor parameters are identified through traditional methods, while frequency response tests determine unknown mechanical subsystem parameters. The Extended Kalman Filter serves as an observer, estimating forces by integrating system dynamics with geometry-based tool-workpiece interaction data. Five distinct estimation methods are developed. The first method uses the entire spindle model; the second addresses asynchronous measurements; the third employs a reduced model focusing only on the mechanical subsystem; the fourth accommodates cases with unknown cutting geometry; and the fifth compensates for measurement drift, enhancing robustness over time. The methods are implemented and validated on a Deckel CNC milling machine setup. Tests are conducted under various process parameters, with tools of differing diameters and teeth counts, to evaluate performance and robustness. Results demonstrate the effec-

tiveness and adaptability of these estimation methods for practical cutting operations, underscoring the proposed approach's suitability for real-time applications in industrial settings.

Keywords: Real-Time Estimation, CNC Machining, Milling Force, Force Estimation, Kalman Filter

ÖZ

FREZE KUVVETİNİN İŞ MİLİ MODEL TABANLI KESTİRİMİ

Altınel, Batuhan
Yüksek Lisans, Makina Mühendisliği Bölümü
Tez Yöneticisi: Dr. Öğr. Üyesi. Hakan Çalışkan
Ortak Tez Yöneticisi: Prof. Dr. Umut Orguner

Kasım 2024 , 227 sayfa

Bu tez, motor akımları, voltajları ve açısal enkoder geri bildirimi gibi içsel sinyalleri kullanarak frezeleme kesme kuvvetlerinin gerçek zamanlı tahmini için bir yöntem önermektedir. Yaklaşım, elektrik alt sistemi bir AC indüksiyon motorunu içeren ve mekanik alt sistemi iki ataletli bir sistem olarak temsil edilen bir iğ modeli üzerine kuruludur. Bilinmeyen motor parametreleri geleneksel yöntemlerle, mekanik alt sistemin bilinmeyen parametreleri ise frekans yanıt testleri ile belirlenmiştir. Genişletilmiş Kalman Filtresi, takım-iş parçası etkileşimi hakkındaki geometrik bilgileri sistem dinamikleriyle birleştirerek kesme kuvvetlerini tahmin eden bir gözlemci olarak kullanılmaktadır. Beş farklı tahmin yöntemi geliştirilmiştir. İlk yöntem tüm iğ modelini kullanmakta, ikinci yöntem senkron olmayan ölçümleri ele almakta, üçüncü yöntem yalnızca mekanik alt sisteme odaklanan indirgenmiş bir model uygulamakta, dördüncü yöntem ise kesme geometrisinin bilinmediği durumları ele almakta ve beşinci yöntem zamanla ölçüm sapmalarını telafi ederek dayanıklılığı artırmaktadır. Yöntemler, Deckel CNC freze tezgahı üzerinde uygulanmış ve doğrulanmıştır. Çeşitli proses parametreleri altında, farklı çap ve diş sayısına sahip takımlar kullanılarak perfor-

mans ve dayanıklılık değerlendirilmiştir. Sonuçlar, bu tahmin yöntemlerinin pratik kesme işlemleri için etkili ve uyarlanabilir olduğunu göstererek önerilen yaklaşımın endüstriyel ortamlarda gerçek zamanlı uygulamalara uygunluğunu vurgulamaktadır.

Anahtar Kelimeler: Gerçek Zamanlı Kestirim, CNC İşleme, Frezeleme Kuvveti, Kuvvet Kestirimi, Kalman Filtre

To my family and my beloved

ACKNOWLEDGMENTS

First and foremost, I would like to express my deepest gratitude to my thesis supervisor, Assist.Prof.Dr. Hakan Çalışkan, for their invaluable guidance, support, and encouragement throughout the course of my research. Their expertise and insights have been instrumental in shaping this thesis.

I am also immensely grateful to my co-supervisor, Prof.Dr. Umut Orguner, for their continuous support and constructive feedback. Their detailed and thoughtful comments have been crucial in refining my work.

I extend my heartfelt thanks to my colleagues and friends for their camaraderie, assistance, and the stimulating discussions we shared. Their support has made this journey more enjoyable and rewarding.

I would like to thank my family for their unwavering support and encouragement. To my parents, İsmail and Serap Altınel, thank you for your constant belief in me and for providing me with the opportunities and motivation to pursue my dreams.

Lastly, but most importantly, I want to thank my beloved Melisa Tuncel for their endless love, patience, and understanding. Your support has been my anchor through the ups and downs of this journey.

TABLE OF CONTENTS

ABSTRACT v

ÖZ vii

ACKNOWLEDGMENTS x

TABLE OF CONTENTS xi

LIST OF TABLES xv

LIST OF FIGURES xvii

LIST OF ABBREVIATIONS xxix

NOMENCLATURE xxx

CHAPTERS

1 INTRODUCTION 1

1.1 Introduction 1

1.2 Research Motivation and Challenges 3

1.2.1 Research Motivation 3

1.2.2 Research Challenges 3

1.3 Objective of the Thesis 4

2 MATHEMATICAL MODELING 7

2.1 System Definition 7

2.2 Electric Subsystem 7

2.2.1 Notation in Induction Motor Mathematical Model 9
2.3 Mechanical System 13
2.4 Milling Forces 15
3 IDENTIFICATION AND VERIFICATION OF THE MODELS 21
3.1 Identification of the System Model 21
3.1.1 AC Induction Motor Parameter Identification 21
3.1.1.1 DC Test for Stator Resitance 21
3.1.1.2 No-Load Test 22
3.1.1.3 Locked Rotor Test 24
3.1.1.4 Results of the Tests 25
3.1.2 Mechanical Subsystem Identification 25
3.1.2.1 Parameter identification 26
3.2 Identification of the Force Coefficients and Verification of the Force Model 29
3.2.1 Force Model Verification Test 1 30
3.2.2 Force Model Verification Test 2 33
3.2.3 Force Model Verification Test 3 36
3.3 Verification of the System Model 39
3.3.1 Open Loop Verification Test without Disturbance Torque . . . 40
3.3.2 Open Loop Verification Test with Disturbance Torque 46
4 CUTTING TORQUE ESTIMATION 51
4.1 Estimation Methods 52
4.1.1 Method 1 52

4.1.2 Method 2 59
4.1.3 Method 3 61
4.1.4 Method 4 65
4.1.5 Method 5 70
4.2 Verifications of Estimation Methods 76
4.2.1 Test Setup Description 77
4.2.2 Verification Method 1 79
4.2.2.1 Test 1 80
4.2.2.2 Test 2 87
4.2.2.3 Test 3 95
4.2.2.4 Discussion 103
4.2.3 Verification Method 2 104
4.2.3.1 Test 1 105
4.2.3.2 Test 2 113
4.2.3.3 Test 3 120
4.2.3.4 Test 4 126
4.2.3.5 Test 5 134
4.2.3.6 Test 6 141
4.2.3.7 Test 7 148
4.2.3.8 Results 154
4.2.3.9 Discussion 155
5 CONCLUSION 159
5.1 Summary and Conclusion 159

5.2 Future Work 163

REFERENCES 167

APPENDICES 171

A Simulation Blocks for Milling Force Model 171

B AC Induction Motor Parameter Identification 174

C Control System 176

C.1 Velocity Controller 176

C.2 Quadrature Axis Current Controller 177

C.3 Direct Axis Current Controller 178

C.4 Decoupling Controller 178

C.5 Transformation Between Stationary and Synchronous Frames . 179

D Simulation Models for Estimation Methods 181

D.1 Common Blocks in Simulation 181

D.2 Blocks for Estimation Methods in Simulation 185

E Verification Test Setup 220

LIST OF TABLES

TABLES

Table 3.1 DC Test Data 22

Table 3.2 No-Load Test Data 23

Table 3.3 Locked-Rotor Test Data 24

Table 3.4 Equivalent Circuit Parameters 25

Table 3.5 Mechanical System Parameters 29

Table 3.6 Test 1 Process Parameters Table 30

Table 3.7 Force Coefficients Results from Parameter Estimation Tool 31

Table 3.8 Test 2 Process Parameters Table 34

Table 3.9 Force Coefficients Results from Parameter Estimation Tool 35

Table 3.10 Test 3 Process Parameters Table 37

Table 3.11 Force Coefficients Results from Parameter Estimation Tool 38

Table 3.12 Process Parameters 47

Table 4.1 Specifications of the CNC machine test setup 78

Table 4.2 Process Parameters of Cutting Tests 79

Table 4.3 Process Parameters of Cutting Test 1 80

Table 4.4 Process Parameters of Cutting Test 2 87

Table 4.5 Process Parameters of Cutting Test 3 95

Table 4.6 Process Parameters of Cutting Test 1 105

Table 4.7 Process Parameters of Cutting Test 2 113

Table 4.8 Process Parameters of Cutting Test 3 120

Table 4.9 Process Parameters of Cutting Test 4 126

Table 4.10 Process Parameters of Cutting Test 5 134

Table 4.11 Process Parameters of Cutting Test 6 141

Table 4.12 Process Parameters of Cutting Test 2 148

Table 4.13 RMSE and PPE Comparison for K_{tc}, K_{te}, and T_c Across Seven Tests for Two Methods 155

LIST OF FIGURES

FIGURES

Figure 2.1 Whole CNC Milling System 8

Figure 2.2 Induction Motor Equivalent Circuit in Blocked Rotor Test 9

Figure 2.3 Stator Dynamic Model 11

Figure 2.4 Rotor Dynamic Model 12

Figure 2.5 Transmission between motor and spindle in CNC 13

Figure 2.6 Two Inertia Model and Block Diagram Representation 14

Figure 3.1 Induction Motor Equivalent Circuit in No-Load Test 22

Figure 3.2 Induction Motor Equivalent Circuit in Blocked Rotor Test 24

Figure 3.3 Reference velocity test signal 25

Figure 3.4 Fitted Transfer Function from Motor Velocity to Spindle Velocity 28

Figure 3.5 Fitted transfer function from electrical torque to motor speed . . 28

Figure 3.6 Verification of the Force Model for F_x - Test 1 32

Figure 3.7 Verification of the Force Model for F_y - Test 1 33

Figure 3.8 Verification of the Force Model for F_x - Test 2 35

Figure 3.9 Verification of the Force Model for F_y - Test 2 36

Figure 3.10 Verification of the Force Model for F_x - Test 3 38

Figure 3.11 Verification of the Force Model for F_y - Test 3 39

Figure 3.12 General Schematic for the Open Loop Verification Test without Disturbance Torque 40

Figure 3.13 Inverse Park Transform for Input Voltages 41

Figure 3.14 Electric Motor Block Simulation 42

Figure 3.15 Electric Motor Block Simulation 43

Figure 3.16 Simulation and Driver I_{dse} Data Comparison 43

Figure 3.17 Simulation and Driver I_{qse} Data Comparison 44

Figure 3.18 Simulation and Driver ω_m Data Comparison 45

Figure 3.19 General Schematic for the Open Loop Verification Test with Disturbance Torque 46

Figure 3.20 Calculated Tangential Cutting Torque T_c 47

Figure 3.21 Simulation and Driver I_{dse} Data Comparison 48

Figure 3.22 Simulation and Driver I_{qse} Data Comparison 49

Figure 3.23 Simulation and Driver ω_m Data Comparison 50

Figure 4.1 Illustration of Transmission Angular Position Drift 70

Figure 4.2 Full Sloth Cutting Test 78

Figure 4.3 Comparison of I_{dss} Estimation Among Different Estimation Methods 81

Figure 4.4 Comparison of I_{qss} Estimation Among Different Estimation Methods 81

Figure 4.5 Comparison of ω_m Estimation Among Different Estimation Methods 82

Figure 4.6 Comparison of ω_s Estimation Among Different Estimation Methods 83

Figure 4.7 Comparison of θ_T Estimation Among Different Estimation Methods 83

Figure 4.8 Comparison of K_{tc} Estimation Among Different Estimation Methods 84

Figure 4.9 Comparison of Estimation Error for K_{tc} Among Different Estimation Methods 84

Figure 4.10 Comparison of K_{te} Estimation Among Different Estimation Methods 85

Figure 4.11 Comparison of Estimation Error for K_{te} Among Different Estimation Methods 86

Figure 4.12 Comparison of T_c Estimation Among Different Estimation Methods 86

Figure 4.13 Comparison of T_c Estimation Error Among Different Estimation Methods 87

Figure 4.14 Comparison of I_{dss} Estimation Among Different Estimation Methods 88

Figure 4.15 Comparison of I_{qss} Estimation Among Different Estimation Methods 89

Figure 4.16 Comparison of ω_m Estimation Among Different Estimation Methods 89

Figure 4.17 Comparison of ω_s Estimation Among Different Estimation Methods 90

Figure 4.18 Comparison of θ_T Estimation Among Different Estimation Methods 91

Figure 4.19 Comparison of K_{tc} Estimation Among Different Estimation Methods 91

Figure 4.20 Comparison of Estimation Error for the K_{tc} Among Different Estimation Methods 92

Figure 4.21 Comparison of K_{te} Estimation Among Different Estimation Methods 93

Figure 4.22 Comparison of Estimation Error for the K_{te} Among Different Estimation Methods 94

Figure 4.23 Comparison of T_c Estimation Among Different Estimation Methods 94

Figure 4.24 Comparison of T_c Estimation Error Among Different Estimation Methods 95

Figure 4.25 Comparison of I_{dss} Estimation Among Different Estimation Methods 96

Figure 4.26 Comparison of I_{qss} Estimation Among Different Estimation Methods 97

Figure 4.27 Comparison of ω_m Estimation Among Different Estimation Methods 98

Figure 4.28 Comparison of ω_s Estimation Among Different Estimation Methods 98

Figure 4.29 Comparison of θ_T Estimation Among Different Estimation Methods 99

Figure 4.30 Comparison of K_{tc} Estimation Among Different Estimation Methods 99

Figure 4.31 Comparison of Estimation Error for the K_{tc} Among Different Estimation Methods 100

Figure 4.32 Comparison of K_{te} Estimation Among Different Estimation Methods 101

Figure 4.33 Comparison of Estimation Error for the K_{te} Among Different Estimation Methods 102

Figure 4.34 Comparison of T_c Estimation Among Different Estimation Methods 102

Figure 4.35 Comparison of T_c Estimation Error Among Different Estimation Methods 103

Figure 4.36 Comparison of I_{dss} Estimation Among Different Estimation Methods 106

Figure 4.37 Comparison of I_{qss} Estimation Among Different Estimation Methods 106

Figure 4.38 Comparison of ω_m Estimation Among Different Estimation Methods 107

Figure 4.39 Comparison of ω_s Estimation Among Different Estimation Methods 107

Figure 4.40 Comparison of θ_T Estimation Among Different Estimation Methods 108

Figure 4.41 Comparison of K_{tc} Estimation Among Different Estimation Methods 109

Figure 4.42 Comparison of Estimation Error for the K_{tc} Among Different Estimation Methods 110

Figure 4.43 Comparison of K_{te} Estimation Among Different Estimation Methods 110

Figure 4.44 Comparison of Estimation Error for the K_{te} Among Different Estimation Methods 111

Figure 4.45 Comparison of T_c Estimation Among Different Estimation Methods 112

Figure 4.46 Comparison of T_c Estimation Error Among Different Estimation Methods 112

Figure 4.47 Comparison of I_{dss} Estimation Among Different Estimation Methods 113

Figure 4.48 Comparison of I_{qss} Estimation Among Different Estimation Methods 114

Figure 4.49 Comparison of ω_m Estimation Among Different Estimation Methods 114

Figure 4.50 Comparison of ω_s Estimation Among Different Estimation Methods 115

Figure 4.51 Comparison of θ_T Estimation Among Different Estimation Methods 115

Figure 4.52 Comparison of K_{tc} Estimation Among Different Estimation Methods 116

Figure 4.53 Comparison of Estimation Error for the K_{tc} Among Different Estimation Methods 117

Figure 4.54 Comparison of K_{te} Estimation Among Different Estimation Methods 117

Figure 4.55 Comparison of Estimation Error for the K_{te} Among Different Estimation Methods 118

Figure 4.56 Comparison of T_c Estimation Among Different Estimation Methods 119

Figure 4.57 Comparison of T_c Estimation Error Among Different Estimation Methods 119

Figure 4.58 Comparison of I_{dss} Estimation Among Different Estimation Methods 120

Figure 4.59 Comparison of I_{qss} Estimation Among Different Estimation Methods 121

Figure 4.60 Comparison of ω_m Estimation Among Different Estimation Methods 121

Figure 4.61 Comparison of ω_s Estimation Among Different Estimation Methods 122

Figure 4.62 Comparison of θ_T Estimation Among Different Estimation Methods 122

Figure 4.63 Comparison of K_{tc} Estimation Among Different Estimation Methods 123

Figure 4.64 Comparison of Estimation Error for the K_{tc} Among Different Estimation Methods 124

Figure 4.65 Comparison of K_{te} Estimation Among Different Estimation Methods 124

Figure 4.66 Comparison of Estimation Error for the K_{te} Among Different Estimation Methods 125

Figure 4.67 Comparison of T_c Estimation Among Different Estimation Methods 125

Figure 4.68 Comparison of T_c Estimation Error Among Different Estimation Methods 126

Figure 4.69 Comparison of I_{dss} Estimation Among Different Estimation Methods 127

Figure 4.70 Comparison of I_{qss} Estimation Among Different Estimation Methods 127

Figure 4.71 Comparison of ω_m Estimation Among Different Estimation Methods 128

Figure 4.72 Comparison of ω_s Estimation Among Different Estimation Methods 129

Figure 4.73 Comparison of θ_T Estimation Among Different Estimation Methods 129

Figure 4.74 Comparison of K_{tc} Estimation Among Different Estimation Methods 130

Figure 4.75 Comparison of Estimation Error for the K_{tc} Among Different Estimation Methods 131

Figure 4.76 Comparison of K_{te} Estimation Among Different Estimation Methods 131

Figure 4.77 Comparison of Estimation Error for the K_{te} Among Different Estimation Methods 132

Figure 4.78 Comparison of T_c Estimation Among Different Estimation Methods 133

Figure 4.79 Comparison of T_c Estimation Error Among Different Estimation Methods 133

Figure 4.80 Comparison of I_{dss} Estimation Among Different Estimation Methods 134

Figure 4.81 Comparison of I_{qss} Estimation Among Different Estimation Methods 135

Figure 4.82 Comparison of ω_m Estimation Among Different Estimation Methods 135

Figure 4.83 Comparison of ω_s Estimation Among Different Estimation Methods 136

Figure 4.84 Comparison of θ_T Estimation Among Different Estimation Methods . . . 137

Figure 4.85 Comparison of K_{tc} Estimation Among Different Estimation Methods . . . 137

Figure 4.86 Comparison of Estimation Error for the K_{tc} Among Different Estimation Methods . . . 138

Figure 4.87 Comparison of K_{te} Estimation Among Different Estimation Methods . . . 138

Figure 4.88 Comparison of Estimation Error for the K_{te} Among Different Estimation Methods . . . 139

Figure 4.89 Comparison of T_c Estimation Among Different Estimation Methods . . . 140

Figure 4.90 Comparison of T_c Estimation Error Among Different Estimation Methods . . . 140

Figure 4.91 Comparison of I_{dss} Estimation Among Different Estimation Methods . . . 141

Figure 4.92 Comparison of I_{qss} Estimation Among Different Estimation Methods . . . 142

Figure 4.93 Comparison of ω_m Estimation Among Different Estimation Methods . . . 142

Figure 4.94 Comparison of ω_s Estimation Among Different Estimation Methods . . . 143

Figure 4.95 Comparison of θ_T Estimation Among Different Estimation Methods . . . 143

Figure 4.96 Comparison of K_{tc} Estimation Among Different Estimation Methods . . . 144

Figure 4.97 Comparison of Estimation Error for the K_{tc} Among Different Estimation Methods 145

Figure 4.98 Comparison of K_{te} Estimation Among Different Estimation Methods 145

Figure 4.99 Comparison of Estimation Error for the K_{te} Among Different Estimation Methods 146

Figure 4.100 Comparison of T_c Estimation Among Different Estimation Methods 147

Figure 4.101 Comparison of T_c Estimation Error Among Different Estimation Methods 147

Figure 4.102 Comparison of I_{dss} Estimation Among Different Estimation Methods 148

Figure 4.103 Comparison of I_{qss} Estimation Among Different Estimation Methods 149

Figure 4.104 Comparison of ω_m Estimation Among Different Estimation Methods 149

Figure 4.105 Comparison of ω_s Estimation Among Different Estimation Methods 150

Figure 4.106 Comparison of θ_T Estimation Among Different Estimation Methods 150

Figure 4.107 Comparison of K_{tc} Estimation Among Different Estimation Methods 151

Figure 4.108 Comparison of Estimation Error for the K_{tc} Among Different Estimation Methods 152

Figure 4.109 Comparison of K_{te} Estimation Among Different Estimation Methods 152

Figure 4.110 Comparison of Estimation Error for the K_{te} Among Different Estimation Methods 153

Figure 4.111 Comparison of T_c Estimation Among Different Estimation Methods 153

Figure 4.112 Comparison of T_c Estimation Error Among Different Estimation Methods 154

Figure A.1 Calculating Immersion Angle in Simulink ϕ 171

Figure A.2 Calculating ϕ_{st} and ϕ_{ex} 171

Figure A.3 Calculating Cutting Forces and Tangential Cutting Force 173

Figure B.1 AC Induction Motor Data Sheet 174

Figure B.2 Test Setup for Motor Parameter Identification 175

Figure B.3 Lock Mechanism for the Locked Rotor Test 175

Figure C.1 General Control Block Diagram 176

Figure C.2 Velocity Controller Block Diagram 177

Figure C.3 Quadrature Axis Current Controller Block Diagram 177

Figure C.4 Direct Axis Current Controller Block Diagram 178

Figure C.5 Voltage Reference Frame Transformation Block Diagram 179

Figure C.6 Feedback Reference Frame Transformation Block Diagram . . . 180

Figure D.1 Obtaining Electrical Angle θ_e from Motor Angular Position θ_m . 181

Figure D.2 Transformation of V_{dse}, V_{qse} to V_{dss}, V_{qss} 182

Figure D.3 Dynamic Model 183

Figure D.4 Measurement Vector in Simulation 184

Figure D.5 Measurement Vector in Simulation 184

Figure D.6 Simulation Block for Method 1 185

Figure D.7 Simulation Block for Method 2 194

Figure D.8 Simulation Block for Method 3 198

Figure D.9 Simulation Block for Method 4 202

Figure D.10 Simulation Block for Method 5 210

Figure E.1 Beckhoff C6930 221

Figure E.2 Franz Kessler DM112/4L AC Induction Motor 221

Figure E.3 Heidenhain ROD 480 1800 222

Figure E.4 Kistler 9257B Dynamometer 224

Figure E.5 The Kistler LabAmp 5167A 225

LIST OF ABBREVIATIONS

AC	Alternative Current
AEKF	Asynchronous Extended Kalman Filter
CNC	Computer Numerical Control
DAQ	Data Acquisition
DC	Direct Current
DOB	Disturbance Observer
EKF	Extended Kalman Filter
FFT	Fast Fourier Transform
KF	Kalman Filter
MEDOB	Multi-encoder Based Disturbance Observer
NI	National Instrument
PC	Personal Computer
PLC	Programmable Logic Controller
PPE	Peak-to-Peak Error
RMSE	Root Mean Square Error
TTL	Transistor Transistor Logic

NOMENCLATURE

β	Helix Angle of the Cutter
δ_{n_g}	Change in Reduction Ratio
$\hat{\mathbf{x}}_k^-$	Priori State Estimate Vector at Time Step k
$\hat{\mathbf{x}}_k$	State Estimate Vector at Time Step k
λ_{drs}	Rotor Direct Axis Flux Linkage in Stationary Frame
λ_{dse}	Stator Direct Axis Flux Linkage in Synchronous Frame
λ_{dss}	Stator Direct Axis Flux Linkage in Stationary Frame
λ_{qrs}	Rotor Quadrature Axis Flux Linkage in Stationary Frame
λ_{qse}	Stator Quadrature Axis Flux Linkage in Synchronous Frame
λ_{qss}	Stator Quadrature Axis Flux Linkage in Stationary Frame
$\mathbf{H}_k$	Measurement Matrix at Time Step k
$\mathbf{h}_t$	Geometry Matrix
$\mathbf{I}$	Identity Matrix
$\mathbf{J}$	Continuous-Time Jacobian Matrix
$\mathbf{J}_k$	Discrete-Time Jacobian Matrix at Time Step k
$\mathbf{K}_k$	Kalman Gain at Time Step k
$\mathbf{P}_k^-$	Priori Error Covariance Matrix at Time Step k
$\mathbf{P}_k$	Error Covariance Matrix at Time Step k
$\mathbf{Q}_k$	Process Noise Covariance Matrix at Time Step k
$\mathbf{R}_k$	Measurement Noise Covariance Matrix at Time Step k

$\mathbf{u}_k$ Input Vector at Time Step k

$\mathbf{x}_k$ State Vector at Time Step k

$\mathbf{x}_{r,k}$ Reduced State Vector at Time Step k

$\mathbf{z}_k$ Measurement Vector at Time Step k

$\omega_{m,fb}$ Motor Angular Velocity Feedback

$\omega_{m,ref}$ Motor Angular Velocity Reference Input

ω_m Motor Angular Velocity

$\omega_{n,m}$ Natural Frequency Motor Side

$\omega_{n,s}$ Natural Frequency Spindle Side

ω_s Spindle Angular Velocity

ϕ Instantaneous Immersion Angle

ϕ_p Tooth Spacing Angle

ϕ_{ex} Exit Immersion Angle

ϕ_{st} Starting Immersion Angle

ψ The Lag Angle

θ_e Electric Angular Position

θ_m Motor Angular Position

θ_r Rotor Angular Position

θ_s Spinle Angular Position

θ_t Transmission Angular Position

a Edge Contact Length

a_e Radial Depth of Cut

a_p Axial Depth of Cut

b_m Motor Damping Coefficient

b_s Spindle Damping Coefficient

b_t Transmission Damping Coefficient

c Feed Rate

D Diameter of the Cutter

e_{ω_m} Motor Angular Velocity Error

$e_{I_{dse}}$ D Axis Current in Synchronous Reference Frame Error

$e_{I_{qse}}$ Q Axis Current in Synchronous Reference Frame Error

$f(\mathbf{x}, \mathbf{u}, t)$ Nonlinear Continuous-Time Time Varying Function

$f(\mathbf{x}_k, \mathbf{u}_k, t_k)$ Nonlinear Discrete-Time Time Varying Function

F Feed Rate

F_r Radial Cutting Force

F_t Tangential Cutting Force

F_x Feed Cutting Force

F_y Normal Cutting Force

G_{ω_m,T_e} Transfer Function Between Electric Torque and Motor Angular Velocity

G_{ω_s,T_e} Transfer Function Between Electric Torque and Spindle Angular Velocity

h Chip Thickness

h_{tc} Geometry Matrix Component Related to Tangential Cutting Coefficient

h_{te} Geometry Matrix Component Related to Tangential Edge Coefficient

I_R Current in Rotor Branch

I_r Current in Rotor Branch

I_1 Line to Line Current Between Terminal 1 and 2 in No-Load Test

I_3 Line to Line Current Between Terminal 2 and 3 in No-Load Test

I_ϕ Magnetizing Current

I_B Phase Current in Locked Rotor Test

I_c Core-loss Current

I_{drs} Rotor Direct Axis Current in Stationary Frame

I_{dse} Stator Direct Axis Current in Synchronous Frame

I_{dss} Stator Direct Axis Current in Stationary Frame

I_{meas} Measured Current in Test

I_{NL} Phase Current in No-Load Test

I_{qrs} Rotor Quadrature Axis Current in Stationary Frame

$I_{qse,fb}$ D Axis Current in Synchronous Reference Frame Feedback

$I_{qse,fb}$ Q Axis Current in Synchronous Reference Frame Feedback

$I_{qse,ref}$ D Axis Current in Synchronous Reference Frame Input

$I_{qse,ref}$ Q Axis Current in Synchronous Reference Frame Input

I_{qse} Stator Quadrature Axis Current in Synchronous Frame

I_{qss} Stator Quadrature Axis Current in Stationary Frame

J_m Motor Rotor Inertia

J_s Spindle Inertia

K_{ad} Back Calculation Gain for D Current Control

K_{aq} Back Calculation Gain for Q Current Control

K_{as} Back Calculation Gain for Velocity Control

K_{pd} Proportional Gain for D Current Control

K_{pq} Proportional Gain for Q Current Control

K_{ps} Proportional Gain for Velocity Control

K_{rc} Radial Cutting Coefficient

K_{re} Radial Edge Coefficient

K_{tc} Tangential Cutting Coefficient

K_{te} Tangential Edge Coefficient

K_t Electric Torque Constant

L Number of Axial Integration Steps

L_m Magnetizing Inductances

L_r Rotor Self-Inductances

L_s Stator Self-Inductance

L_{lr} Rotor Leakage Inductance

L_{ls} Stator Leakage Inductance

N Number of Teeth on the Cutter

n Gear Reduction Ratio

n_g Gear Reduction Ratio

p Number of Pole Pairs

P_B Input Power in Locked Rotor Test

P_{in} Input Power Measured in Test

P_{NL} Input Power in No-Load Test

R Equivalent Resistance

R_r Rotor Resistance

R_s Stator Resistance

R_{NL} Equivalent Resistance in No-Load Test

s Slip

T_c Tangential Cutting Torque

T_e Electric Torque

T_s Sampling Time

T_t Transmission Torque

T_{nd} Integral Time for D Current Control

T_{nq} Integral Time for Q Current Control

T_{ns} Integral Time for Velocity Control

V_{12} Line to Line Voltage Between Terminal 1 and 2 in No-Load Test

V_{23} Line to Line Voltage Between Terminal 2 and 3 in No-Load Test

v_{ω_m} Measurement Noise for ω_m

v_{ω_s} Measurement Noise for ω_s

v_{θ_t} Measurement Noise for θ_t

V_B Input Voltage in Locked Rotor Test

V_{dc} Input Voltage in DC Test

$V_{dse,dc}$ D Axis Voltage in Synchronous Reference Frame Decoupling Input

$V_{dse,ref}$ D Axis Voltage in Synchronous Reference Frame Input

V_{dse} Stator Direct Axis Voltage in Synchronous Frame

V_{dss} Stator Direct Axis Voltage in Stationary Frame

$v_{I_{dss}}$ Measurement Noise for I_{dss}

$v_{I_{qss}}$ Measurement Noise for I_{qss}

V_{NL} Input Voltage in No-Load Test

$V_{qse,dc}$ Q Axis Voltage in Synchronous Reference Frame Decoupling Input

$V_{qse,ref}$ Q Axis Voltage in Synchronous Reference Frame Input

V_{qse} Stator Quadrature Axis Voltage in Synchronous Frame

V_{qss} Stator Quadrature Axis Voltage in Stationary Frame

w_{ω_m} Process Noise for ω_m

w_{ω_s} Process Noise for ω_s

w_{θ_t} Process Noise for θ_t

$w_{I_{drs}}$ Process Noise for I_{drs}

$w_{I_{dss}}$ Process Noise for I_{dss}

$w_{I_{qrs}}$ Process Noise for I_{qrs}

$w_{I_{qss}}$ Process Noise for I_{qss}

$w_{K_{tc}}$ Process Noise for K_{tc}

$w_{K_{te}}$ Process Noise for K_{te}

w_{T_c} Process Noise for T_c

X_B Equivalent Reactance in Locked Rotor Test

X_{ls} Stator Leakage Reactance

X_m Magnetizing Reactance

X_{NL} Equivalent Reactance in No-Load Test

z Axial Depth of Cut

Z_{NL} Equivalent Impedance in No-Load Test

CHAPTER 1

INTRODUCTION

1.1 Introduction

The study of cutting forces in milling has a rich history, evolving from early empirical methods to modern techniques incorporating advanced sensor technologies and computational models. In the early stages, Taylor's pioneering work on the relationship between cutting speed and tool life laid the groundwork for understanding forces during cutting [1]. Subsequent research expanded to cover the impact of various cutting parameters on tool wear and forces, such as feed rate, depth of cut, and material properties [2]. Over the decades, advancements in signal processing and modeling techniques led to more sophisticated approaches in cutting force estimation, which today includes the use of dynamometers and accelerometers, and in recent years, sensor fusion and CNC intrinsic signals have been explored as cost-effective solutions [3].

Aligned with the Industry 4.0 concept, contemporary research in machine tool systems focuses on process identification and optimization. Cutting force estimation is vital for self-optimizing machine tools, as milling force directly reflects changes in cutting conditions and the tool-workpiece interaction. The use of dynamometers for force measurement is common in literature; however, their cost and fixture requirements limit their industrial applicability.

An alternative to dynamometers is the accelerometer, which estimates cutting forces based on sophisticated models [4, 5]. These techniques often require a profound understanding of the machine dynamics between the cutting tool and the accelerometer mount [6]. Specialized external sensors, such as electromagnetic spindle bearings [7]

or thin-film sensors embedded in cutting inserts, are also utilized [8]. Accelerometers are effective for high-frequency force estimations but are less accurate in reflecting static and low-frequency forces. Sensor fusion has emerged as a promising approach; for example, Mostaghimi et al. [9] combined accelerometer data with spindle motor currents for low-frequency reconstruction of both tangential and radial cutting force components. Since the DC force component is of interest, the relation between spindle current and force is expressed with simple algebraic relations without dynamics.

The use of intrinsic CNC signals requires no additional costs and is advantageous over external sensors in industrial applications, as it does not involve a complex sensor setup or data acquisition system. Based on average cutting forces, force coefficients can be monitored. Liu et al. [10] used nominal spindle motor currents for monitoring cutting forces, which offers an efficient method for real-time estimation of cutting forces.

Yamada and Kakinuma [11] introduced a sensorless cutting force estimation method for full-closed loop ball-screw-driven stages. Their method uses a multi-encoder-based disturbance observer (MEDOB), which leverages motor current, motor angular position, and stage displacement data to estimate cutting forces. This dual-inertia system model compensates for friction and phase lag, achieving force estimation accuracy up to 400 Hz. The authors validated their approach through simulations and experimental tests, showing that it offers high accuracy over a wide bandwidth, suitable for precision machining applications.

Yamamoto et al. [12] propose an enhancement to multi-encoder-based cutting force estimation by employing a Kalman filter (KF) combined with a multiple inertia model. This method improves the accuracy of force estimation along the stationary axis in machine tools, using data from rotary and linear encoders to capture relative position information. The proposed method is validated experimentally and shows significantly improved estimation bandwidth, achieving force estimation up to 1000 Hz, outperforming traditional current-based and disturbance observer (DOB) methods.

1.2 Research Motivation and Challenges

1.2.1 Research Motivation

The advancement of machining processes is integral to meeting the demands of modern manufacturing, where precision, efficiency, and adaptability are paramount. As part of the Industry 4.0 initiative, there is a growing need for self-optimizing machine tools capable of real-time process monitoring and control. One of the critical aspects of machining is the estimation of cutting forces, as they directly influence tool wear, surface quality, and overall productivity. Traditional methods for measuring cutting forces, such as the use of dynamometers, while highly accurate, are not feasible for widespread industrial application due to their high cost and limited adaptability to various machining setups.

The use of indirect methods for cutting force estimation, particularly by utilizing data from internal sensors such as spindle motor currents and accelerometers, presents an attractive alternative. These approaches allow for cutting force estimation without the need for additional expensive sensors, providing a more seamless integration into existing CNC systems. Consequently, developing methods that leverage internal CNC signals to estimate cutting forces not only enhances machine performance but also supports more cost-effective and adaptable solutions for industrial environments.

1.2.2 Research Challenges

Despite the promise of internal CNC signals for force estimation, several challenges remain. These challenges include:

1. **Nonlinear Dynamics and Model Complexity**: The interaction between the tool and the workpiece in milling processes involves complex, nonlinear dynamics. Modeling these dynamics accurately to estimate cutting forces reliably is a significant challenge, requiring sophisticated algorithms like the Extended Kalman Filter (EKF) to handle nonlinearity.
2. **Parameter Identification and Model Validation**: Accurate estimation of cut-

ting forces depends on the precise identification of system parameters, including tool geometry, material properties, and machine dynamics. Model validation also poses a challenge, as it requires extensive testing to ensure the reliability of the estimated forces across various machining conditions.

3. **Handling of Measurement Noise and Drifting**: Real-world data is prone to noise and sensor drift, particularly in position and velocity measurements. Accurate force estimation relies on mitigating the impact of noise and drift, which can obscure true force dynamics and affect the reliability of estimation methods.

4. **Asynchronous Data Acquisition**: In practice, measurements from various sensors, such as motor currents and accelerometer signals, may not be synchronized. This lack of synchronicity can lead to discrepancies in data interpretation and reduced accuracy in force estimation. Addressing this issue requires estimation methods that can handle asynchronous data inputs effectively.

By addressing these challenges, the research aims to develop a practical and robust approach to cutting force estimation that enhances the efficiency and adaptability of modern CNC systems.

1.3 Objective of the Thesis

The primary objective of this thesis is to develop and validate a robust method for estimating the tangential cutting torque (T_c) during milling operations using an integrated approach that leverages internal machine signals, such as spindle motor currents and position data, rather than relying on external force measurement devices. This approach aims to enhance the adaptability and cost-effectiveness of force estimation in CNC systems, making it more feasible for industrial applications.

To achieve this objective, the thesis will focus on the following specific goals:

1. **Modeling of the Milling Process Dynamics**: Develop a comprehensive model that represents both the electric and mechanical subsystems of the spindle and

tool assembly. This model will incorporate the nonlinear dynamics of AC induction motor currents and the mechanical interactions within the spindle-tool system.

2. **Parameter Identification and Verification**: Identify critical parameters in the developed model, such as inertia, damping, and force coefficients, through experimental tests. The identified parameters will then be used to verify the model's accuracy in replicating real cutting conditions.

3. **Implementation of Estimation Methods Using Extended Kalman Filter (EKF)**: Implement various estimation methods utilizing EKF to account for the nonlinearities in the milling process dynamics. The methods will be tailored to estimate cutting forces indirectly from internal machine signals, with special consideration for cases involving asynchronous data and sensor drift.

4. **Simulation and Real-World Validation of the Estimation Methods**: Perform a series of simulations and real-world experiments to validate the developed estimation methods. Verification tests will be conducted to compare the estimated cutting torque with actual force measurements obtained from dynamometer data, thereby evaluating the accuracy and reliability of the estimation methods under different cutting conditions.

Through these objectives, the thesis aims to contribute to the field of CNC machining by advancing methods for cutting force estimation that are more adaptable, cost-effective, and suitable for modern industrial practices, in alignment with the Industry 4.0 paradigm.

CHAPTER 2

MATHEMATICAL MODELING

2.1 System Definition

The system under investigation is a complex entity composed of three interdependent components: two distinct subsystems and a milling force model, as illustrated in Figure 2.1. The electric subsystem establishes the link between electrical and mechanical domains, generating electrical torque that drives the mechanical rotation in the mechanical subsystem. The mechanical subsystem, in turn, defines the mechanical interaction between the motor shaft and the spindle shaft. Finally, the milling force model describes the interaction between the cutting tool and the workpiece during the cutting process. This tripartite structure provides a cohesive framework for analyzing the system's behavior.

2.2 Electric Subsystem

The CNC spindle in this system employs an AC induction motor, a widely used electromechanical device in industrial applications. This motor operates on alternating current and consists of two primary components: the stator and the rotor. To facilitate a comprehensive understanding of the motor's electrical characteristics, an equivalent circuit model is presented in Figure 2.2. While the mathematical model of an induction motor can be expressed in various reference frames, this study utilizes the stationary reference frame for its analysis. The operational principle of an AC induction motor is based on electromagnetic induction. When an alternating current is applied to the stator windings, it generates a rotating magnetic field. This field induces

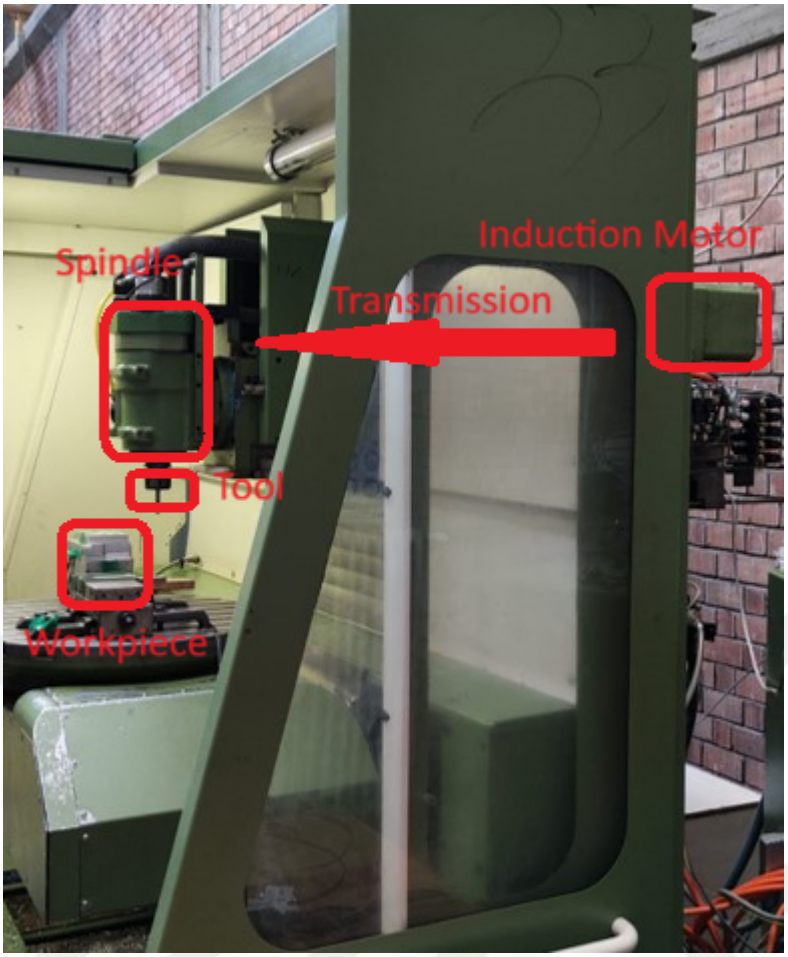


Figure 2.1: Whole CNC Milling System

currents in the rotor, which is typically constructed of aluminum or copper bars short-circuited at the ends. The interaction between the stator's rotating magnetic field and the induced currents in the rotor produces a torque, causing the rotor to rotate. The rotor's speed is slightly less than the synchronous speed of the stator's magnetic field, a difference known as slip, which is crucial for the motor's operation [13]. The motor's performance characteristics, including torque-speed relationship, efficiency, and power factor, are governed by its design parameters and the applied voltage and frequency. In CNC applications, precise control of these parameters through advanced drive systems allows for accurate speed and position control of the spindle, which is essential for high-precision machining operations.

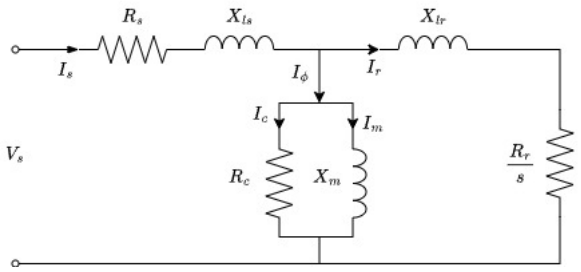


Figure 2.2: Induction Motor Equivalent Circuit in Blocked Rotor Test

2.2.1 Notation in Induction Motor Mathematical Model

In the mathematical model of the induction motor, a systematic notation is employed to denote various parameters and variables. This notation utilizes a three-part subscript system for precise identification:

1. The first subscript, denoted as $i \in \{d, q\}$, designates the axis of reference:
   - d: direct axis component
   - q: quadrature axis component
2. The second subscript, denoted as $j \in \{s, r\}$, indicates the motor element:
   - s: stator parameter
   - r: rotor parameter
3. The third subscript, denoted as k, specifies the frame of reference. In this model, $k = s$ represents the stationary frame.

Thus, a variable in this model is generally represented as $X_{i,j,k}$, where X is the variable symbol, and i, j, and k are as defined above.

This notational convention enables a clear and unambiguous representation of the motor's electromagnetic variables and parameters, facilitating a comprehensive analysis of its behavior under various operating conditions.

The structural equations of the induction motor are given as:

$$V_{dss} = R_s I_{dss} + \dot{\lambda}_{dss} \tag{2.1}$$

$$V_{qss} = R_s I_{qss} + \dot{\lambda}_{qss} \tag{2.2}$$

$$0 = R_r I_{drs} + \dot{\lambda}_{drs} + \omega_r \lambda_{qrs} \tag{2.3}$$

$$0 = R_r I_{qrs} + \dot{\lambda}_{qrs} - \omega_r \lambda_{drs} \tag{2.4}$$

The continuity equations of the induction motor are given as:

$$I_{dss} = \frac{L_r \lambda_{dss} - L_m \lambda_{drs}}{L_s L_r - L_m^2} \tag{2.5}$$

$$I_{qss} = \frac{L_r \lambda_{qss} - L_m \lambda_{qrs}}{L_s L_r - L_m^2} \tag{2.6}$$

$$I_{drs} = \frac{L_s \lambda_{drs} - L_m \lambda_{dss}}{L_s L_r - L_m^2} \tag{2.7}$$

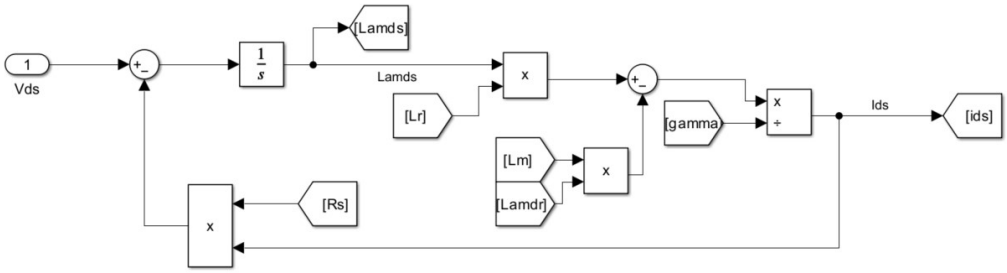
$$I_{qrs} = \frac{L_s \lambda_{qrs} - L_m \lambda_{qss}}{L_s L_r - L_m^2} \tag{2.8}$$

$$T_e = \frac{3}{2}\frac{p}{2} L_m (I_{qss} I_{drs} - I_{dss} I_{qrs}) \tag{2.9}$$

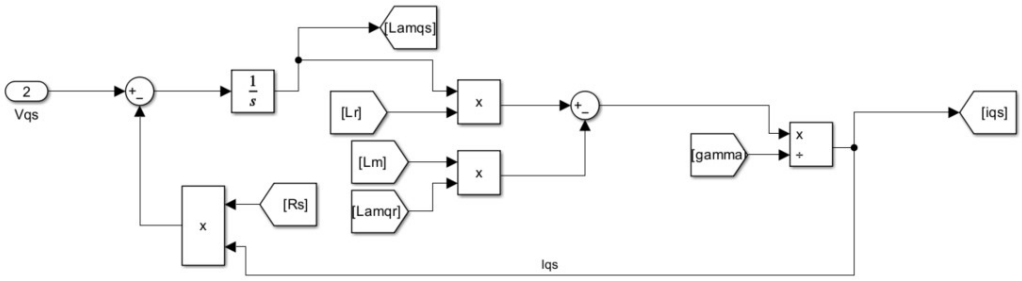
The motor's electrical system is represented by two interconnected circuit models, each described by its own set of equations:

- Induction Motor Stator Dynamic Model
- Induction Motor Rotor Dynamic Model

These models are mathematically coupled, reflecting the electromagnetic interaction between the stator and rotor. Using the differential equations that describe these models, a comprehensive dynamic model of the AC induction motor was developed and implemented in a simulation environment. The structure of this simulated model is illustrated in Figure 2.3 and Figure 2.4.

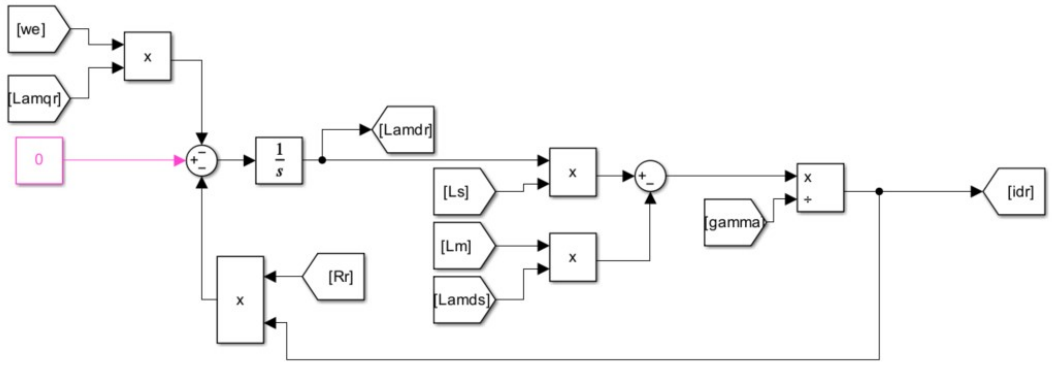


(a) Stator Direct Axis Dynamic Model

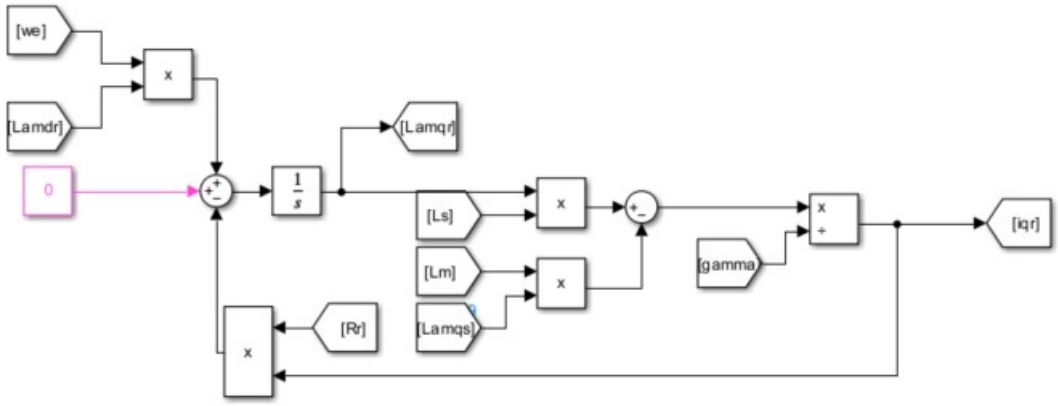


(b) Stator Quadrature Axis Dynamic Model

Figure 2.3: Stator Dynamic Model



(a) Rotor Direct Axis Dynamic Model



(b) Rotor Quadrature Axis Dynamic Model

Figure 2.4: Rotor Dynamic Model

In order to exclusively employ the stator currents I_{dss}, I_{qss} and rotor currents I_{drs}, I_{qrs} as state variables in subsequent sections, the differential equations can be reformulated as follows:

$$\dot{I}_{dss} = -\frac{L_r R_s}{\gamma} I_{dss} + \frac{L_m^2 \omega_r}{\gamma} I_{qss} + \frac{L_m R_r}{\gamma} I_{drs} + \frac{L_m L_r \omega_r}{\gamma} I_{qrs} + \frac{Lr}{\gamma} V_{dss} \quad (2.10)$$

$$\dot{I}_{qss} = -\frac{L_m^2 \omega_r}{\gamma} I_{dss} - \frac{L_r R_s}{\gamma} I_{qss} - \frac{L_m L_r \omega_r}{\gamma} I_{drs} + \frac{L_m R_r}{\gamma} I_{qrs} + \frac{Lr}{\gamma} V_{qss} \quad (2.11)$$

$$\dot{I}_{drs} = \frac{L_m R_s}{\gamma} I_{dss} - \frac{L_s L_m \omega_r}{\gamma} I_{qss} - \frac{R_r L_s}{\gamma} I_{drs} - \frac{L_s L_r \omega_r}{\gamma} I_{qrs} - \frac{Lm}{\gamma} V_{dss} \quad (2.12)$$

$$\dot{I}_{qrs} = \frac{L_s L_m \omega_r}{\gamma} I_{dss} + \frac{L_m R_s}{\gamma} I_{qss} + \frac{L_r L_s \omega_r}{\gamma} I_{drs} - \frac{R_r L_s}{\gamma} I_{qrs} - \frac{Lm}{\gamma} V_{qss} \quad (2.13)$$

where γ is defined as $\gamma = L_s L_r - L_m^2$.

2.3 Mechanical System

The mechanical subsystem comprises the electric motor shaft, belt drive, gearbox, transmission, and spindle shaft. A physical representation of the mechanical system is depicted in Figure 2.5.

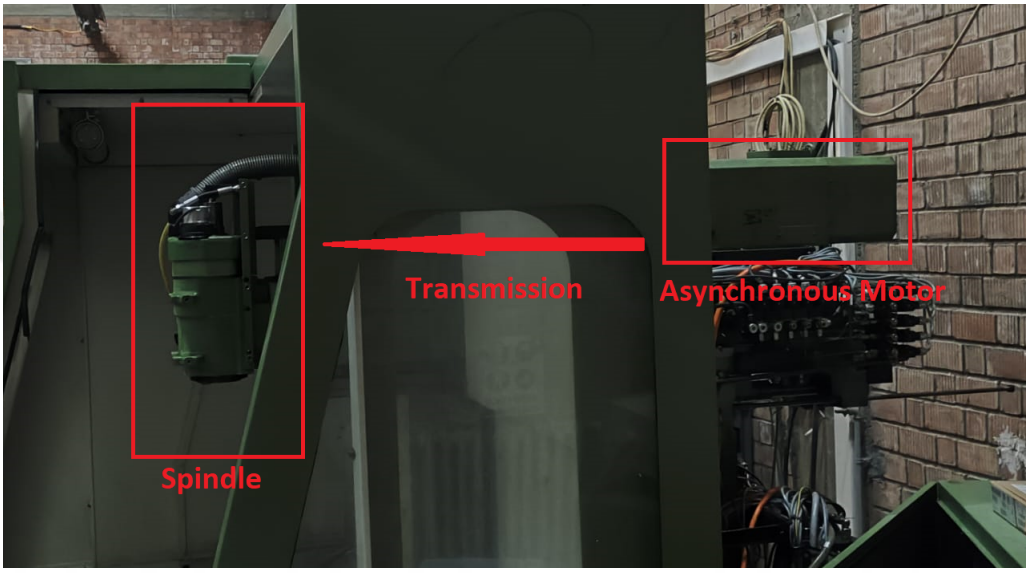


Figure 2.5: Transmission between motor and spindle in CNC

The entire subsystem is modeled as a two-inertia system, as illustrated in Figure 2.6-(a). The parameters J_m and J_s represent the equivalent lumped inertias on the motor and spindle sides, respectively. Two separate damping forces are introduced, characterized by the damping coefficients b_m and b_s. The transmission is modeled as a single gear reduction with ratio n, stiffness k, and damping coefficient b_t. The subsystem inputs consist of the electric torque T_e, acting on the motor side, and the cutting torque T_c, acting as a disturbance on the spindle side.

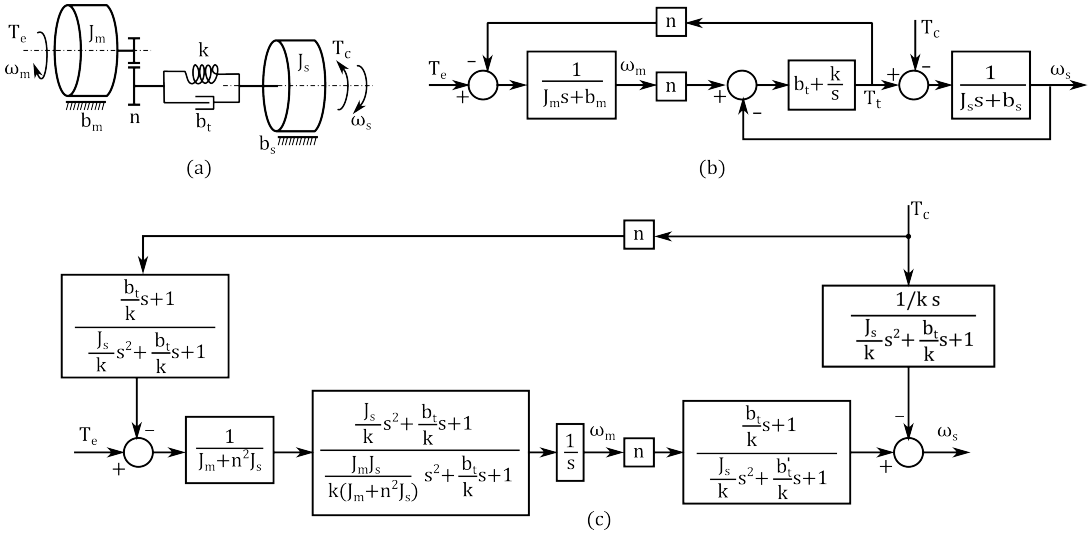


Figure 2.6: Two Inertia Model and Block Diagram Representation

The complete system can be represented by the torque continuity equations formulated for the inertias on the motor and spindle sides, as follows:

$$T_e - nT_t = J_m\dot{\omega}_m + b_m\omega_m \tag{2.14}$$

$$T_t - T_c = J_s\dot{\omega}_s + b_s\omega_s \tag{2.15}$$

where T_t is the transmitted force defined as

$$T_t = b_t(n\omega_m - \omega_s) + k(n\theta_m - \theta_s) \tag{2.16}$$

Using the above three structural equations the block diagram representation of the system is constructed as shown in Figure 2.6-(b). Note that each continuity equation corresponds to a summation block.

The corresponding state space representation of the mechanical subsystem is stated below:

$$\begin{bmatrix} \dot{\omega}_m \\ \dot{\theta}_T \\ \dot{\omega}_s \end{bmatrix} = \begin{bmatrix} -\frac{(b_t n_g^2 + b_m)}{J_m} & -\frac{(kn_g)}{J_m} & \frac{(b_t n_g)}{J_m} \\ n_g & 0 & -1 \\ -\frac{(b_t n_g)}{J_s} & \frac{k}{J_s} & -\frac{(b_t + b_s)}{J_s} \end{bmatrix} \begin{bmatrix} \omega_m \\ \theta_T \\ \omega_s \end{bmatrix} + \begin{bmatrix} \frac{1}{J_m} & 0 \\ 0 & 0 \\ 0 & -\frac{1}{J_s} \end{bmatrix} \begin{bmatrix} T_e \\ T_c \end{bmatrix} \tag{2.17}$$

2.4 Milling Forces

The milling process is characterized by an intermittent cutting operation, where a rotating cutter with one or more teeth is used. The cutter is attached to a spindle, while the workpiece remains securely clamped on the table and moves linearly towards the cutter. Each tooth of the milling cutter traces a trochoidal trajectory [14], which leads to a periodically varying chip thickness during each pass [14]. The instantaneous chip thickness in milling changes as a function of time-varying immersion, and can be described as follows [14]:

$$h(\phi) = c\sin(\phi) \tag{2.18}$$

Here, c represents the feed rate in mm/rev-tooth, and ϕ denotes the instantaneous immersion angle. The tangential cutting force, $F_t(\phi)$, and the radial cutting force, $F_r(\phi)$, are defined based on the varying uncut chip area, $ah(\phi)$, and the edge contact length, a, as follows:

$$F_t(\phi) = K_{tc}ah(\phi) + K_{te}a \tag{2.19}$$

$$F_r(\phi) = K_{rc}ah(\phi) + K_{re}a \tag{2.20}$$

Here, K_{tc} and K_{rc} represent the cutting forces due to the shearing action in the tangential and radial directions, respectively, while K_{te} and K_{re} are the edge constants. The cutting coefficients are considered constant for a given tool-workpiece material pair. The conversion between the tangential-radial and feed-normal directions force components can be carried out using the following equations:

$$F_x(\phi) = -F_t\cos(\phi) - F_r\sin(\phi) \tag{2.21}$$

$$F_y(\phi) = F_t\sin(\phi) - F_r\cos(\phi) \tag{2.22}$$

It is important to note that cutting forces are generated only when the cutting tool is within the cutting zone. The forces $F_t(\phi)$, $F_r(\phi)$, $F_x(\phi)$, and $F_y(\phi)$ are greater than zero when $\phi_{st} \leq \phi \leq \phi_{ex}$. It is also important to mention that multiple teeth may be engaged in cutting simultaneously, depending on the number of teeth on the cutter and the radial depth of cut. The tooth spacing angle, ϕ_p, is defined as:

$$\phi_p = \frac{2\pi}{N} \tag{2.23}$$

Here, N represents the number of teeth on the cutting tool. For a helical end milling tool, the helical geometry of the flutes results in a progressively increasing chip load along the cutting edges. Given a helix angle β on the cutter, any point along the cutting edge will exhibit a phase lag relative to the tool's end point. The lag angle, denoted as ψ, at an axial depth of cut z, is determined by the following expression:

$$\psi = \frac{2z\tan(\beta)}{D} \tag{2.24}$$

At an axial depth of cut z, the lag angle is given by $\psi = k_\beta z$, where $k_\beta = \frac{2\tan(\beta)}{D}$. Consequently, the immersion angle for the j^{th} flute at an axial depth of cut z is expressed as: [14] expressed force integration as following:

$$\phi_j(z) = \phi + j\phi_p - k_\beta z \tag{2.25}$$

The tangential force, $dF_{t,j}$, and the radial force, $dF_{r,j}$, exerted on a differential flute element of height dz, can be represented as:

$$dF_{t,j}(\phi, z) = (K_{tc}h_j(\phi_j(z)) + K_{te})dz \tag{2.26}$$

$$dF_{r,j}(\phi, z) = (K_{rc}h_j(\phi_j(z)) + K_{re})dz \tag{2.27}$$

Here, the chip thickness can be expressed as :

$$h_j(\phi, z) = c\sin(\phi) \tag{2.28}$$

The elemental forces are decomposed into the feed (x) and normal (y) directions through the following transformation:

$$dF_{x,j}(\phi, z) = -F_{t,j}\cos(\phi_j(z)) - F_{r,j}\sin(\phi_j(z)) \tag{2.29}$$

$$dF_{y,j}(\phi, z) = F_{t,j}\sin(\phi_j(z)) - F_{r,j}\cos(\phi_j(z)) \tag{2.30}$$

The differential cutting forces are analytically integrated over the in-cut portion of flute j to obtain the total cutting force generated by the flute, as follows:

$$F_t(\phi_j(z)) = \int_{z_{j,1}}^{z_{j,2}} (dF_t(\phi_j(z)))dz \tag{2.31}$$

$$F_r(\phi_j(z)) = \int_{z_{j,1}}^{z_{j,2}} (dF_r(\phi_j(z)))dz \tag{2.32}$$

$$F_x(\phi_j(z)) = \int_{z_{j,1}}^{z_{j,2}} (dF_x(\phi_j(z)))dz \tag{2.33}$$

$$F_y(\phi_j(z)) = \int_{z_{j,1}}^{z_{j,2}} (dF_y(\phi_j(z)))dz \tag{2.34}$$

The procedure for computing the tangential cutting force, F_t, and the tangential cutting torque, T_c, is provided in Algorithm 1. Detailed explanation of the steps in Algorithm 1 is provided as follows:

1. Inputs:
    - ϕ : Spindle angle, rad
    - ϕ_{st} : Starting (entry) angle, rad
    - ϕ_{ex} : Exit angle, rad
    - β : Helix angle of the cutter, rad
    - D : Diameter of the cutter, mm
    - N : Number of teeth on the cutter
    - a : Axial depth of cut (a_p), mm
2. Outputs:
    - F_t : Tangential cutting force, N
    - F_r : Radial cutting force, N
    - F_x : Feed cutting force, N
    - F_y : Normal cutting force, N
    - T_c : Tangential cutting torque, Nm
3. Calculation Steps:
    - Determining number of axial integration steps, L
    - Calculating pitch angle, ϕ_p
    - Calculating integration of height, da
    - Initializing geometry matrix for the tangential cutting force, h_t
    - Initializing geometry matrix for the radial cutting force, h_r
    - Initializing geometry matrix for the feed cutting force, h_x
    - Initializing geometry matrix for the normal cutting force, h_y
    - Loop for the contributions of all teeth to the cutting forces
    - Calculation for the immersion angle for the tooth k, ϕ_1

- Loop for the calculation of integration along the axial depth of cut
- Updating immersion angle due to helix, ϕ_2
- Starting conditional statement to control whether immersion angle is in the cutting zone
- Calculating chip thickness at this point,h
- Calculating infinetisimal part of geometry matrix for tangential force, dh_t
- Calculating infinetisimal part of geometry matrix for radial force, dh_r
- Updating geometry matrix for the tangential force, h_t
- Updating geometry matrix for the radial force, h_r
- Updating geometry matrix for the feed force using transformation, h_x
- Updating geometry matrix for the normal force using transformation, h_y
- Ending conditional statement
- Updating integration step ,j
- Ending loop for the integration
- Updating the tooth, k
- Ending loop for the teeth contributions
- Calculating the tangential cutting torque, T_c

Algorithm 1 Calculation of Cutting Force and Tangential Cutting Torque

Require: ϕ, ϕ_{st},ϕ_{ex},β,D,N,a_p,K_{tc},K_{te},K_{rc},K_{re}

Ensure: F_t,F_r,F_x,F_y,T_c

$L = 25$
$\phi_p = \frac{2\pi}{N}$
$da = \frac{a_p}{L}$
$h_t = [0, 0]$
$h_r = [0, 0]$
$h_x = [0, 0, 0, 0]$
$h_y = [0, 0, 0, 0]$
while $k \leq N$ **do**
    $\phi_1 = \phi + (k-1)\phi_p$
    while $j \leq L$ **do**
        $\phi_2 = \phi_1 + \frac{2\tan(\beta)}{D}(jd_a)$
        if $\phi_{st} \leq mod(\phi_2, 2\pi)$ & $\phi_{ex} \geq mod(\phi_2, 2\pi)$ **then**
            $h = c\sin(\phi_2)$
            $dh_t = [dah, da]$
            $dh_r = [dah, da]$
            $h_t = h_t + dh_t$
            $h_r = h_r + dh_r$
            $h_x = h_x - dh_t\cos(\phi_2) - dh_r\sin(\phi_2)$
            $h_y = h_y + dh_t\cos(\phi_2) - dh_r\cos(\phi_2)$
        end if
        $j = j + 1$
    end while
    $k = k + 1$
end while
$T_c = \frac{D}{2}F_t$

CHAPTER 3

IDENTIFICATION AND VERIFICATION OF THE MODELS

3.1 Identification of the System Model

In this chapter, the identification of unknown subsystem parameters employed in the mathematical modeling of the system will be addressed. A comprehensive discussion of the tests and methods used for parameter identification will be provided.

3.1.1 AC Induction Motor Parameter Identification

Most modern electric motors provide the necessary parameters for constructing an accurate mathematical model. The CNC milling machine is equipped with updated axis motors and drivers; however, the spindle motor has not undergone an upgrade. Although a datasheet exists for the spindle motor, as shown in Figure B.1, it lacks sufficient information to determine all the necessary parameters for the equivalent circuit. Consequently, the equivalent circuit parameters, as depicted in Figure 2.2, are identified through the application of three distinct test methods.

3.1.1.1 DC Test for Stator Resitance

In this test, a DC voltage is applied to any two of the three-phase windings of the AC induction motor. The applied voltage and the resulting currents are then measured, after which Ohm's law is used to determine the equivalent resistance. Since the motor is assumed to be delta-connected, the per-phase resistance of the stator is calculated

from the equivalent resistance value.

$$V_{dc} = I_{dc}R \tag{3.1}$$

$$R_s = 1.5R \tag{3.2}$$

Measurement for the DC test and results for the equivalent resistance are depicted in Table 3.1.

Table 3.1: DC Test Data

$V_{dc}[V]$	$I_{dc}[A]$	$R[\Omega]$
0.6	1.2	0.5
0.9	1.8	0.5
1.6	3.2	0.5

3.1.1.2 No-Load Test

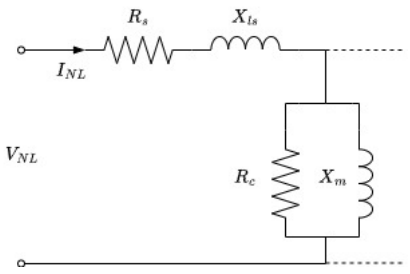


Figure 3.1: Induction Motor Equivalent Circuit in No-Load Test

Another method used to determine the stator circuit parameter $L_{ls} + L_m$ and the parameter representing the loss due to rotational movement and core loss, R_c, is the "No-Load Test." This test is referred to as no-load because, during the test, the motor's rotor moves freely without any external load, causing the motor's slip to approach zero. Consequently, the rotor circuit branch in Figure 2.2 can be neglected, as under near-zero slip conditions $R_r/s \approx \infty$, leading to $I_R \approx 0$. As a result, the circuit behaves as an open circuit, as illustrated in Figure 3.1.

In this test, the input power P_{NL}, input voltage V_{NL}, and phase current I_{NL} of the motor must be measured. The measured input power can be assumed to represent the total losses, which include stator copper loss, core loss, rotational friction, and windage losses. These losses can be modeled in the equivalent circuit as R_c and R_s. Since R_s is determined from the DC test, R_c can then be calculated by using the following equations

$$I_{NL} = \frac{I_{meas}}{\sqrt{3}} \tag{3.3}$$

$$P_{NL} = 3I_{NL}(R_c + Rs) \tag{3.4}$$

$$R_c = \frac{P_{NL}}{3I_{NL}^2} \tag{3.5}$$

Additionally, the equivalent reactance $X_{NL} = X_{ls} + X_m$ can be determined using the following equations.

$$Z_{NL} = \frac{V_{NL}}{I_{NL}} \tag{3.6}$$

$$R_{NL} = \frac{P_{NL}}{3I_{NL}^2} \tag{3.7}$$

$$X_{NL} = \sqrt{Z_{NL}^2 - R_{NL}^2} \tag{3.8}$$

The measurements of the No-Load test are presented in Table 3.2.

Table 3.2: No-Load Test Data

$V_{12}[V]$	$V_{23}[V]$	$I_1[A]$	$I_3[A]$	$P_{in}[kW]$
327	326	13.23	12.71	0.75
330	329	13.78	12.78	0.73

3.1.1.3 Locked Rotor Test

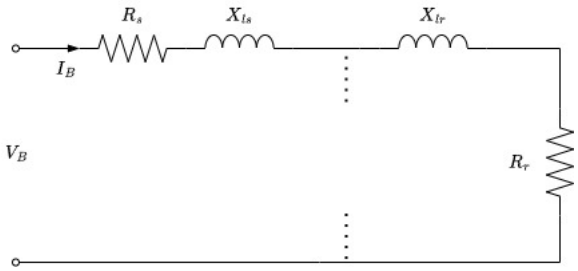


Figure 3.2: Induction Motor Equivalent Circuit in Blocked Rotor Test

The locked rotor test is performed to determine the remaining parameters of an induction motor's equivalent circuit that were not found in the no-load test. Specifically, it helps calculate the sum of the leakage inductances of the stator and rotor ($L_{ls} + L_{lr}$) and the rotor resistance (R_r). During this test, the rotor is physically locked to prevent any rotation which leads slip (s) to be 1. This allows for the omission of the magnetizing current branch, reducing the equivalent circuit to a short circuit.

$$I_B = \frac{I_{meas}}{\sqrt{3}} \tag{3.9}$$

$$P_B = 3I_B^2(R_r + R_s) \tag{3.10}$$

$$R_r = \frac{P_B}{3I_B^2} \tag{3.11}$$

$$Z_B = \frac{V_B}{\sqrt{3}I_B} \tag{3.12}$$

$$X_B = \sqrt{Z_B^2 - (R_s + R_r)^2} \tag{3.13}$$

$$X_B = X_{ls} + X_{lr} \tag{3.14}$$

$$X_{ls} = X_{lr} = 0.5X_B \tag{3.15}$$

Table 3.3: Locked-Rotor Test Data

$V_{12}[V]$	$V_{23}[V]$	$I_1[A]$	$I_3[A]$	$P_{in}[kW]$
32.4	33.3	18.73	19.52	0.767

3.1.1.4 Results of the Tests

Equivalent circuit parameters of the motor resulting from the conducted tests are shown in the Table 3.4.

Table 3.4: Equivalent Circuit Parameters

$R_s[\Omega]$	$R_r[\Omega]$	$L_m[mH]$	$L_{lr}[mH]$	$L_{ls}[mH]$
0.75	1.35	113.9	2.8	2.8

3.1.2 Mechanical Subsystem Identification

The mechanical subsystem, defined in Section 2.3, includes unknown parameters such as J_m, J_s, k, b_m, b_t, and b_s. The identification of these parameters is discussed in detail in this section.

A system identification test is performed to determine these unknown parameters. In this test, sinusoidal reference motor velocity signal is applied as input to the closed-loop system. The sinusoidal signal varies from 1 Hz to 50 Hz with decreasing amplitudes, as illustrated in Figure 3.3. A mean motor velocity of 1000 rpm is selected to avoid the field weakening effect, with amplitudes set to decrease in order to prevent saturation in the electrical system.

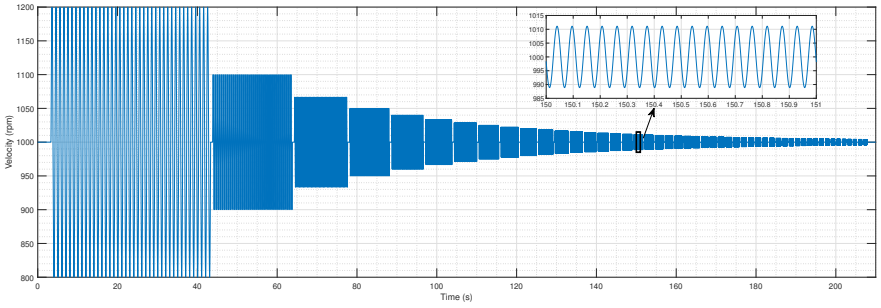


Figure 3.3: Reference velocity test signal

3.1.2.1 Parameter identification

For the identification test, a Fast Fourier Transform is performed on the steady-state portion of the signals at each frequency to derive the magnitude and phase relationship between two selected signals. Specifically, the two selected signals are electrical torque and motor speed, as well as motor speed and spindle speed. Consequently, Bode diagrams for the electrical torque versus motor speed and motor speed versus spindle speed are generated. Using this experimental data, transfer functions are fitted employing optimization methods and system identification tools.

To facilitate the independent identification of these parameters, it is proposed to develop sub-functions that utilize only measurable quantities. Additionally, for the purpose of analytical parameter identification, the order of the transfer function is constrained to two. In this analysis, it is assumed that the damping coefficients on both the motor and spindle sides, b_m and b_s, are negligible. By manipulating the block diagram in Figure Figure 2.6-(b), the resulting representation is provided in Figure 2.6-(c). The transfer function between the input electric torque, T_e, and the motor velocity, ω_m, can thus be formulated as:

$$G_{\omega_m,T_e}(s) = \frac{\Omega_m(s)}{T_e(s)} = \frac{1}{J_m + n^2 J_s} \cdot \frac{\frac{J_s}{k}s^2 + \frac{b_t}{k}s + 1}{\frac{J_s J_m}{k(J_m+n^2 J_s)}s^2 + \frac{b_t}{k}s + 1} \tag{3.16}$$

Similarly, the transfer function relating the input motor velocity, ω_m, to the output spindle velocity, ω_s, is expressed as:

$$G_{\omega_s,\omega_m}(s) = \frac{\Omega_m(s)}{\Omega_s(s)} = n \cdot \frac{\frac{b_t}{k}s + 1}{\frac{J_s}{k}s^2 + \frac{b_t}{k}s + 1} \tag{3.17}$$

It is important to note that both transfer functions are measurable. Once identified using a sine sweep, the parameters can be readily derived through analytical methods. The identification procedure, based on the transfer functions, is outlined as follows:

- Determine the spindle-side natural frequency, $\omega_{n,s}$, from $G_{\omega_s,\omega_m}(s)$ or from the numerator of $G_{\omega_m,T_e}(s)$.
- Determine the motor-side natural frequency, $\omega_{n,m}$, from $G_{\omega_m,T_e}(s)$.
- Calculate the total equivalent inertia, $J_m+n^2 J_s$, from the DC gain of $G_{\omega_m,T_e}(s)$.

- Estimate the gear ratio, n, from the DC gain of $G_{\omega_s,\omega_m}(s)$.
- Derive J_m and J_s based on $\omega_{n,s}$, $\omega_{n,m}$, and the gear ratio n.
- Independently identify J_m and J_s from the expression $J_m + n^2 J_s$.
- Compute the stiffness constant, k, from $\omega_{n,s}$.
- Determine the damping coefficient, b_t, from the numerator of $G_{\omega_s,\omega_m}(s)$.

It can be concluded that the resonance and anti-resonance frequencies, along with the DC gain of the transfer function $G_{\omega_m,T_e}(s)$, are of critical importance. Once these are identified, the remaining parameters can be derived and validated through cross-checking. It is reasonable to neglect the motor damping, b_m, by consolidating all frictional losses into the spindle side, denoted as b_s. The damping coefficient b_s can be independently extracted from the transfer function $G_{\omega_s,\omega_m}(s)$. The second term in the denominator corresponds to $b_t' = b_t + b_s$, and once b_t is determined, b_s can be easily obtained.

It is worth noting that the gear ratio can be determined by measurements from both spindle and motor side encoders, and will serve as a control parameter to verify the identification process.

A transfer function is established between motor velocity ω_m and spindle velocity ω_s to identify the mechanical subsystem, as illustrated in Figure 3.4, where the dots on the experimental data line represent the derived values.

Thus, the fitted transfer function between the input motor velocity ω_m and the output spindle velocity ω_s is given by

$$G_{\omega_s,\omega_m}(s) = 0.789 \cdot \frac{0.0009259s + 1}{0.000077s^2 + 0.003335s + 1} = n \cdot \frac{\frac{b_t}{k}s + 1}{\frac{J_s}{k}s^2 + \frac{b_t}{k}s + 1} \tag{3.18}$$

A transfer function is derived between the electric torque, T_e, and the motor velocity, ω_m, to characterize the mechanical subsystem, as depicted in Figure 3.5. The markers on the experimental data curve correspond to the computed values.

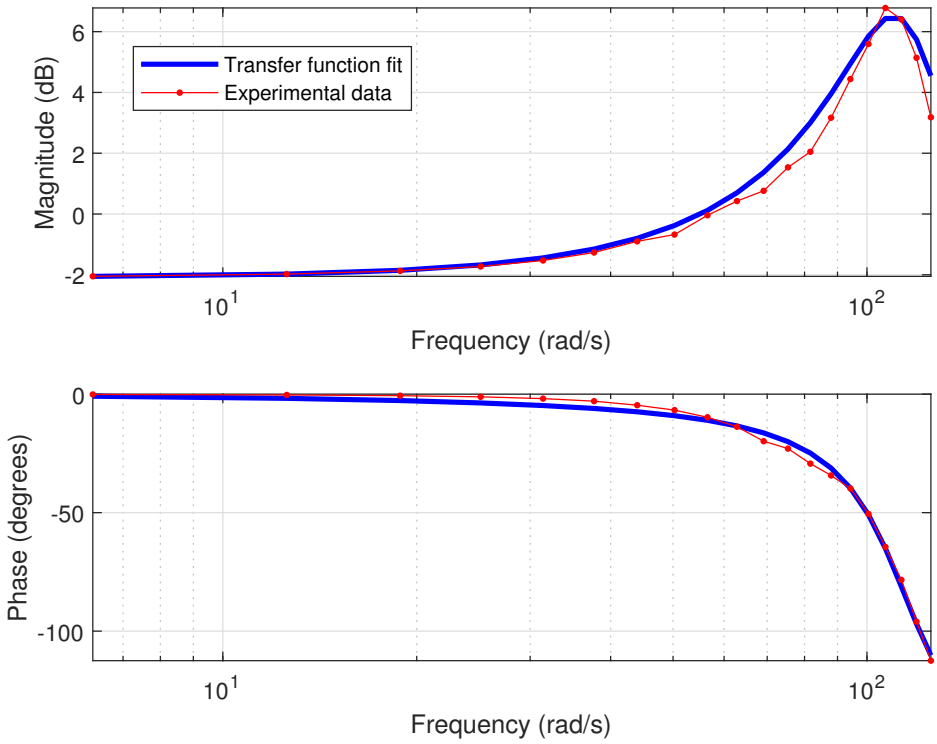


Figure 3.4: Fitted Transfer Function from Motor Velocity to Spindle Velocity

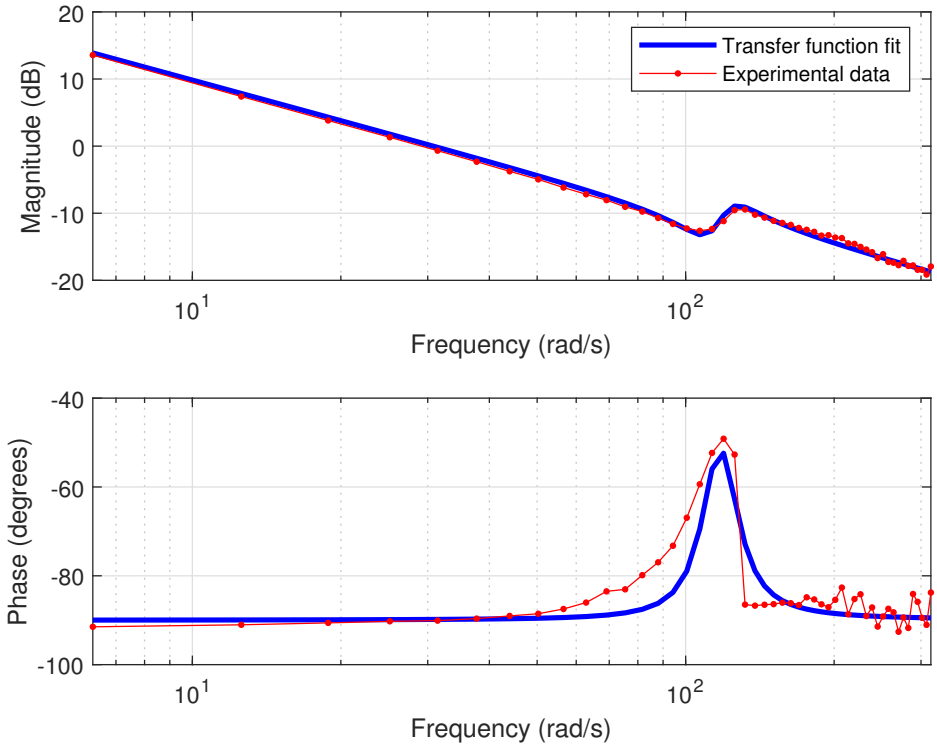


Figure 3.5: Fitted transfer function from electrical torque to motor speed

$$G_{\omega_m,T_e}(s) = \frac{1}{J_m + n^2 J_s} \cdot \frac{\frac{J_s}{k}s^2 + \frac{b_t}{k}s + 1}{\frac{J_s J_m}{k(J_m+n^2 J_s)}s^2 + \frac{b_t}{k}s + 1} \tag{3.19}$$

$$G_{\omega_m,T_e}(s) = \frac{1}{0.0322} \cdot \frac{0.000077s^2 + 0.00168s + 1}{0.000068s^2 + 0.00161s + 1} \tag{3.20}$$

Given equations 3.18 and 3.20, parameters are identified as given in Table 3.5.

Table 3.5: Mechanical System Parameters

$J_s[kg.m^2]$	$J_m[kg.m^2]$	$k[N/m]$	$b_t[Ns/m]$	$b_s[Ns/m]$	n
0.0061	0.0284	79.2	0.0733	0.1908	0.789

3.2 Identification of the Force Coefficients and Verification of the Force Model

In this section, both the identification of the force coefficients and verification of the Force Model are discussed.

The identification of force coefficients is essential because, in the test setup, only the forces in the feed direction (F_x) and the normal direction (F_y) can be measured using the dynamometer. Since the focus of this thesis is on the tangential force (F_t) or the tangential cutting torque, which are crucial for the verification of the estimation methods, transforming F_x and F_y into F_t and F_r requires calculating the forces using the identified force coefficients.

Verification of the force model is also necessary because the geometry matrix $\mathbf{h}_t$ will be utilized in certain estimation methods, with the assumption that this matrix can be calculated during the cutting processes.

For both identification and verification, cutting tests with varying process parameters are conducted.

For the purposes of identification and verification, the simulation setup remains unchanged. To recall, the tool angle, or immersion angle, is calculated from the spindle encoder data recorded during the cutting tests, as shown in Figure A.1. To calculate

the entry and exit angles for both the transient and steady states, the simulation block shown in Figure A.2 is utilized, following the algorithm described in Algorithm 3. To calculate the forces F_x, F_y, F_t, and F_r, the force model algorithm discussed in Algorithm 1 is used, along with the simulation model that implements this algorithm, as shown in Figure A.3.

For all verification tests, the real-time recorded spindle position data, which is a necessary input for calculating the forces, as well as the real-time recorded F_x and F_y forces, which are crucial for verification and identification, are utilized.

3.2.1 Force Model Verification Test 1

The first test can be described with the process parameters that are depicted in Table 3.8

Table 3.6: Test 1 Process Parameters Table

Process Parameters	**Unit**	**Value**
Feedrate, F	mm/min	1500
Spindle Speed, ω_s	rpm	2000
Axial Depth of Cut, a_p	mm	2
Radial Depth of Cut, a_e	mm	12
Number of tooth on Cutter, N	-	3
Diameter of the Cutter,D	mm	12
Helix angle, β	°	45

In this test, the spindle position data is recorded at a sampling rate of 1,000 Hz, while the forces F_x and F_y are recorded at a sampling rate of 12,800 Hz.

During the identification of the unknown force coefficients K_{tc}, K_{te}, K_{rc}, and K_{re}, the built-in Simulink tool, 'Parameter Estimation', is employed to determine these parameters using the following identification options:

- **Optimization Method**: Nonlinear Least Squares

- **Algorithm**: Trust-Region Reflective
- **Parameter Tolerance**: 0.001
- **Function Tolerance**: 0.001
- **Maximum Iterations**: 100
- **Number of Experiment Inputs**: 2
- **Input 1**: Real data of F_x from the dynamometer
- **Input 2**: Real data of F_y from the dynamometer
- **Number of Experiment Outputs**: 2
- **Output 1**: Calculated force, F_x, from the Force Model
- **Output 2**: Calculated force, F_y, from the Force Model

The cutting force coefficients, determined through optimization methods, are presented in Table 3.7.

Table 3.7: Force Coefficients Results from Parameter Estimation Tool

$K_{tc}\ [\frac{N}{mm^2}]$	$K_{te}\ [\frac{N}{mm}]$	$K_{rc}\ [\frac{N}{mm^2}]$	$K_{re}\ [\frac{N}{mm}]$
593.53	43.13	112.36	35.11

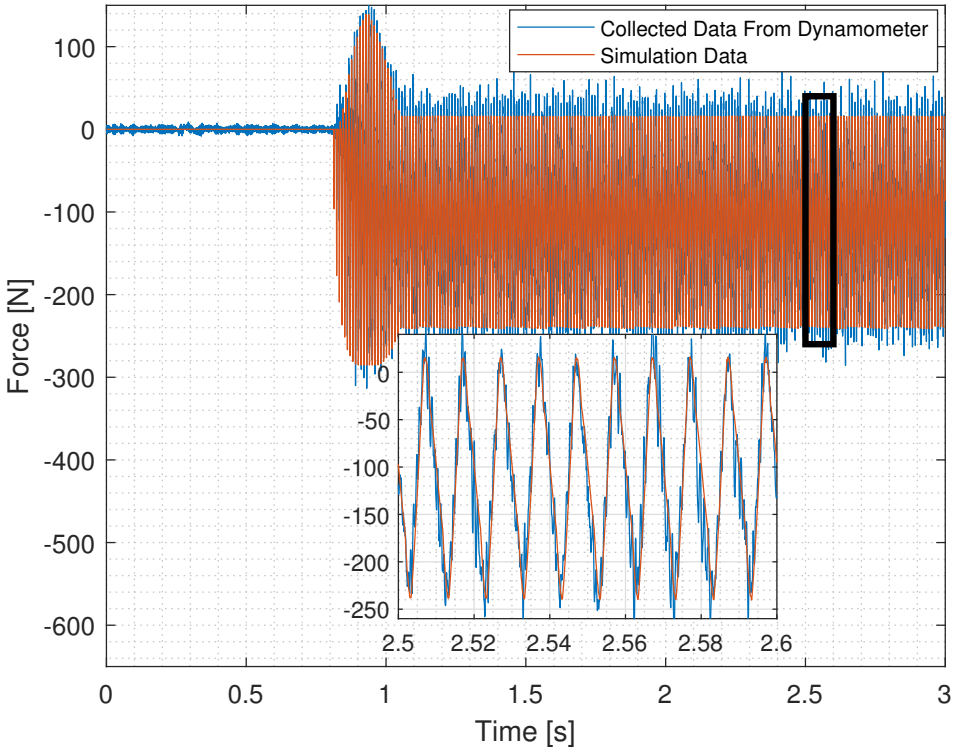


Figure 3.6: Verification of the Force Model for F_x - Test 1

Verification of F_x is conducted by comparing the simulation data, calculated using the identified force coefficients, with the collected force data from the dynamometer. The detailed results are shown in Figure 3.6.

It can be concluded that both the identified parameters and the force model perform accurately in this test for the feed force direction, F_x.

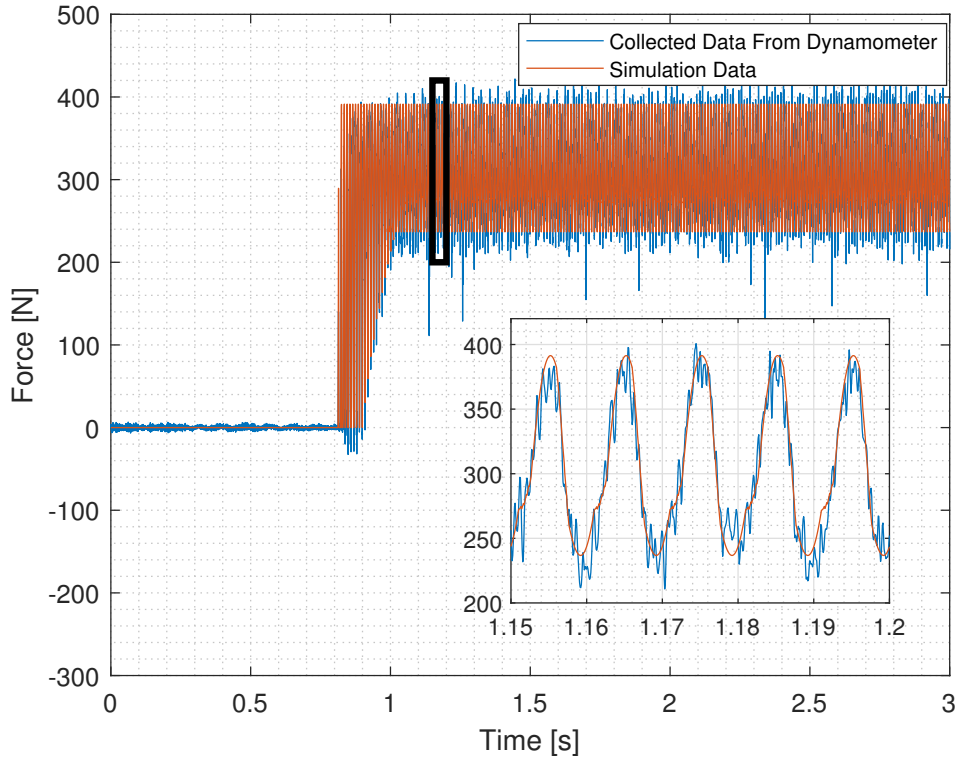


Figure 3.7: Verification of the Force Model for F_y - Test 1

Verification of F_y is performed by comparing the simulation data, calculated using the identified force coefficients, with the collected force data from the dynamometer. The detailed results are presented in Figure 3.7.

It can be concluded that both the identified parameters and the force model demonstrate accurate performance in this test for the normal force direction, F_y.

3.2.2 Force Model Verification Test 2

The second test can be described with the process parameters that are depicted in Table 3.8

In this test, the spindle position data is recorded at a sampling rate of 1,000 Hz, while the forces F_x and F_y are recorded at a sampling rate of 12,800 Hz.

During the identification of the unknown force coefficients K_{tc}, K_{te}, K_{rc}, and K_{re},

Table 3.8: Test 2 Process Parameters Table

Process Parameters	**Unit**	**Value**
Feedrate, F	mm/min	1000
Spindle Speed, ω_s	rpm	2400
Axial Depth of Cut, a_p	mm	3
Radial Depth of Cut, a_e	mm	16
Number of tooth on Cutter, N	-	3
Diameter of the Cutter,D	mm	16
Helix angle, β	$^\circ$	45

the built-in Simulink tool, 'Parameter Estimation', is employed to determine these parameters using the following identification options:

- **Optimization Method**: Nonlinear Least Squares
- **Algorithm**: Trust-Region Reflective
- **Parameter Tolerance**: 0.001
- **Function Tolerance**: 0.001
- **Maximum Iterations**: 100
- **Number of Experiment Inputs**: 2
- **Input 1**: Real data of F_x from the dynamometer
- **Input 2**: Real data of F_y from the dynamometer
- **Number of Experiment Outputs**: 2
- **Output 1**: Calculated force, F_x, from the Force Model
- **Output 2**: Calculated force, F_y, from the Force Model

The cutting force coefficients for the tool, determined through optimization methods, are presented in Table 3.9.

Table 3.9: Force Coefficients Results from Parameter Estimation Tool

$K_{tc}\ [\frac{N}{mm^2}]$	$K_{te}\ [\frac{N}{mm}]$	$K_{rc}\ [\frac{N}{mm^2}]$	$K_{re}\ [\frac{N}{mm}]$
682.27	30.22	106.96	34.652

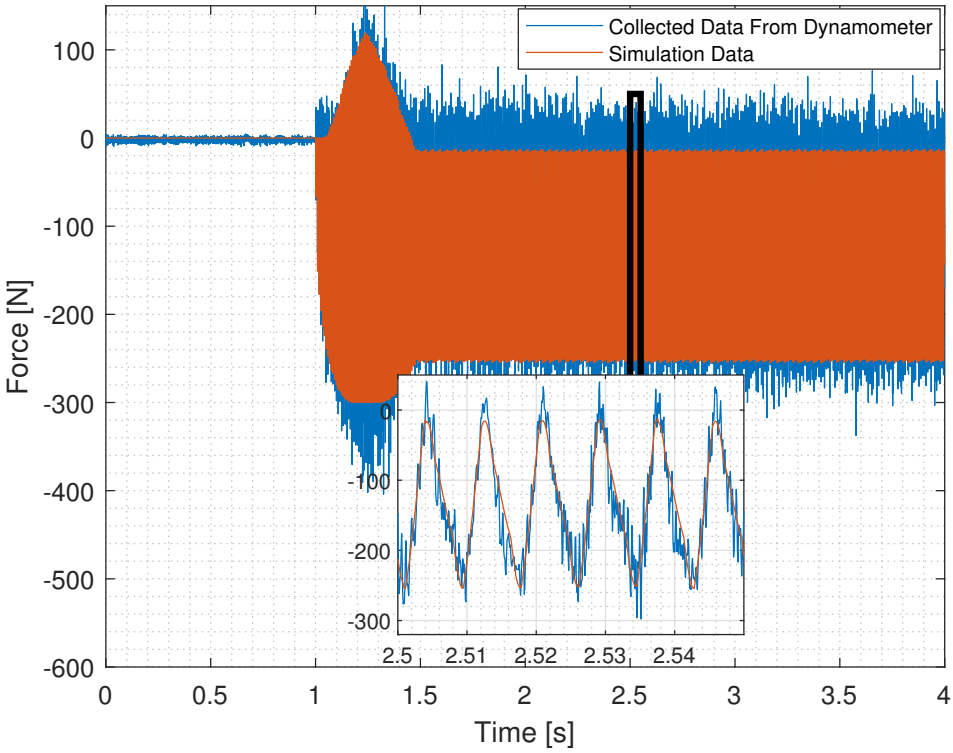


Figure 3.8: Verification of the Force Model for F_x - Test 2

Verification of F_x is conducted by comparing the simulation data, calculated using the identified force coefficients, with the collected force data from the dynamometer. The detailed results are shown in Figure 3.8.

It can be concluded that both the identified parameters and the force model perform accurately in this test for the feed force direction, F_x.

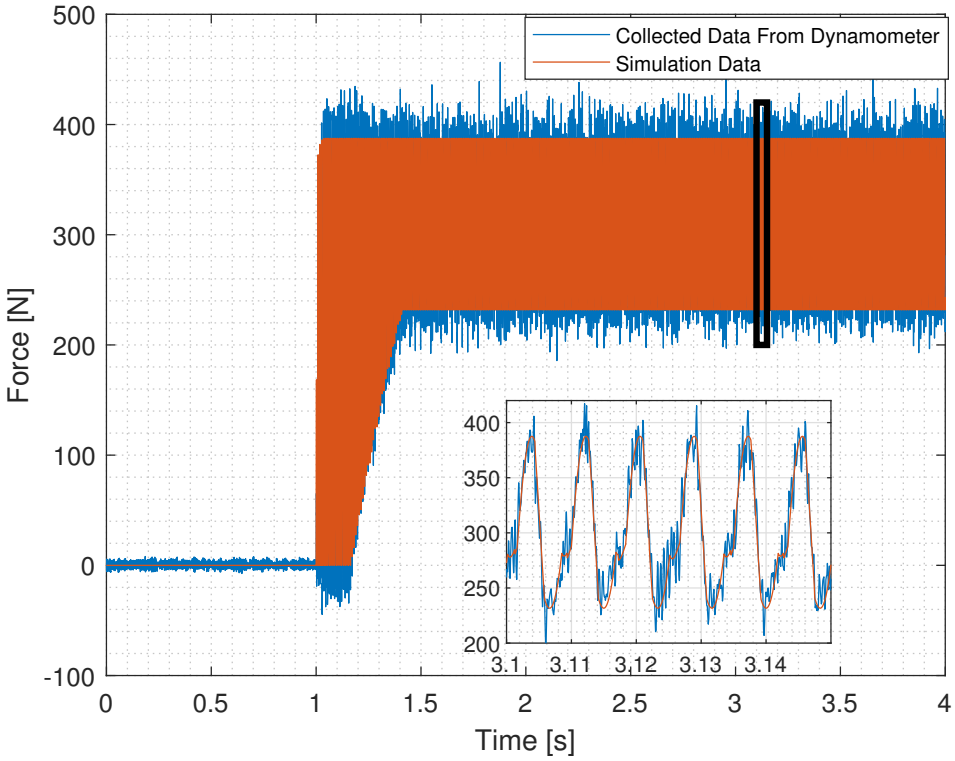


Figure 3.9: Verification of the Force Model for F_y - Test 2

Verification of F_y is performed by comparing the simulation data, calculated using the identified force coefficients, with the collected force data from the dynamometer. The detailed results are presented in Figure 3.9.

It can be concluded that both the identified parameters and the force model demonstrate accurate performance in this test for the normal force direction, F_y.

3.2.3 Force Model Verification Test 3

The first test can be described with the process parameters that are depicted in Table 3.10

In this test, the spindle position data is recorded at a sampling rate of 1,000 Hz, while the forces F_x and F_y are recorded at a sampling rate of 12,800 Hz.

During the identification of the unknown force coefficients K_{tc}, K_{te}, K_{rc}, and K_{re},

Table 3.10: Test 3 Process Parameters Table

Process Parameters	**Unit**	**Value**
Feedrate, F	mm/min	3000
Spindle Speed, ω_s	rpm	1500
Axial Depth of Cut, a_p	mm	1
Radial Depth of Cut, a_e	mm	8
Number of tooth on Cutter, N	-	4
Diameter of the Cutter,D	mm	16
Helix angle, β	$^\circ$	45

the built-in Simulink tool, 'Parameter Estimation', is employed to determine these parameters using the following identification options:

- **Optimization Method**: Nonlinear Least Squares
- **Algorithm**: Trust-Region Reflective
- **Parameter Tolerance**: 0.001
- **Function Tolerance**: 0.001
- **Maximum Iterations**: 100
- **Number of Experiment Inputs**: 2
- **Input 1**: Real data of F_x from the dynamometer
- **Input 2**: Real data of F_y from the dynamometer
- **Number of Experiment Outputs**: 2
- **Output 1**: Calculated force, F_x, from the Force Model
- **Output 2**: Calculated force, F_y, from the Force Model

The cutting force coefficients for the tool, which has a diameter of 12 mm, determined through optimization methods, are presented in Table 3.11.

Table 3.11: Force Coefficients Results from Parameter Estimation Tool

$K_{tc}\ [\frac{N}{mm^2}]$	$K_{te}\ [\frac{N}{mm}]$	$K_{rc}\ [\frac{N}{mm^2}]$	$K_{re}\ [\frac{N}{mm}]$
716.38	28.71	112.31	32.92

The cutting force coefficients for the tool, which has a diameter of 16 mm and three teeth on the cutter, determined through optimization methods, are presented in Table 3.11.

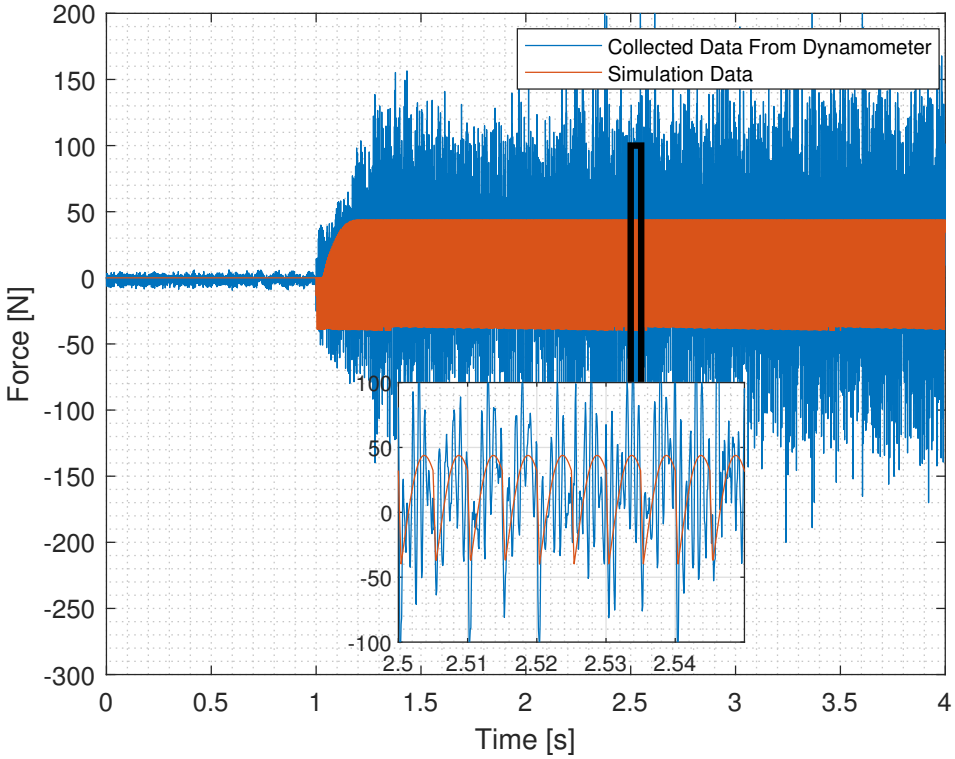


Figure 3.10: Verification of the Force Model for F_x - Test 3

Verification of F_x is conducted by comparing the simulation data, calculated using the identified force coefficients, with the collected force data from the dynamometer. The detailed results are shown in Figure 3.10.

It can be concluded that both the identified parameters and the force model perform accurately in this test for the feed force direction, F_x.

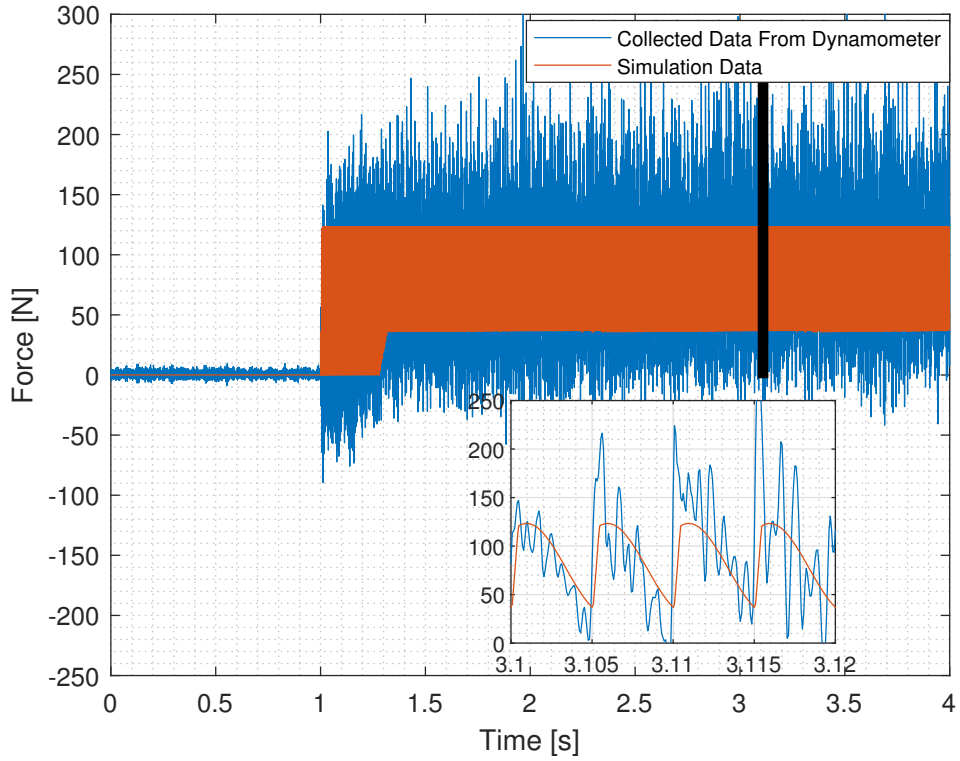


Figure 3.11: Verification of the Force Model for F_y - Test 3

Verification of F_y is performed by comparing the simulation data, calculated using the identified force coefficients, with the collected force data from the dynamometer. The detailed results are presented in Figure 3.11.

It can be concluded that both the identified parameters and the force model demonstrate accurate performance in this test for the normal force direction, F_y.

3.3 Verification of the System Model

In this section, the verification of the system model, which encompasses both the electrical and mechanical subsystems, is discussed by testing the mathematical model using the identified unknown parameters. Two verification tests are performed.

In the first verification test, the system is evaluated using the inputs V_{dss} and V_{qss}, which are the transformed values of the recorded driver data, V_{dse} and V_{qse}, without

any external load or disturbance torque. This test is referred to as the "Open Loop Verification Test without Disturbance Torque."

In the second verification test, the system is subjected to similar inputs, V_{dss} and V_{qss}, but with an added disturbance torque. Consequently, this test is termed the "Open Loop Verification Test with Disturbance Torque."

3.3.1 Open Loop Verification Test without Disturbance Torque

In this verification test, the voltages V_{dse} and V_{qse}, measured by the driver, are transformed into V_{dss} and V_{qss}. These transformed voltages are then applied to the system as inputs. During this verification, both the electrical and mechanical subsystem models are evaluated. Additionally, the results of the identification methods and tests discussed in Subsections 3.1.1 and 3.1.2 are similarly validated.

For verification purposes, the currents I_{dse} and I_{qse}, which are transformed from the simulation data I_{dse} and I_{qse}, are compared with the simulation results. Additionally, the recorded motor velocity data, ω_m, is also compared with the corresponding simulation output.

The general schematic for this verification process is illustrated in Figure 3.12.

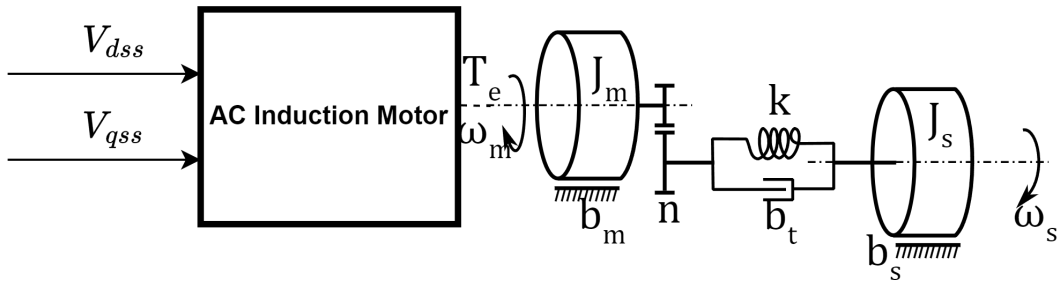


Figure 3.12: General Schematic for the Open Loop Verification Test without Disturbance Torque

The recorded driver data, V_{dse} and V_{qse}, are transformed into V_{dss} and V_{qss} using the "Inverse Park Transform" within the simulation. The corresponding Simulink block and its inputs are depicted in Figure 3.13.

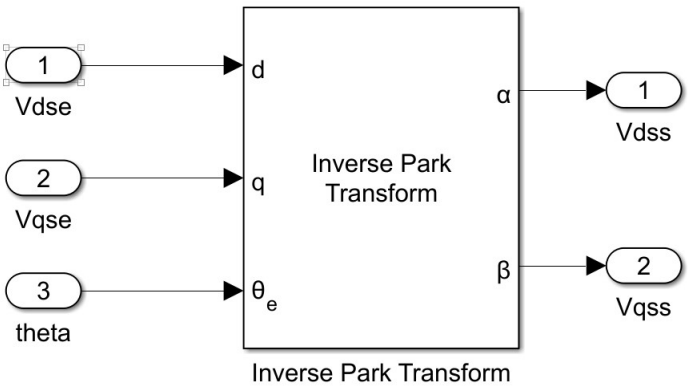


Figure 3.13: Inverse Park Transform for Input Voltages

The following mathematical relationship is utilized for the Inverse Park Transform of the voltages:

$$\begin{bmatrix} V_{dss} \\ V_{qss} \end{bmatrix} = \begin{bmatrix} \cos(\theta_e) & -\sin(\theta_e) \\ \sin(\theta_e) & \cos(\theta_e) \end{bmatrix} \begin{bmatrix} V_{dse} \\ V_{qse} \end{bmatrix} \tag{3.21}$$

The electrical angle, θ_e, is obtained from the motor shaft angle, θ_m, using the following mathematical relationship, with the assumption that the slip angle is approximately zero. This assumption holds due to the use of slip compensation in the driver controller, a method aimed at minimizing slip during operation.

$$\theta_r = \theta_m p \tag{3.22}$$

$$\theta_e \approx \theta_r \tag{3.23}$$

In the simulation, the block for induction motor that incorporates the stator dynamic model, as shown in Figure 2.3, and the rotor dynamic model, as depicted in Figure 2.4, is presented in Figure 3.14.

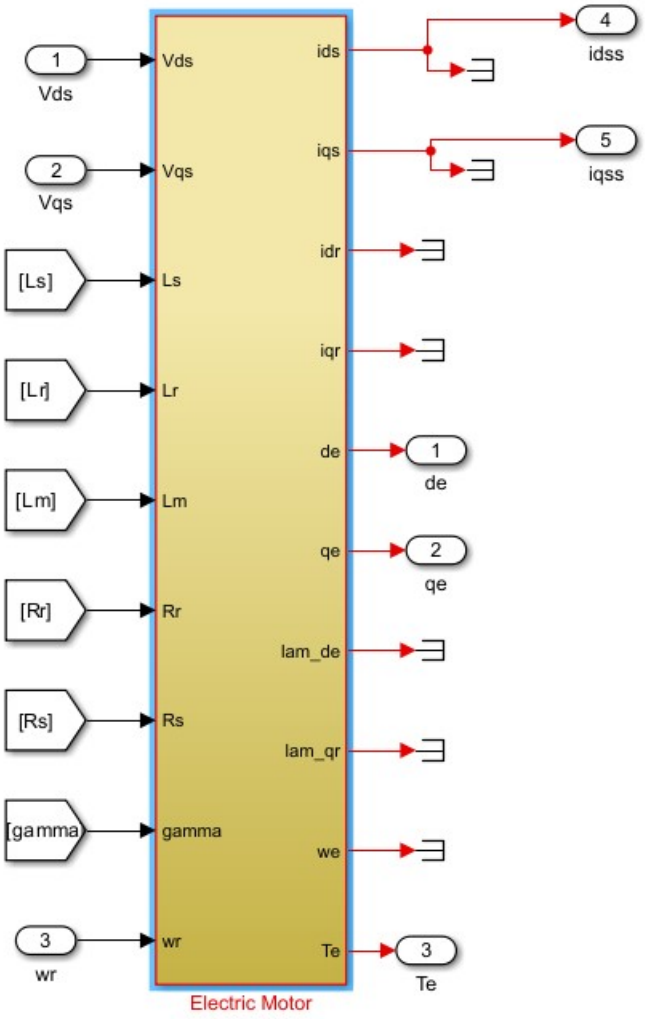


Figure 3.14: Electric Motor Block Simulation

In the simulation, the block for mechanical subsystem which uses block diagram, as shown in Figure 2.6-(b), is presented in Figure 3.15

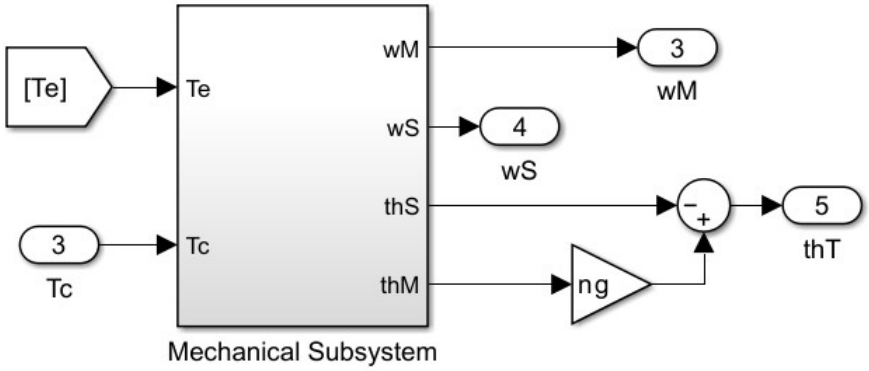


Figure 3.15: Electric Motor Block Simulation

For the Open-Loop Test, reference motor velocity input $\omega_{m,ref}$ is given to the driver starting from 1000 rpm to 3750 rpm.

Figure 3.16 presents a comparison between the simulation results and the collected driver data for the direct axis synchronous reference frame current, I_{dse}.

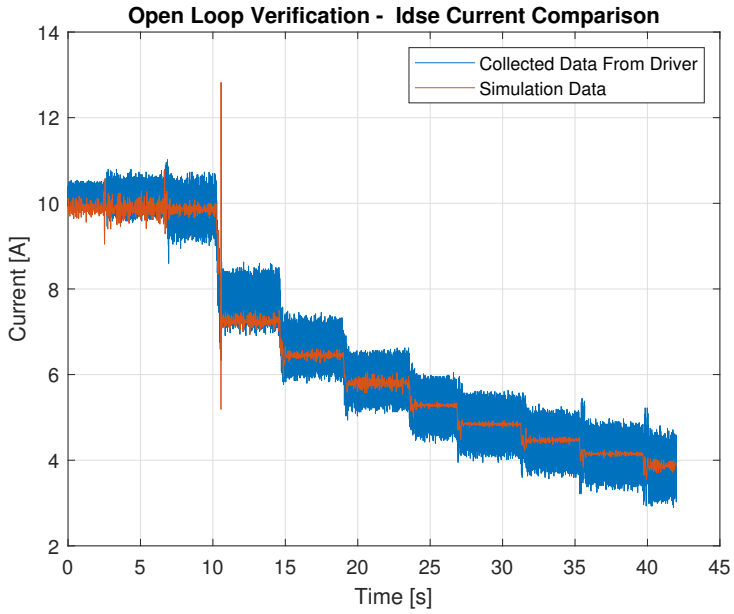


Figure 3.16: Simulation and Driver I_{dse} Data Comparison

Figure 3.16 demonstrates that the simulation results and the collected driver data for I_{dse} show similar trends across different velocity references. As expected, the sim-

ulation data appears clearer, as noise from current sensors and other sources is not modeled in the simulation. During the onset of field weakening, the absolute magnitude of the error between the simulation and driver data increases, which is noticeable between 10 and 15 seconds in the figure. However, beyond this region, the error between the mean values of the driver data and the simulation data decreases.

Figure 3.17 presents a comparison between the simulation results and the collected driver data for the quadrature axis synchronous reference frame current, I_{qse}.

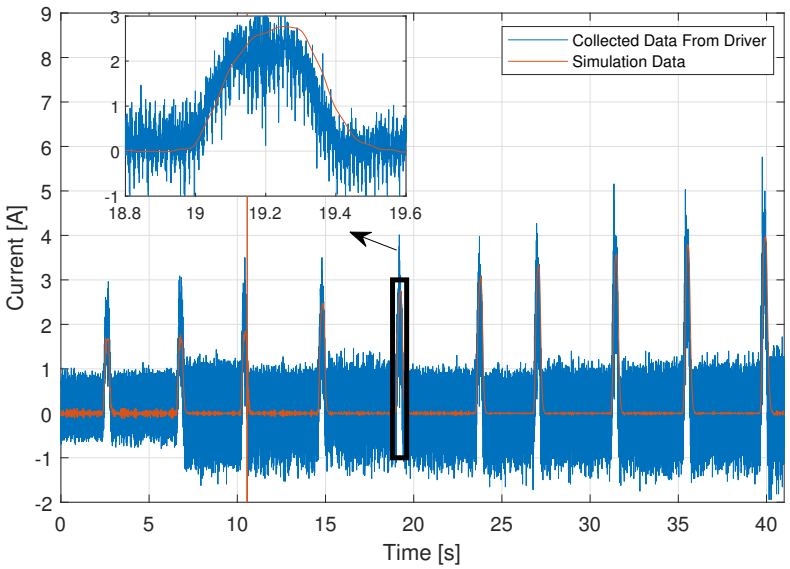


Figure 3.17: Simulation and Driver I_{qse} Data Comparison

Figure 3.17 illustrates that the simulation results and the collected driver data for I_{qse} exhibit similar behavior across different velocity references. It is also observed that the driver data contains some noise, which is not accounted for in the simulation model. Since I_{qse} is more closely related to the torque than I_{dse}, it is expected to increase as the velocity reference increases and to approach nearly zero after the system reaches steady-state velocity, depending on the friction in the mechanical subsystem. A more detailed investigation of this trend, as shown in the zoomed region of the figure between 18.8 and 19.6 seconds, reveals that both datasets yield comparable results.

Figure 3.18 presents a comparison between the simulation results and the collected

driver data for motor velocity, ω_m.

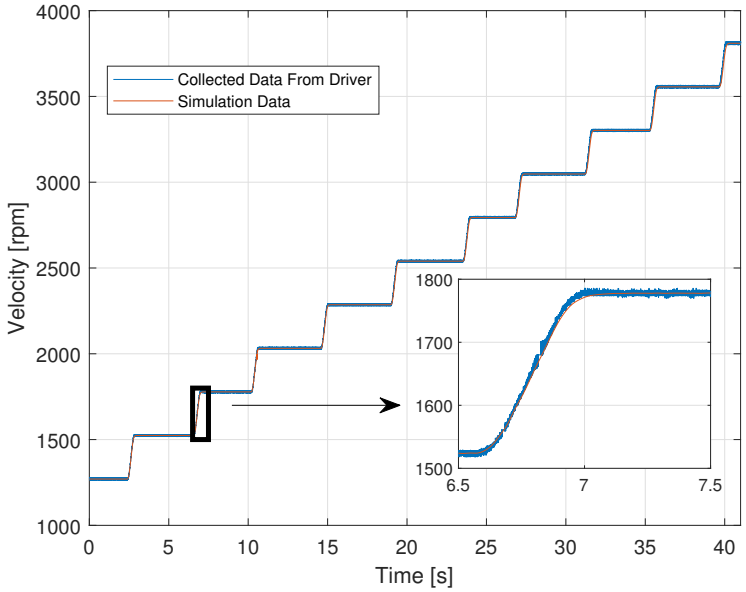


Figure 3.18: Simulation and Driver ω_m Data Comparison

Figure 3.18 demonstrates that the simulation results and the collected driver data for ω_m exhibit similar behavior across different velocity references. It is also observed that the driver motor velocity data contains some noise, which is not modeled in the simulation. In this comparison, particular attention should be given to the transient state, where the reference signal is increasing, as it highlights the effect of acceleration on the inertia of the mechanical subsystem. From zoomed area between 6.5 and 7.5 seconds in the Figure, it can be concluded that these trends are consistent with each other.

Figures 3.16, 3.17, and 3.18 illustrate the performance of the mathematical model in representing the real system and the accuracy of the identified unknown parameters. Figures 3.16 and 3.17 depict the performance of the electrical subsystem, and it can be clearly stated that the electrical subsystem is modeled with an accurate mathematical representation and precise parameter identification. Figure 3.18 demonstrates the performance of the mechanical subsystem model and the accuracy of the identified unknown mechanical parameters. Consequently, it can be concluded that, in the absence of disturbance torque, the system model yields accurate results.

3.3.2 Open Loop Verification Test with Disturbance Torque

In this verification test, the voltages V_{dse} and V_{qse}, measured by the driver, are transformed into V_{dss} and V_{qss}. These transformed voltages are then applied to the system as inputs.

The verification assesses the performance of both the electrical and mechanical subsystems under disturbance torque. Additionally, this evaluation tests the accuracy of the identification methods discussed in Subsections 3.1.1 and 3.1.2.

For verification purposes and generating input data for the simulation, voltages and currents that are represented in synchronous reference frame are transformed into stationary reference frame by using the same method discussed in Subsection 3.3.1

The general schematic for this verification process is depicted in Figure 3.19.

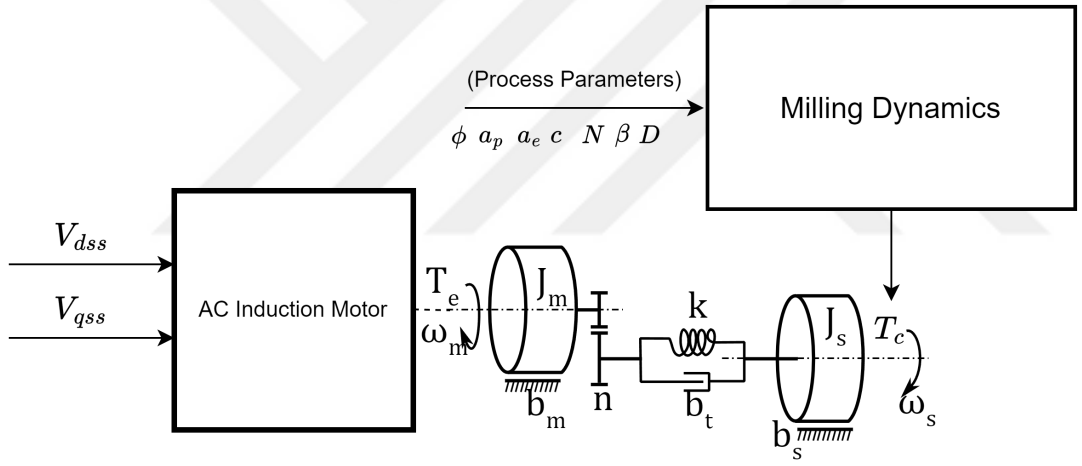


Figure 3.19: General Schematic for the Open Loop Verification Test with Disturbance Torque

As shown in Figure 3.19, the disturbance torque applied to the system is computed using the milling force dynamics model and corresponds to the tangential cutting torque, T_c.

The same simulation blocks depicted in Figures 3.14 and 3.15 are utilized for this verification test as well.

In this verification test, the disturbance torque, calculated from the milling force dynamics, is applied to the system. The process parameters for the cutting operation, used to calculate the tangential cutting torque T_c (applied as the disturbance torque T_d), are presented in Table 3.12.

Table 3.12: Process Parameters

$\omega_s[rpm]$	$F[mm/min]$	$a_p[mm]$	$a_e[mm]$
2000	1500	2	12

The calculated tangential cutting torque, T_c, is shown in Figure 3.20.

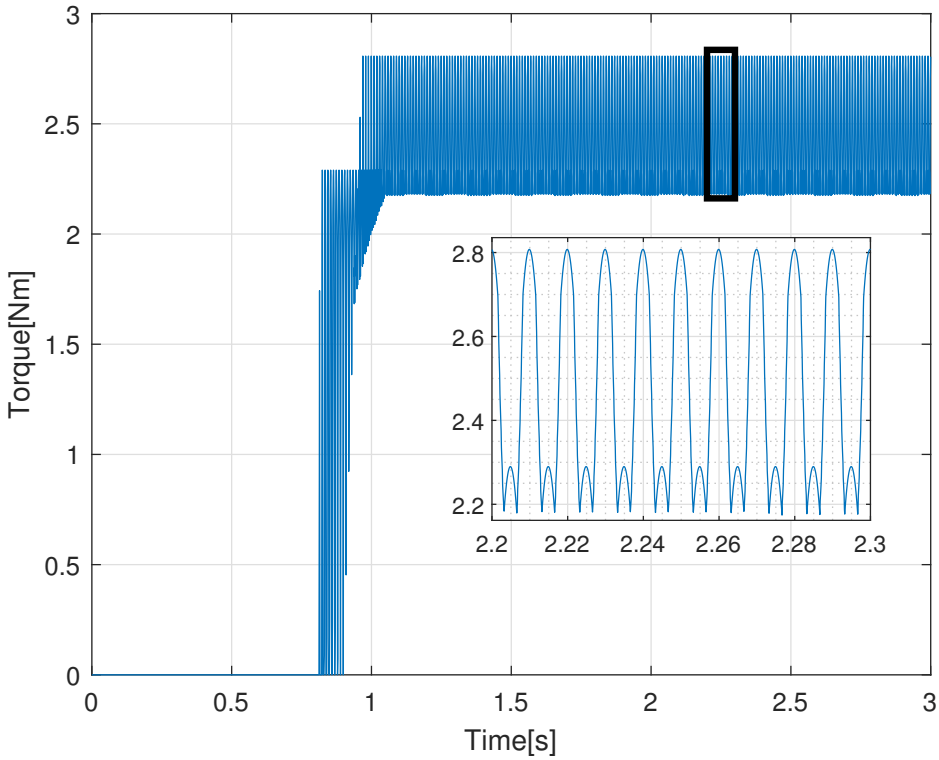


Figure 3.20: Calculated Tangential Cutting Torque T_c

Figure 3.21 presents a comparison between the simulation data and the collected driver data for the direct axis synchronous reference frame current, I_{dse}.

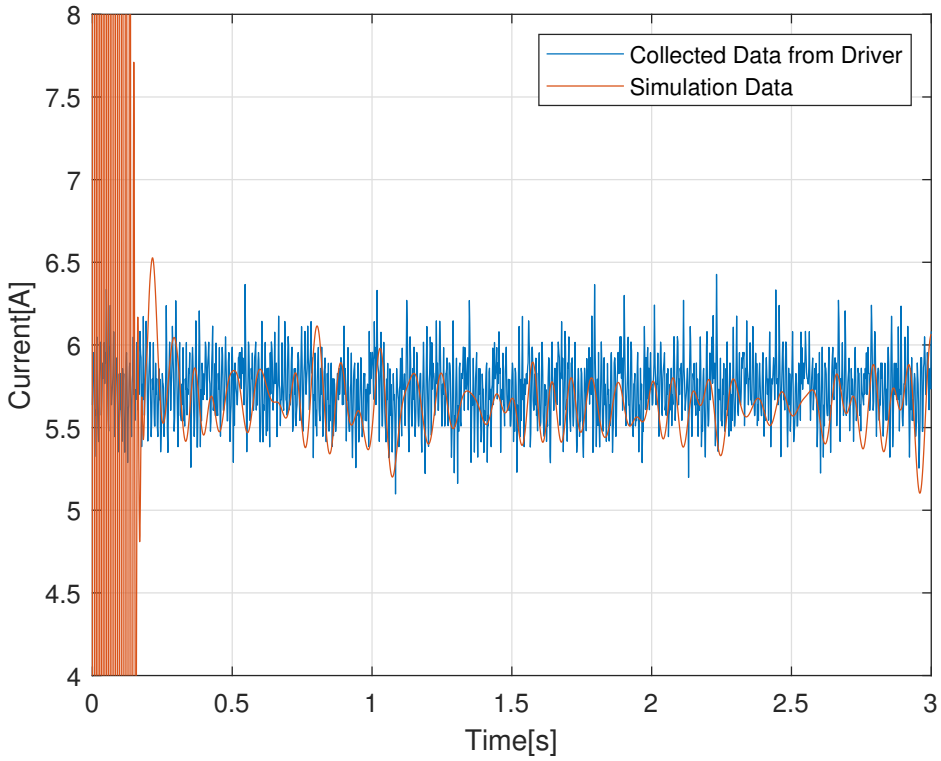


Figure 3.21: Simulation and Driver I_{dse} Data Comparison

Figure 3.21 shows that the simulation results and the collected driver data for I_{dse} exhibit similar trends in both regions, with and without the disturbance effect. As expected, the simulation data appears clearer, as noise sources are not modeled in the simulation.

Figure 3.22 presents a comparison between the simulation data and the collected driver data for the direct axis synchronous reference frame current, I_{dse}.

It should also be noted that in Figures 3.21 and 3.22, the initial results of the simulation display some oscillatory behavior. This occurs because the initial values of variables are assumed to be unknown, and all simulation variables are initialized to zero, which leads to this oscillatory response.

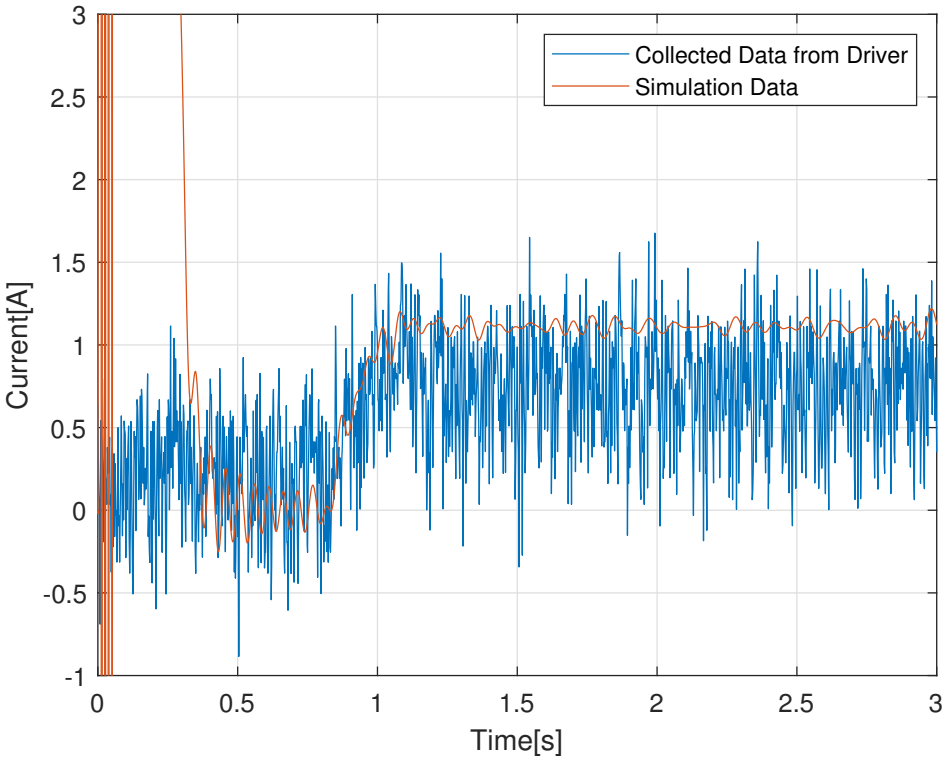


Figure 3.22: Simulation and Driver I_{qse} Data Comparison

Figure 3.22 illustrates that the simulation results and the collected driver data for I_{qse} exhibit similar trends in both the disturbance-free and disturbance-affected regions. As expected, the simulation data appears clearer, as noise sources are not modeled in the simulation.

Upon closer inspection, it can be observed that the error between the real and simulation data is negative prior to the disturbance effect and positive afterward. This suggests there may be minor inaccuracies in the identified parameters of either the mechanical or electrical subsystem. However, given the small magnitude of the error, it can be considered negligible.

Figure 3.23 presents a comparison between the simulation data and the collected driver data for the motor velocity, ω_m.

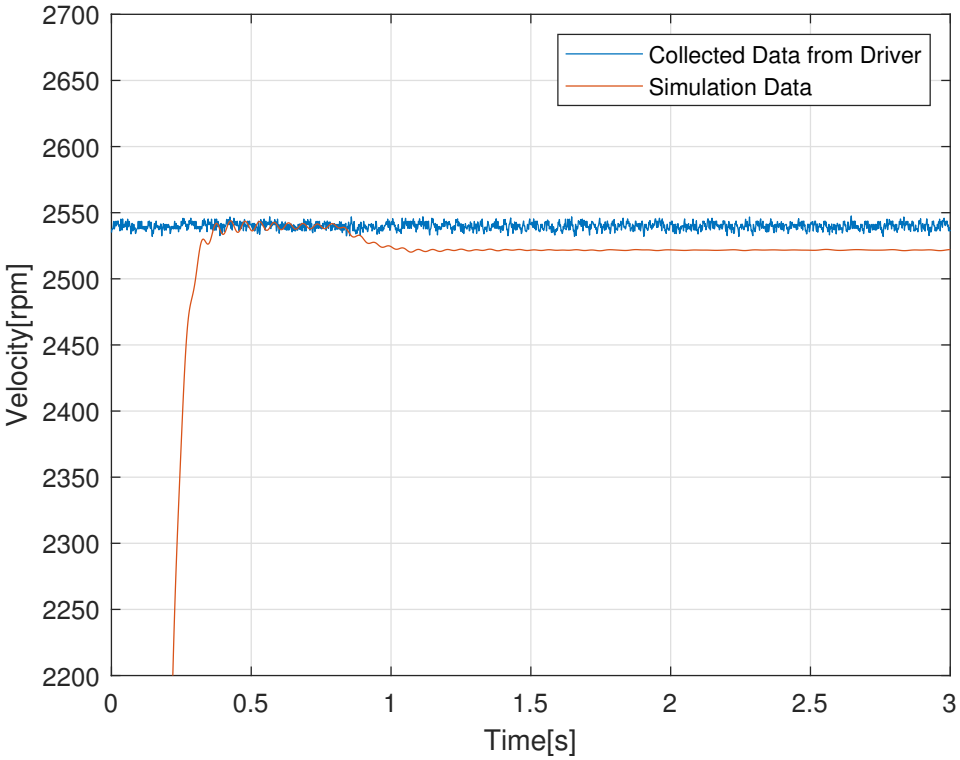


Figure 3.23: Simulation and Driver ω_m Data Comparison

Figure 3.23 shows that the simulation results and the collected data for ω_m exhibit similar trends in both the disturbance-free and disturbance-affected regions. As expected, the simulation data appears clearer, as noise sources are not modeled in the simulation.

Upon closer examination, it can be observed that the motor velocity in the simulation is more affected by the disturbance torque than the real data. This discrepancy may be attributed to slight inaccuracies in the identification of mechanical subsystem parameters, such as the inertias J_m, J_s, or the stiffness k. However, since the error in this region is less than 1%, it can be considered negligible.

CHAPTER 4

CUTTING TORQUE ESTIMATION

This chapter will address the estimation of cutting torque, which constitutes the central focus of this thesis. Various estimation algorithms utilizing the Kalman Filter, each adapted to specific scenarios, will be analyzed. The system model, as outlined in Chapter 2 and validated in Chapter 3, will serve as the foundation for these estimation methods. Additionally, the verification process for these methods and the conditions under which the verification tests are conducted will be discussed.

Five distinct methods are selected for examination. All estimation methods, with the exception of Method 3, utilize the complete system model encompassing both electric and mechanical subsystems, whereas Method 3 exclusively employs the mathematical model of the mechanical subsystem.

For methods utilizing the full system model, the Extended Kalman Filter (EKF) is applied in place of the standard Kalman Filter to manage the nonlinearities introduced by the interdependencies between the variables in the electric and mechanical subsystems. The EKF, designed for nonlinear systems, linearizes the system around the current estimate at each iteration, enabling real-time parameter estimation even amidst noise and uncertainties within the model. This approach proves particularly effective for handling nonlinearities in the cutting process while still delivering accurate and recursive state estimations.

The reduction of the system model to a linear form for the application of the Kalman Filter will also be explored in Method 3.

For all methods except Method 4, which is specifically designed to directly estimate the tangential cutting torque T_c, the primary focus is on estimating the force coeffi-

cients K_{tc} and K_{te} rather than the torque itself. These coefficients are directly related to the tangential cutting force that generates the torque. This approach incorporates the geometric relationship at the cutting instance into the estimation process by utilizing the geometric matrix $\mathbf{h}_t$, which is derived from the force model detailed in Section 2.4 and validated in Section 3.2.

4.1 Estimation Methods

In this section, the estimation methods will be discussed in detail.

4.1.1 Method 1

In Method 1, the comprehensive system model, which requires the voltages V_{dss} and V_{qss} as inputs and integrates both the electrical and mechanical subsystems, is employed as the mathematical framework. This estimation technique calculates the tangential cutting torque T_c by evaluating the tangential cutting force coefficients K_{tc} and K_{te}. This method is selected as it enables the integration of the geometric relationship into the estimation process by determining the geometric matrix $\mathbf{h}_t$ utilizing a force model grounded in process parameters and spindle position.

Given that the tangential cutting torque can be represented as $T_c = r(K_{tc}h_{tc}(\phi) + K_{te}h_{te}(\phi))$, the nonlinear differential equations governing the complete system are expressed as follows:

$$\dot{\mathbf{x}} = \mathbf{f}(\mathbf{x}, \mathbf{u}, \phi) + \mathbf{w} \tag{4.1}$$

where the state matrix, $\mathbf{x}$, is defined as follows:

$$\mathbf{x} = \begin{bmatrix} I_{dss} & I_{qss} & I_{drs} & I_{qrs} & \omega_m & \theta_t & \omega_s \end{bmatrix}^T \tag{4.2}$$

where the input matrix ,$\mathbf{u}$, is expressed as follows:

$$\mathbf{u} = \begin{bmatrix} V_{dss} & V_{qss} \end{bmatrix}^T \tag{4.3}$$

Here, $\mathbf{w}$ is the process noise matrix.

where $\mathbf{f}(\mathbf{x}, \mathbf{u}, \phi)$ is expressed as follows:

$$\mathbf{f}(\mathbf{x}, \mathbf{u}, \phi) = \begin{bmatrix} -\frac{L_r R_s}{\gamma} I_{dss} + \frac{L_m^2 \omega_e}{\gamma} I_{qss} + \frac{L_m R_r}{\gamma} I_{drs} + \frac{L_m L_r \omega_e}{\gamma} I_{qrs} + \frac{L_r}{\gamma} V_{dss} \\ -\frac{L_m^2 \omega_e}{\gamma} I_{dss} - \frac{L_r R_s}{\gamma} I_{qss} - \frac{L_m L_r \omega_e}{\gamma} I_{drs} + \frac{L_m R_r}{\gamma} I_{qrs} + \frac{L_r}{\gamma} V_{qss} \\ \frac{L_m R_s}{\gamma} I_{dss} - \frac{L_s L_m \omega_e}{\gamma} I_{qss} - \frac{R_r L_s}{\gamma} I_{drs} - \frac{L_s L_r \omega_e}{\gamma} I_{qrs} - \frac{L_m}{\gamma} V_{dss} \\ \frac{L_s L_m \omega_e}{\gamma} I_{dss} + \frac{L_m R_s}{\gamma} I_{qss} + \frac{L_s L_r \omega_e}{\gamma} I_{drs} - \frac{R_r L_s}{\gamma} I_{qrs} - \frac{L_m}{\gamma} V_{qss} \\ \frac{1}{J_m}[K_t(I_{qss} I_{drs} - I_{qrs} I_{dss}) - (n_g^2 b_t + b_m)\omega_m - k n_g \theta_t + b_t n_g \omega_s] \\ n_g \omega_m - \omega_s \\ \frac{1}{J_s}[n_g b_t \omega_m + k\theta_t - (b_t + b_s)\omega_s - r(K_{tc} h_{tc}(\phi) + K_{te} h_{te}(\phi))] \end{bmatrix} \tag{4.4}$$

As this estimation method primarily estimates the coefficients, these coefficients should be incorporated as additional state variables by augmenting the equations in Equation 4.1. This can be expressed as follows:

$$\dot{\mathbf{x}}' = f'(\mathbf{x}', \mathbf{u}, \phi) + \mathbf{w}' \tag{4.5}$$

where the augmented state matrix, $\mathbf{x}'$, is defined as follows:

$$\mathbf{x}' = \begin{bmatrix} I_{dss} & I_{qss} & I_{drs} & I_{qrs} & \omega_m & \theta_t & \omega_s & K_{tc} & K_{te} \end{bmatrix}^T \tag{4.6}$$

where $f'(\mathbf{x}', \mathbf{u}, \phi)$ is expressed as follows:

$$f'(\mathbf{x}', \mathbf{u}, \phi) = \begin{bmatrix} -\frac{L_r R_s}{\gamma} I_{dss} + \frac{L_m^2 \omega_e}{\gamma} I_{qss} + \frac{L_m R_r}{\gamma} I_{drs} + \frac{L_m L_r \omega_e}{\gamma} I_{qrs} + \frac{L_r}{\gamma} V_{dss} \\ -\frac{L_m^2 \omega_e}{\gamma} I_{dss} - \frac{L_r R_s}{\gamma} I_{qss} - \frac{L_m L_r \omega_e}{\gamma} I_{drs} + \frac{L_m R_r}{\gamma} I_{qrs} + \frac{L_r}{\gamma} V_{qss} \\ \frac{L_m R_s}{\gamma} I_{dss} - \frac{L_s L_m \omega_e}{\gamma} I_{qss} - \frac{R_r L_s}{\gamma} I_{drs} - \frac{L_s L_r \omega_e}{\gamma} I_{qrs} - \frac{L_m}{\gamma} V_{dss} \\ \frac{L_s L_m \omega_e}{\gamma} I_{dss} + \frac{L_m R_s}{\gamma} I_{qss} + \frac{L_s L_r \omega_e}{\gamma} I_{drs} - \frac{R_r L_s}{\gamma} I_{qrs} - \frac{L_m}{\gamma} V_{qss} \\ \frac{1}{J_m}[K_t(I_{qss} I_{drs} - I_{qrs} I_{dss}) - (n_g^2 b_t + b_m)\omega_m - k n_g \theta_t + b_t n_g \omega_s] \\ n_g \omega_m - \omega_s \\ \frac{1}{J_s}[n_g b_t \omega_m + k\theta_t - (b_t + b_s)\omega_s - r(K_{tc} h_{tc}(\phi) + K_{te} h_{te}(\phi))] \\ 0 \\ 0 \end{bmatrix} \tag{4.7}$$

Equation 4.5 can be discretized using the Forward Euler method, as shown in Equation 4.8

$$\mathbf{x}_{k+1} = \mathbf{x}_k + T_s(\mathbf{f}(\mathbf{x}_k, \mathbf{u}_k, \phi_k) + \mathbf{w}) \tag{4.8}$$

where $\mathbf{x}_k = [I_{dss,k}, I_{qss,k}, I_{drs,k}, I_{qrs,k}, \omega_{m,k}, \theta_{T,k}, \omega_{s,k}, K_{tc,k}, K_{te,k}]^T$ represents the augmented state vector, and $\mathbf{u}_k = [V_{dss,k}, V_{qss,k}]^T$ denotes the input vector.

$\mathbf{f}(\mathbf{x}_k, \mathbf{u}_k, \phi_k)$ is represented by the following equation:

$$\mathbf{f}(\mathbf{x}_k, \mathbf{u}_k, \phi_k) = \begin{bmatrix} -\frac{L_r R_s}{\gamma} I_{dss,k} + \frac{L_m^2 \omega_e}{\gamma} I_{qss,k} + \frac{L_m R_r}{\gamma} I_{drs,k} + \frac{L_m L_r \omega_e}{\gamma} I_{qrs,k} + \frac{L_r}{\gamma} V_{dss,k} \\ -\frac{L_m^2 \omega_e}{\gamma} I_{dss,k} - \frac{L_r R_s}{\gamma} I_{qss,k} - \frac{L_m L_r \omega_e}{\gamma} I_{drs,k} + \frac{L_m R_r}{\gamma} I_{qrs,k} + \frac{L_r}{\gamma} V_{qss,k} \\ \frac{L_m R_s}{\gamma} I_{dss,k} - \frac{L_s L_m \omega_e}{\gamma} I_{qss,k} - \frac{R_r L_s}{\gamma} I_{drs,k} - \frac{L_s L_r \omega_e}{\gamma} I_{qrs,k} - \frac{L_m}{\gamma} V_{dss,k} \\ \frac{L_s L_m \omega_e}{\gamma} I_{dss,k} + \frac{L_m R_s}{\gamma} I_{qss,k} + \frac{L_s L_r \omega_e}{\gamma} I_{drs,k} - \frac{R_r L_s}{\gamma} I_{qrs,k} - \frac{L_m}{\gamma} V_{qss,k} \\ \frac{1}{J_m}\left[T_{e,k} - (n_g^2 b_t + b_m)\omega_{m,k} - k n_g \theta_{t,k} + b_t n_g \omega_{s,k}\right] \\ n_g \omega_{m,k} - \omega_{s,k} \\ \frac{1}{J_s}\left[n_g b_t \omega_{m,k} + k\theta_{t,k} - b_t' \omega_{s,k} - r(K_{tc,k} h_{tc,k}(\phi_k) + K_{te,k} h_{te,k}(\phi_k))\right] \\ 0 \\ 0 \end{bmatrix} \tag{4.9}$$

where $T_{e,k} = K_t(I_{qss,k} I_{drs,k} - I_{qrs,k} I_{dss,k})$ and $b_t' = b_t + b_s$

Algorithm 2 Calculation of Geometry Matrix Components

Require: ϕ, ϕ_{st},ϕ_{ex},β,D,N,a_p

Ensure: $h_{tc}(\phi)$,$h_{te}(\phi)$

$L = 25$
$\phi_p = \frac{2\pi}{N}$
$d_a = \frac{a_p}{L}$
$h_{tc}(\phi) = 0$
$h_{te}(\phi) = 0$
while $k \leq N$ **do**
    $\phi_1 = \phi + (k-1)\phi_p$
    while $j \leq L$ **do**
        $\phi_2 = \phi_1 + \frac{2\tan(\beta)}{D}(jd_a)$
        if $\phi_{st} \leq mod(\phi_2, 2\pi)$ & $\phi_{ex} \geq mod(\phi_2, 2\pi)$ **then**
            $h = c\sin(\phi_2)$
            $dh_{tc}(\phi) = d_a h$
            $dh_{te}(\phi) = d_a$
            $h_{tc}(\phi) = h_{tc}(\phi) + dh_{tc}(\phi)$
            $h_{te}(\phi) = h_{te}(\phi) + dh_{te}(\phi)$
        end if
        $j = j + 1$
    end while
    $k = k + 1$
end while

Algorithm 2 presents the steps for calculating the geometry matrix components $h_{tc}(\phi)$ and $h_{te}(\phi)$.

As a result, the Extended Kalman Filter is employed as an observer to address the nonlinearities within the equations. The formulation of the Extended Kalman Filter, as detailed in [15], and applied through the recursive steps of the algorithm, can be defined as follows:

$$\mathbf{K}_k = \mathbf{P}_k^- \mathbf{H}_k^T (\mathbf{H}_k \mathbf{P}_k^- \mathbf{H}_k^T + \mathbf{R}_k)^{-1} \tag{4.10}$$

$$\hat{\mathbf{x}}_k = \hat{\mathbf{x}}_k^- + \mathbf{K}_k (\mathbf{z}_k - \mathbf{H}_k \hat{\mathbf{x}}_k^-) \tag{4.11}$$

$$\mathbf{P}_k = (\mathbf{I} - \mathbf{K}_k \mathbf{H}_k) \mathbf{P}_k^- \tag{4.12}$$

$$\hat{\mathbf{x}}_{k+1}^- = \hat{\mathbf{x}}_k + T_s \mathbf{f}(\hat{\mathbf{x}}_k, \mathbf{u}_k, \phi_k) \tag{4.13}$$

$$\mathbf{P}_{k+1}^- = \mathbf{J}_k \mathbf{P}_k \mathbf{J}_k^T + \mathbf{Q}_k \tag{4.14}$$

As the computation of the prior covariance matrix $\mathbf{P}_k^-$ necessitates the linearization of $\mathbf{f}(\mathbf{x}, \mathbf{u}, t)$, it is essential to calculate the Jacobian matrix of this nonlinear function. The Jacobian matrix, $\mathbf{J}$, is expressed as follows:

$$\mathbf{J} = \left[\begin{array}{c|c} \mathbf{J}_1 \text{ (4x4)} & \mathbf{J}_2\text{(4x5)} \\ \hline \mathbf{J}_3\text{(5x4)} & \mathbf{J}_4\text{(5x5)} \end{array}\right] \tag{4.15}$$

$$\mathbf{J_1} = \begin{bmatrix} -\frac{L_r R_s}{\gamma} & \frac{L_m^2 \omega_e}{\gamma} & \frac{L_m R_r}{\gamma} & \frac{L_m L_r \omega_e}{\gamma} \\ -\frac{L_m^2 \omega_e}{\gamma} & -\frac{L_r R_s}{\gamma} & -\frac{L_m L_r \omega_e}{\gamma} & \frac{L_m R_r}{\gamma} \\ \frac{L_m R_s}{\gamma} & -\frac{L_s L_m \omega_e}{\gamma} & -\frac{R_r L_s}{\gamma} & -\frac{L_s L_r \omega_e}{\gamma} \\ \frac{L_s L_m \omega_e}{\gamma} & \frac{L_m R_s}{\gamma} & \frac{L_s L_r \omega_e}{\gamma} & -\frac{R_r L_s}{\gamma} \end{bmatrix} \tag{4.16}$$

$$\mathbf{J_2} = \begin{bmatrix} \frac{L_m^2 I_{qss} + L_m L_r I_{qrs}}{\gamma} & 0 & 0 & 0 & 0 \\ -\frac{L_m^2 I_{dss} + L_m L_r I_{drs}}{\gamma} & 0 & 0 & 0 & 0 \\ -\frac{L_m^2 I_{dss} + L_m L_r I_{drs}}{\gamma} & 0 & 0 & 0 & 0 \\ \frac{L_s L_m I_{dss} + L_s L_r I_{drs}}{\gamma} & 0 & 0 & 0 & 0 \end{bmatrix} \tag{4.17}$$

$$\mathbf{J_3} = \begin{bmatrix} -\frac{k_t I_{qrs}}{J_m} & \frac{k_t I_{drs}}{J_m} & \frac{k_t I_{qss}}{J_m} & -\frac{k_t I_{dss}}{J_m} \\ 0 & 0 & 0 & 0 \\ 0 & 0 & 0 & 0 \\ 0 & 0 & 0 & 0 \\ 0 & 0 & 0 & 0 \end{bmatrix} \tag{4.18}$$

$$\mathbf{J_4} = \begin{bmatrix} -\frac{b_t n_g^2 + b_m}{J_m} & -\frac{k n_g}{J_m} & \frac{b_t n_g}{J_m} & 0 & 0 \\ n_g & 0 & -1 & 0 & 0 \\ \frac{n_g b_t}{J_s} & \frac{k}{J_s} & -\frac{b_t + b_s}{J_s} & -\frac{r h_{tc}(\phi)}{J_s} & -\frac{r h_{te}(\phi)}{J_s} \\ 0 & 0 & 0 & 0 & 0 \\ 0 & 0 & 0 & 0 & 0 \end{bmatrix} \tag{4.19}$$

Since the EKF operates in discrete time, $\mathbf{J}$ needs to be discretized. The discretization of $\mathbf{J}$ is performed using the following formulas:

$$\mathbf{J}_k = e^{\mathbf{J}T_s} \tag{4.20}$$

It can be also approximately discretized with using Forward Euler Method as follows:

$$\mathbf{J}_k = \mathbf{I} + T_s\mathbf{J} \tag{4.21}$$

Since the test setup provides measurement data for I_{dse}, I_{qse}, ω_m, θ_T, and ω_s, and it is known that the conversion between the synchronous and stationary frames for the currents can be performed using the 'Inverse Park Transformation', the measurement vector, $\mathbf{z}_k$, and the measurement matrix, $\mathbf{H}_k$, are defined as shown in Equations 4.22 and 4.23.

$$\mathbf{z}_k = \begin{bmatrix} I_{dss,k} & I_{qss,k} & \omega_{m,k} & \theta_{t,k} & \omega_s \end{bmatrix}^T \tag{4.22}$$

$$\mathbf{H}_k = \begin{bmatrix} 1 & 0 & 0 & 0 & 0 & 0 & 0 & 0 & 0 \\ 0 & 1 & 0 & 0 & 0 & 0 & 0 & 0 & 0 \\ 0 & 0 & 0 & 0 & 1 & 0 & 0 & 0 & 0 \\ 0 & 0 & 0 & 0 & 0 & 1 & 0 & 0 & 0 \\ 0 & 0 & 0 & 0 & 0 & 0 & 1 & 0 & 0 \end{bmatrix} \tag{4.23}$$

In Method 1, the process noise covariance matrix, $\mathbf{Q}_k$, is defined as a diagonal matrix to represent the assumption that the process noise components are uncorrelated.

$$\mathbf{Q}_k = diag(w^2_{I_{dss}}, w^2_{I_{qss}}, w^2_{I_{drs}}, w^2_{I_{qrs}}, w^2_{\omega_m}, w^2_{\theta_t}, w^2_{\omega_s}, w^2_{K_{tc}}, w^2_{K_{te}})T_s^2 \tag{4.24}$$

The diagonal elements of the process noise covariance matrix are defined as follows:

- Through model testing, it was determined that the process noise for I_{dss} between the real system and the model can be at most $w_{I_{dss}} = 0.25\,\text{A}$.
- Similarly, model testing revealed that the process noise for I_{qss} can reach a maximum of $w_{I_{qss}} = 0.25\,\text{A}$.

- Since I_{drs} is not directly measurable, its process noise was identified by analyzing the simulation results, and estimated as $w_{I_{drs}} = \frac{w_{I_{dss}}}{10}$.
- As with I_{drs}, I_{qrs} is not directly measurable. Its process noise was identified through simulation, and estimated as $w_{I_{qrs}} = \frac{w_{I_{qss}}}{10}$.
- After evaluating the model, the process noise for motor speed ω_m was found to be at most $w_{\omega_m} = 0.15\,\text{rad/s}$.
- Similarly, the process noise for spindle speed ω_s was found to be at most $w_{\omega_s} = 0.1\,\text{rad/s}$.
- Since θ_t represents the relative angular position between θ_m and θ_s, the process noise is assumed to be $w_{\theta_t} = \min([w_{\omega_m}, w_{\omega_s}])/10$.
- The process noise for the tangential force coefficient K_{tc} is selected based on the average variation observed during the sampling time, and is set to $w_{K_{tc}} = 10^4\,\frac{\text{N}}{\text{mm}^2}$.
- Similarly, the process noise for the edge force coefficient K_{te} is set based on the observed sampling time variation, with $w_{K_{te}} = 10^3\,\frac{\text{N}}{\text{mm}}$.

The measurement noise covariance matrix, $\mathbf{R}_k$, is chosen as a diagonal matrix, with the following measurement noise covariances assigned to its diagonal elements:

$$\mathbf{R}_k = diag(v^2_{I_{dss}}, v^2_{I_{qss}}, v^2_{\omega_m}, v^2_{\theta_T}, v^2_{\omega_s}) \tag{4.25}$$

- Based on model testing, it is appropriate to select $v_{I_{dss}} = \frac{w_{I_{dss}}}{10}$.
- Based on model testing, it is suitable to define $v_{I_{qss}} = \frac{w_{I_{qss}}}{10}$.
- Based on model testing, it is reasonable to choose $v_{\omega_m} = 10w_{\omega_m}$.
- Based on model testing, it is determined that $v_{\theta_T} = 1000w_{\theta_T}$ is an appropriate choice.
- Based on model testing, it is practical to set $v_{\omega_s} = 100w_{\omega_s}$.

4.1.2 Method 2

Method 2 is proposed as an adaptation of Method 1 for cases where the measurements are not synchronized due to differing sampling times. Since the same model and coefficient estimation approach is employed to estimate the tangential cutting torque, this method can be regarded as a specialized version of Method 1.

To accommodate asynchronous measurement data, this method utilizes the Asynchronous Extended Kalman Filter. An example scenario involves the asynchronous measurement of currents I_{dss} and I_{qss}, which may occur when an alternative current measurement device, such as the Beckhoff EL3773 used in the setup, is employed to achieve a higher sampling frequency for current measurements.

In this case, the measurement sampling frequencies can be classified as $\mathbf{z}_{k,1}$ ($\mathbf{z}_{k,1} = [I_{dss}, I_{qss}]^T$), updated at a higher sampling rate, and $\mathbf{z}_{k,2}$ ($\mathbf{z}_{k,2} = [\omega_m, \theta_t, \omega_s]^T$), updated at a lower sampling rate.

For the measurement group with a higher sampling frequency, the following Extended Kalman Filter equations are applied:

$$\mathbf{K}_k = \mathbf{P}_k^- \mathbf{H}_{k,1}^T (\mathbf{H}_{k,1} \mathbf{P}_k^- \mathbf{H}_{k,1}^T + \mathbf{R}_{k,1})^{-1} \tag{4.26}$$

$$\hat{\mathbf{x}}_k = \hat{\mathbf{x}}_k^- + \mathbf{K}_k (\mathbf{z}_{k,1} - \mathbf{H}_{k,1} \hat{\mathbf{x}}_k^-) \tag{4.27}$$

$$\mathbf{P}_k = (\mathbf{I} - \mathbf{K}_k \mathbf{H}_{k,1}) \mathbf{P}_k^- \tag{4.28}$$

$$\hat{\mathbf{x}}_{k+1}^- = \hat{\mathbf{x}}_k + T_s \mathbf{f}(\hat{\mathbf{x}}_k, \mathbf{u}_k, \phi_k) \tag{4.29}$$

$$\mathbf{P}_{k+1}^- = \mathbf{J}_k \mathbf{P}_k \mathbf{J}_k^T + \mathbf{Q}_k \tag{4.30}$$

For the measurement vector $\mathbf{z}_{k,1}$, the corresponding measurement matrix $\mathbf{H}_{k,1}$ can be expressed as:

$$\mathbf{H}_{k,1} = \begin{bmatrix} 1 & 0 & 0 & 0 & 0 & 0 & 0 & 0 & 0 \\ 0 & 1 & 0 & 0 & 0 & 0 & 0 & 0 & 0 \end{bmatrix} \tag{4.31}$$

For the measurement group with a slower sampling frequency, the following Ex-

tended Kalman Filter equations are applied:

$$\mathbf{K}_k = \mathbf{P}_k^- \mathbf{H}_{k,2}^T (\mathbf{H}_{k,2} \mathbf{P}_k^- \mathbf{H}_{k,2}^T + \mathbf{R}_{k,2})^{-1} \tag{4.32}$$

$$\hat{\mathbf{x}}_k = \hat{\mathbf{x}}_k^- + \mathbf{K}_k (\mathbf{z}_{k,2} - \mathbf{H}_{k,2} \hat{\mathbf{x}}_k^-) \tag{4.33}$$

$$\mathbf{P}_k = (\mathbf{I} - \mathbf{K}_k \mathbf{H}_{k,2}) \mathbf{P}_k^- \tag{4.34}$$

$$\hat{\mathbf{x}}_{k+1}^- = \hat{\mathbf{x}}_k + T_s \mathbf{f}(\hat{\mathbf{x}}_k, \mathbf{u}_k, \phi_k) \tag{4.35}$$

$$\mathbf{P}_{k+1}^- = \mathbf{J}_k \mathbf{P}_k \mathbf{J}_k^T + \mathbf{Q}_k \tag{4.36}$$

For the measurement vector $\mathbf{z}_{k,2}$, the corresponding measurement matrix $\mathbf{H}_{k,2}$ can be expressed as:

$$\mathbf{H}_{k,2} = \begin{bmatrix} 0 & 0 & 0 & 0 & 1 & 0 & 0 & 0 & 0 \\ 0 & 0 & 0 & 0 & 0 & 1 & 0 & 0 & 0 \\ 0 & 0 & 0 & 0 & 0 & 0 & 1 & 0 & 0 \end{bmatrix} \tag{4.37}$$

In Method 2, the process noise covariance matrix, $\mathbf{Q}_k$, is selected as a diagonal matrix, reflecting the assumption that the process noise components are uncorrelated. The parameters of $\mathbf{Q}_k$ are identical to those used in Method 1.

$$\mathbf{Q}_k = diag(w_{I_{dss}}^2, w_{I_{qss}}^2, w_{I_{drs}}^2, w_{I_{qrs}}^2, w_{\omega_m}^2, w_{\theta_t}^2, w_{\omega_s}^2, w_{K_{tc}}^2, w_{K_{te}}^2) T_s^2 \tag{4.38}$$

The measurement noise covariance matrix for the group of variables with a higher sampling frequency, $\mathbf{R}_{k,1}$, is selected as a diagonal matrix, with the same measurement noise covariances assigned to its diagonal elements as in Method 1:

$$\mathbf{R}_{k,1} = diag(v_{I_{dss}}^2, v_{I_{qss}}^2) \tag{4.39}$$

The measurement noise covariance matrix for the group of variables with a smaller sampling frequency, $\mathbf{R}_{k,2}$, is selected as a diagonal matrix, with the same measurement noise covariances assigned to its diagonal elements as in Method 1:

$$\mathbf{R}_{k,2} = diag(v_{\omega_m}^2, v_{\theta_T}^2, v_{\omega_s}^2) \tag{4.40}$$

However, if the sampling frequency of the faster measurement group is 8kHz and that of the slower group is 1kHz, only the EKF updates using the faster group measurements are required for time steps where only the faster group measurements are available. When measurements from the slower group are available, all measurements are used in the EKF. In this case, rather than separately calculating for group 1 and group 2, the entire set of measurements can be processed together, similar to Method 1.

4.1.3 Method 3

In Method 3, the system model includes only the mechanical subsystem, which represents the two-inertia model. This method can be viewed as a reduced version of the system model used in Method 1.

The state-space equations that define the reduced system model can be represented as follows:

$$\frac{d}{dt}\begin{bmatrix}\omega_m\\ \theta_t\\ \omega_s\end{bmatrix} = \begin{bmatrix}-\frac{(b_t n_g^2+b_m)}{J_m} & -\frac{(kn_g)}{J_m} & \frac{(b_t n_g)}{J_m}\\ n_g & 0 & -1\\ -\frac{(b_t n_g)}{J_s} & \frac{k}{J_s} & -\frac{(b_t+b_s)}{J_s}\end{bmatrix}\begin{bmatrix}\omega_m\\ \theta_t\\ \omega_s\end{bmatrix} + \begin{bmatrix}\frac{1}{J_m} & 0\\ 0 & 0\\ 0 & -\frac{1}{J_s}\end{bmatrix}\begin{bmatrix}T_e\\ T_c\end{bmatrix} \tag{4.41}$$

In this system, however, the electric torque T_e, generated by the induction motor, must be supplied as an input, necessitating its calculation from current measurements. Additionally, it is known that the cutting torque can be expressed as $T_c = r(K_{tc}h_{tc}(\phi) + K_{te}h_{te}(\phi))$. Consequently, the updated state-space equations can be formulated as follows:

$$\dot{\mathbf{x}}_1 = \mathbf{A}_{11}\mathbf{x}_1 + \mathbf{A}_{12}(x_2) + \mathbf{B}\mathbf{u} \tag{4.42}$$

$$\dot{\mathbf{x}}_2 = 0 \tag{4.43}$$

where $\mathbf{x}_1$ is defined as follow:

$$\mathbf{x}_1 = \begin{bmatrix} \omega_m & \theta_t & \omega_s \end{bmatrix}^T \tag{4.44}$$

where $\mathbf{x}_2$ is defined as follows:

$$\mathbf{x}_2 = \begin{bmatrix} K_{tc} & K_{te} \end{bmatrix}^T \tag{4.45}$$

where $\mathbf{A}_{11}$ is expressed as follows

$$\mathbf{A}_{11} = \begin{bmatrix} -\frac{(b_t n_g^2 + b_m)}{J_m} & -\frac{(k n_g)}{J_m} & \frac{(b_t n_g)}{J_m} \\ n_g & 0 & -1 \\ -\frac{(b_t n_g)}{J_s} & \frac{k}{J_s} & -\frac{(b_t + b_s)}{J_s} \end{bmatrix} \tag{4.46}$$

where $\mathbf{A}_{12}$ is expressed as follows

$$\mathbf{A}_{12} = \begin{bmatrix} 0 & 0 \\ 0 & 0 \\ -\frac{h_{tc}(\phi)}{J_s} & -\frac{h_{te}(\phi)}{J_s} \end{bmatrix} \tag{4.47}$$

where $\mathbf{B}$ is expressed as follows

$$\mathbf{B} = \begin{bmatrix} \frac{1}{J_m} & 0 & 0 \end{bmatrix}^T \tag{4.48}$$

It is important to note that the elements of the geometry matrix, $h_{tc}(\phi)$ and $h_{te}(\phi)$, are computed using Algorithm 2.

In this method, the geometry matrix, which describes the relationship between the cutting tool and workpiece geometry during cutting, is provided to the system as in Method 1. Thus, the tangential cutting force coefficients can be estimated instead of directly estimating the cutting torque. Thus, K_{tc} and K_{te} can be used as new states, and new state space equations can be formulated in discrete time as follow:

$$\mathbf{x}_{r,k} = \mathbf{F}_k \mathbf{x}_{r,k} + \mathbf{G}_k u_{r,k} \tag{4.49}$$

where $u_{r,k} = T_{e,k}$ and $\mathbf{x}_{r,k}$ is defined as follows:

$$\mathbf{x}_{r,k} = \begin{bmatrix} \omega_{m,k} & \theta_{t,k} & \omega_{s,k} & K_{tc,k} & K_{te,k} \end{bmatrix}^T \tag{4.50}$$

where $\mathbf{F}_k$ is the discretized augmented state matrix. The discretization of the augmented state matrix $\mathbf{F}$ is performed by:

$$\mathbf{F}_k = \left[\begin{array}{c|c} \mathbf{A}_k \text{ (3x3)} & \mathbf{A}_1\text{(3x2)} \\ \hline \mathbf{Z}_1\text{(2x3)} & \mathbf{I}\text{(2x2)} \end{array}\right] \tag{4.51}$$

$$\mathbf{A}_k = e^{\mathbf{A}_{11}T_s} \tag{4.52}$$

$$\mathbf{A}_1 = \mathbf{A}_{11}^{-1}(e^{\mathbf{A}_{11}T_s} - \mathbf{I}_{3x3})\mathbf{A}_{12} \tag{4.53}$$

$$\mathbf{Z}_1 = \begin{bmatrix} 0 & 0 & 0 \\ 0 & 0 & 0 \end{bmatrix} \tag{4.54}$$

$$\mathbf{I} = \begin{bmatrix} 1 & 0 \\ 0 & 1 \end{bmatrix} \tag{4.55}$$

Since discretization is required in this process, discretization for the input matrix can be done using the following equation:

$$\mathbf{B}_k = \mathbf{A}_{11}^{-1}(\mathbf{A}_k - \mathbf{I}_{3x3})\mathbf{B} \tag{4.56}$$

The augmented input matrix,$\mathbf{G}_k$, can be obtained by:

$$\mathbf{G}_k = \left[\begin{array}{c} \mathbf{B}_k \\ \hline 0 \\ 0 \end{array}\right] \tag{4.57}$$

Moreover, by decoupling the system from the dynamics of the electric motor, the model is rendered linear, thus allowing for the application of the standard Kalman Filter and eliminating the necessity for the Extended Kalman Filter.

The Kalman Filter, as described in [15], is utilized for estimating the tangential cutting torque. The algorithm's recursive steps are presented in the following formulation:

$$\mathbf{K}_k = \mathbf{P}_k^- \mathbf{H}_k^T (\mathbf{H}_k \mathbf{P}_k \mathbf{H}_k^T + \mathbf{R}_k)^{-1} \tag{4.58}$$

$$\hat{\mathbf{x}}_{r,k} = \hat{\mathbf{x}}_{r,k}^- + \mathbf{K}_k (\mathbf{z}_k - \mathbf{H}_k \hat{\mathbf{x}}_{r,k}^-) \tag{4.59}$$

$$\mathbf{P}_k = (\mathbf{I} - \mathbf{K}_k \mathbf{H}_k) \mathbf{P}_k^- \tag{4.60}$$

$$\hat{\mathbf{x}}_{r,k+1}^- = \mathbf{F}_k \hat{\mathbf{x}}_{r,k} + \mathbf{G}_k u_{r,k} \tag{4.61}$$

$$\mathbf{P}_k^- = \mathbf{F}_k \mathbf{P}_k \mathbf{F}_k^T + \mathbf{Q}_k \tag{4.62}$$

The measurement vector $\mathbf{z}_k$ can be expressed as follows, given that all mechanical variables can either be directly measured or calculated from other measurements (such as θ_t) within the system.

$$\mathbf{z}_k = \begin{bmatrix} \omega_{m,k} & \theta_{t,k} & \omega_{s,k} \end{bmatrix}^T \tag{4.63}$$

The corresponding measurement matrix can be represented as follows:

$$\mathbf{H}_k = \begin{bmatrix} 1 & 0 & 0 & 0 & 0 \\ 0 & 1 & 0 & 0 & 0 \\ 0 & 0 & 1 & 0 & 0 \end{bmatrix} \tag{4.64}$$

In Method 3, the process noise covariance matrix, $\mathbf{Q}_k$, is selected as a diagonal matrix:

$$\mathbf{Q}_k = \text{diag}(w_{\omega_m}^2, w_{\theta_t}^2, w_{\omega_s}^2, w_{K_{tc}}^2, w_{K_{te}}^2) T_s^2 \tag{4.65}$$

The diagonal parameters are defined as follows:

- Based on model testing, the process noise for ω_m between the real system and the model is found to be at most $w_{\omega_m} = 0.15$ rad/s.
- Similarly, the process noise for ω_s is found to be at most $w_{\omega_s} = 0.1$ rad/s.

- Since θ_t represents the difference between θ_m and θ_s, the process noise is assumed to be $w_{\theta_t} = \min([w_{\omega_m}, w_{\omega_s}])/10$.
- The process noise for K_{tc} is selected based on the average variation during the sampling time, and is set to $w_{K_{tc}} = 10^4 \, \frac{\text{N}}{\text{mm}^2}$.
- Similarly, the process noise for K_{te} is set based on the observed sampling time variation, with $w_{K_{te}} = 10^3 \, \frac{\text{N}}{\text{mm}}$.

The measurement noise covariance matrix, $\mathbf{R}_k$, is selected as a diagonal matrix, with the following measurement noise covariances assigned to its diagonal elements:

$$\mathbf{R}_k = \text{diag}(v_{\omega_m}^2, v_{\theta_T}^2, v_{\omega_s}^2) \tag{4.66}$$

The diagonal parameters are defined as follows:

- Based on model testing, it is appropriate to select $v_{\omega_m} = 10 w_{\omega_m}$.
- Based on model testing, it is suitable to allocate $v_{\theta_T} = 1000 w_{\theta_T}$.
- Based on model testing, it is practical to choose $v_{\omega_s} = 100 w_{\omega_s}$.

4.1.4 Method 4

In Method 4, the complete system model is employed, akin to Method 1 and Method 2. Due to the use of the full model, nonlinearity is introduced into the system. However, in this approach, the geometry matrix is considered unknown. Consequently, the system model is applied without any augmentation, as explained in Equation 4.1.

The tangential cutting torque T_c is introduced as a new state variable; thus, the revised nonlinear differential equations become:

$$\dot{\mathbf{x}} = \mathbf{f}(\mathbf{x}, \mathbf{u}) + \mathbf{w} \tag{4.67}$$

where the state matrix, $\mathbf{x}$, is defined as follows:

$$\mathbf{x} = \begin{bmatrix} I_{dss} & I_{qss} & I_{drs} & I_{qrs} & \omega_m & \theta_t & \omega_s & T_c \end{bmatrix}^T \tag{4.68}$$

where the input matrix ,$\mathbf{u}$, is expressed as follows:

$$\mathbf{u} = \begin{bmatrix} V_{dss} & V_{qss} \end{bmatrix}^T \tag{4.69}$$

Here, $\mathbf{w}$ is the process noise matrix.

where $\mathbf{f}(\mathbf{x}, \mathbf{u})$ is expressed as follows:

$$\mathbf{f}(\mathbf{x}, \mathbf{u}) = \begin{bmatrix} -\frac{L_r R_s}{\gamma} I_{dss} + \frac{L_m^2 \omega_e}{\gamma} I_{qss} + \frac{L_m R_r}{\gamma} I_{drs} + \frac{L_m L_r \omega_e}{\gamma} I_{qrs} + \frac{L_r}{\gamma} V_{dss} \\ -\frac{L_m^2 \omega_e}{\gamma} I_{dss} - \frac{L_r R_s}{\gamma} I_{qss} - \frac{L_m L_r \omega_e}{\gamma} I_{drs} + \frac{L_m R_r}{\gamma} I_{qrs} + \frac{L_r}{\gamma} V_{qss} \\ \frac{L_m R_s}{\gamma} I_{dss} - \frac{L_s L_m \omega_e}{\gamma} I_{qss} - \frac{R_r L_s}{\gamma} I_{drs} - \frac{L_s L_r \omega_e}{\gamma} I_{qrs} - \frac{L_m}{\gamma} V_{dss} \\ \frac{L_s L_m \omega_e}{\gamma} I_{dss} + \frac{L_m R_s}{\gamma} I_{qss} + \frac{L_s L_r \omega_e}{\gamma} I_{drs} - \frac{R_r L_s}{\gamma} I_{qrs} - \frac{L_m}{\gamma} V_{qss} \\ \frac{1}{J_m}[K_t(I_{qss} I_{drs} - I_{qrs} I_{dss}) - (n_g^2 b_t + b_m)\omega_m - k n_g \theta_t + b_t n_g \omega_s] \\ n_g \omega_m - \omega_s \\ \frac{1}{J_s}[n_g b_t \omega_m + k\theta_t - (b_t + b_s)\omega_s - T_c] \\ 0 \end{bmatrix} \tag{4.70}$$

This function can be discretized using Forward Euler method which is shown in the Equation 4.71

$$\mathbf{x}_{k+1} = \mathbf{x}_k + T_s \mathbf{f}(\mathbf{x}_k, \mathbf{u}_k) \tag{4.71}$$

where $\mathbf{x}_k = [I_{dss,k}, I_{qss,k}, I_{drs,k}, I_{qrs,k}, \omega_{m,k}, \theta_{t,k}, \omega_{s,k}, T_{c,k}]^T$ represents the state vector, and $\mathbf{u}_k = [V_{dss,k}, V_{qss,k}]^T$ denotes the input vector.

$\mathbf{f}(\mathbf{x}_k, \mathbf{u}_k)$ is represented by the following equation:

$$\mathbf{f}(\mathbf{x}_k, \mathbf{u}_k) = \begin{bmatrix} -\frac{L_r R_s}{\gamma} I_{dss,k} + \frac{L_m^2 \omega_e}{\gamma} I_{qss,k} + \frac{L_m R_r}{\gamma} I_{drs,k} + \frac{L_m L_r \omega_e}{\gamma} I_{qrs,k} + \frac{L_r}{\gamma} V_{dss,k} \\ -\frac{L_m^2 \omega_e}{\gamma} I_{dss,k} - \frac{L_r R_s}{\gamma} I_{qss,k} - \frac{L_m L_r \omega_e}{\gamma} I_{drs,k} + \frac{L_m R_r}{\gamma} I_{qrs,k} + \frac{L_r}{\gamma} V_{qss,k} \\ \frac{L_m R_s}{\gamma} I_{dss,k} - \frac{L_s L_m \omega_e}{\gamma} I_{qss,k} - \frac{R_r L_s}{\gamma} I_{drs,k} - \frac{L_s L_r \omega_e}{\gamma} I_{qrs,k} - \frac{L_m}{\gamma} V_{dss,k} \\ \frac{L_s L_m \omega_e}{\gamma} I_{dss,k} + \frac{L_m R_s}{\gamma} I_{qss,k} + \frac{L_s L_r \omega_e}{\gamma} I_{drs,k} - \frac{R_r L_s}{\gamma} I_{qrs,k} - \frac{L_m}{\gamma} V_{qss,k} \\ \frac{1}{J_m}\left[T_{e,k} - (n_g^2 b_t + b_m)\omega_{m,k} - k n_g \theta_{t,k} + b_t n_g \omega_{s,k}\right] \\ n_g \omega_{m,k} - \omega_{s,k} \\ \frac{1}{J_s}\left[n_g b_t \omega_{m,k} + k\theta_{t,k} - (b_t + b_s)\omega_{s,k} - T_{c,k})\right] \\ T_{c,k} \end{bmatrix} \tag{4.72}$$

where $T_{e,k} = K_t(I_{qss,k} I_{drs,k} - I_{qrs,k} I_{dss,k})$

As nonlinearity is present, the EKF is employed as the observer. The Extended Kalman Filter, as detailed in [15], is proposed for estimating the tangential cutting torque, T_c, exerted on the spindle tool. The formulation of the Extended Kalman Filter, implemented in the algorithm's recursive steps, is defined as follows:

$$\mathbf{K}_k = \mathbf{P}_k^- \mathbf{H}_k^T (\mathbf{H}_k \mathbf{P}_k^- \mathbf{H}_k^T + \mathbf{R}_k)^{-1} \tag{4.73}$$

$$\hat{\mathbf{x}}_k = \hat{\mathbf{x}}_k^- + \mathbf{K}_k(\mathbf{z}_k - \mathbf{H}_k \hat{\mathbf{x}}_k^-) \tag{4.74}$$

$$\mathbf{P}_k = (\mathbf{I} - \mathbf{K}_k \mathbf{H}_k)\mathbf{P}_k^- \tag{4.75}$$

$$\hat{\mathbf{x}}_{k+1}^- = \hat{\mathbf{x}}_k + T_s \mathbf{f}(\hat{\mathbf{x}}_k, \mathbf{u}_k) \tag{4.76}$$

$$\mathbf{P}_{k+1}^- = \mathbf{J}_k \mathbf{P}_k \mathbf{J}_k^T + \mathbf{Q}_k \tag{4.77}$$

The calculation of the prior covariance matrix, $\mathbf{P}_k^-$, necessitates the linearization of $\mathbf{f}(\mathbf{x}, \mathbf{u})$. Therefore, the Jacobian matrix for this nonlinear differential equation must be derived. The Jacobian matrix, $\mathbf{J}$, is expressed as follows:

$$\mathbf{J} = \left[\begin{array}{c|c} \mathbf{J}_1 \text{ (4x4)} & \mathbf{J}_2\text{(4x4)} \\ \hline \mathbf{J}_3\text{(4x4)} & \mathbf{J}_4\text{(4x4)} \end{array}\right] \tag{4.78}$$

$$\mathbf{J_1} = \begin{bmatrix} -\frac{L_r R_s}{\gamma} & \frac{L_m^2 \omega_e}{\gamma} & \frac{L_m R_r}{\gamma} & \frac{L_m L_r \omega_e}{\gamma} \\ -\frac{L_m^2 \omega_e}{\gamma} & -\frac{L_r R_s}{\gamma} & -\frac{L_m L_r \omega_e}{\gamma} & \frac{L_m R_r}{\gamma} \\ \frac{L_m R_s}{\gamma} & -\frac{L_s L_m \omega_e}{\gamma} & -\frac{R_r L_s}{\gamma} & -\frac{L_s L_r \omega_e}{\gamma} \\ \frac{L_s L_m \omega_e}{\gamma} & \frac{L_m R_s}{\gamma} & \frac{L_s L_r \omega_e}{\gamma} & -\frac{R_r L_s}{\gamma} \end{bmatrix} \tag{4.79}$$

$$\mathbf{J_2} = \begin{bmatrix} \frac{L_m^2 I_{qss} + L_m L_r I_{qrs}}{\gamma} & 0 & 0 & 0 \\ -\frac{L_m^2 I_{dss} + L_m L_r I_{drs}}{\gamma} & 0 & 0 & 0 \\ -\frac{L_m^2 I_{dss} + L_m L_r I_{drs}}{\gamma} & 0 & 0 & 0 \\ \frac{L_s L_m I_{dss} + L_s L_r I_{drs}}{\gamma} & 0 & 0 & 0 \end{bmatrix} \tag{4.80}$$

$$\mathbf{J_3} = \begin{bmatrix} -\frac{k_t I_{qrs}}{J_m} & \frac{k_t I_{drs}}{J_m} & \frac{k_t I_{qss}}{J_m} & -\frac{k_t I_{dss}}{J_m} \\ 0 & 0 & 0 & 0 \\ 0 & 0 & 0 & 0 \\ 0 & 0 & 0 & 0 \end{bmatrix} \tag{4.81}$$

$$\mathbf{J_4} = \begin{bmatrix} -\frac{b_t n_g^2 + b_m}{J_m} & -\frac{k n_g}{J_m} & \frac{b_t n_g}{J_m} & 0 \\ n_g & 0 & -1 & 0 \\ \frac{n_g b_t}{J_s} & \frac{k}{J_s} & -\frac{b_t + b_s}{J_s} & -\frac{1}{J_s} \\ 0 & 0 & 0 & 0 \end{bmatrix} \tag{4.82}$$

Since the EKF operates in discrete time, $\mathbf{J}$ needs to be discretized. The discretization of $\mathbf{J}$ is performed using the following formulas:

$$J_k = e^{\mathbf{J} T_s} \tag{4.83}$$

Given that the test setup provides measurement data for $I_{dse,k}$, $I_{qse,k}$, $\omega_{m,k}$, $\theta_{t,k}$, and $\omega_{s,k}$, and that the conversion between synchronous and stationary frames for the currents can be achieved using the 'Inverse Park Transformation', the measurement vector, $\mathbf{z}_k$, and the measurement matrix, $\mathbf{H}_k$, are defined as in Equations 4.84 and 4.85.

$$\mathbf{z}_k = \begin{bmatrix} I_{dss,k} & I_{qss,k} & \omega_{m,k} & \theta_{t,k} & \omega_{s,k} \end{bmatrix}^T \tag{4.84}$$

$$\mathbf{H}_k = \begin{bmatrix} 1 & 0 & 0 & 0 & 0 & 0 & 0 & 0 \\ 0 & 1 & 0 & 0 & 0 & 0 & 0 & 0 \\ 0 & 0 & 0 & 0 & 1 & 0 & 0 & 0 \\ 0 & 0 & 0 & 0 & 0 & 1 & 0 & 0 \\ 0 & 0 & 0 & 0 & 0 & 0 & 1 & 0 \end{bmatrix} \tag{4.85}$$

In Method 4, the process noise covariance matrix, $\mathbf{Q}_k$, is defined as a diagonal matrix to represent the assumption that the process noise components are uncorrelated.

$$\mathbf{Q}_k = diag(w_{I_{dss}}^2, w_{I_{qss}}^2, w_{I_{drs}}^2, w_{I_{qrs}}^2, w_{\omega_m}^2, w_{\theta_t}^2, w_{\omega_s}^2, w_{T_c}^2) T_s^2 \tag{4.86}$$

The diagonal elements of the process noise covariance matrix are specified as follows:

- Based on model testing, the process noise for I_{dss} between the real system and the model was found to be at most $w_{I_{dss}} = 0.25\,\text{A}$.
- Similarly, testing revealed that the process noise for I_{qss} could reach a maximum of $w_{I_{qss}} = 0.25\,\text{A}$.
- Since I_{drs} is not directly measurable, its process noise was estimated through simulation analysis, and determined as $w_{I_{drs}} = \frac{w_{I_{dss}}}{10}$.
- Similarly, I_{qrs}, which is also not directly measurable, had its process noise estimated from simulation, with $w_{I_{qrs}} = \frac{w_{I_{qss}}}{10}$.
- After evaluating the model, the process noise for motor speed ω_m was determined to be at most $w_{\omega_m} = 0.15\,\text{rad/s}$.
- Likewise, the process noise for spindle speed ω_s was determined to be at most $w_{\omega_s} = 0.1\,\text{rad/s}$.
- Since θ_t represents the relative angular position between θ_m and θ_s, its process noise is assumed to be $w_{\theta_t} = \min([w_{\omega_m}, w_{\omega_s}])/10$.
- The process noise for the tangential cutting torque T_c was set based on observed variations during sampling, with $w_{T_c} = 10^2\,\text{Nm}$.

The measurement noise covariance matrix, $\mathbf{R}_k$, is selected as a diagonal matrix, with the following measurement noise covariances assigned to its diagonal elements:

$$\mathbf{R}_k = \text{diag}(v_{I_{dss}}^2, v_{I_{qss}}^2, v_{\omega_m}^2, v_{\theta_t}^2, v_{\omega_s}^2) \tag{4.87}$$

- Based on model testing, it is appropriate to set $v_{I_{dss}} = \frac{w_{I_{dss}}}{10}$.
- Similarly, $v_{I_{qss}} = \frac{w_{I_{qss}}}{10}$ is selected based on model testing.
- For the motor speed ω_m, $v_{\omega_m} = 10w_{\omega_m}$ is chosen as a reasonable value based on testing.
- For the relative angular position θ_t, $v_{\theta_t} = 1000w_{\theta_t}$ is determined to be an appropriate choice.
- Finally, $v_{\omega_s} = 100w_{\omega_s}$ is selected as a practical value based on model testing.

4.1.5 Method 5

In this method, the special case where the spindle or motor encoder, or both, experience minimal tracking loss, causing the transition angle θ_t to drift, is addressed. Since this issue occurs during cutting tests, Method 1 is modified to mitigate this phenomenon.

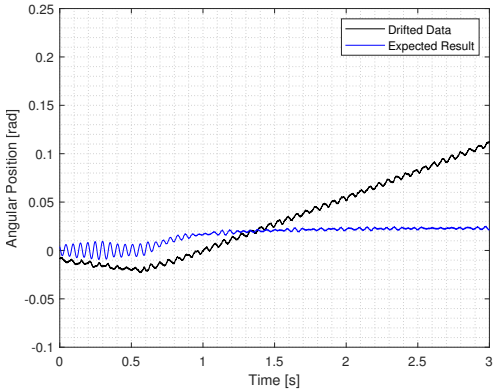


Figure 4.1: Illustration of Transmission Angular Position Drift

It is assumed that the drift is caused by a slight variation in the transmission ratio n_g during the test, as illustrated in Figure 4.1. This phenomenon is represented by the following equation for the transmission angle θ_t:

$$\theta_t = n_g\theta_m - \theta_s + \delta_{n_g}\omega_m \tag{4.88}$$

Given that the tangential cutting torque can be represented as $T_c = r(K_{tc}h_{tc}(\phi) + K_{te}h_{te}(\phi))$, the nonlinear differential equations governing the complete system are expressed as follows:

$$\dot{\mathbf{x}} = \mathbf{f}(\mathbf{x}, \mathbf{u}, \phi) + \mathbf{w} \tag{4.89}$$

where the state matrix, $\mathbf{x}$, is defined as follows:

$$\mathbf{x} = \begin{bmatrix} I_{dss} & I_{qss} & I_{drs} & I_{qrs} & \omega_m & \theta_t & \omega_s & \delta_{n_g} \end{bmatrix}^T \tag{4.90}$$

where the input matrix ,$\mathbf{u}$, is expressed as follows:

$$\mathbf{u} = \begin{bmatrix} V_{dss} & V_{qss} \end{bmatrix}^T \tag{4.91}$$

where $\mathbf{f}(\mathbf{x}, \mathbf{u}, \phi)$ is expressed as follows:

$$\mathbf{f}(\mathbf{x}, \mathbf{u}, \phi) = \begin{bmatrix} -\frac{L_r R_s}{\gamma} I_{dss} + \frac{L_m^2 \omega_e}{\gamma} I_{qss} + \frac{L_m R_r}{\gamma} I_{drs} + \frac{L_m L_r \omega_e}{\gamma} I_{qrs} + \frac{L_r}{\gamma} V_{dss} \\ -\frac{L_m^2 \omega_e}{\gamma} I_{dss} - \frac{L_r R_s}{\gamma} I_{qss} - \frac{L_m L_r \omega_e}{\gamma} I_{drs} + \frac{L_m R_r}{\gamma} I_{qrs} + \frac{L_r}{\gamma} V_{qss} \\ \frac{L_m R_s}{\gamma} I_{dss} - \frac{L_s L_m \omega_e}{\gamma} I_{qss} - \frac{R_r L_s}{\gamma} I_{drs} - \frac{L_s L_r \omega_e}{\gamma} I_{qrs} - \frac{L_m}{\gamma} V_{dss} \\ \frac{L_s L_m \omega_e}{\gamma} I_{dss} + \frac{L_m R_s}{\gamma} I_{qss} + \frac{L_s L_r \omega_e}{\gamma} I_{drs} - \frac{R_r L_s}{\gamma} I_{qrs} - \frac{L_m}{\gamma} V_{qss} \\ \frac{1}{J_m}[K_t(I_{qss}I_{drs} - I_{qrs}I_{dss}) - (n_g^2 b_t + b_m)\omega_m - k n_g \theta_t + b_t n_g \omega_s] \\ n_g\omega_m - \omega_s + \delta_{n_g}\omega_m \\ \frac{1}{J_s}[n_g b_t \omega_m + k\theta_t - (b_t + b_s)\omega_s - T_c] \\ 0 \end{bmatrix} \tag{4.92}$$

As this estimation method primarily estimates the coefficients, these coefficients should be incorporated as additional state variables by augmenting the equations in Equation 4.89. This can be expressed as follows:

$$\dot{\mathbf{x}}' = f'(\mathbf{x}', \mathbf{u}, \phi) + \mathbf{w}' \tag{4.93}$$

where the augmented state matrix, $\mathbf{x}'$, is defined as follows:

$$\mathbf{x}' = \begin{bmatrix} I_{dss} & I_{qss} & I_{drs} & I_{qrs} & \omega_m & \theta_t & \omega_s & \delta_{n_g} & K_{tc} & K_{te} \end{bmatrix}^T \tag{4.94}$$

where $f'(\mathbf{x}, \mathbf{u}, \phi)$ is expressed as follows:

$$\mathbf{f}'(\mathbf{x}, \mathbf{u}, \phi) = \begin{bmatrix} -\frac{L_r R_s}{\gamma} I_{dss} + \frac{L_m^2 \omega_e}{\gamma} I_{qss} + \frac{L_m R_r}{\gamma} I_{drs} + \frac{L_m L_r \omega_e}{\gamma} I_{qrs} + \frac{L_r}{\gamma} V_{dss} \\ -\frac{L_m^2 \omega_e}{\gamma} I_{dss} - \frac{L_r R_s}{\gamma} I_{qss} - \frac{L_m L_r \omega_e}{\gamma} I_{drs} + \frac{L_m R_r}{\gamma} I_{qrs} + \frac{L_r}{\gamma} V_{qss} \\ \frac{L_m R_s}{\gamma} I_{dss} - \frac{L_s L_m \omega_e}{\gamma} I_{qss} - \frac{R_r L_s}{\gamma} I_{drs} - \frac{L_s L_r \omega_e}{\gamma} I_{qrs} - \frac{L_m}{\gamma} V_{dss} \\ \frac{L_s L_m \omega_e}{\gamma} I_{dss} + \frac{L_m R_s}{\gamma} I_{qss} + \frac{L_s L_r \omega_e}{\gamma} I_{drs} - \frac{R_r L_s}{\gamma} I_{qrs} - \frac{L_m}{\gamma} V_{qss} \\ \frac{1}{J_m}[K_t(I_{qss} I_{drs} - I_{qrs} I_{dss}) - (n_g^2 b_t + b_m)\omega_m - k n_g \theta_t + b_t n_g \omega_s] \\ n_g \omega_m - \omega_s + \delta_{n_g} \omega_m \\ \frac{1}{J_s}[n_g b_t \omega_m + k\theta_t - (b_t + b_s)\omega_s - r(K_{tc} h_{tc}(\phi) + K_{te} h_{te}(\phi))] \\ 0 \\ 0 \\ 0 \end{bmatrix} \tag{4.95}$$

It is important to note that the elements of the geometry matrix, $h_{tc}(\phi)$ and $h_{te}(\phi)$, are computed using Algorithm 2.

This function can be discretized using the Forward Euler method, as shown in Equation 4.96.

$$\mathbf{x}_{k+1} = \mathbf{x}_k + T_s \mathbf{f}(\mathbf{x}_k, \mathbf{u}_k, \phi_k) \tag{4.96}$$

where $\mathbf{x}_k = [I_{dss,k}, I_{qss,k}, I_{drs,k}, I_{qrs,k}, \omega_{m,k}, \theta_{T,k}, \omega_{s,k}, \delta_{n_g,k}, K_{tc}, K_{te}]^T$ represents the state vector, and $\mathbf{u}_k = [V_{dss,k}, V_{qss,k}]^T$ denotes the input vector.

$\mathbf{f}(\mathbf{x}_k, \mathbf{u}_k, \phi_k)$ is represented by the following equation:

$$\mathbf{f}(\mathbf{x}_k, \mathbf{u}_k, \phi_k) = \begin{bmatrix} -\frac{L_r R_s}{\gamma} I_{dss,k} + \frac{L_m^2 \omega_e}{\gamma} I_{qss,k} + \frac{L_m R_r}{\gamma} I_{drs,k} + \frac{L_m L_r \omega_e}{\gamma} I_{qrs,k} + \frac{L_r}{\gamma} V_{dss,k} \\ -\frac{L_m^2 \omega_e}{\gamma} I_{dss,k} - \frac{L_r R_s}{\gamma} I_{qss,k} - \frac{L_m L_r \omega_e}{\gamma} I_{drs,k} + \frac{L_m R_r}{\gamma} I_{qrs,k} + \frac{L_r}{\gamma} V_{qss,k} \\ \frac{L_m R_s}{\gamma} I_{dss,k} - \frac{L_s L_m \omega_e}{\gamma} I_{qss,k} - \frac{R_r L_s}{\gamma} I_{drs,k} - \frac{L_s L_r \omega_e}{\gamma} I_{qrs,k} - \frac{L_m}{\gamma} V_{dss,k} \\ \frac{L_s L_m \omega_e}{\gamma} I_{dss,k} + \frac{L_m R_s}{\gamma} I_{qss,k} + \frac{L_s L_r \omega_e}{\gamma} I_{drs,k} - \frac{R_r L_s}{\gamma} I_{qrs,k} - \frac{L_m}{\gamma} V_{qss,k} \\ \frac{1}{J_m} \left[T_{e,k} - (n_g^2 b_t + b_m)\omega_{m,k} - k n_g \theta_{t,k} + b_t n_g \omega_{s,k} \right] \\ n_g \omega_{m,k} - \omega_{s,k} + \delta_{n_g,k} \omega_{m,k} \\ \frac{1}{J_s} \left[n_g b_t \omega_{m,k} + k\theta_{t,k} - b_t' \omega_{s,k} - r(K_{tc,k} h_{tc,k}(\phi) + K_{te,k} h_{te,k}(\phi)) \right] \\ 0 \\ 0 \\ 0 \end{bmatrix} \tag{4.97}$$

where $T_{e,k} = K_t(I_{qss,k} I_{drs,k} - I_{qrs,k} I_{dss,k})$ and $b_t' = b_t + b_s$

The modification does not alter the formulation of the Extended Kalman Filter, which is applied in the recursive steps of the algorithm and is defined as follows:

$$\mathbf{K}_k = \mathbf{P}_k^- \mathbf{H}_k^T (\mathbf{H}_k \mathbf{P}_k^- \mathbf{H}_k^T + \mathbf{R}_k)^{-1} \tag{4.98}$$

$$\hat{\mathbf{x}}_k = \hat{\mathbf{x}}_k^- + \mathbf{K}_k (\mathbf{z}_k - \mathbf{H}_k \hat{\mathbf{x}}_k^-) \tag{4.99}$$

$$\mathbf{P}_k = (\mathbf{I} - \mathbf{K}_k \mathbf{H}_k) \mathbf{P}_k^- \tag{4.100}$$

$$\hat{\mathbf{x}}_{k+1}^- = \hat{\mathbf{x}}_k + T_s \mathbf{f}(\hat{\mathbf{x}}_k, \mathbf{u}_k, \phi_k) \tag{4.101}$$

$$\mathbf{P}_{k+1}^- = \mathbf{J}_k \mathbf{P}_k \mathbf{J}_k^T + \mathbf{Q}_k \tag{4.102}$$

Similar to Method 1, the calculation of the prior covariance matrix, $\mathbf{P}_k^-$, requires the linearization of $\mathbf{f}(\mathbf{x}, \mathbf{u}, \phi)$. Therefore, the Jacobian matrix of this nonlinear differential equation must be computed. The Jacobian matrix, $\mathbf{J}$, can be expressed as follows:

$$\mathbf{J} = \left[\begin{array}{c|c} \mathbf{J}_1\ (4\text{x}4) & \mathbf{J}_2(4\text{x}6) \\ \hline \mathbf{J}_3(6\text{x}4) & \mathbf{J}_4(6\text{x}6) \end{array}\right] \tag{4.103}$$

$$\mathbf{J_1} = \begin{bmatrix} -\frac{L_r R_s}{\gamma} & \frac{L_m^2 \omega_e}{\gamma} & \frac{L_m R_r}{\gamma} & \frac{L_m L_r \omega_e}{\gamma} \\ -\frac{L_m^2 \omega_e}{\gamma} & -\frac{L_r R_s}{\gamma} & -\frac{L_m L_r \omega_e}{\gamma} & \frac{L_m R_r}{\gamma} \\ \frac{L_m R_s}{\gamma} & -\frac{L_s L_m \omega_e}{\gamma} & -\frac{R_r L_s}{\gamma} & -\frac{L_s L_r \omega_e}{\gamma} \\ \frac{L_s L_m \omega_e}{\gamma} & \frac{L_m R_s}{\gamma} & \frac{L_s L_r \omega_e}{\gamma} & -\frac{R_r L_s}{\gamma} \end{bmatrix} \tag{4.104}$$

$$\mathbf{J_2} = \begin{bmatrix} \frac{L_m^2 I_{qss} + L_m L_r I_{qrs}}{\gamma} & 0 & 0 & 0 & 0 & 0 \\ -\frac{L_m^2 I_{dss} + L_m L_r I_{drs}}{\gamma} & 0 & 0 & 0 & 0 & 0 \\ -\frac{L_m^2 I_{dss} + L_m L_r I_{drs}}{\gamma} & 0 & 0 & 0 & 0 & 0 \\ \frac{L_s L_m I_{dss} + L_s L_r I_{drs}}{\gamma} & 0 & 0 & 0 & 0 & 0 \end{bmatrix} \tag{4.105}$$

$$\mathbf{J_3} = \begin{bmatrix} -\frac{k_t I_{qrs}}{J_m} & \frac{k_t I_{drs}}{J_m} & \frac{k_t I_{qss}}{J_m} & -\frac{k_t I_{dss}}{J_m} \\ 0 & 0 & 0 & 0 \\ 0 & 0 & 0 & 0 \\ 0 & 0 & 0 & 0 \\ 0 & 0 & 0 & 0 \\ 0 & 0 & 0 & 0 \end{bmatrix} \tag{4.106}$$

$$\mathbf{J_4} = \begin{bmatrix} -\frac{b_t n_g^2 + b_m}{J_m} & -\frac{k n_g}{J_m} & \frac{b_t n_g}{J_m} & 0 & 0 & 0 \\ n_g + \delta_{n_g} & 0 & -1 & \omega_m & 0 & 0 \\ \frac{n_g b_t}{J_s} & \frac{k}{J_s} & -\frac{b_t + b_s}{J_s} & 0 & -\frac{r h_{tc}(\phi)}{J_s} & -\frac{r h_{te}(\phi)}{J_s} \\ 0 & 0 & 0 & 0 & 0 & 0 \\ 0 & 0 & 0 & 0 & 0 & 0 \\ 0 & 0 & 0 & 0 & 0 & 0 \end{bmatrix} \tag{4.107}$$

Since the EKF operates in discrete time, $\mathbf{J}$ needs to be discretized. The discretization of $\mathbf{J}$ is performed using the following formulas:

$$J_k = e^{\mathbf{J} T_s} \tag{4.108}$$

Since the test setup provides measurement data for I_{dse}, I_{qse}, ω_m, θ_T, and ω_s, and it is known that the conversion between the synchronous and stationary frames for the

currents can be performed using the 'Inverse Park Transformation', the measurement vector, $\mathbf{z}_k$, and the measurement matrix, $\mathbf{H}_k$, are defined as shown in Equations 4.109 and 4.110.

$$\mathbf{z}_k = \begin{bmatrix} I_{dss} & I_{qss} & \omega_m & \theta_t & \omega_s \end{bmatrix}^T \tag{4.109}$$

$$\mathbf{H}_k = \begin{bmatrix} 1 & 0 & 0 & 0 & 0 & 0 & 0 & 0 & 0 \\ 0 & 1 & 0 & 0 & 0 & 0 & 0 & 0 & 0 \\ 0 & 0 & 0 & 0 & 1 & 0 & 0 & 0 & 0 \\ 0 & 0 & 0 & 0 & 0 & 1 & 0 & 0 & 0 \\ 0 & 0 & 0 & 0 & 0 & 0 & 1 & 0 & 0 \end{bmatrix} \tag{4.110}$$

In Method 1, the process noise covariance matrix, $\mathbf{Q}_k$, is defined as a diagonal matrix to represent the assumption that the process noise components are uncorrelated.

$$\mathbf{Q}_k = diag(w_{I_{dss}}^2, w_{I_{qss}}^2, w_{I_{drs}}^2, w_{I_{qrs}}^2, w_{\omega_m}^2, w_{\theta_t}^2, w_{\omega_s}^2, w_{\delta_{n_g}}^2, w_{K_{tc}}^2, w_{K_{te}}^2) T_s^2 \tag{4.111}$$

The diagonal elements of the process noise covariance matrix are defined as follows:

- Through model testing, it was determined that the process noise for I_{dss} between the real system and the model can be at most $w_{I_{dss}} = 0.25\,\text{A}$.
- Similarly, model testing revealed that the process noise for I_{qss} can reach a maximum of $w_{I_{qss}} = 0.25\,\text{A}$.
- Since I_{drs} is not directly measurable, its process noise was identified by analyzing the simulation results, and estimated as $w_{I_{drs}} = \frac{w_{I_{dss}}}{10}$.
- As with I_{drs}, I_{qrs} is not directly measurable. Its process noise was identified through simulation, and estimated as $w_{I_{qrs}} = \frac{w_{I_{qss}}}{10}$.
- After evaluating the model, the process noise for motor speed ω_m was found to be at most $w_{\omega_m} = 0.15\,\text{rad/s}$.
- Similarly, the process noise for spindle speed ω_s was found to be at most $w_{\omega_s} = 0.1\,\text{rad/s}$.

- Since θ_t represents the relative angular position between θ_m and θ_s, the process noise is assumed to be $w_{\theta_t} = \min([w_{\omega_m}, w_{\omega_s}])/10$.
- The process noise for the tangential force coefficient K_{tc} is selected based on the average variation observed during the sampling time, and is set to $w_{K_{tc}} = 10^4 \frac{\text{N}}{\text{mm}^2}$.
- Similarly, the process noise for the edge force coefficient K_{te} is set based on the observed sampling time variation, with $w_{K_{te}} = 10^3 \frac{\text{N}}{\text{mm}}$.

The measurement noise covariance matrix, $\mathbf{R}_k$, is chosen as a diagonal matrix, with the following measurement noise covariances assigned to its diagonal elements:

$$\mathbf{R}_k = diag(v_{I_{dss}}^2, v_{I_{qss}}^2, v_{\omega_m}^2, v_{\theta_T}^2, v_{\omega_s}^2) \tag{4.112}$$

- Based on model testing, it is appropriate to select $v_{I_{dss}} = \frac{w_{I_{dss}}}{10}$.
- Based on model testing, it is suitable to define $v_{I_{qss}} = \frac{w_{I_{qss}}}{10}$.
- Based on model testing, it is reasonable to choose $v_{\omega_m} = 10w_{\omega_m}$.
- Based on model testing, it is determined that $v_{\theta_T} = 1000w_{\theta_T}$ is an appropriate choice.
- Based on model testing, it is practical to set $v_{\omega_s} = 100w_{\omega_s}$.

4.2 Verifications of Estimation Methods

In this section, the verification of the estimation methods described in Section 4.1 is conducted using simulation. Two groups of verification are performed, utilizing the respective simulation models discussed in Appendix D.

In the first group, verification is carried out within the simulation environment, where measurement data is generated by the dynamic model. It should be noted, however, that real input data for V_{dss}, V_{qss}, and T_c from cutting tests is used as input to the dynamic model in this group.

For the second group, the verification is similarly conducted within the simulation model, but here, real data collected from cutting tests is used for both inputs and measurements. In this case, both the voltages V_{dss} and V_{qss}, as well as the cutting torque T_c, are real data derived directly from the cutting tests.

The same cutting test data is used across both verification groups. All real data, for both measurements and inputs, are collected from cutting tests conducted with the same test setup, which will be described in greater detail in this section.

4.2.1 Test Setup Description

In the test setup, the retrofitted CNC machine with new motor drivers and PLC PC unit are utilized. For the PC unit, a Beckhoff PLC PC is used.

The spindle axis is controlled by a Beckhoff AX5125 driver, which has a maximum continuous current output. The spindle motor is an older AC induction motor, 'Franz Kessler DM 112/4L', whose parameters were identified through conventional tests, as discussed in Subsection 3.1.1.

Two rotary encoders are employed in the CNC system: one for measuring the spindle motor position and the other for measuring the spindle position. A TTL (Transistor-Transistor Logic) encoder is used for the motor. The TTL encoder outputs digital signals representing the angular position of the rotating shaft, operates at a standard 5V level, and provides square wave pulses on two channels (A and B) to indicate direction and position.

For the spindle position, a Sin-Cos encoder is used. This encoder outputs analog sine and cosine waveforms that represent the angular position, providing continuous signals over a 360° rotation. These signals allow for high-resolution position feedback due to their smooth variation.

For verification purposes, a dynamometer is employed to measure the forces applied to the workpiece in the x and y axes. An accelerometer is also placed on the workpiece to capture additional data in the x and y directions. Additionally, for high-resolution current and voltage measurements in the A-B-C reference frame of the AC motor, a

power monitoring terminal, the Beckhoff EtherCat-compatible 'EL3773', is used.

Table 4.1: Specifications of the CNC machine test setup

Test Set Up			
CNC	CNC Unit	Beckhoff	C6930
	CNC Software	Beckhoff	TwinCAT-3
Spindle	Spindle Motor	Franz Kessler	DM 112/4L
	Spindle Driver	Beckhoff	AX5125
	Spindle Encoder	Heidenhain	ROD 480 1800
X-Y Axes	Motor	Beckhoff	AM8062
	Driver	Beckhoff	AX8640
	Encoder	Heidenhain	LS 403-0870
Measurement	Dynamometer	Kistler	9257B
	Amplifier	Kistler	LabAmp 5167A
	DAQ	NI	cDAQ-9174
	Analog Input Module	NI	9234
Workpiece	Al7075		

In Figure 4.2, the workpiece used in the cutting tests is illustrated. Accelerometers, which are used in conjunction with the dynamometer for verification purposes, are attached to this workpiece.

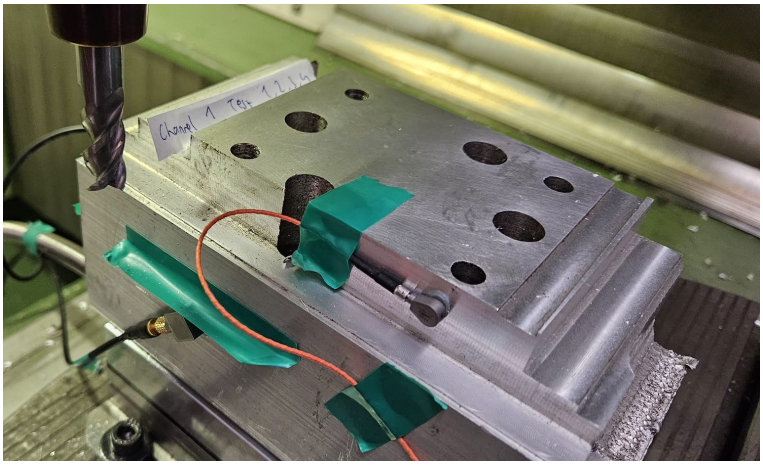


Figure 4.2: Full Sloth Cutting Test

The cutting test process parameters can be seen in Table 4.2, where D represents the diameter of the tool, N is the number of teeth of the tool, F denotes the feed rate, a_p is the axial depth of cut, a_e is the radial depth of cut, and β represents the helix angle of the tool.

Table 4.2: Process Parameters of Cutting Tests

No	D [mm]	N	ω_s [rpm]	F [mm/min]	a_p [mm]	a_e [mm]	β [deg]
1	12	3	2000	1200	3	6	45
2	12	3	2500	1500	2	12	45
3	12	3	2500	600	5	3	45
4	12	3	2500	1500	4	12	45
5	16	3	2400	1000	3	16	45
6	16	3	2400	500	11	2	45
7	16	4	3000	1500	1	8	45

4.2.2 Verification Method 1

In this subsection, Verification Method 1 is discussed. In this approach, the real data for V_{dse} and V_{qse}, collected during the cutting tests, are transformed into V_{dss} and V_{qss} using the motor angular position ω_m and the 'Inverse Park Transform,' as described in Equation 3.21.

These input voltages are used in both the dynamic model, which generates the measurements of I_{dss}, I_{qss}, ω_m, θ_T, and ω_s for the estimation methods in simulation, and in all estimation methods except Method 3. For Estimation Method 3, the input torque T_e is also generated by the same dynamic model in simulation.

The cutting torque T_c is fed into the dynamic model and is calculated from process parameters and spindle angular position ω_s using the force model. To verify this torque, a comparison is made between the output forces F_x and F_y calculated by the force model and the actual cutting forces recorded by the dynamometer.

For the geometry matrix $\mathbf{h}_t$, required as input for all estimation methods except

Method 4, the process data from the cutting tests and spindle angular position ω_s are utilized to calculate the matrix through the force model.

The results of the methods are presented together in the figures shown in this subsection for comparison purposes. However, since the state variables of some methods differ, certain methods may not be included in specific figures.

It is important to note that all currents in the model exhibit an initial oscillatory behavior until they stabilize, as the initial current values are assumed to be zero. This initial oscillatory behavior can be observed across all current graphs.

4.2.2.1 Test 1

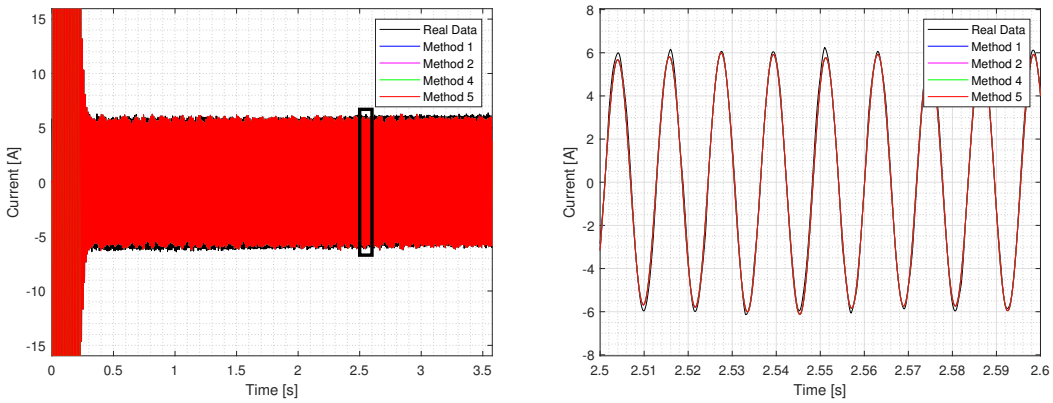
Table 4.3: Process Parameters of Cutting Test 1

No	D [mm]	N	ω_s [rpm]	F [mm/min]	a_p [mm]	a_e [mm]	β [deg]
1	12	3	2000	1200	3	6	45

The process parameters for Test 1, commonly referred to as the 'half-slot cutting', are presented in Table 4.3.

For the state variables I_{dss} and I_{qss}, which denote the direct and quadrature currents in the stationary reference frame, a comparison of state estimations was conducted for all methods, with the exception of Method 3, as it does not incorporate the electric subsystem within the system model.

Figure 4.3 presents a comparison of the estimation results for I_{dss} from all methods, excluding Method 3, against the collected data. The estimations from all methods exhibit close alignment with the real data, demonstrating similar performance in estimating this state.

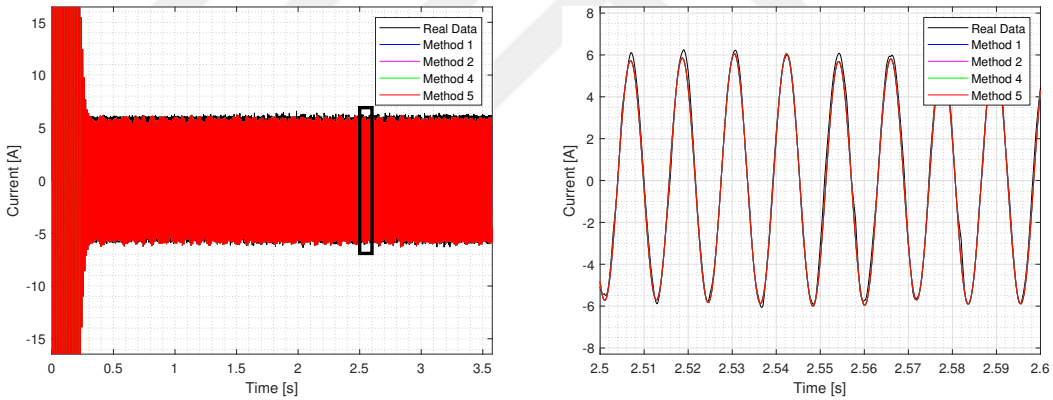


(a) Comparison Between 0-3.6 Seconds

(b) Zoomed Region

Figure 4.3: Comparison of I_{dss} Estimation Among Different Estimation Methods

In Figure 4.4, the estimation results for I_{qss} from all methods, except Method 3, are compared with the collected data. The results indicate that all methods provide similar estimations for this state, showing a close alignment with the actual data.



(a) Comparison Between 0-3.6 Seconds

(b) Zoomed Region

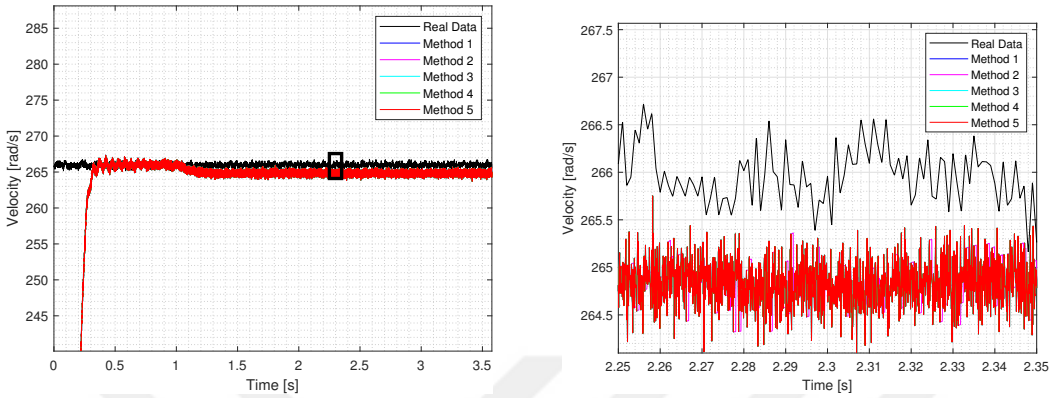
Figure 4.4: Comparison of I_{qss} Estimation Among Different Estimation Methods

For the state variables associated with the mechanical subsystem, namely ω_m, θ_t, and ω_s, all methods are compared with one another based on their estimation results.

Figure 4.5 presents a comparison of the estimation results for ω_m across all methods against the collected data. The results indicate that all methods yield similar estima-

tions for this state, with close alignment to the actual data.

As shown in Figure 4.5b, all methods estimate ω_m with a slight negative bias. This discrepancy is attributable to differences between the real and simulation models; however, the bias is considered negligible.



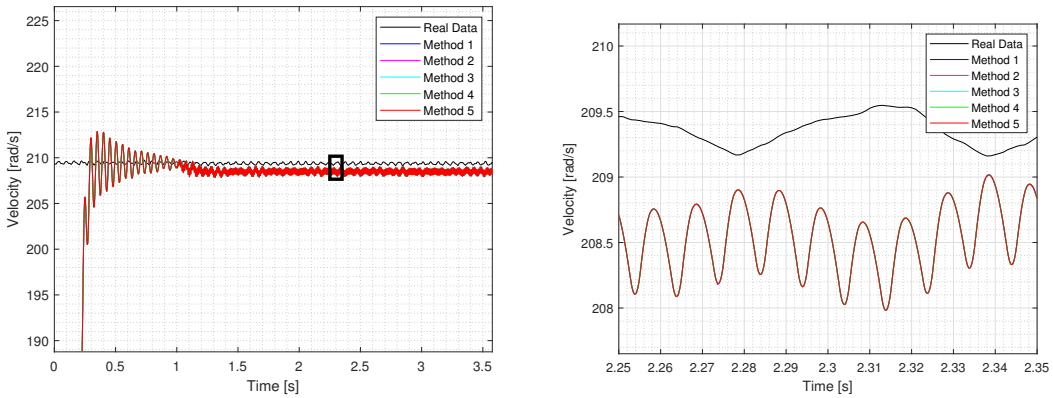
(a) Comparison Between 0-3.6 Seconds

(b) Zoomed Region

Figure 4.5: Comparison of ω_m Estimation Among Different Estimation Methods

Figure 4.6 illustrates a comparison of the estimation results for ω_s across all methods in relation to the collected data. The findings show that all methods produce similar estimations for this state, with close alignment to the actual data.

Figure 4.6b reveals that all methods estimate ω_s with a slight negative bias, and the trend exhibits minor deviations. This discrepancy is likely due to differences between the real and simulation models; nevertheless, the bias remains negligible.



(a) Comparison Between 0-3.6 Seconds

(b) Zoomed Region

Figure 4.6: Comparison of ω_s Estimation Among Different Estimation Methods

Figure 4.7 compares the estimation results for θ_T from all methods with the collected data. Due to drifting observed in the real data, a logical comparison is not feasible in this instance.

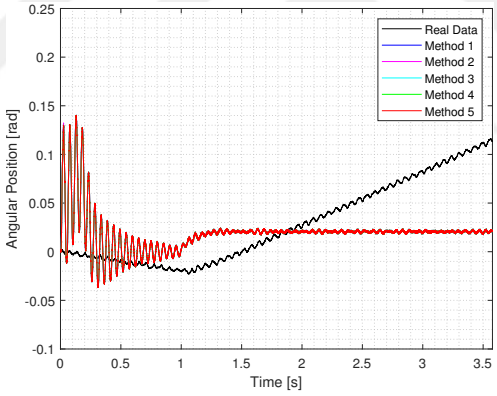


Figure 4.7: Comparison of θ_T Estimation Among Different Estimation Methods

For the comparison of state estimations for K_{tc} and K_{te}, Method 4 is excluded, as it does not incorporate these variables within its algorithm, relying instead on direct estimation of T_c.

Figure 4.8 presents a comparison of the tangential cutting force coefficient K_{tc} estimated by all relevant methods against the identified parameter. The results indicate that all methods estimate this parameter with a slight negative bias.

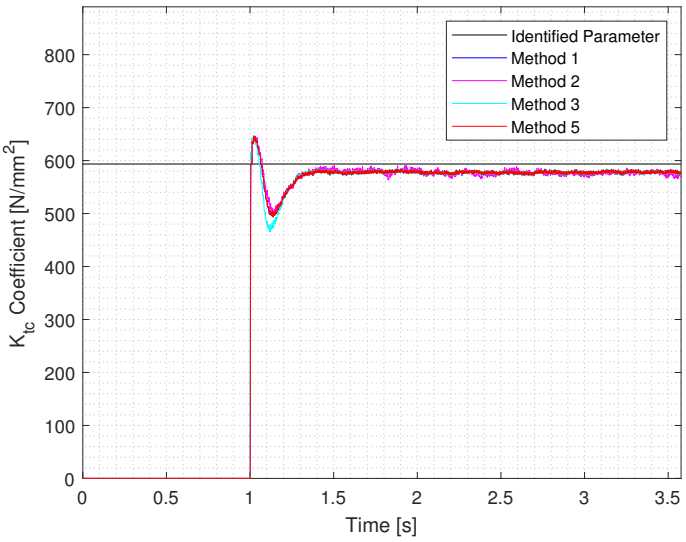
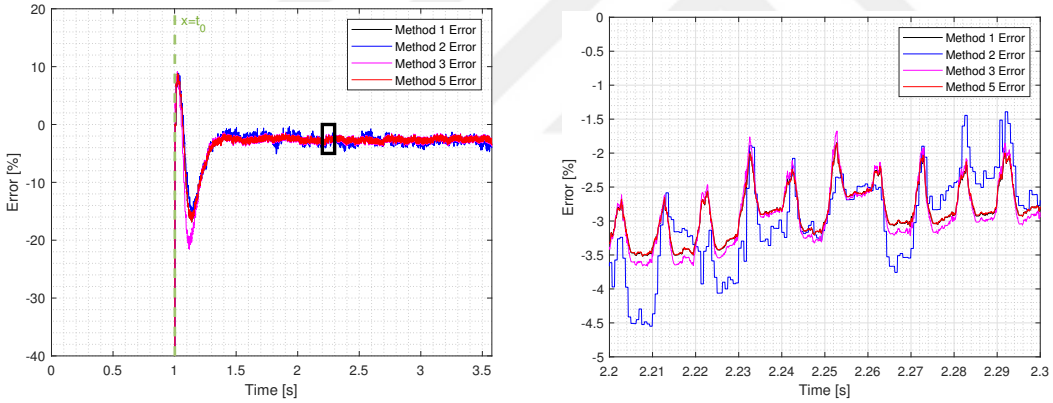


Figure 4.8: Comparison of K_{tc} Estimation Among Different Estimation Methods

Figure 4.9 illustrates the estimation errors for the state K_{tc}, comparing different estimation methods. The green dashed line indicates the initial moment when the disturbance torque starts to influence the system.



(a) Comparison Between 0-3.6 Seconds

(b) Zoomed Region

Figure 4.9: Comparison of Estimation Error for K_{tc} Among Different Estimation Methods

Upon further examination of Figure 4.9a, it can be observed that all methods exhibit similar estimation errors for this state. Additionally, a closer inspection of the zoomed region in Figure 4.9b reveals a comparable oscillatory trend in the estimation errors across the methods.

Figure 4.10 shows a comparison of the tangential edge force coefficient K_{te} as estimated by all relevant methods in relation to the identified parameter. The findings suggest that each method estimates this parameter with a minor positive bias.

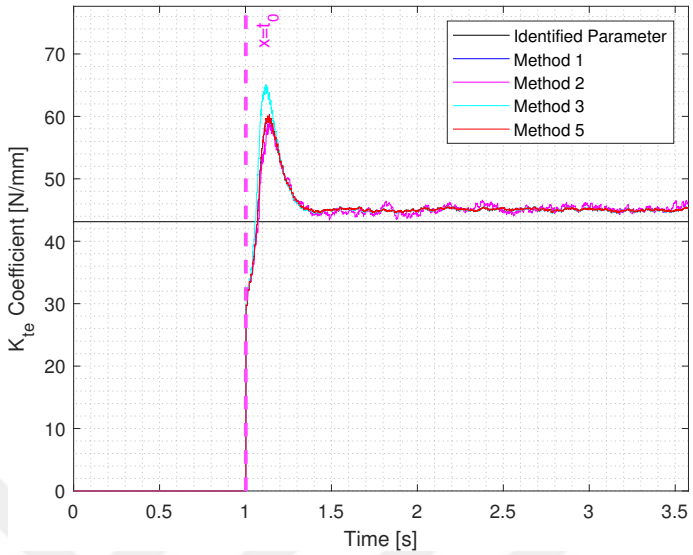
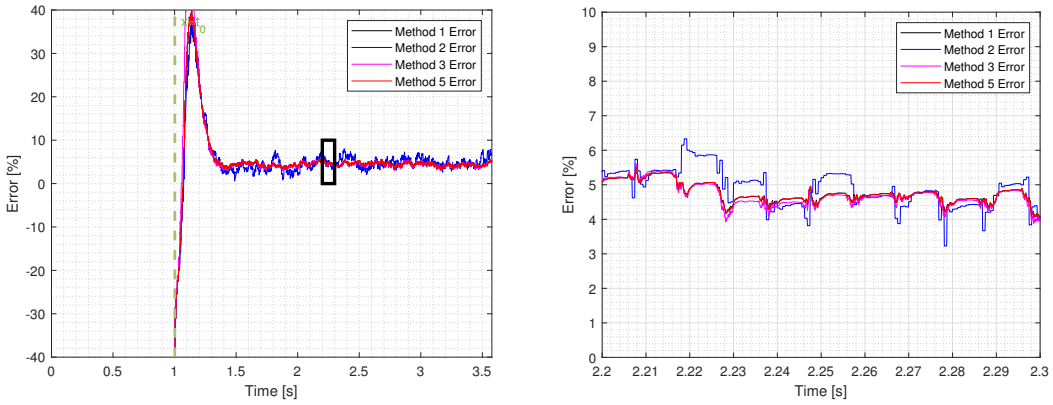


Figure 4.10: Comparison of K_{te} Estimation Among Different Estimation Methods

Figure 4.11 depicts the estimation errors for the state K_{te}, comparing various estimation methods. The green dashed line represents the initial point at which the disturbance torque starts affecting the system.

A detailed examination of Figure 4.11a shows that all methods yield similar estimation errors for this state, with errors remaining within the range of $3 - 6\%$. Additionally, the zoomed region in Figure 4.11b highlights a recurring oscillatory pattern in the estimation errors across the methods.

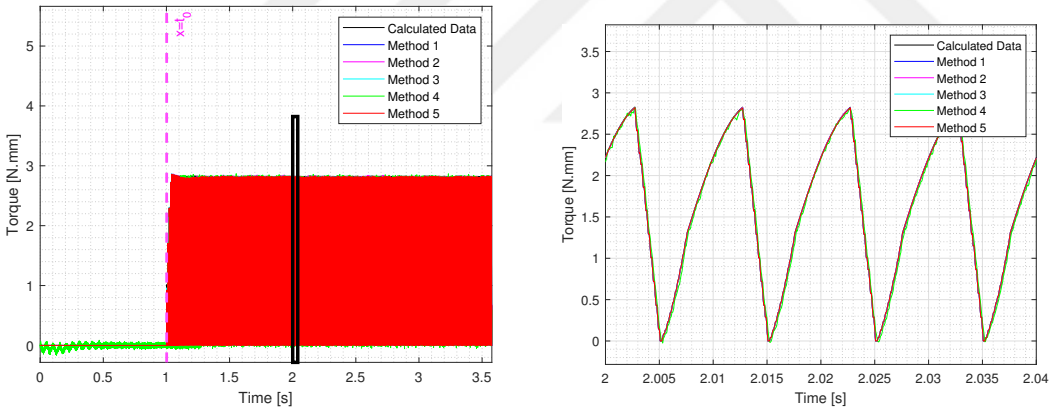


(a) Comparison Between 0-3.6 Seconds

(b) Zoomed Region

Figure 4.11: Comparison of Estimation Error for K_{te} Among Different Estimation Methods

In Figure 4.12, the estimated tangential cutting torque T_c from all methods is compared with the calculated torque. It is clear that all methods provide similar results.

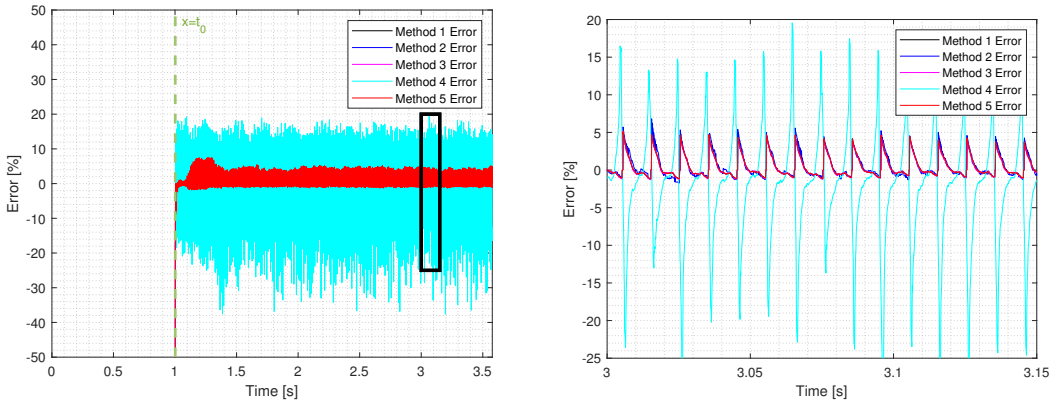


(a) Comparison Between 0-3.6 Seconds

(b) Zoomed Region

Figure 4.12: Comparison of T_c Estimation Among Different Estimation Methods

In Figure 4.13, the estimation error for T_c is shown for all methods. An examination of the zoomed region reveals that all methods, except Method 4, demonstrate similar error patterns and magnitudes. Method 4 is identified as the least effective method in this test.



(a) Comparison Between 0-3.6 Seconds

(b) Zoomed Region

Figure 4.13: Comparison of T_c Estimation Error Among Different Estimation Methods

Figure 4.13b provides a clearer view of the estimation error trends. It can be observed that all methods, except Method 4, exhibit similar error trends and magnitudes. The deviation in Method 4 can be attributed to insufficient information regarding the geometry between the tool and the workpiece.

4.2.2.2 Test 2

Table 4.4: Process Parameters of Cutting Test 2

No	D [mm]	N	ω_s [rpm]	F [mm/min]	a_p [mm]	a_e [mm]	β [deg]
2	12	3	2500	1500	2	12	45

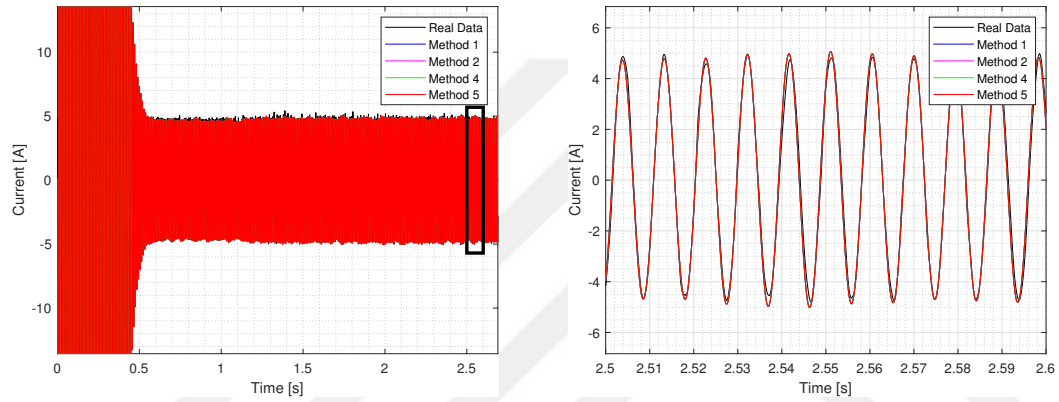
The process parameters for Test 2, often designated as the 'full-slot cutting' are provided in Table 4.4.

For the state variables I_{dss} and I_{qss}, representing the direct and quadrature currents in the stationary reference frame, state estimation comparisons were performed across all methods, excluding Method 3, as this method omits the electric subsystem from the system model.

Figure 4.14 illustrates the estimation outcomes for I_{dss} from all methods, with the exception of Method 3, alongside the actual data. The estimates from each method closely align with the observed data, indicating a consistent level of accuracy in state estimation across these methods.

Upon examining Figure 4.14b, a slight phase shift and minor magnitude difference can be observed; however, these discrepancies are minimal and can be considered negligible.

When compared to Test 1, known as the 'half-slot cutting' test, the estimation methods that incorporate electric subsystem states yielded comparably similar results.



(a) Comparison Between 0-2.6 Seconds

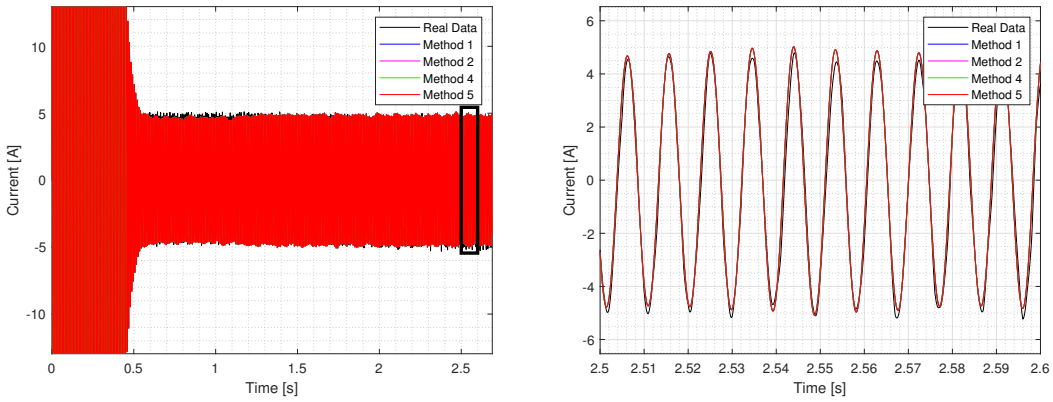
(b) Zoomed Region

Figure 4.14: Comparison of I_{dss} Estimation Among Different Estimation Methods

Figure 4.15 depicts the estimation results for I_{qss} from all methods, excluding Method 3, alongside the actual data. The estimations from each method are closely aligned with the observed data, demonstrating a consistent accuracy in state estimation across these methods.

In Figure 4.15b, a minor phase shift and slight magnitude difference are noticeable; however, these variations are minimal and can be regarded as negligible.

When compared with Test 1, referred to as the 'half-slot cutting' test, the methods incorporating electric subsystem states produced similarly accurate results, as expected, given the analogous nature of the I_{qss} and I_{dss} currents.



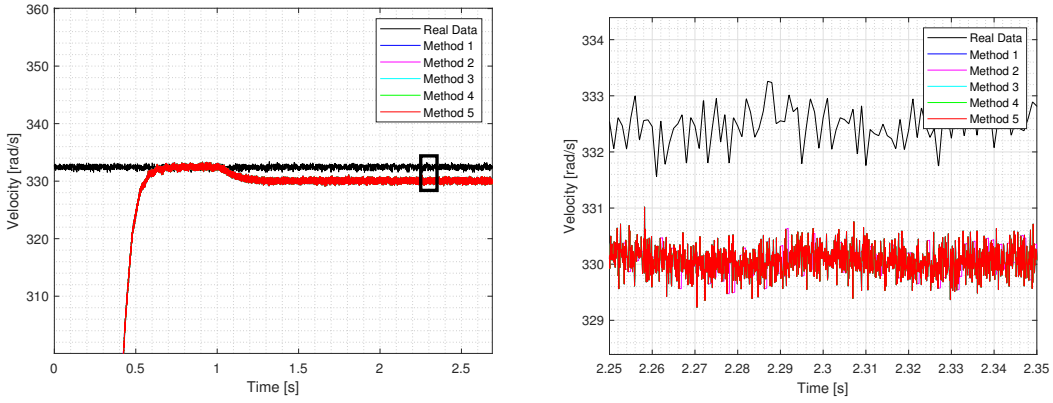
(a) Comparison Between 0-2.6 Seconds (b) Zoomed Region

Figure 4.15: Comparison of I_{qss} Estimation Among Different Estimation Methods

For the state variables associated with the mechanical subsystem, specifically ω_m, θ_t, and ω_s, the estimation results from all methods are compared.

Figure 4.16 provides a comparison of the estimation outcomes for ω_m from all methods against the actual data. The results show that all methods produce similar estimations for this state, closely aligning with the observed data.

As illustrated in Figure 4.16b, a slight negative bias is present in the estimations of ω_m across all methods. This bias is attributed to differences between the actual and simulated models; however, it is deemed negligible.

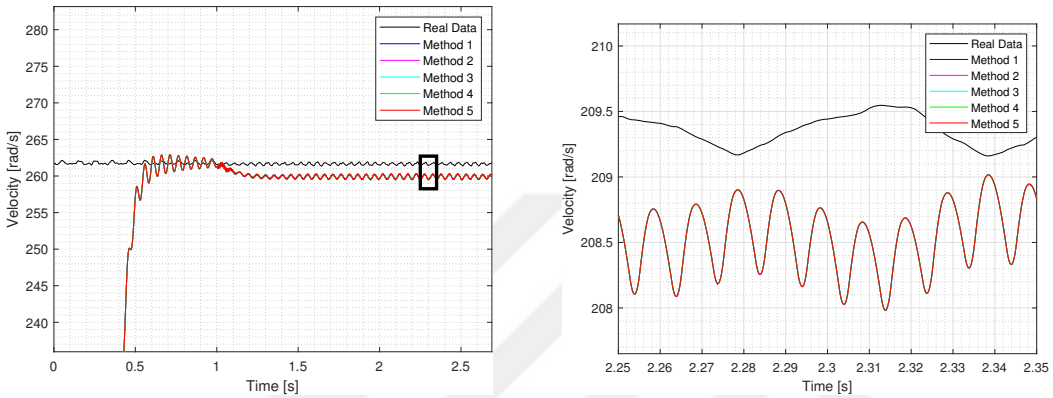


(a) Comparison Between 0-2.6 Seconds (b) Zoomed Region

Figure 4.16: Comparison of ω_m Estimation Among Different Estimation Methods

In contrast to the results obtained in the first test, the error magnitude for ω_m estimations in this test is somewhat larger. This discrepancy can be explained by the fact that the mechanical system identification, as detailed in Section 3.1.2, was conducted near 1000 rpm, whereas the speed in this test is approximately 2500 rpm.

Figure 4.17 illustrates a comparison of the estimation results for ω_s from all methods against the collected data. The findings indicate that all methods yield similar estimations for this state, with close alignment to the actual data.



(a) Comparison Between 0-2.6 Seconds

(b) Zoomed Region

Figure 4.17: Comparison of ω_s Estimation Among Different Estimation Methods

Compared to the results from the first test, the error magnitude for ω_s estimations in this test is slightly larger. This discrepancy can be attributed to the fact that the mechanical system identification, as discussed in Section 3.1.2, was performed near 1000 rpm, while the speed in this test is approximately 2500 rpm.

Figure 4.18 compares the estimation results for θ_T from all methods with the collected data. However, due to drifting observed in the actual data, a meaningful comparison is not feasible in this case.

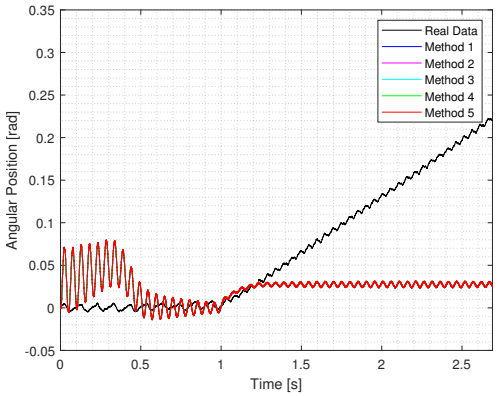


Figure 4.18: Comparison of θ_T Estimation Among Different Estimation Methods

For the comparison of state estimations for K_{tc} and K_{te}, Method 4 is excluded, as it does not incorporate these variables within its algorithm, instead relying on direct estimation of T_c.

Figure 4.19 presents a comparison of the tangential cutting force coefficient K_{tc} estimated by all relevant methods against the identified parameter. The results indicate that all methods estimate this parameter with a very slight negative bias.

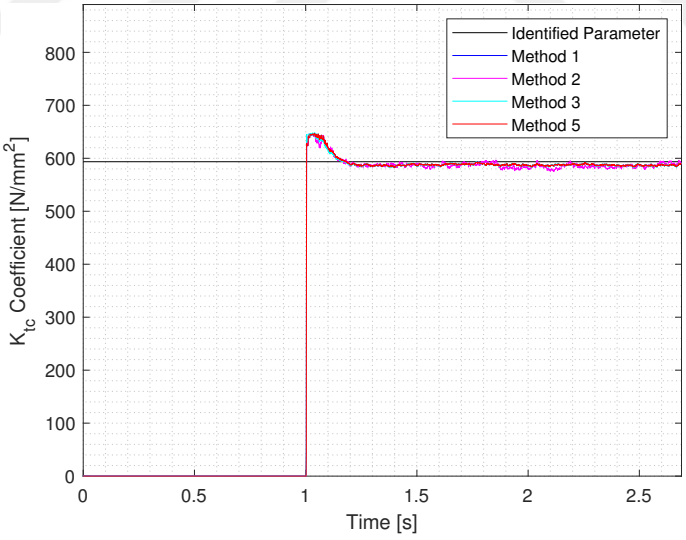
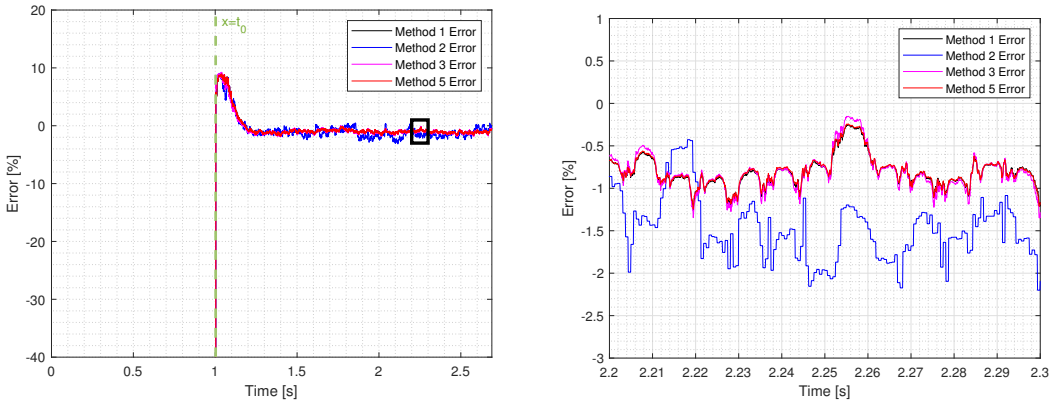


Figure 4.19: Comparison of K_{tc} Estimation Among Different Estimation Methods

Figure 4.20 illustrates the estimation errors for the state K_{tc} across various estimation methods. The green dashed line marks the initial moment when the disturbance torque begins to affect the system.



(a) Comparison Between 0-2.6 Seconds

(b) Zoomed Region

Figure 4.20: Comparison of Estimation Error for the K_{tc} Among Different Estimation Methods

Upon further examination of Figure 4.20a, it can be observed that all methods exhibit similar estimation errors for this state. Additionally, a closer inspection of the zoomed region in Figure 4.20b reveals a comparable oscillatory trend in the estimation errors across the methods. Compared to Test 1, the methods demonstrate improved accuracy in estimating the coefficient. The error ranges from -1% to 0% for all methods, except for Method 2, which exhibits an error range between -2% and 0.5%. This represents an improvement over the error range observed in Test 1, which was between -4.5% and 1.5%.

Figure 4.21 shows a comparison of the tangential edge force coefficient K_{te} estimated by all relevant methods against the identified parameter. The findings suggest that each method estimates this parameter with a very slight positive bias.

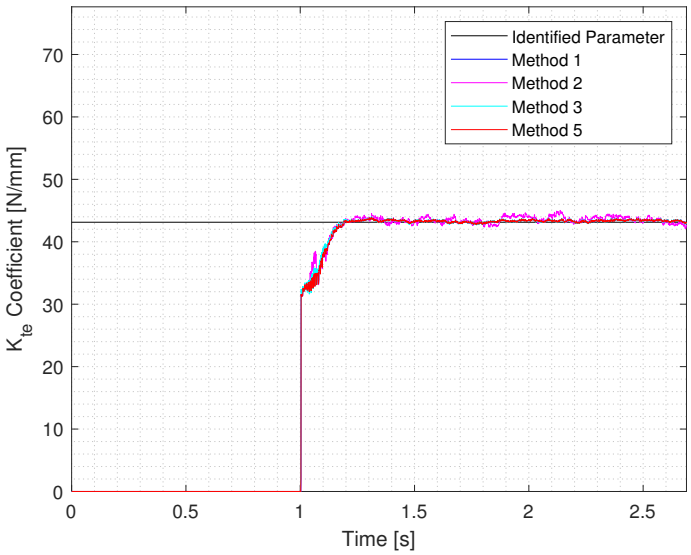
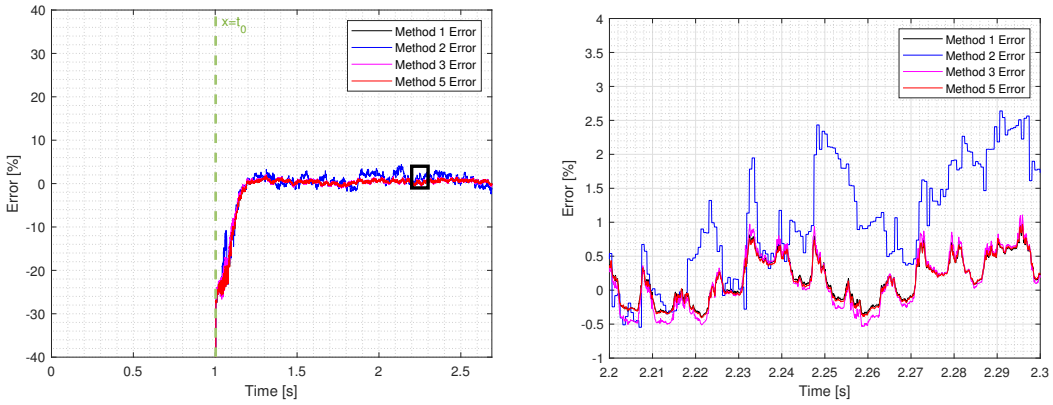


Figure 4.21: Comparison of K_{te} Estimation Among Different Estimation Methods

Figure 4.22 depicts the estimation errors for the state K_{te} across various estimation methods. The green dashed line indicates the initial point at which the disturbance torque begins to affect the system.

Upon further examination of Figure 4.22a, it can be observed that all methods exhibit similar estimation errors for this state. Additionally, a closer inspection of the zoomed region in Figure 4.22b reveals a comparable oscillatory trend in the estimation errors across the methods. Similar to the errors observed for K_{tc}, the methods demonstrate improved accuracy in estimating the coefficient compared to Test 1. The error ranges from -0.5% to 1% for all methods, except for Method 2, which shows an error range between -0.5% and 2.5%. This reflects an improvement over the error range in Test 1, which was between 4% and 6.25%.



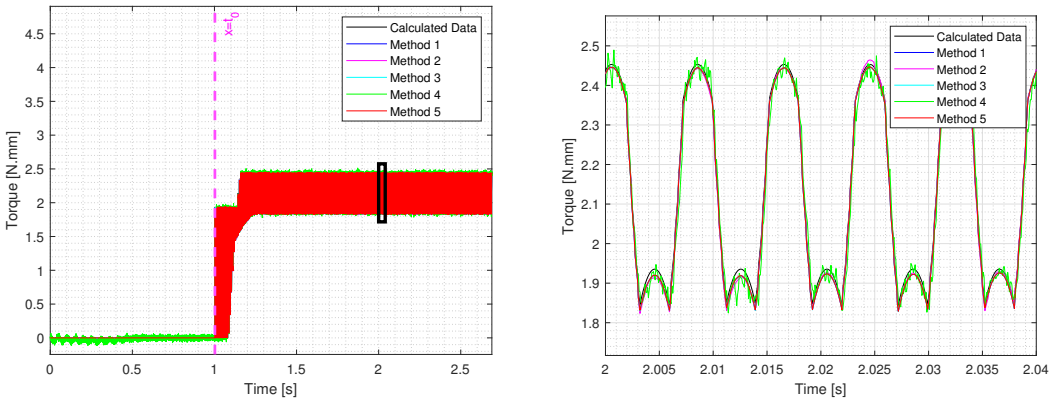
(a) Comparison Between 0-2.6 Seconds

(b) Zoomed Region

Figure 4.22: Comparison of Estimation Error for the K_{te} Among Different Estimation Methods

In Figure 4.23, the estimated tangential cutting torque T_c from all methods is compared with the calculated torque. It is evident that all methods yield similar results.

However, compared to the other methods, Method 4 estimates the tangential cutting torque T_c with a greater degree of oscillation.



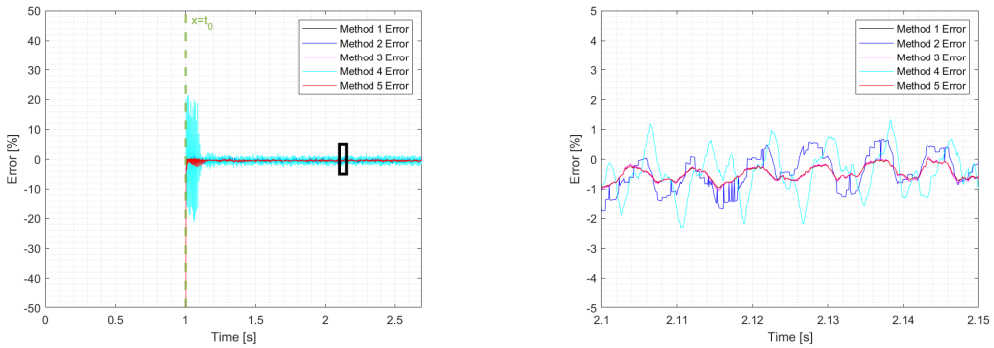
(a) Comparison Between 0-2.6 Seconds

(b) Zoomed Region

Figure 4.23: Comparison of T_c Estimation Among Different Estimation Methods

In Figure 4.24, the estimation error for T_c is shown across all methods. A closer examination of the zoomed region reveals that all methods, except for Method 4 and

Method 2, exhibit similar error patterns and magnitudes. Method 4 is identified as the least effective method in this test.



(a) Comparison Between 0-2.6 Seconds

(b) Zoomed Region

Figure 4.24: Comparison of T_c Estimation Error Among Different Estimation Methods

Compared to Test 1, all methods demonstrate improved estimation accuracy, with a particularly notable improvement in Method 4. In the first test, Method 4's error oscillated between -20% and 15%, whereas in this test, the error range has significantly decreased to between -2% and 1%. The other methods also show improvements; their error range previously spanned from 0% to 5.5%, but in this test, it has decreased to between -1% and 0% for Methods 1, 3, and 5, and between -1.7% and 0% for Method 2, as can be seen from Figure 4.24b.

4.2.2.3 Test 3

Table 4.5: Process Parameters of Cutting Test 3

No	D [mm]	N	ω_s [rpm]	F [mm/min]	a_p [mm]	a_e [mm]	β [deg]
3	12	3	2500	600	5	3	45

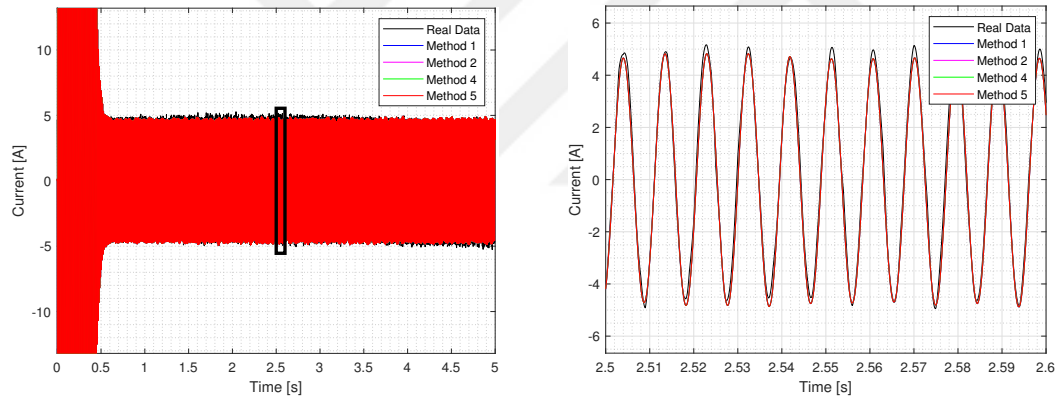
The process parameters for Test 3, also referred to as the 'quarter-slot cutting,' are listed in Table 4.5.

For the state variables I_{dss} and I_{qss}, which represent the direct and quadrature currents within the stationary reference frame, state estimation comparisons were conducted across all methods except Method 3, as this method excludes the electric subsystem from the model.

Figure 4.25 displays the estimation results for I_{dss} from all methods, apart from Method 3, alongside the actual data. The results demonstrate that each method provides estimates closely aligned with the observed data, indicating similar accuracy levels in state estimation.

Upon further inspection of Figure 4.25b, a minor phase shift and slight magnitude discrepancy can be seen. However, these variations are small and can be considered negligible.

In comparison to Test 1 and Test 2, the methods that include the electric subsystem states show similarly consistent results.



(a) Comparison Between 0-5 Seconds

(b) Zoomed Region

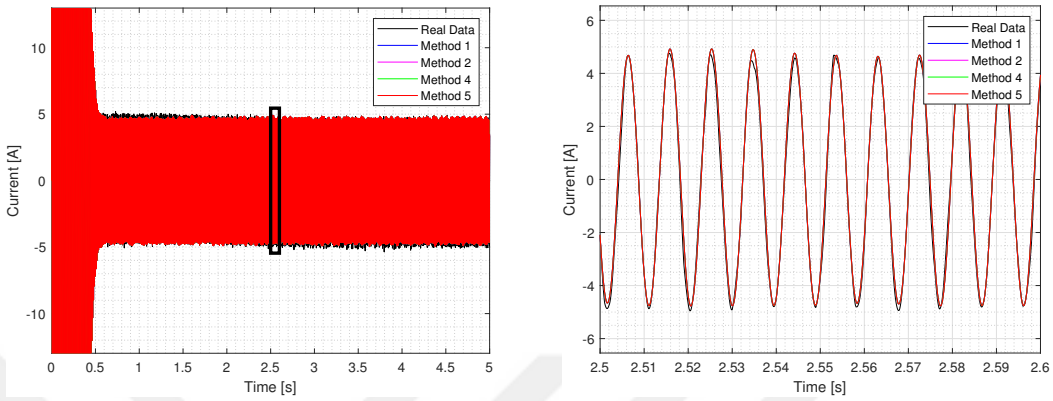
Figure 4.25: Comparison of I_{dss} Estimation Among Different Estimation Methods

Figure 4.26 presents the estimation results for I_{qss} across all methods, except Method 3, alongside the actual measurements. The estimates from each method closely correspond to the observed data, indicating reliable accuracy in state estimation among these methods.

In Figure 4.26b, a slight phase shift and small magnitude discrepancy can be ob-

served. Nevertheless, these differences are minor and can be considered insignificant.

Compared to Tests 1 and 2, the methods that include the electric subsystem states yielded equally precise results, as anticipated, due to the comparable characteristics of the I_{qss} and I_{dss} currents.



(a) Comparison Between 0-5 Seconds

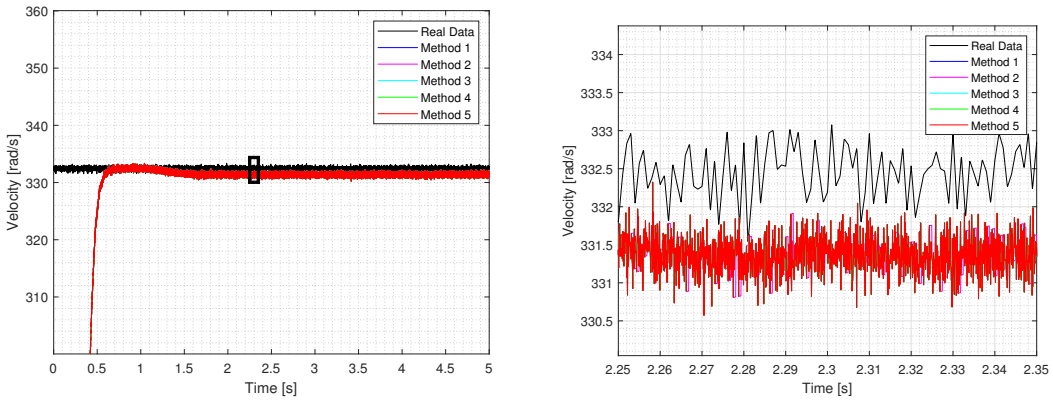
(b) Zoomed Region

Figure 4.26: Comparison of I_{qss} Estimation Among Different Estimation Methods

For the state variables related to the mechanical subsystem, namely ω_m, θ_t, and ω_s, the estimation results from all methods are evaluated.

Figure 4.27 shows a comparison of the estimation results for ω_m from each method against the real data. The findings indicate that all methods yield similar estimates for this state, showing a close match with the actual measurements.

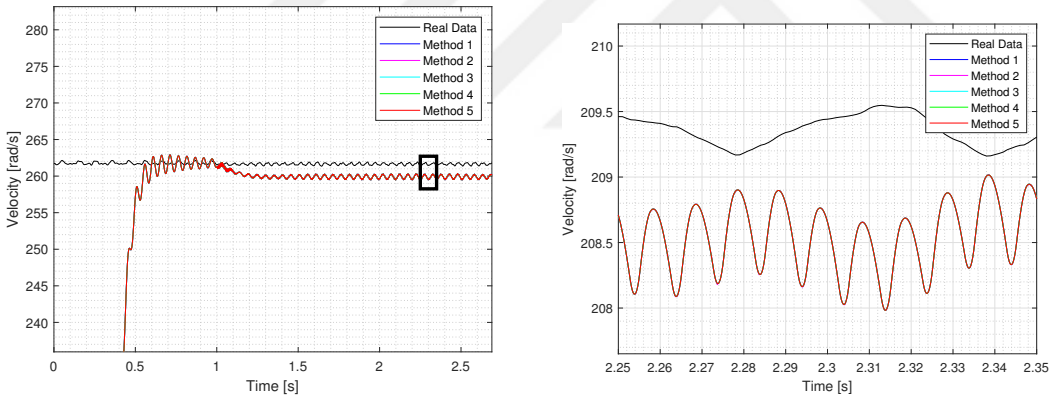
As seen in Figure 4.27b, a minor negative bias is apparent in the ω_m estimations across all methods. This bias is likely due to discrepancies between the real and simulated models; nonetheless, it is considered negligible.



(a) Comparison Between 0-5 Seconds (b) Zoomed Region

Figure 4.27: Comparison of ω_m Estimation Among Different Estimation Methods

Figure 4.28 presents a comparison of the estimation results for ω_s from each method alongside the observed data. The results demonstrate that all methods provide similar estimates for this state, with a strong alignment to the actual measurements.



(a) Comparison Between 0-5 Seconds (b) Zoomed Region

Figure 4.28: Comparison of ω_s Estimation Among Different Estimation Methods

Figure 4.29 displays a comparison of the estimation results for θ_T across all methods with the recorded data. However, due to drift observed in the actual data, a direct comparison is not practical in this instance.

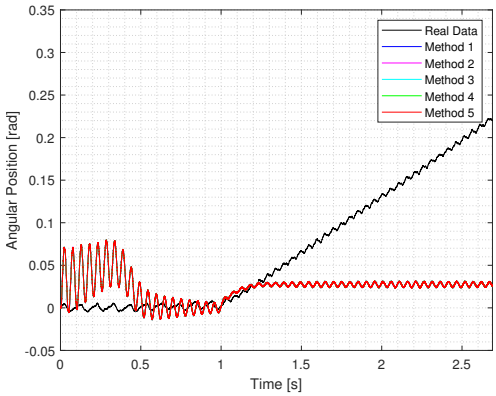


Figure 4.29: Comparison of θ_T Estimation Among Different Estimation Methods

For the comparison of state estimations for K_{tc} and K_{te}, Method 4 is excluded, as it does not incorporate these variables within its algorithm, instead relying on direct estimation of T_c.

Figure 4.30 shows a comparison of the tangential cutting force coefficient K_{tc} as estimated by all relevant methods in relation to the identified parameter. The results reveal that each method estimates this parameter with a noticeable negative bias, which is larger than that observed in both Test 1 and Test 2.

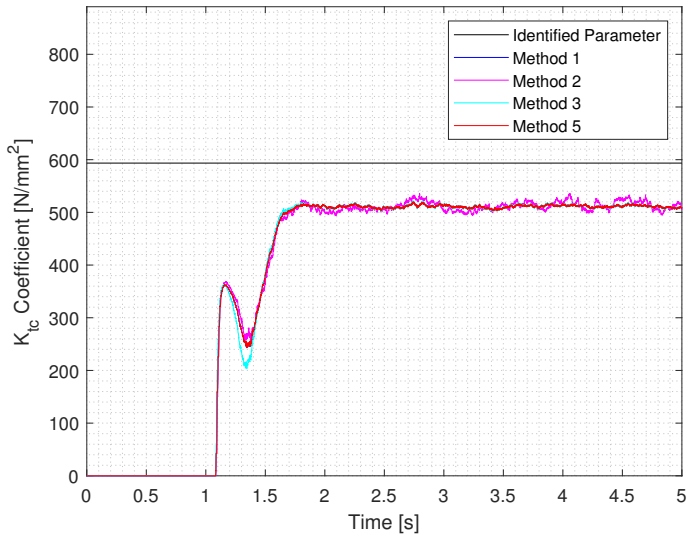
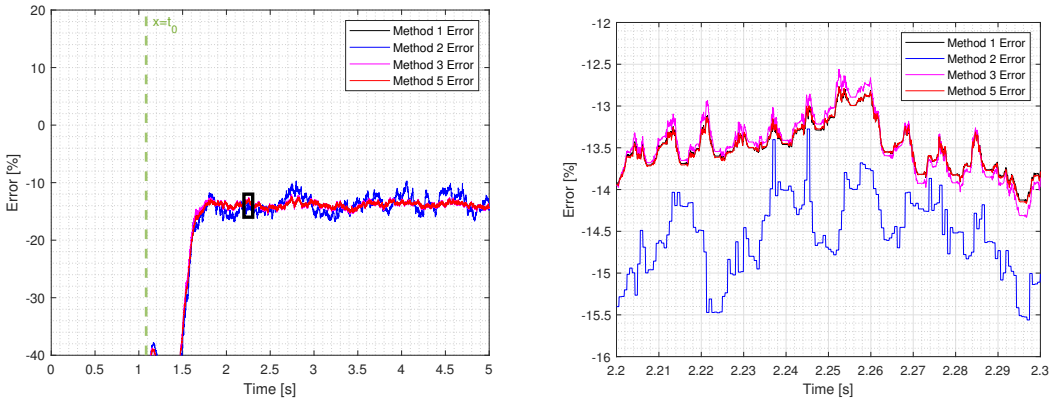


Figure 4.30: Comparison of K_{tc} Estimation Among Different Estimation Methods

Figure 4.31 illustrates the estimation errors for the state K_{tc} across various estimation methods. The green dashed line marks the initial moment when the disturbance torque

begins to affect the system.



(a) Comparison Between 0-5 Seconds

(b) Zoomed Region

Figure 4.31: Comparison of Estimation Error for the K_{tc} Among Different Estimation Methods

Upon closer analysis of Figure 4.31a, it is evident that all methods show similar estimation errors for this state. Furthermore, examining the zoomed-in section in Figure 4.31b reveals a consistent oscillatory pattern in the estimation errors across the methods. Compared to Tests 1 and 2, the methods display reduced accuracy in estimating the coefficient. The error varies between -14% and 12.5% for all methods, except for Method 2, which shows an error range from -15.5% to -13.5%.

Figure 4.32 presents a comparison of the tangential edge force coefficient K_{te} as estimated by each relevant method relative to the identified parameter. The results indicate that all methods estimate this parameter with a slightly noticeable positive bias.

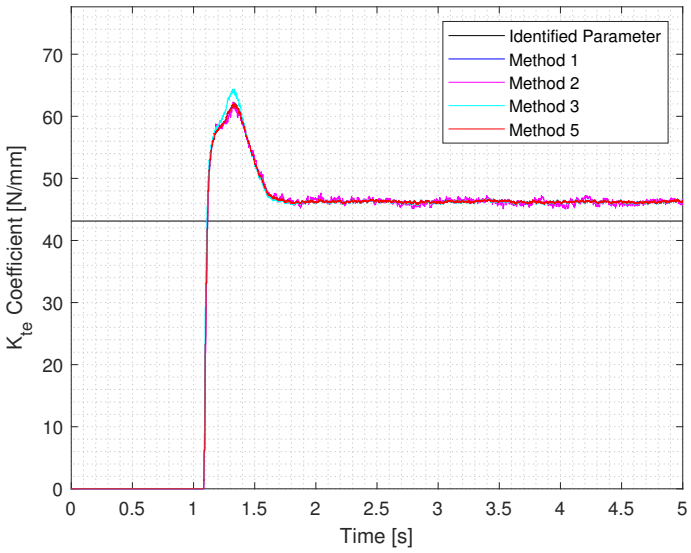
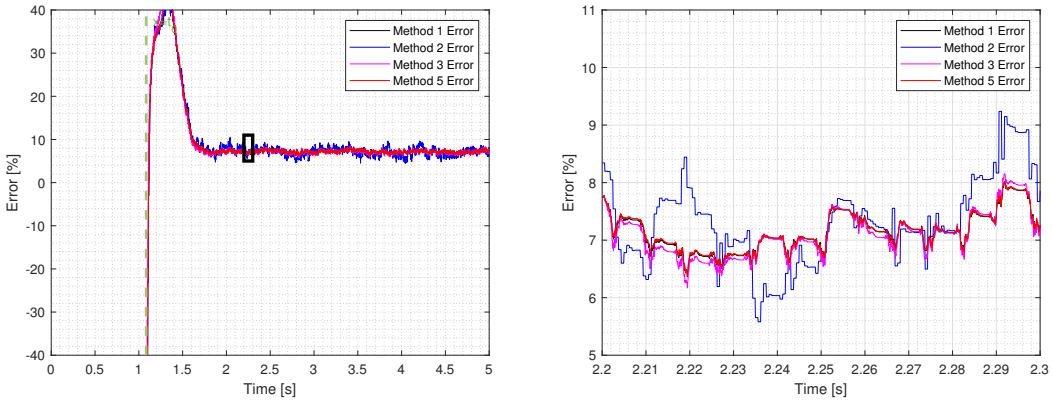


Figure 4.32: Comparison of K_{te} Estimation Among Different Estimation Methods

Figure 4.33 depicts the estimation errors for the state K_{te} across various estimation methods. The green dashed line indicates the initial point at which the disturbance torque begins to affect the system.

Upon closer inspection of Figure 4.33a, it is apparent that all methods display similar estimation errors for this state. Moreover, examining the zoomed section in Figure 4.33b reveals a comparable oscillatory pattern in the estimation errors across the methods. In line with the errors seen for K_{te}, the methods show reduced accuracy in estimating this coefficient compared to Test 2. The error ranges between 5.5% and 9.5% across all methods.



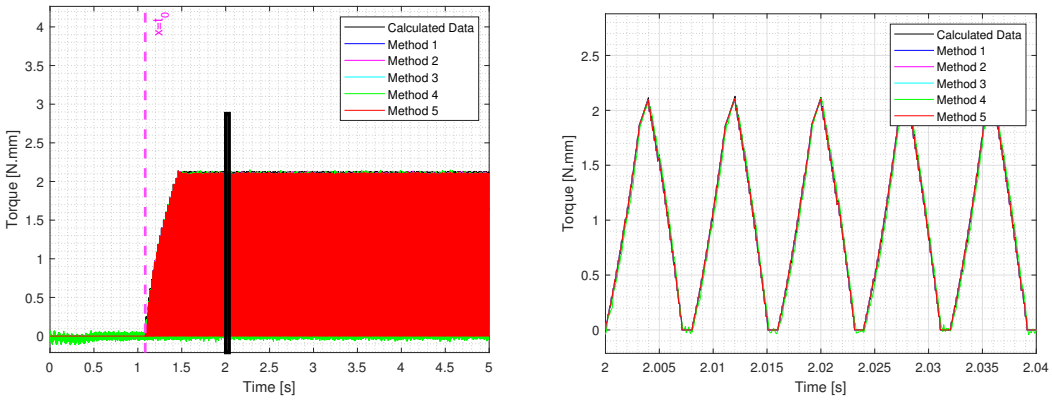
(a) Comparison Between 0-5 Seconds

(b) Zoomed Region

Figure 4.33: Comparison of Estimation Error for the K_{te} Among Different Estimation Methods

In Figure 4.34, the estimated tangential cutting torque T_c from each method is compared to the calculated torque. The results clearly show that all methods produce similar estimates.

However, in contrast to the other methods, Method 4 exhibits a higher level of oscillation in its estimation of the tangential cutting torque T_c.



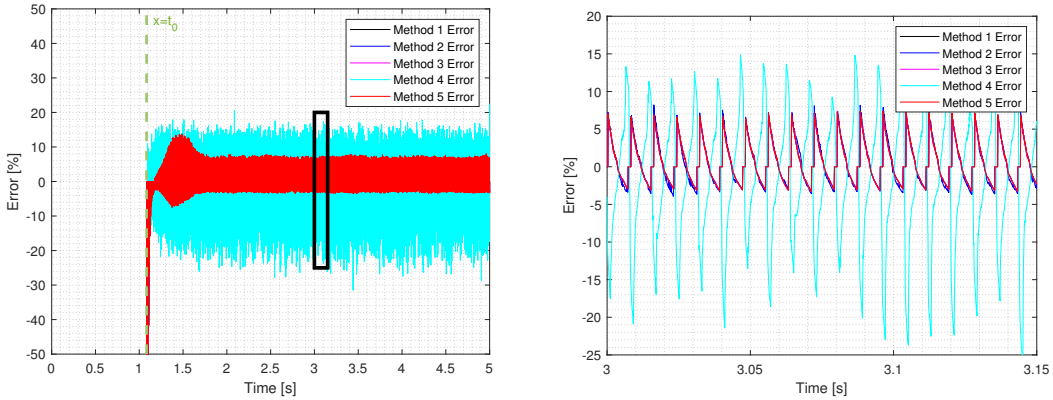
(a) Comparison Between 0-5 Seconds

(b) Zoomed Region

Figure 4.34: Comparison of T_c Estimation Among Different Estimation Methods

In Figure 4.35, the estimation error for T_c is displayed for all methods. A detailed look

at the zoomed region shows that, aside from Method 4 and Method 2, the methods demonstrate similar error patterns and magnitudes. Method 4 emerges as the least effective method in this test.



(a) Comparison Between 0-5 Seconds

(b) Zoomed Region

Figure 4.35: Comparison of T_c Estimation Error Among Different Estimation Methods

Compared to Tests 1 and 2, all methods show reduced accuracy in their estimations. In this test, Method 4's error fluctuates between -20% and 15%. The error range for the other methods spans from -3% to 7%, as illustrated in Figure 4.35b.

4.2.2.4 Discussion

In this verification approach, five distinct methods are employed to estimate the tangential cutting torque, either directly or through the estimation of tangential coefficients. Three different test datasets are utilized within a simulation environment to compare these methods.

The measurement data is generated by a simulation model that utilizes real input data for voltages V_{dss} and V_{qss}, along with the tangential cutting torque T_c derived from dynamometer force measurements.

In the first test, half-slot cutting data is used. All methods related to current measurements provide similar results for the estimation of currents I_{dss} and I_{qss}, and the

relevant methods produce comparable outputs for the mechanical subsystem states ω_m, θ_t, and ω_s.

Differences between methods become apparent in the estimation of tangential force coefficients. Methods 1 and 5 yield similar results and are regarded as the most stable. Method 2 displays slightly oscillatory behavior due to asynchronous mechanical measurements occurring at one-eighth the frequency of the other methods. Method 3, which relies solely on the mechanical subsystem dynamics, performs less effectively in transient states.

For cutting torque estimation, Method 4 demonstrates the weakest performance, likely due to limited knowledge of the cutting tool-workpiece geometry, resulting in insufficient cutting information.

In the second test, full-slot cutting data is used. The performance of all estimation methods improves without changing any Kalman filter parameters, and the comparison results are consistent with Test 1.

In the third test, quarter-slot cutting data is used. All estimation methods exhibit the worst performance compared to the other tests.

In conclusion, based on the results from all three tests, Methods 1 and 5 are considered the most reliable estimation methods within the simulation environment. Method 2 is advantageous when current measurements can be obtained at a higher frequency than those of the mechanical subsystem. Method 3 is not a feasible alternative, as it depends on current measurements to estimate electric torque T_e, and estimating it without knowledge of rotor currents introduces errors during transient states, making the other methods more practical choices. Method 4 is applicable when cutting geometry information is unavailable; however, when this information is accessible, the other methods are preferable.

4.2.3 Verification Method 2

In this subsection, the verification of the estimation methods using real measurement data recorded during the cutting tests is discussed. The geometry matrix used in rel-

evant methods is also calculated using the force model, based on process parameters and the recorded spindle angular position, θ_s.

All currents and voltages are recorded in the synchronous reference frame and transformed into the stationary reference frame using the motor angular position and the 'Inverse Park Transform'.

Due to errors in the measurement data, only two methods—Method 1 and Method 5—are used for these verification tests, as they handle such errors more effectively than the others.

It is important to note that all currents in the model exhibit an initial oscillatory behavior until they stabilize, as the initial current values are assumed to be zero. This initial oscillatory behavior can be observed across all current graphs.

4.2.3.1 Test 1

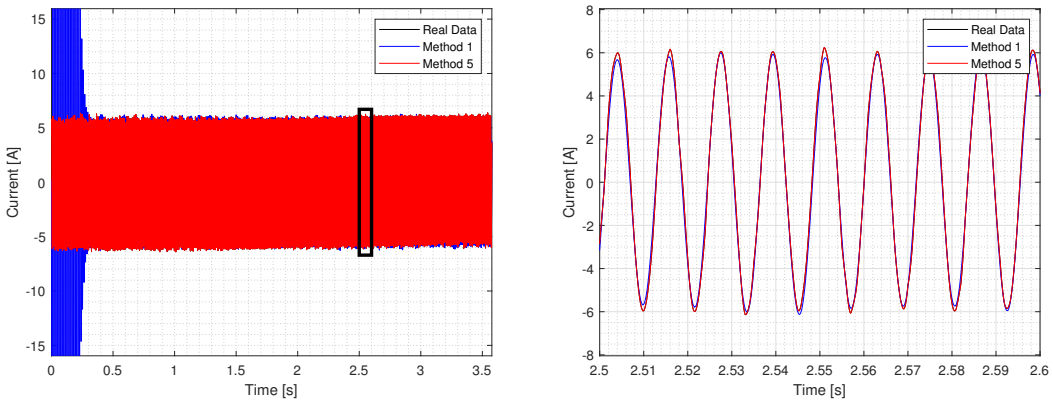
Table 4.6: Process Parameters of Cutting Test 1

No	D [mm]	N	ω_s [rpm]	F [mm/min]	a_p [mm]	a_e [mm]	β [deg]
1	12	3	2000	1200	3	6	45

The process parameters for Test 1, commonly referred to as the 'half-slot cutting', are presented in Table 4.6.

In Figure 4.36, the estimation results for I_{dss} from both methods are compared with the collected data. Both methods produce similar estimations for this state, closely aligning with the real data.

A detailed inspection of Figure 4.36b reveals that Method 5 more closely aligns with the measurement data, likely due to the additional term incorporated into Method 5 as an enhancement over Method 1.



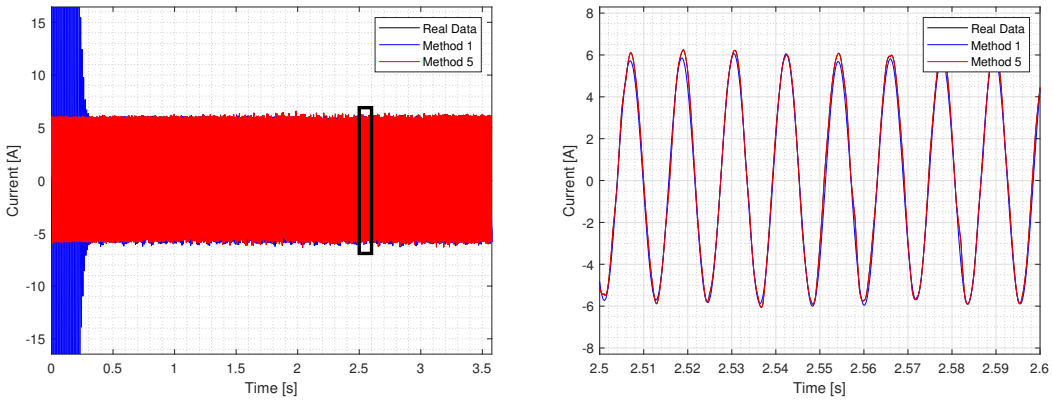
(a) Comparison Between 0-3 Seconds

(b) Zoomed Region

Figure 4.36: Comparison of I_{dss} Estimation Among Different Estimation Methods

In Figure 4.37, the estimation results for I_{qss} from both methods are compared with the collected data. Both methods produce similar estimations for this state, closely aligning with the real data.

Given that I_{qss} exhibits a similar trend in the stationary reference frame, Method 5 provides results that more closely match the measurement data.



(a) Comparison Between 0-3 Seconds

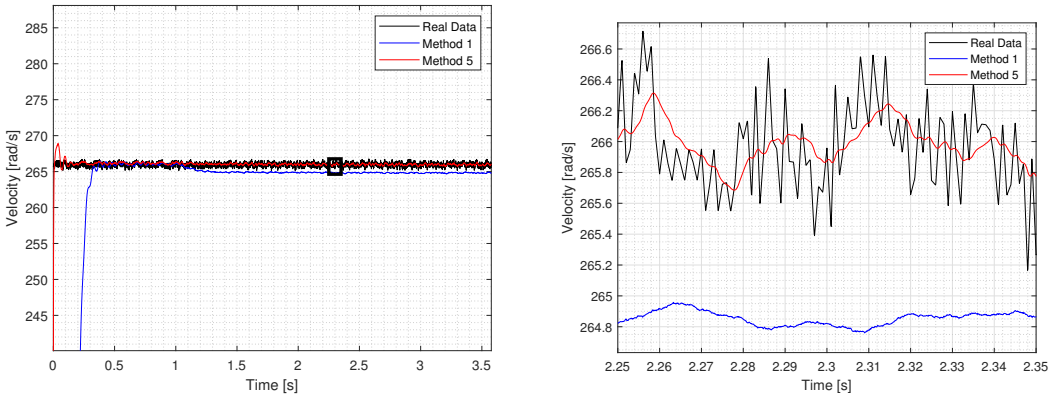
(b) Zoomed Region

Figure 4.37: Comparison of I_{qss} Estimation Among Different Estimation Methods

In Figure 4.38, the estimation results for ω_m from both methods are compared with the collected data. Both methods provide similar estimations for this state, closely

aligning with the real data.

Figure 4.38b shows that Method 5 more closely follows the trend of the real data compared to Method 1.

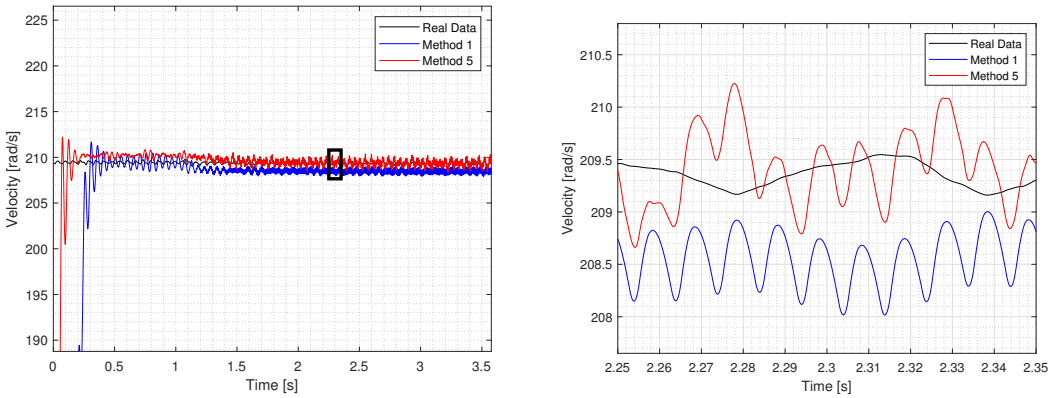


(a) Comparison Between 0-3 Seconds (b) Zoomed Region

Figure 4.38: Comparison of ω_m Estimation Among Different Estimation Methods

In Figure 4.39, the estimation results for ω_s from both methods are compared with the collected data. Both methods provide similar estimations for this state, closely aligning with the real data.

As seen in Figure 4.39b, Method 5 aligns more accurately with the magnitude of the real data in comparison to Method 1.



(a) Comparison Between 0-3 Seconds (b) Zoomed Region

Figure 4.39: Comparison of ω_s Estimation Among Different Estimation Methods

In Figure 4.40, the estimation results for θ_T from both methods are compared with the collected data. Drifting occurs in the real data, which is reflected in the methods' estimations upon closer inspection.

Both estimation methods attempt to adjust the drift towards the expected model value in a similar manner.

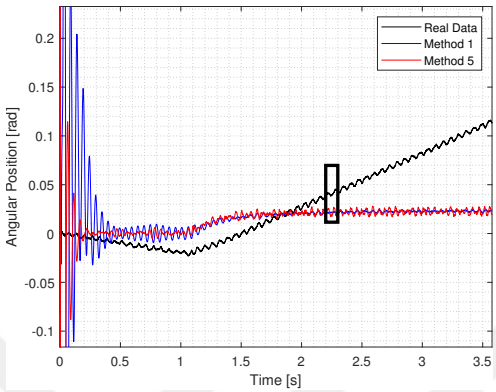


Figure 4.40: Comparison of θ_T Estimation Among Different Estimation Methods

In Figure 4.41, the estimation of the tangential cutting force coefficient K_{tc} from both methods is compared with the identified parameter. The figure shows that both methods estimate the parameter with a small positive bias.

Method 5 provides better coefficient estimates compared to Method 1, as it includes an additional term specifically designed to address the drift occurring in θ_t, thereby improving the estimation of other states as well.

Figure 4.42 shows the estimation errors for the state K_{tc} across the both methods. The green dashed line indicates the initial point at which the disturbance torque begins to impact the system.

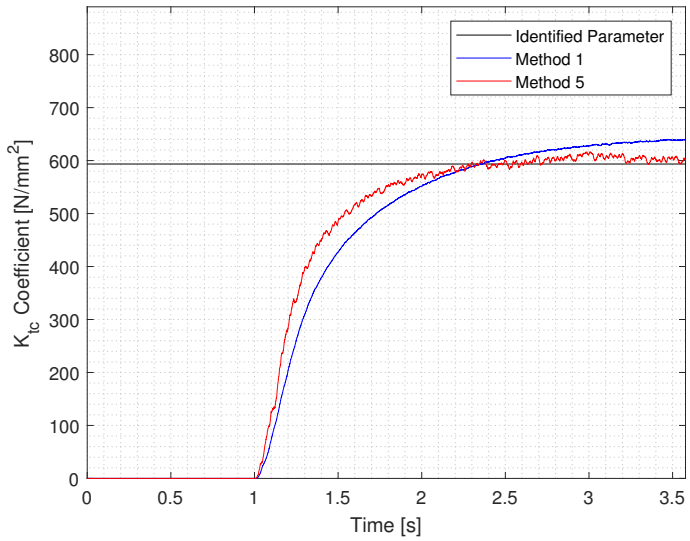
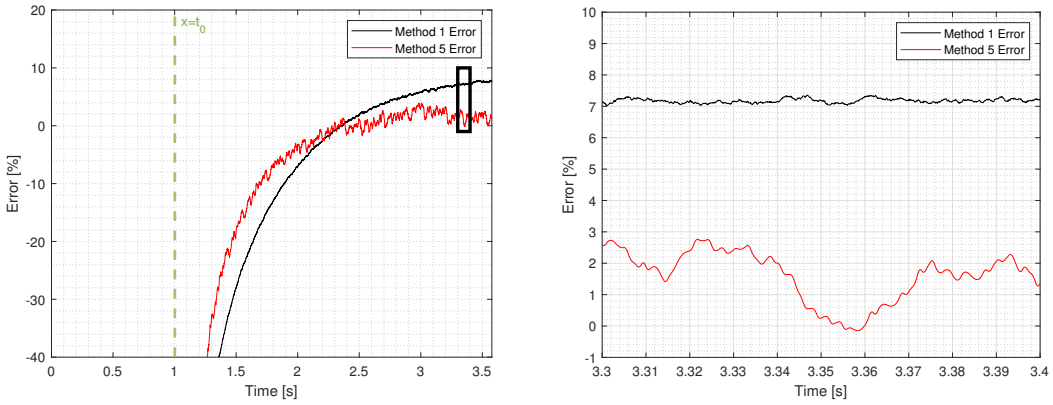


Figure 4.41: Comparison of K_{tc} Estimation Among Different Estimation Methods

A closer inspection of Figure 4.42b reveals that, in the region where the estimation methods appear to stabilize, Method 1 has an error margin between 7% and 7.2%, while Method 5 shows an error margin between 0% and 3%.

Therefore, when compared to the simulation results, Method 1 aligns closely with the simulation, whereas Method 5 exhibits an improvement over the simulation result, as seen in Figure 4.42b.

When comparing the methods, Method 1 exhibits greater stability with less oscillation, whereas Method 5 provides significantly more accurate results for estimating the coefficient K_{tc}.



(a) Comparison Between 0-3.6 Seconds

(b) Zoomed Region

Figure 4.42: Comparison of Estimation Error for the K_{tc} Among Different Estimation Methods

In Figure 4.44a, the estimation of the tangential cutting force coefficient K_{te} from both methods is compared with the identified parameter. The figure shows a positive bias in both methods, with a relatively high magnitude.

While Method 5 delivers superior accuracy for estimating the K_{tc} coefficient, the situation is reversed for this coefficient. Method 1 provides slightly more accurate results, with reduced oscillations in its estimates.

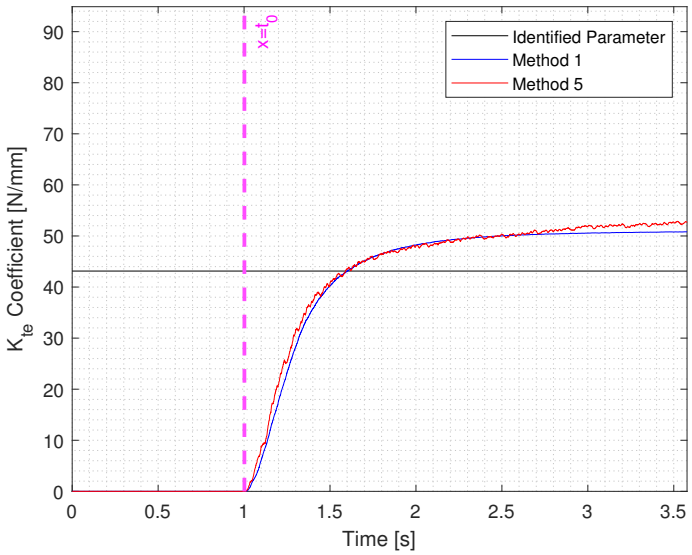
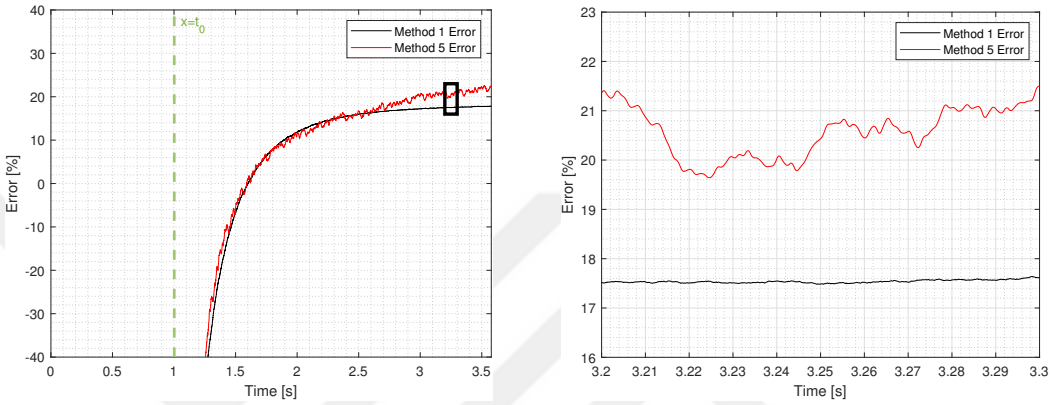


Figure 4.43: Comparison of K_{te} Estimation Among Different Estimation Methods

Figure 4.44 illustrates the estimation errors for the state K_{te}, comparing both estimation methods. The green dashed line indicates the initial point at which the disturbance torque begins to influence the system.

A closer look at Figure 4.44 reveals that the estimation error for Method 5 ranges between 19.8% and 21.5%, while for Method 1, it is between 17.4% and 17.6%. This suggests that Method 1 not only provides a more accurate estimate for this coefficient but also demonstrates greater stability compared to Method 5.



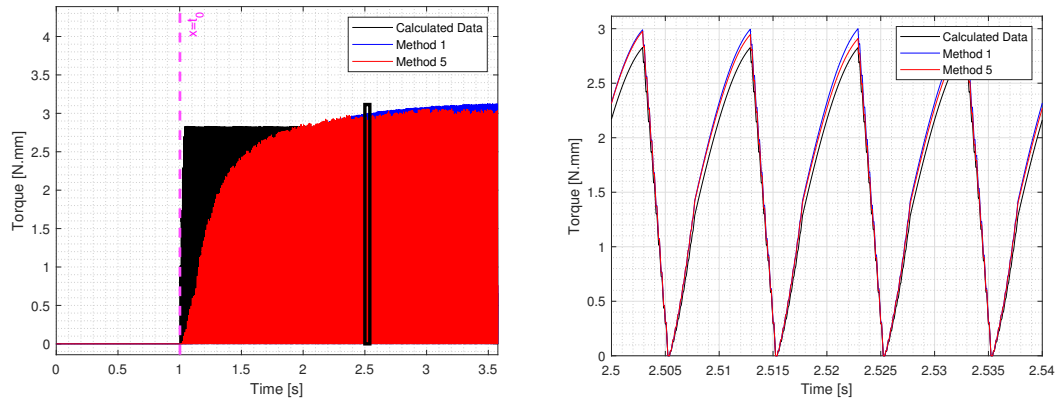
(a) Comparison Between 0-3.6 Seconds

(b) Zoomed Region

Figure 4.44: Comparison of Estimation Error for the K_{te} Among Different Estimation Methods

In Figure 4.45, the estimated tangential cutting torque T_c from both methods is compared with the calculated torque. It is evident that Method 5 provides a more stable and closer estimation to the real data for T_c.

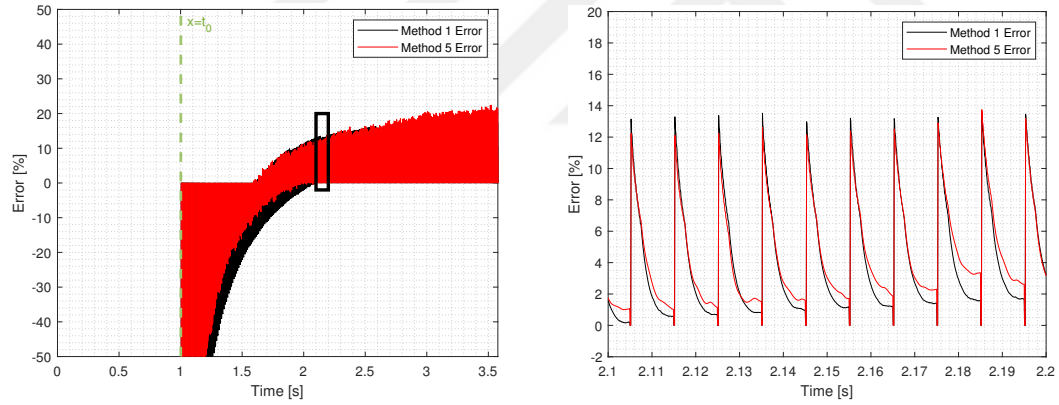
A more detailed view reveals that Method 5 converges to the result slightly faster than Method 1.



(a) Comparison Between 0-3 Seconds (b) Zoomed Region

Figure 4.45: Comparison of T_c Estimation Among Different Estimation Methods

In Figure 4.46, the estimation error for T_c is displayed for both methods. Upon examining the zoomed region, it is observed that both methods exhibit similar error patterns and magnitudes.



(a) Comparison Between 0-3 Seconds (b) Zoomed Region

Figure 4.46: Comparison of T_c Estimation Error Among Different Estimation Methods

4.2.3.2 Test 2

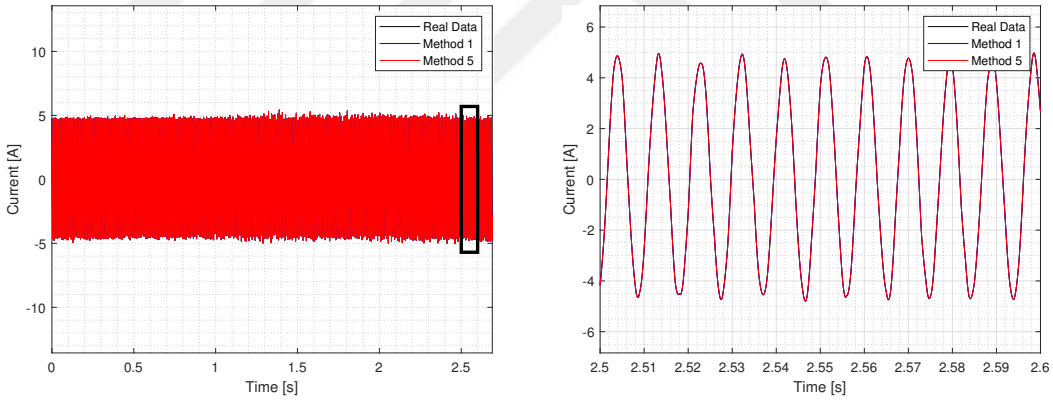
Table 4.7: Process Parameters of Cutting Test 2

No	D [mm]	N	ω_s [rpm]	F [mm/min]	a_p [mm]	a_e [mm]	β [deg]
2	12	3	2500	1500	2	12	45

The process parameters for Test 2, often designated as the 'full-slot cutting' are provided in Table 4.7.

In Figure 4.47, the estimation results for I_{dss} from both methods are compared with the collected data. Both methods produce similar estimations for this state, closely matching the real data.

A closer look at Figure 4.47b shows that both methods provide nearly perfect estimation results.



(a) Comparison Between 0-3 Seconds

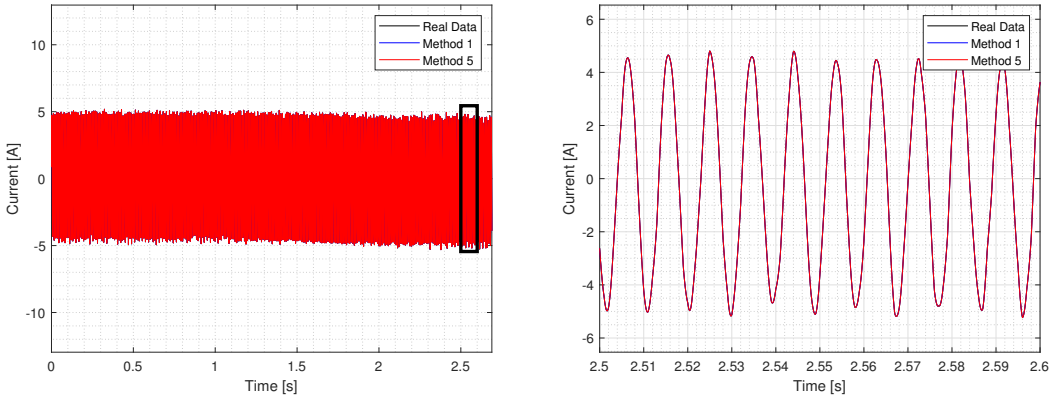
(b) Zoomed Region

Figure 4.47: Comparison of I_{dss} Estimation Among Different Estimation Methods

In Figure 4.48, the estimation results for I_{qss} from both methods are compared with the collected data. Both methods produce similar estimations for this state, closely matching the real data.

A closer look at Figure 4.48b shows that both methods provide nearly perfect estima-

tion results.



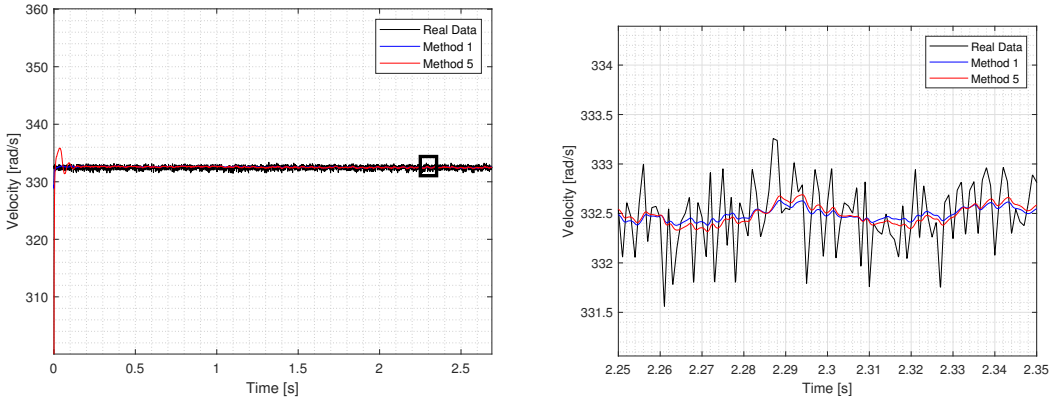
(a) Comparison Between 0-3 Seconds

(b) Zoomed Region

Figure 4.48: Comparison of I_{qss} Estimation Among Different Estimation Methods

In Figure 4.49, the estimation results for ω_m from both methods are compared with the collected data. Both methods yield similar estimations for this state, closely matching the real data.

Figure 4.49b indicates that both methods follow similar trends, which align well with the real data.



(a) Comparison Between 0-3 Seconds

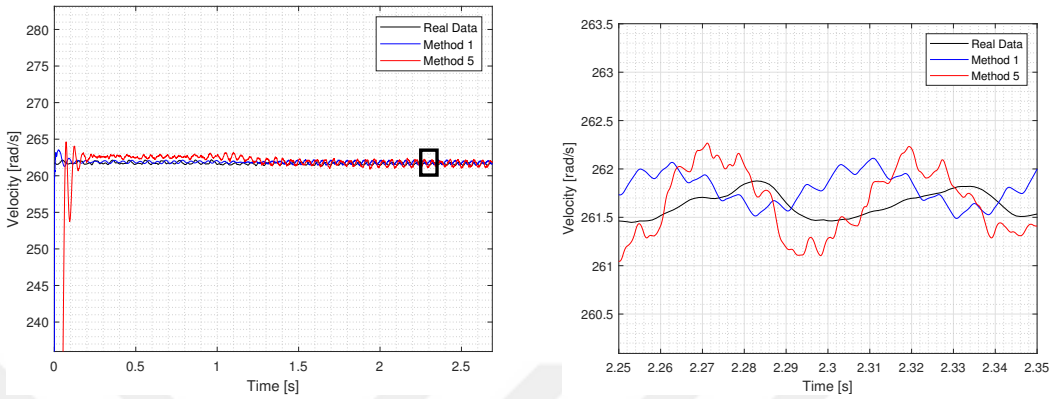
(b) Zoomed Region

Figure 4.49: Comparison of ω_m Estimation Among Different Estimation Methods

In Figure 4.50, the estimation results for ω_s from both methods are compared with

the collected data. The estimations from both methods are closely aligned with the real data for this state.

A closer look at Figure 4.50b reveals that both methods exhibit trends that are consistent with the actual data.



(a) Comparison Between 0-3 Seconds

(b) Zoomed Region

Figure 4.50: Comparison of ω_s Estimation Among Different Estimation Methods

In Figure 4.51, the estimation results for θ_T from both methods are compared with the collected data. A drift is apparent in the real data, which is also mirrored in the estimation results upon further examination.

Both methods aim to compensate for this drift by adjusting towards the model's expected values in a similar way.

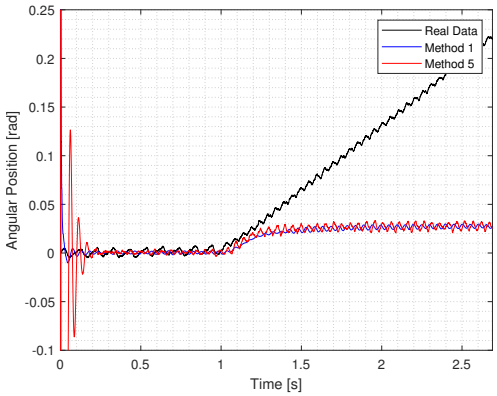


Figure 4.51: Comparison of θ_T Estimation Among Different Estimation Methods

In Figure 4.52, the estimation of the tangential cutting force coefficient K_{tc} from both methods is compared with the identified parameter. The results indicate that both methods estimate the parameter with a slight negative bias.

Method 5 yields more accurate coefficient estimates than Method 1, as it incorporates an additional term to counteract the drift observed in θ_t, which enhances the estimation of the other state variables as well.

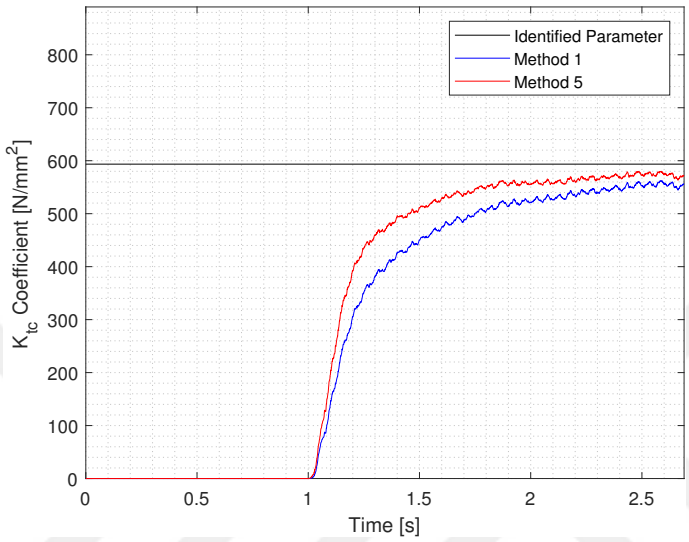
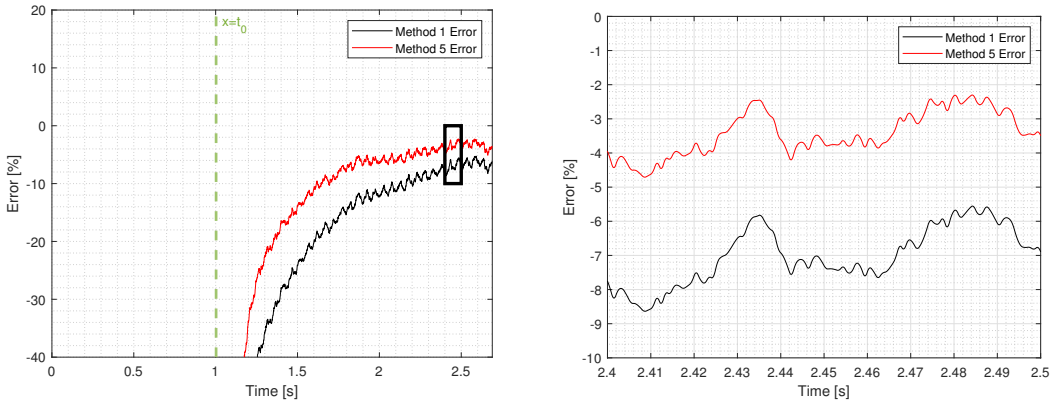


Figure 4.52: Comparison of K_{tc} Estimation Among Different Estimation Methods

A closer examination of Figure 4.53b reveals that, in the region where the estimation methods seem to stabilize, Method 1 exhibits an error margin between -8.8% and -5.8%, while Method 5 displays an error margin between -2.2% and -4.8%.

Thus, when compared to the simulation results, both Method 1 and Method 5 yield less accurate estimates, as observed in Figure 4.53b.

In comparing the methods, Method 1 demonstrates higher stability with reduced oscillation, whereas Method 5 offers notably more accurate estimates for the coefficient K_{tc}.



(a) Comparison Between 0-3.6 Seconds

(b) Zoomed Region

Figure 4.53: Comparison of Estimation Error for the K_{tc} Among Different Estimation Methods

In Figure 4.54, the estimation of the tangential cutting force coefficient K_{te} from both methods is compared with the identified parameter. The results reveal a positive bias in both methods, with a relatively high magnitude.

Additionally, Method 5 demonstrates enhanced accuracy in estimating the K_{te} coefficient.

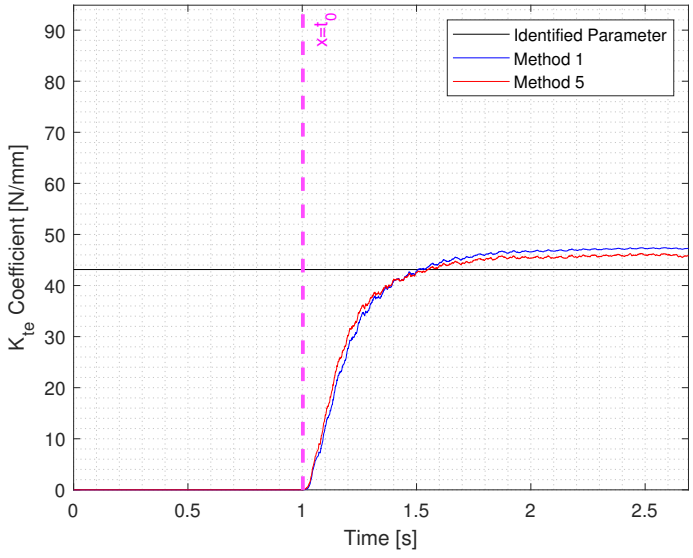
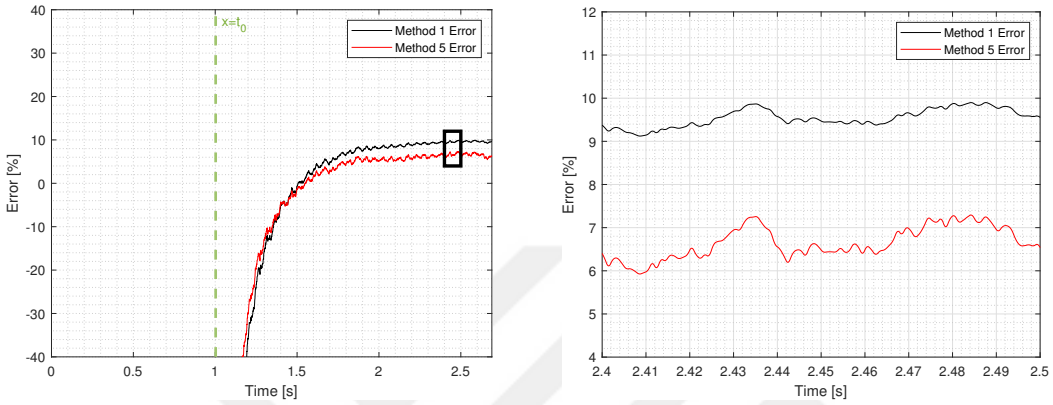


Figure 4.54: Comparison of K_{te} Estimation Among Different Estimation Methods

Figure 4.55 depicts the estimation errors for the state K_{te}, comparing both estimation methods. The green dashed line marks the initial point at which the disturbance torque starts to affect the system.

A detailed examination of Figure 4.55 shows that the estimation error for Method 5 falls between 6% and 7.2%, while for Method 1, it ranges from 9.1% to 9.9%. This indicates that Method 5 produces more accurate results.



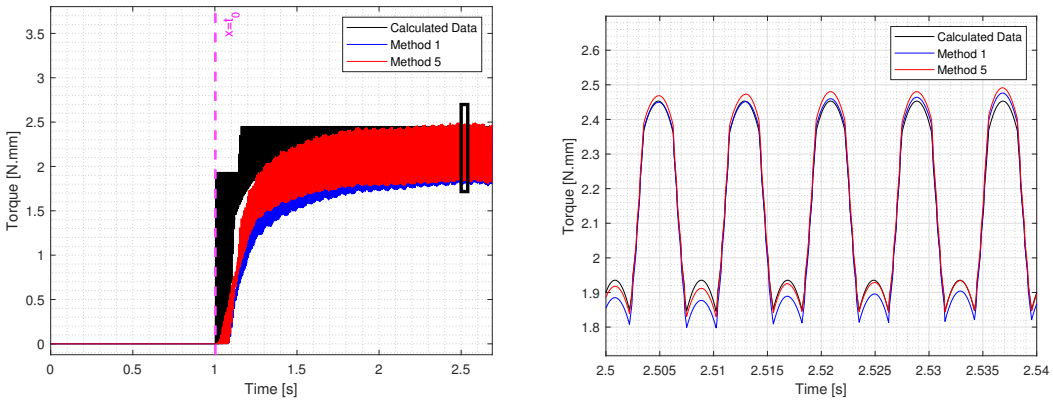
(a) Comparison Between 0-3.6 Seconds

(b) Zoomed Region

Figure 4.55: Comparison of Estimation Error for the K_{te} Among Different Estimation Methods

In Figure 4.56, the estimated tangential cutting torque T_c from both methods is compared with the calculated torque. It is evident that Method 5 provides a more stable and closer estimation to the real data for T_c.

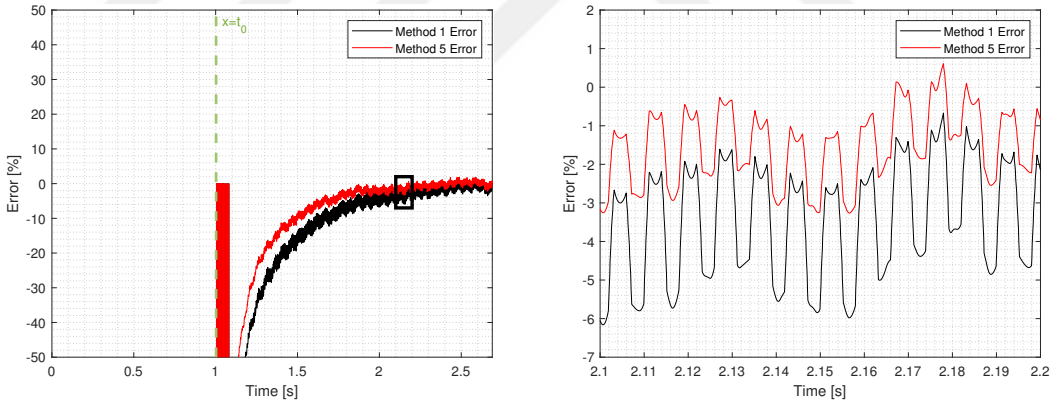
Examining the details reveals that Method 5 converges to the result slightly faster and with greater accuracy than Method 1.



(a) Comparison Between 0-3 Seconds (b) Zoomed Region

Figure 4.56: Comparison of T_c Estimation Among Different Estimation Methods

In Figure 4.57, the estimation error for T_c is displayed for both methods. A detailed view of the zoomed region reveals that both methods exhibit similar error patterns; however, Method 5 outperforms Method 1 when the magnitude of the errors is considered.



(a) Comparison Between 0-3 Seconds (b) Zoomed Region

Figure 4.57: Comparison of T_c Estimation Error Among Different Estimation Methods

4.2.3.3 Test 3

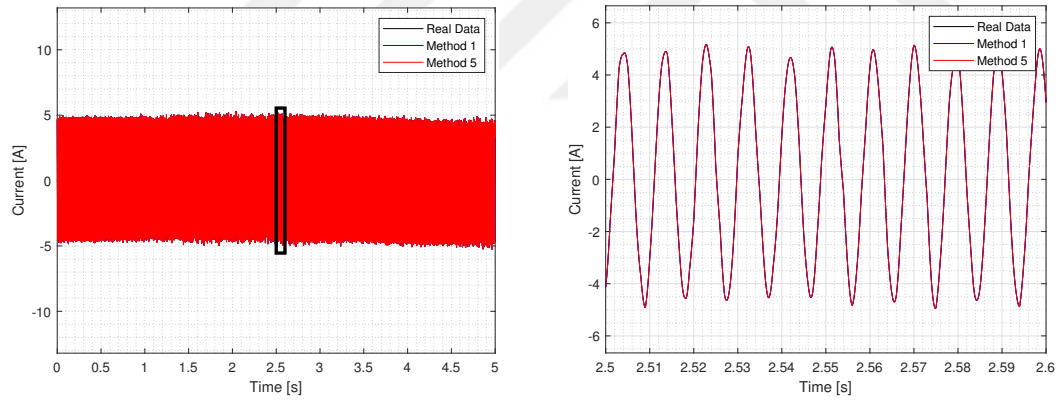
Table 4.8: Process Parameters of Cutting Test 3

No	D [mm]	N	ω_s [rpm]	F [mm/min]	a_p [mm]	a_e [mm]	β [deg]
3	12	3	2500	600	5	3	45

The process parameters for Test 3, also referred to as the 'quarter-slot cutting,' are listed in Table 4.8.

In Figure 4.58, the estimation results for I_{dss} from both methods are compared with the collected data. Both methods yield similar estimations for this state, closely aligning with the real data.

A detailed view of Figure 4.58b indicates that both methods deliver almost perfect estimation results.



(a) Comparison Between 0-3 Seconds

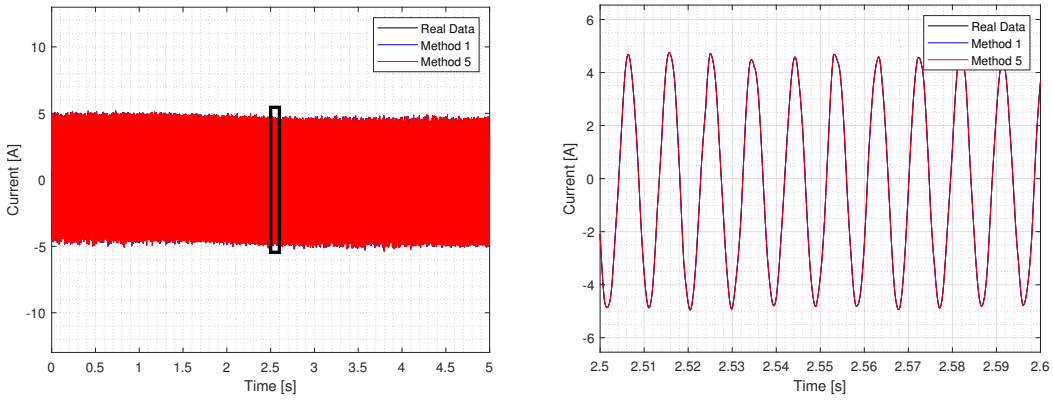
(b) Zoomed Region

Figure 4.58: Comparison of I_{dss} Estimation Among Different Estimation Methods

In Figure 4.59, the estimation results for I_{qss} from both methods are compared with the collected data. Both methods provide similar estimations for this state, aligning closely with the real data.

A closer examination of Figure 4.59b reveals that both methods achieve nearly flaw-

less estimation results.



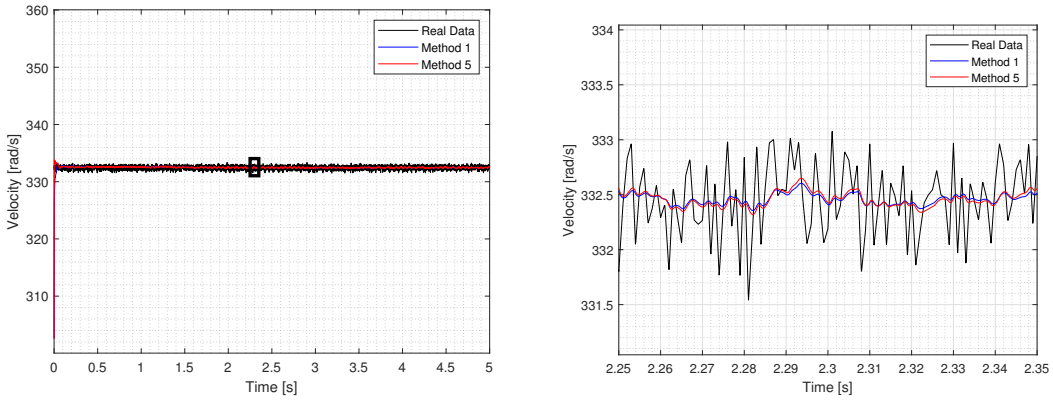
(a) Comparison Between 0-3 Seconds

(b) Zoomed Region

Figure 4.59: Comparison of I_{qss} Estimation Among Different Estimation Methods

In Figure 4.60, the estimation results for ω_m from both methods are compared with the collected data. Both methods yield similar estimations for this state, closely aligning with the actual data.

Figure 4.60b reveals that both methods exhibit comparable trends, which correspond well with the real data.



(a) Comparison Between 0-3 Seconds

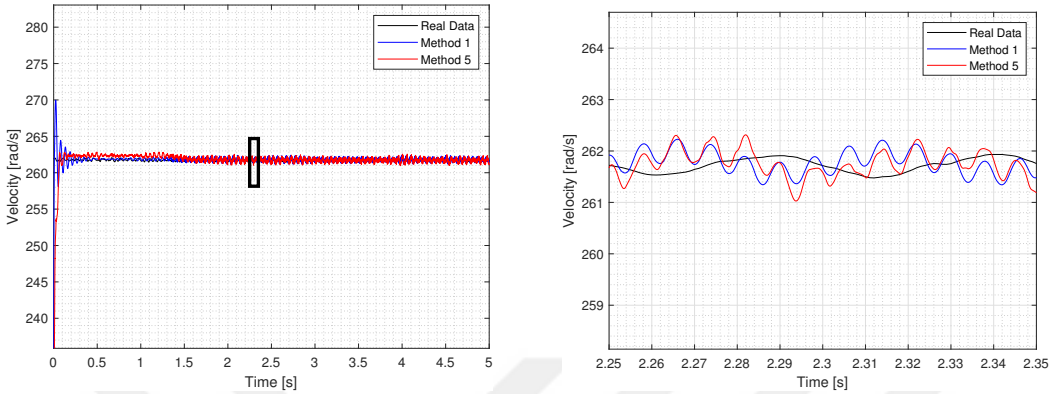
(b) Zoomed Region

Figure 4.60: Comparison of ω_m Estimation Among Different Estimation Methods

In Figure 4.61, the estimation results for ω_s from both methods are compared with

the collected data. Both methods provide estimations that are well-aligned with the real data for this state.

A detailed view in Figure 4.61b shows that both methods demonstrate trends that correlate closely with the actual data.



(a) Comparison Between 0-3 Seconds

(b) Zoomed Region

Figure 4.61: Comparison of ω_s Estimation Among Different Estimation Methods

In Figure 4.62, the estimation results for θ_T from both methods are compared with the collected data. A drift is apparent in the real data, which is also mirrored in the estimation results upon closer examination.

Both methods aim to counteract this drift by adjusting toward the model's expected values, using process noise and measurement noise parameter adjustments in a similar fashion.

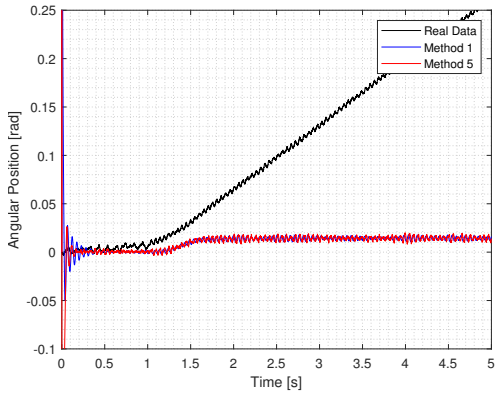


Figure 4.62: Comparison of θ_T Estimation Among Different Estimation Methods

In Figure 4.63, the estimation of the tangential cutting force coefficient K_{tc} from both methods is compared with the identified parameter. The results suggest that both methods estimate the parameter with a slight positive bias.

Both Method 1 and Method 5 produce nearly identical coefficient estimates. Although Method 5 includes an additional term to mitigate the drift in θ_t, the overall impact on the estimation of K_{tc} remains similar between the two methods.

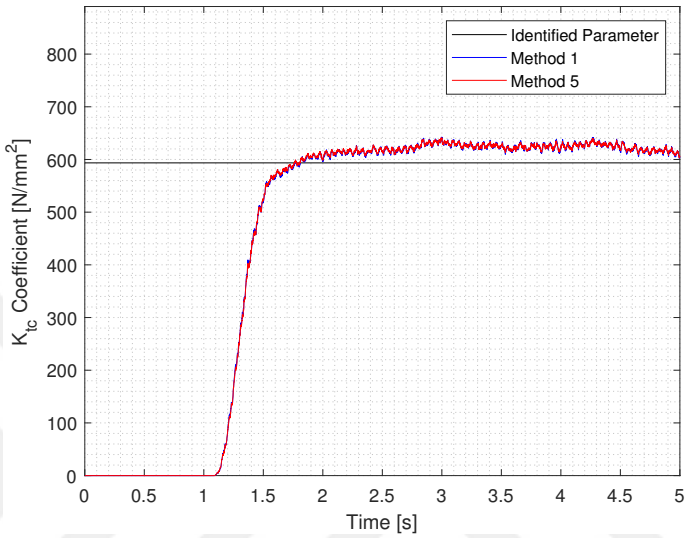
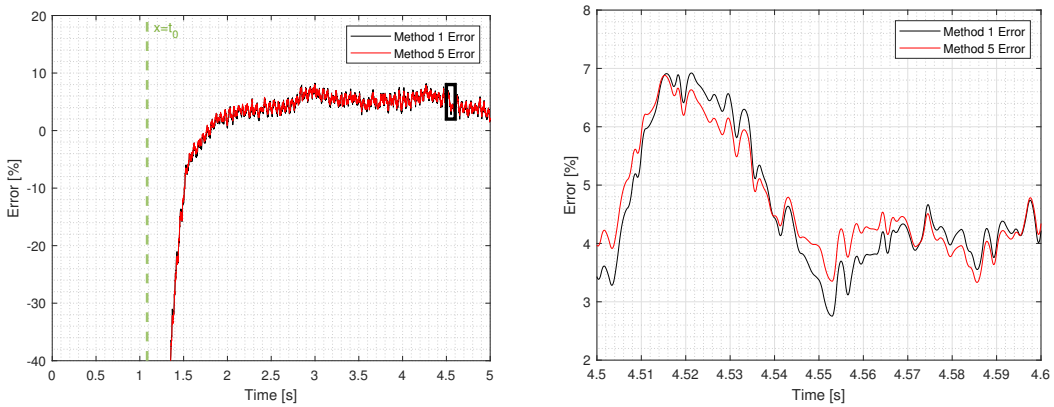


Figure 4.63: Comparison of K_{tc} Estimation Among Different Estimation Methods

A closer inspection of Figure 4.64b reveals that, in the region where the estimation methods appear to stabilize, both methods exhibit an error margin between 2.8% and 6.8%.

Therefore, compared to the simulation results, both Method 1 and Method 5 produce less accurate estimates, as shown in Figure 4.64b.



(a) Comparison Between 0-3.6 Seconds

(b) Zoomed Region

Figure 4.64: Comparison of Estimation Error for the K_{tc} Among Different Estimation Methods

In Figure 4.65, the estimation of the tangential cutting force coefficient K_{te} from both methods is compared with the identified parameter. The results reveal a positive bias in both methods, with a relatively high magnitude. Both methods produce nearly the same estimation results.

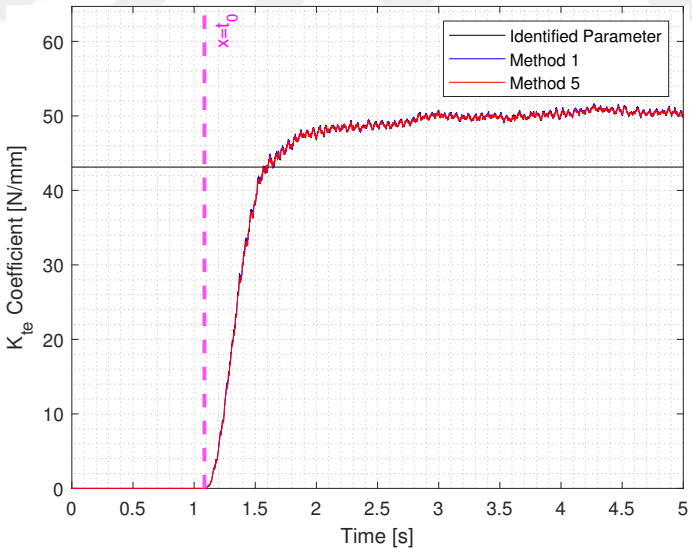
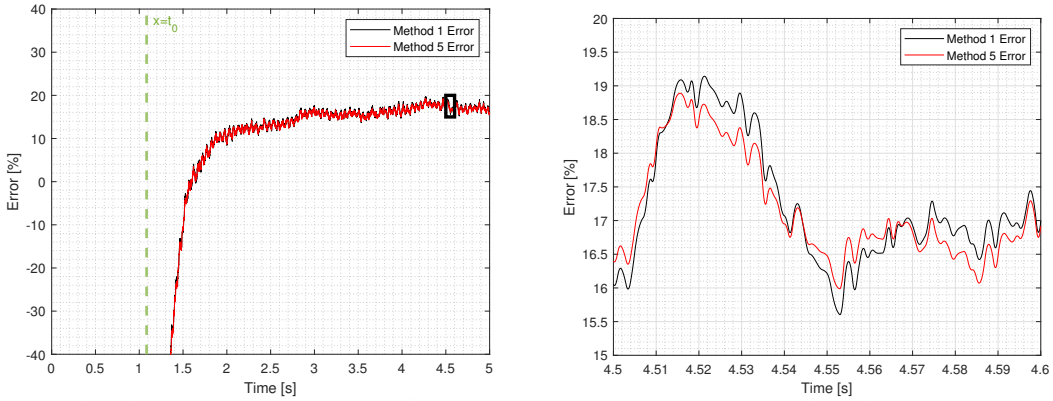


Figure 4.65: Comparison of K_{te} Estimation Among Different Estimation Methods

Figure 4.66 illustrates the estimation errors for the state K_{te}, comparing the two estimation methods. The green dashed line indicates the initial point at which the distur-

bance torque begins to impact the system.

A closer inspection of Figure 4.66 reveals that the estimation error for both methods ranges between 15.5% and 19%.



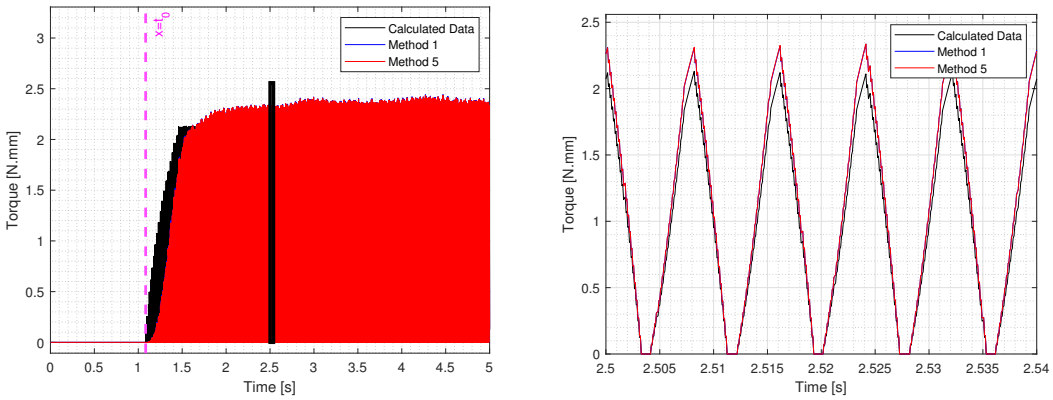
(a) Comparison Between 0-3.6 Seconds

(b) Zoomed Region

Figure 4.66: Comparison of Estimation Error for the K_{te} Among Different Estimation Methods

In Figure 4.67, the estimated tangential cutting torque T_c from both methods is compared with the calculated torque. Both methods provide similar results.

A closer look shows that both methods yield nearly indistinguishable outcomes.

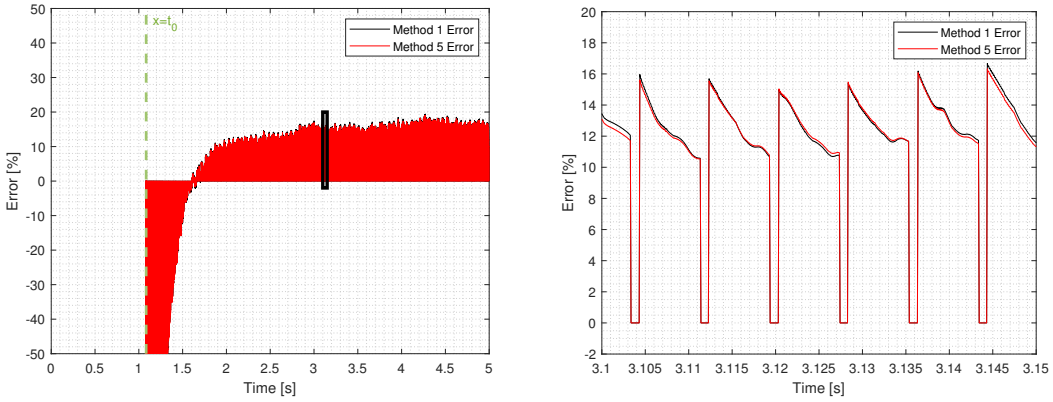


(a) Comparison Between 0-3 Seconds

(b) Zoomed Region

Figure 4.67: Comparison of T_c Estimation Among Different Estimation Methods

In Figure 4.68, the estimation error for T_c is displayed for both methods. The errors of both methods follow a similar trend with almost identical magnitudes, oscillating within a range of 0 to 20.



(a) Comparison Between 0-3 Seconds

(b) Zoomed Region

Figure 4.68: Comparison of T_c Estimation Error Among Different Estimation Methods

4.2.3.4 Test 4

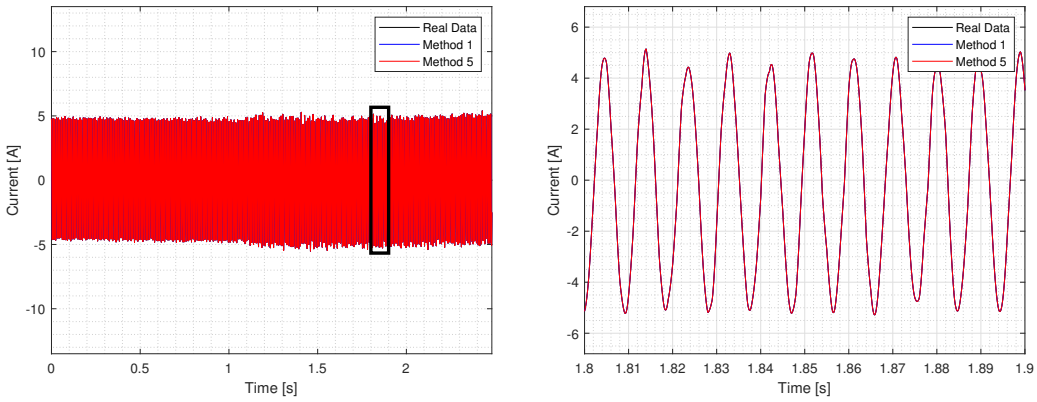
Table 4.9: Process Parameters of Cutting Test 4

No	D [mm]	N	ω_s [rpm]	F [mm/min]	a_p [mm]	a_e [mm]	β [deg]
4	12	3	2500	1500	4	12	45

The process parameters for Test 4, also referred to as the 'full-slot cutting,' are listed in Table 4.9.

In Figure 4.69, the estimation results for I_{dss} from both methods are compared with the collected data. Both methods yield similar estimations for this state, closely aligning with the real data.

A detailed view of Figure 4.69b indicates that both methods deliver almost perfect estimation results.

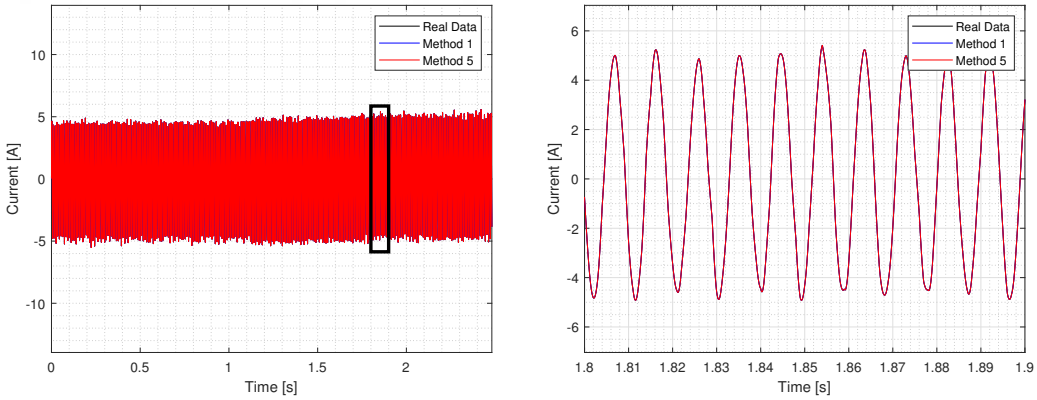


(a) Comparison Between 0-3 Seconds (b) Zoomed Region

Figure 4.69: Comparison of I_{dss} Estimation Among Different Estimation Methods

In Figure 4.70, the estimation results for I_{qss} from both methods are compared with the collected data. Both methods provide similar estimations for this state, aligning closely with the real data.

A closer examination of Figure 4.70b reveals that both methods achieve nearly flawless estimation results.



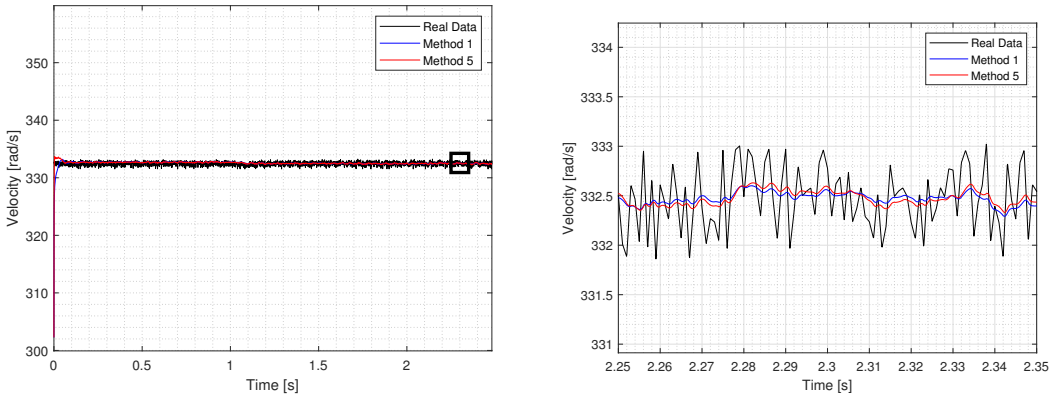
(a) Comparison Between 0-3 Seconds (b) Zoomed Region

Figure 4.70: Comparison of I_{qss} Estimation Among Different Estimation Methods

In Figure 4.71, the estimation results for ω_m from both methods are compared with the collected data. Both methods yield similar estimations for this state, closely aligning

with the actual data.

Figure 4.71b reveals that both methods exhibit comparable trends, though not exactly the same, with a similar mean that corresponds well with the real data.



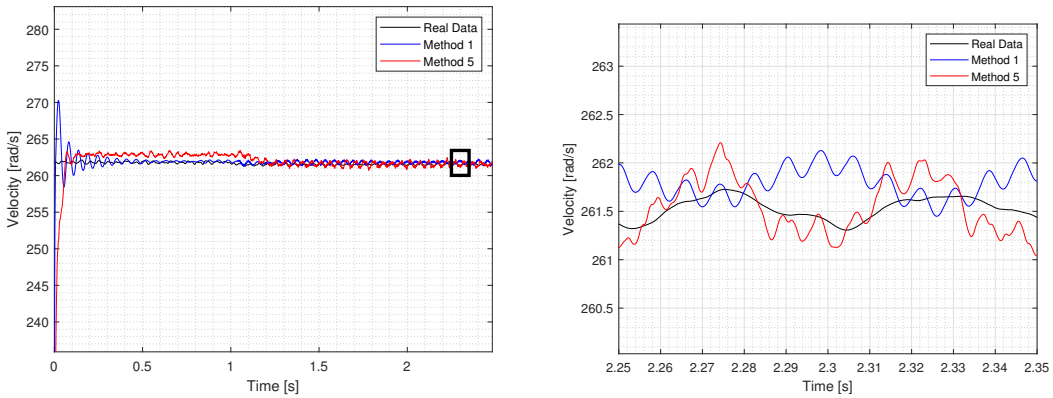
(a) Comparison Between 0-3 Seconds

(b) Zoomed Region

Figure 4.71: Comparison of ω_m Estimation Among Different Estimation Methods

In Figure 4.72, the estimation results for ω_s from both methods are compared with the collected data. Both methods provide estimations that are well-aligned with the real data for this state.

A detailed view in Figure 4.72b shows that both methods demonstrate trends that, while not exactly the same, have a similar mean that closely correlates with the actual data.



(a) Comparison Between 0-3 Seconds

(b) Zoomed Region

Figure 4.72: Comparison of ω_s Estimation Among Different Estimation Methods

In Figure 4.73, the estimation results for θ_T from both methods are compared with the collected data. A noticeable drift in the real data is reflected in the estimation results when closely examined.

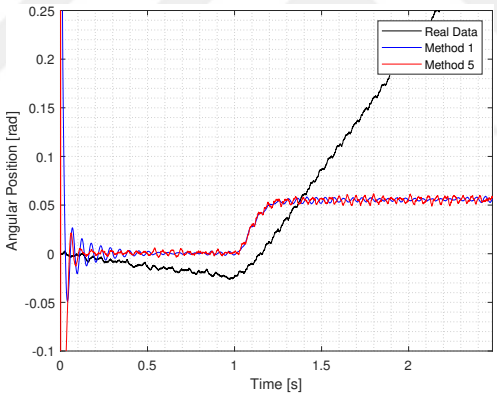


Figure 4.73: Comparison of θ_T Estimation Among Different Estimation Methods

Both methods attempt to mitigate this drift by adjusting toward the model's expected values, using similar adjustments in process noise and measurement noise parameters.

In Figure 4.74, the estimation of the tangential cutting force coefficient K_{tc} from both methods is compared with the identified parameter. The results indicate that both methods estimate the parameter with a slight negative bias.

Both Method 1 and Method 5 provide almost identical estimates for the coefficient.

Although Method 5 incorporates an additional term to reduce the drift in θ_t, its overall effect on the estimation of K_{tc} is similar to that of Method 1.

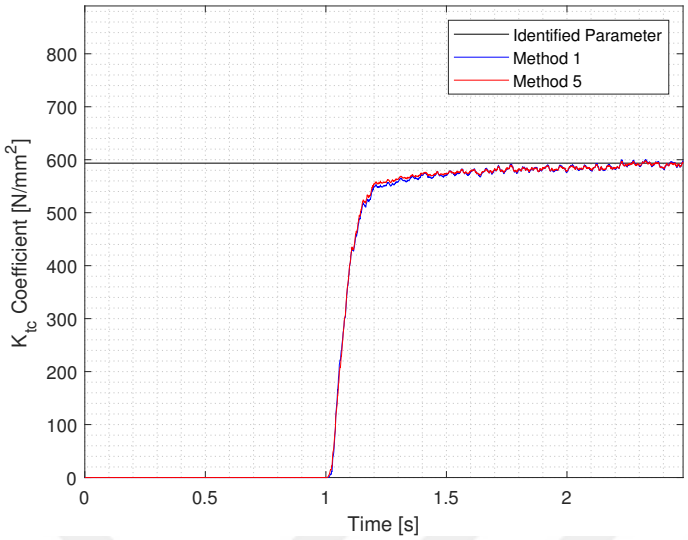
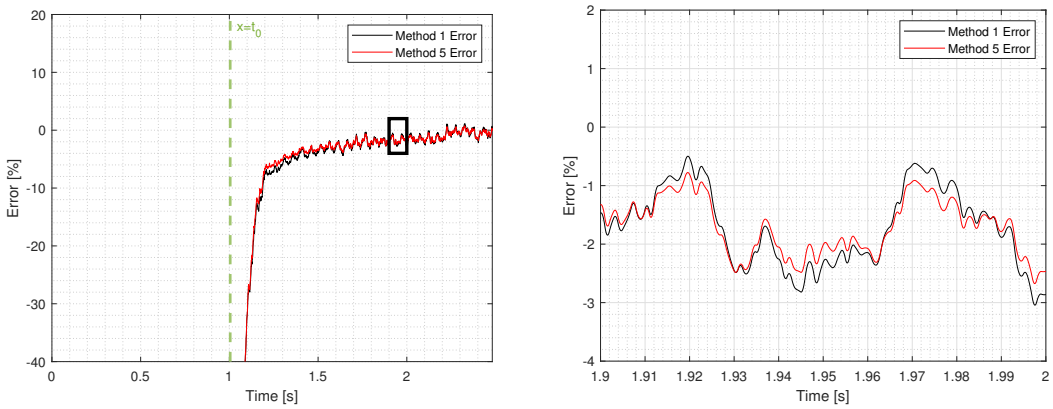


Figure 4.74: Comparison of K_{tc} Estimation Among Different Estimation Methods

A closer examination of Figure 4.75b shows that in the region where the estimation methods begin to stabilize, both methods exhibit an error margin ranging from -0.5% to -3%.

Thus, compared to the simulation results, both Method 1 and Method 5 provide less accurate estimates, as demonstrated in Figure 4.75b.

In comparison with Test 2, which is also a "full slot cutting test," this test involves a greater depth of cut. When comparing the results for estimating K_{tc}, both tests yield better estimates overall.



(a) Comparison Between 0-3.6 Seconds

(b) Zoomed Region

Figure 4.75: Comparison of Estimation Error for the K_{tc} Among Different Estimation Methods

In Figure 4.76, the estimation of the tangential cutting force coefficient K_{te} from both methods is compared with the identified parameter. The results show a positive bias in both methods, with a relatively large magnitude. Both methods yield almost identical estimation results.

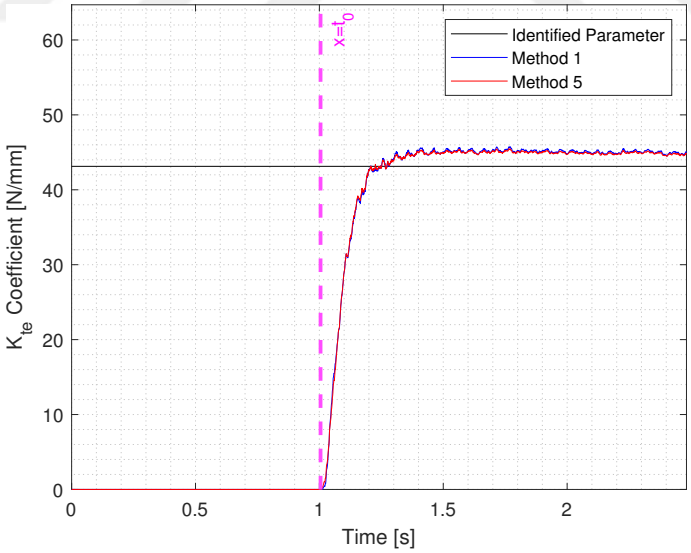


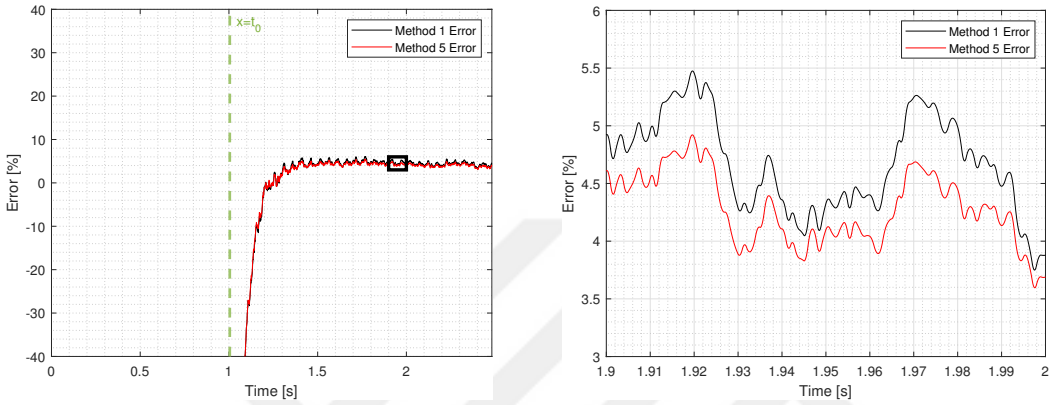
Figure 4.76: Comparison of K_{te} Estimation Among Different Estimation Methods

Figure 4.77 shows the estimation errors for the state K_{te}, comparing the two estimation methods. The green dashed line marks the point at which the disturbance torque

begins to affect the system.

A closer look at Figure 4.77 reveals that the estimation error for both methods falls within the range of 3.5% to 5.5%.

Compared to Test 2, which is also a "full slot cutting test," this test involves a greater depth of cut. When comparing the results for estimating K_{te}, both tests provide improved estimates overall.



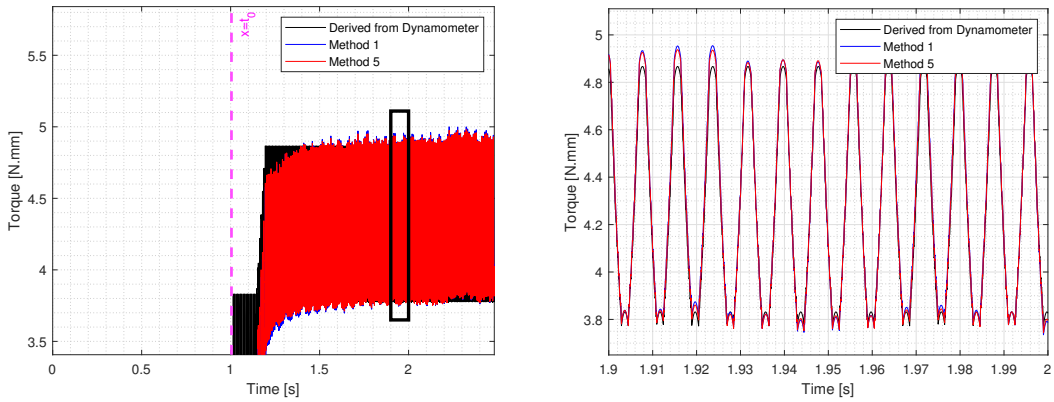
(a) Comparison Between 0-3.6 Seconds

(b) Zoomed Region

Figure 4.77: Comparison of Estimation Error for the K_{te} Among Different Estimation Methods

In Figure 4.78, the estimated tangential cutting torque T_c from both methods is compared with the calculated torque. Both methods produce comparable results.

A closer inspection reveals that the outcomes from both methods are nearly identical.

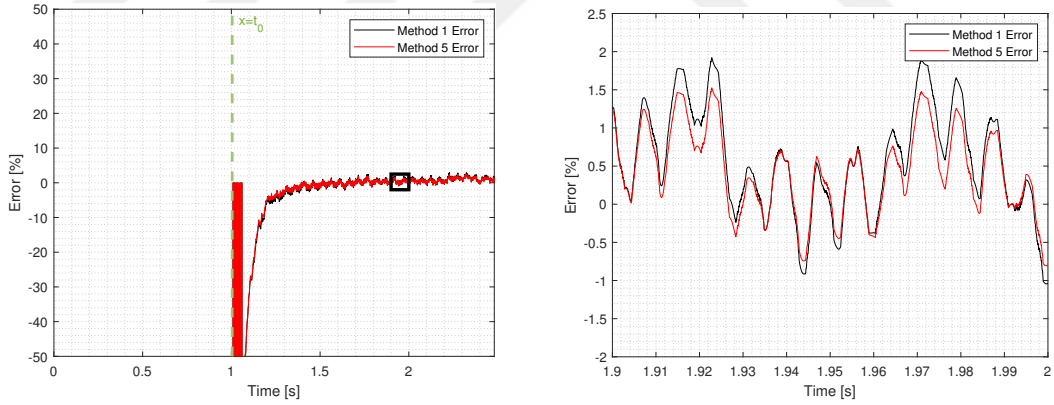


(a) Comparison Between 0-3 Seconds (b) Zoomed Region

Figure 4.78: Comparison of T_c Estimation Among Different Estimation Methods

In Figure 4.79, the estimation error for T_c is shown for both methods. The errors from both methods exhibit a similar pattern, with nearly identical magnitudes, fluctuating within a range of -1% to 2%.

These results are also an improvement compared to Test 2.



(a) Comparison Between 0-3 Seconds (b) Zoomed Region

Figure 4.79: Comparison of T_c Estimation Error Among Different Estimation Methods

4.2.3.5 Test 5

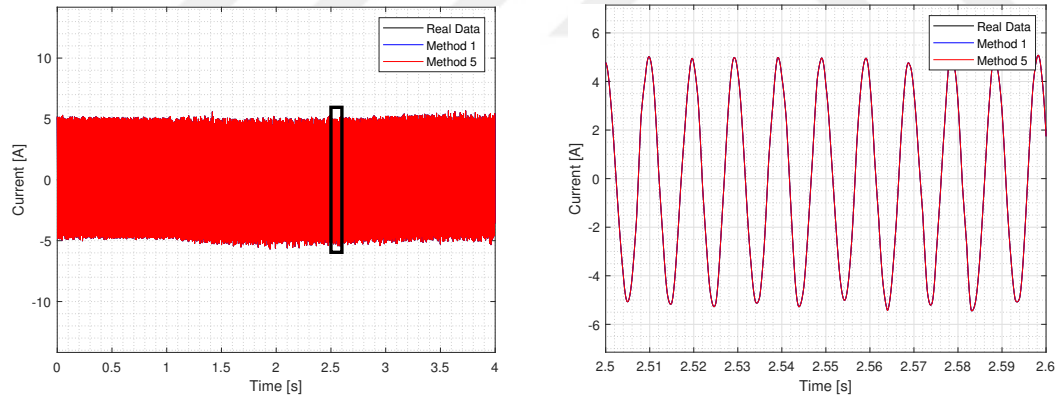
Table 4.10: Process Parameters of Cutting Test 5

No	D [mm]	N	ω_s [rpm]	F [mm/min]	a_p [mm]	a_e [mm]	β [deg]
5	16	3	2400	1000	3	16	45

The process parameters for Test 5, also referred to as the 'full-slot cutting,' are listed in Table 4.10. This test differs from the first four tests as the cutter's diameter is different in this case.

In Figure 4.80, the estimation results for I_{dss} from both methods are compared with the collected data. Both methods provide similar estimations for this state, closely matching the real data.

A closer look at Figure 4.80b shows that both methods deliver nearly perfect estimation results.



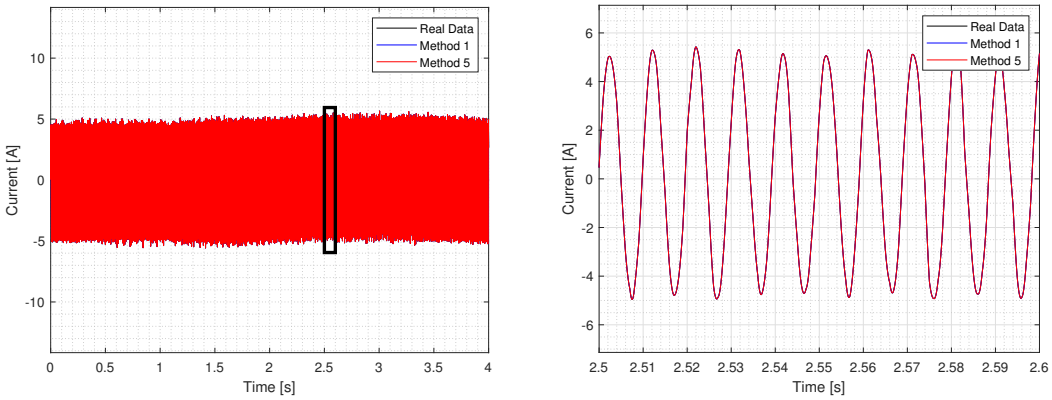
(a) Comparison Between 0-3 Seconds

(b) Zoomed Region

Figure 4.80: Comparison of I_{dss} Estimation Among Different Estimation Methods

In Figure 4.81, the estimation results for I_{qss} from both methods are compared with the collected data. Both methods provide similar estimations for this state, closely aligning with the real data.

A closer inspection of Figure 4.81b shows that both methods achieve almost flawless estimation results.

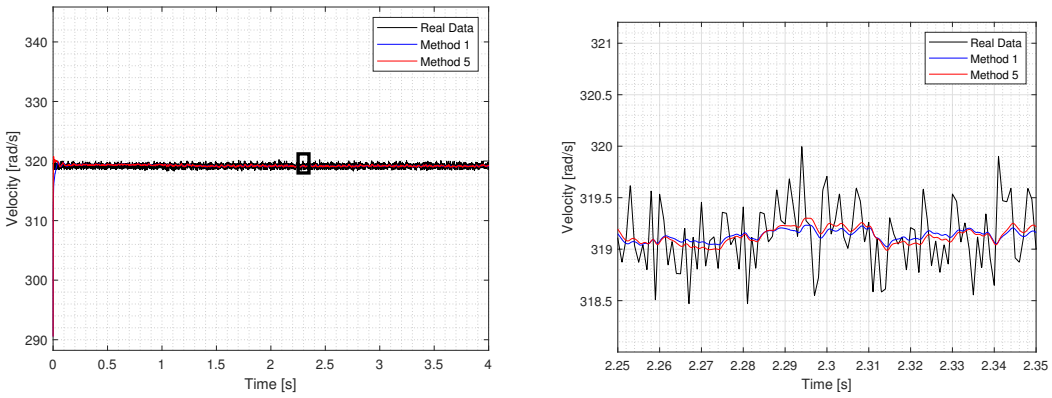


(a) Comparison Between 0-3 Seconds (b) Zoomed Region

Figure 4.81: Comparison of I_{qss} Estimation Among Different Estimation Methods

In Figure 4.82, the estimation results for ω_m from both methods are compared with the collected data. Both methods produce similar estimations for this state, closely aligning with the actual data.

Figure 4.82b shows that both methods display comparable trends that correspond well with the real data.

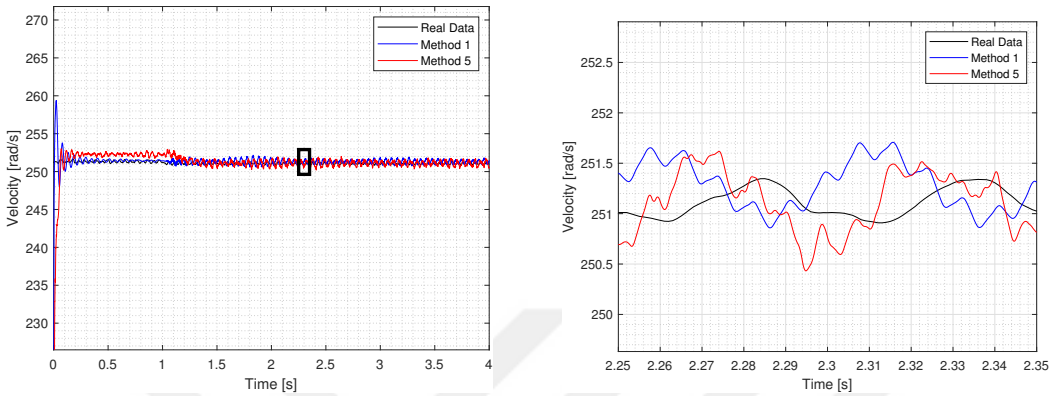


(a) Comparison Between 0-3 Seconds (b) Zoomed Region

Figure 4.82: Comparison of ω_m Estimation Among Different Estimation Methods

In Figure 4.83, the estimation results for ω_s from both methods are compared with the collected data. Both methods provide estimations that are well-aligned with the real data for this state.

A closer view in Figure 4.83b shows that both methods display trends that closely correlate with the actual data.



(a) Comparison Between 0-3 Seconds

(b) Zoomed Region

Figure 4.83: Comparison of ω_s Estimation Among Different Estimation Methods

In Figure 4.84, the estimation results for θ_T from both methods are compared with the collected data. A noticeable drift is observed in the real data, which is also reflected in the estimation results upon closer inspection.

Both methods attempt to counteract this drift by adjusting toward the model's expected values, using similar adjustments to the process noise and measurement noise parameters.

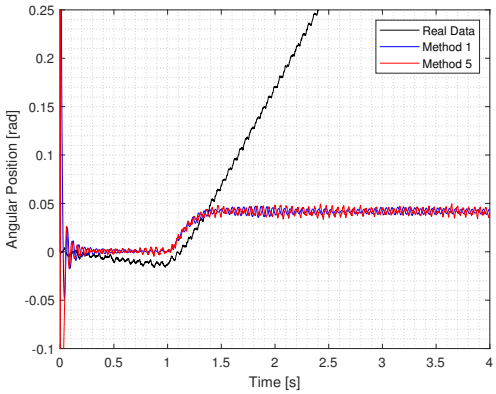


Figure 4.84: Comparison of θ_T Estimation Among Different Estimation Methods

In Figure 4.85, the estimation of the tangential cutting force coefficient K_{tc} from both methods is compared with the identified parameter. The results indicate that both methods estimate the parameter with near-perfect accuracy.

Both Method 1 and Method 5 produce almost identical coefficient estimates, yielding similar results overall.

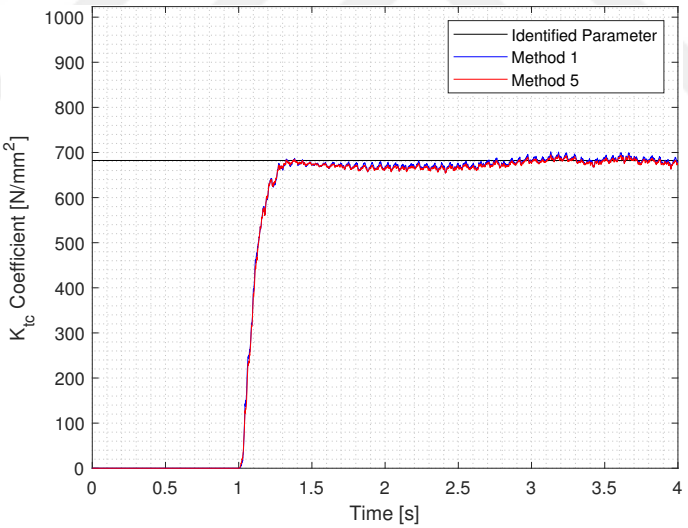
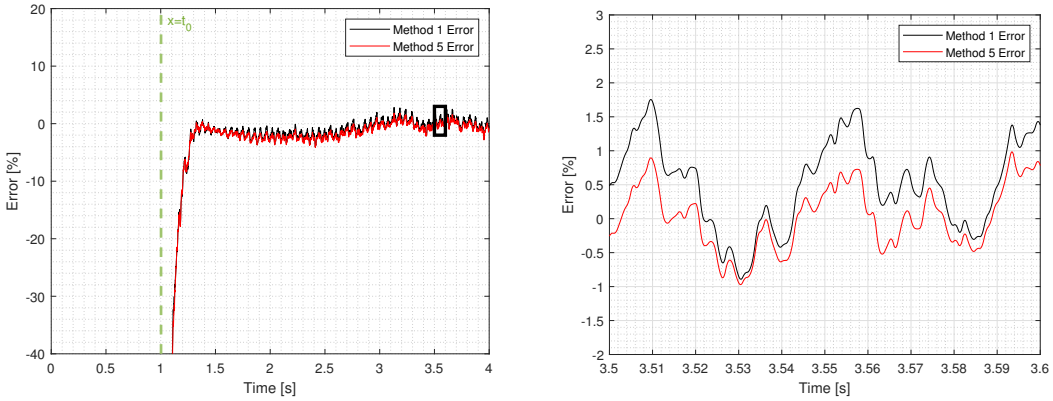


Figure 4.85: Comparison of K_{tc} Estimation Among Different Estimation Methods

A closer inspection of Figure 4.86b reveals that, in the region where the estimation methods stabilize, both methods exhibit an error margin between -1% and 2%.

Compared to the results of Test 4, the estimation of this coefficient in this test is

slightly more accurate.



(a) Comparison Between 0-3.6 Seconds

(b) Zoomed Region

Figure 4.86: Comparison of Estimation Error for the K_{tc} Among Different Estimation Methods

In Figure 4.87, the estimation of the tangential cutting force coefficient K_{te} from both methods is compared with the identified parameter. The results show a positive bias in both methods, with a relatively large magnitude. Both methods produce almost identical estimation results.

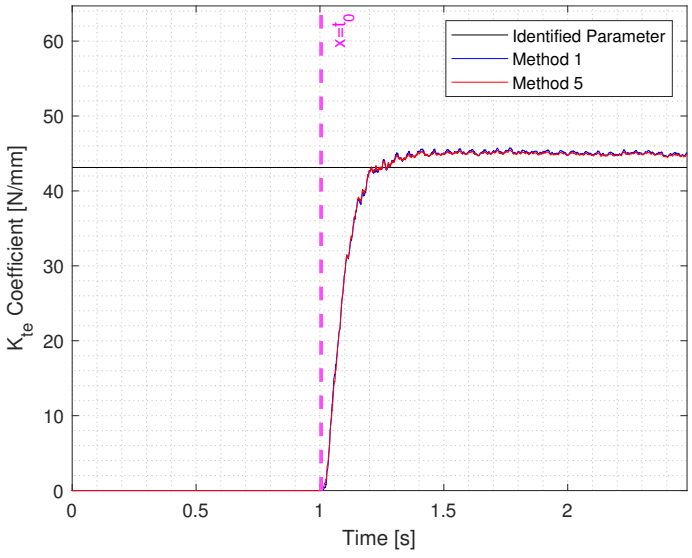
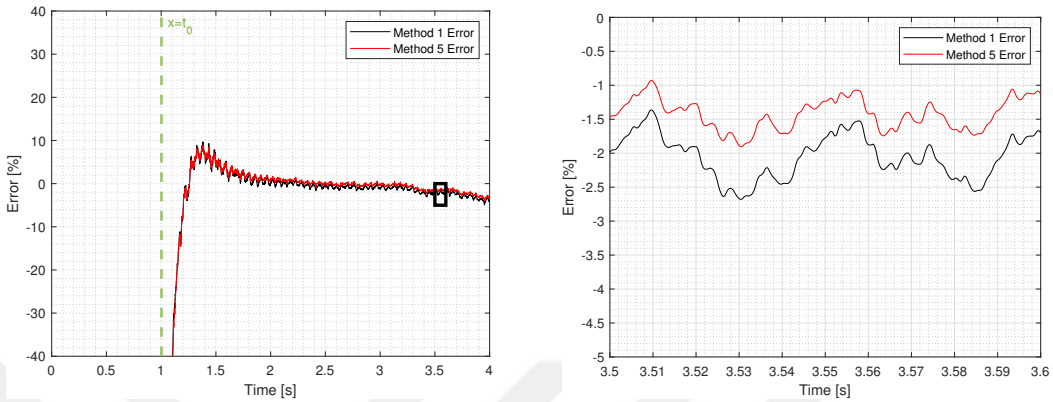


Figure 4.87: Comparison of K_{te} Estimation Among Different Estimation Methods

Figure 4.88 illustrates the estimation errors for the state K_{te}, comparing the two esti-

mation methods. The green dashed line marks the point where the disturbance torque begins to influence the system.

A closer inspection of Figure 4.88 reveals that the estimation error ranges from -1% to -2% for Method 5 and from -1.5% to -3% for Method 1.



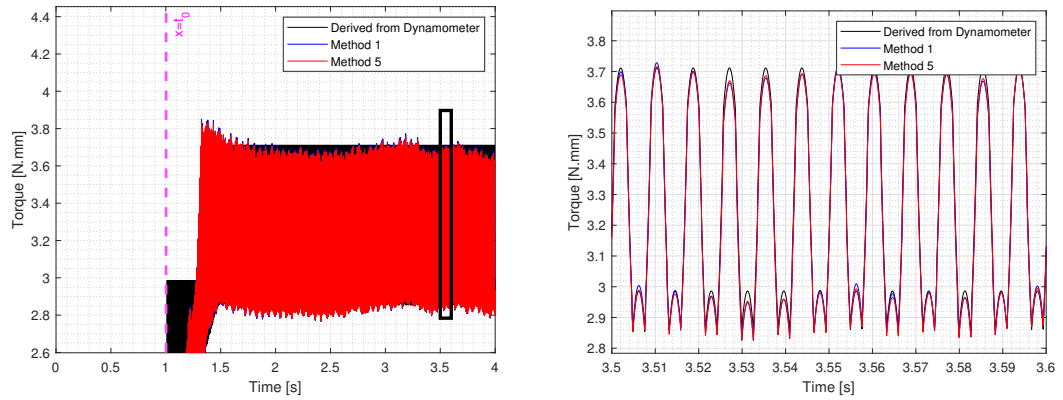
(a) Comparison Between 0-3.6 Seconds

(b) Zoomed Region

Figure 4.88: Comparison of Estimation Error for the K_{te} Among Different Estimation Methods

In Figure 4.89, the estimated tangential cutting torque T_c from both methods is compared with the calculated torque. Both methods produce similar results.

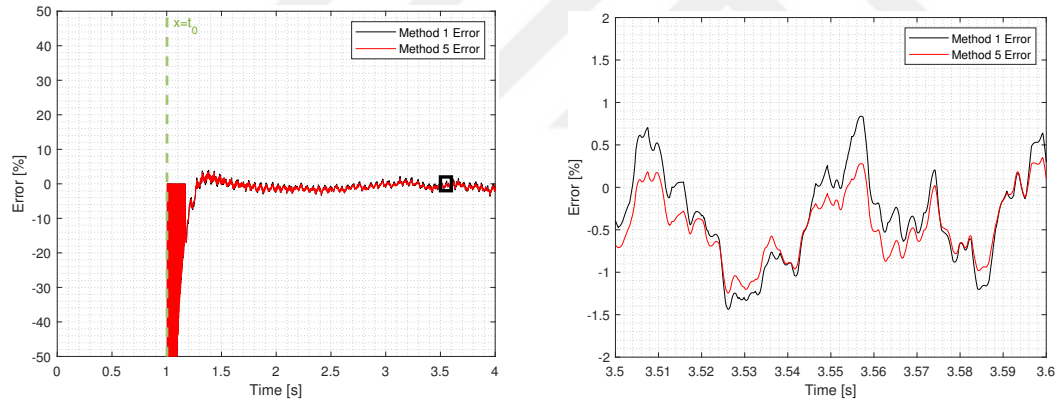
A closer inspection shows that the outcomes from both methods are nearly indistinguishable.



(a) Comparison Between 0-3 Seconds (b) Zoomed Region

Figure 4.89: Comparison of T_c Estimation Among Different Estimation Methods

In Figure 4.90, the estimation error for T_c is shown for both methods. The errors of both methods follow a similar trend, with nearly identical magnitudes, oscillating within a range of -1.5 to 0.5.



(a) Comparison Between 0-3 Seconds (b) Zoomed Region

Figure 4.90: Comparison of T_c Estimation Error Among Different Estimation Methods

4.2.3.6 Test 6

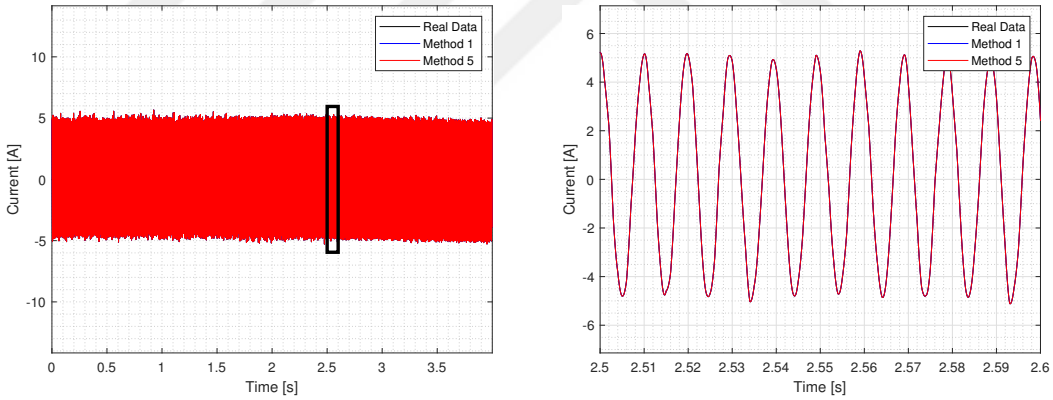
Table 4.11: Process Parameters of Cutting Test 6

No	D [mm]	N	ω_s [rpm]	F [mm/min]	a_p [mm]	a_e [mm]	β [deg]
6	16	3	2400	500	11	2	45

The process parameters for Test 3 are listed in Table 4.11. This test differs from the others as all the other tests are 'down-milling,' while this one is 'up-milling.'

In Figure 4.91, the estimation results for I_{dss} from both methods are compared with the collected data. Both methods provide similar estimations for this state, closely matching the real data.

A closer look at Figure 4.91b shows that both methods deliver nearly perfect estimation results.



(a) Comparison Between 0-3 Seconds

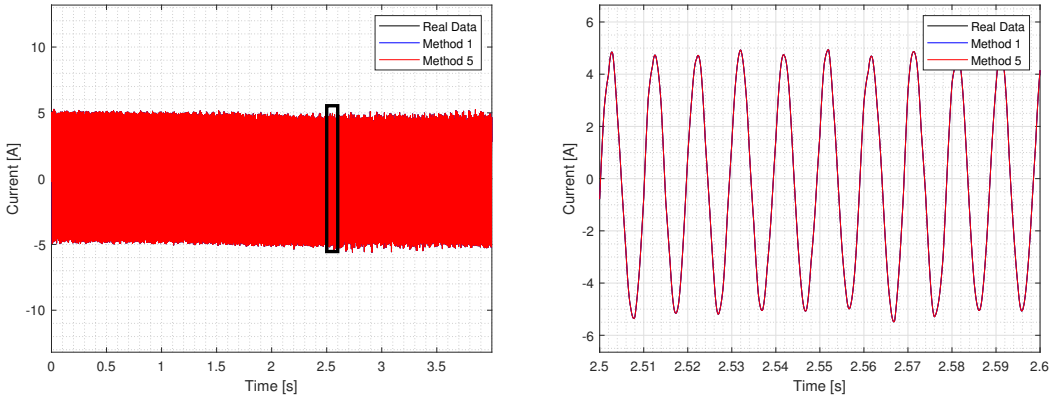
(b) Zoomed Region

Figure 4.91: Comparison of I_{dss} Estimation Among Different Estimation Methods

In Figure 4.92, the estimation results for I_{qss} from both methods are compared with the collected data. Both methods provide similar estimations for this state, closely aligning with the real data.

A closer inspection of Figure 4.92b shows that both methods achieve nearly flawless

estimation results.

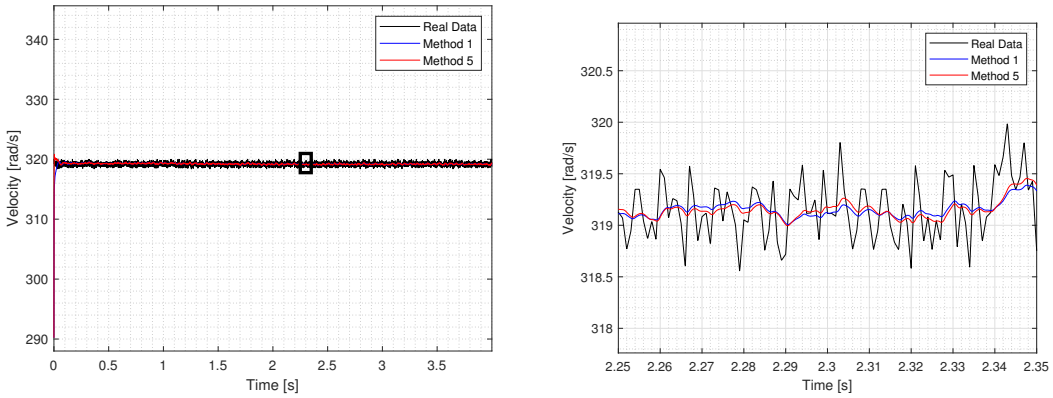


(a) Comparison Between 0-3 Seconds (b) Zoomed Region

Figure 4.92: Comparison of I_{qss} Estimation Among Different Estimation Methods

In Figure 4.93, the estimation results for ω_m from both methods are compared with the collected data. Both methods produce similar estimations for this state, closely matching the actual data.

Figure 4.93b shows that both methods display comparable trends, which correspond well with the real data.



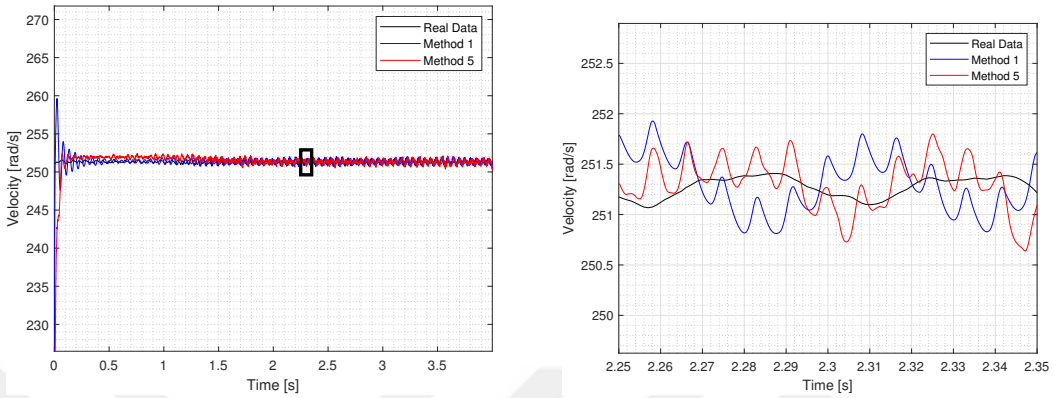
(a) Comparison Between 0-3 Seconds (b) Zoomed Region

Figure 4.93: Comparison of ω_m Estimation Among Different Estimation Methods

In Figure 4.94, the estimation results for ω_s from both methods are compared with

the collected data. Both methods provide estimations that are well-aligned with the real data for this state.

A closer view in Figure 4.94b shows that both methods exhibit trends that closely correlate with the actual data.



(a) Comparison Between 0-3 Seconds

(b) Zoomed Region

Figure 4.94: Comparison of ω_s Estimation Among Different Estimation Methods

In Figure 4.95, the estimation results for θ_T from both methods are compared with the collected data. A noticeable drift is observed in the real data, which is also reflected in the estimation results upon closer inspection.

Both methods attempt to counteract this drift by adjusting toward the model's expected values, using similar adjustments to the process noise and measurement noise parameters.

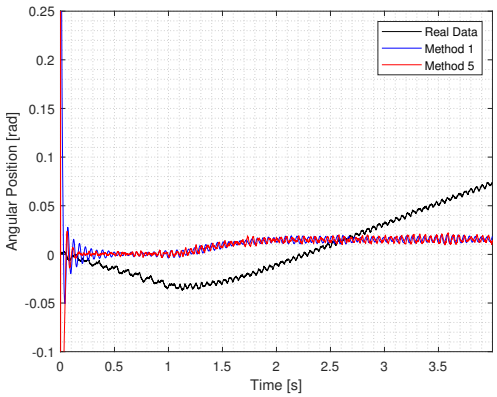


Figure 4.95: Comparison of θ_T Estimation Among Different Estimation Methods

In Figure 4.96, the estimation of the tangential cutting force coefficient K_{tc} from both methods is compared with the identified parameter. The results suggest that both methods estimate the parameter with a positive bias.

Both Method 1 and Method 5 produce almost identical coefficient estimates.

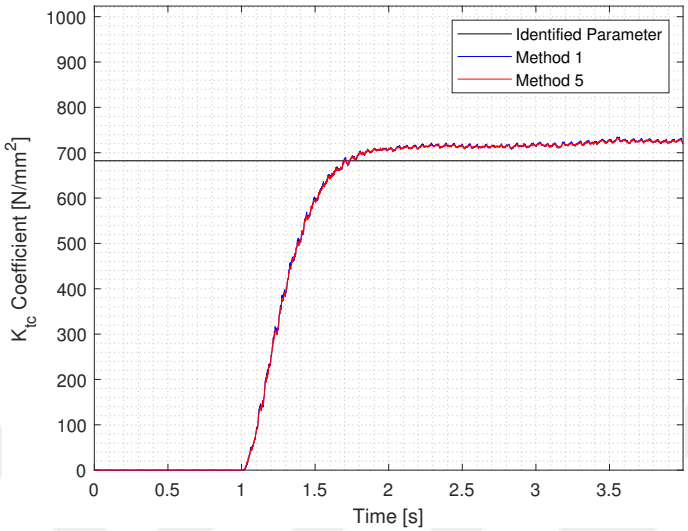
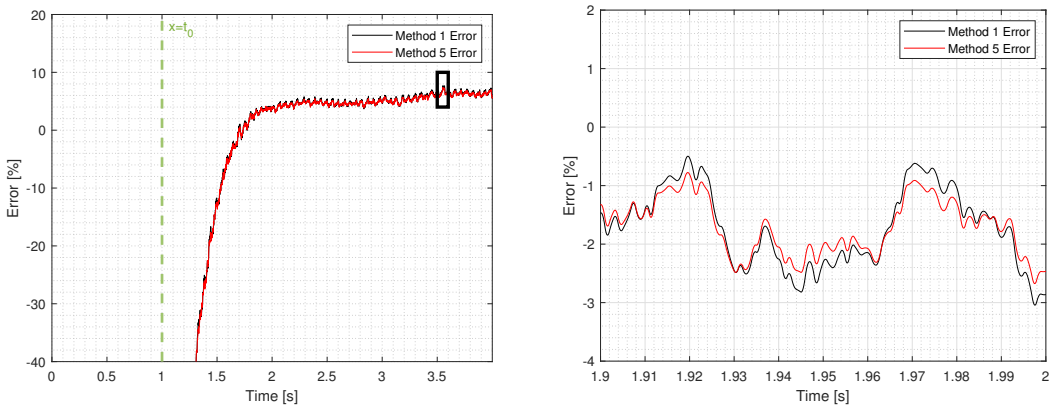


Figure 4.96: Comparison of K_{tc} Estimation Among Different Estimation Methods

A closer inspection of Figure 4.97b reveals that, in the region where the estimation methods appear to stabilize, both methods exhibit an error margin between -0.5% and 3%.

Therefore, compared to the simulation results, both Method 1 and Method 5 produce less accurate estimates, as shown in Figure 4.97b.



(a) Comparison Between 0-3.6 Seconds

(b) Zoomed Region

Figure 4.97: Comparison of Estimation Error for the K_{tc} Among Different Estimation Methods

In Figure 4.98, the estimation of the tangential cutting force coefficient K_{te} from both methods is compared with the identified parameter. The results show a positive bias in both methods, with a relatively large magnitude. Both methods produce almost identical estimation results.

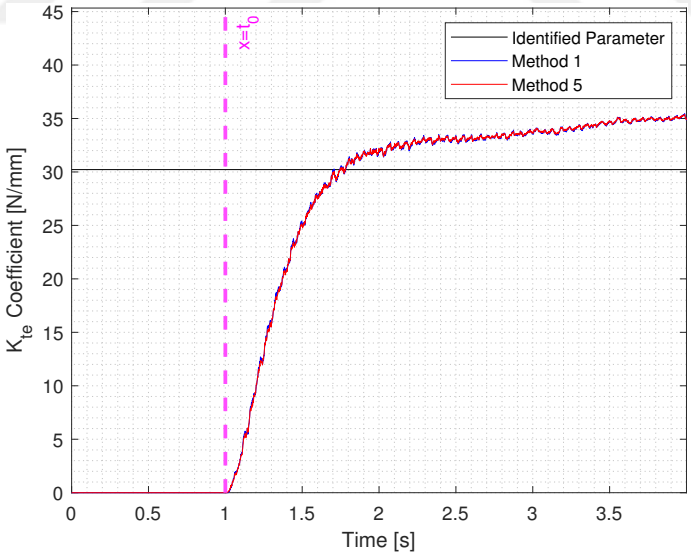
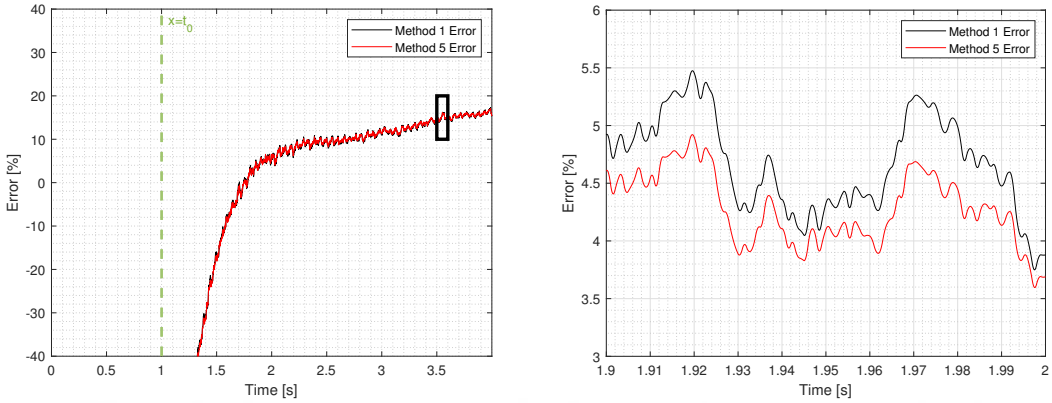


Figure 4.98: Comparison of K_{te} Estimation Among Different Estimation Methods

Figure 4.99 illustrates the estimation errors for the state K_{te}, comparing the two estimation methods. The green dashed line marks the point where the disturbance torque

begins to affect the system.

A closer inspection of Figure 4.99 reveals that the estimation error for both methods ranges from 3.5% to 5.5%.



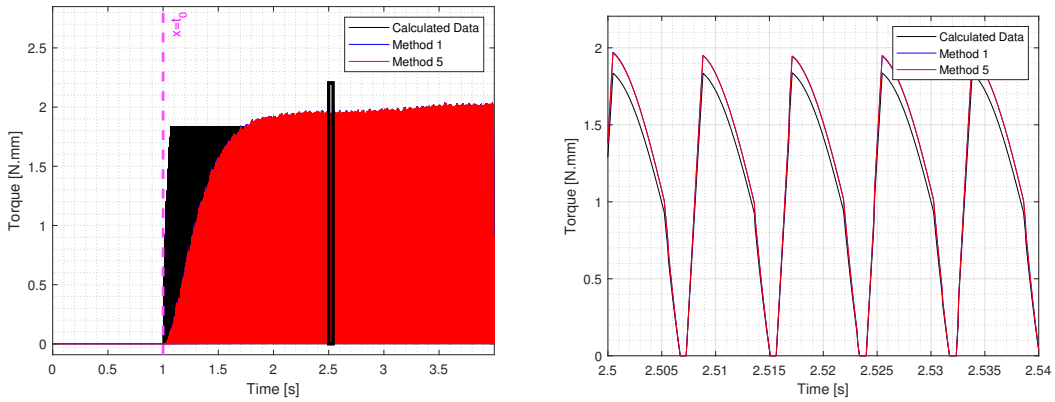
(a) Comparison Between 0-3.6 Seconds

(b) Zoomed Region

Figure 4.99: Comparison of Estimation Error for the K_{te} Among Different Estimation Methods

In Figure 4.100, the estimated tangential cutting torque T_c from both methods is compared with the calculated torque. Both methods produce similar results.

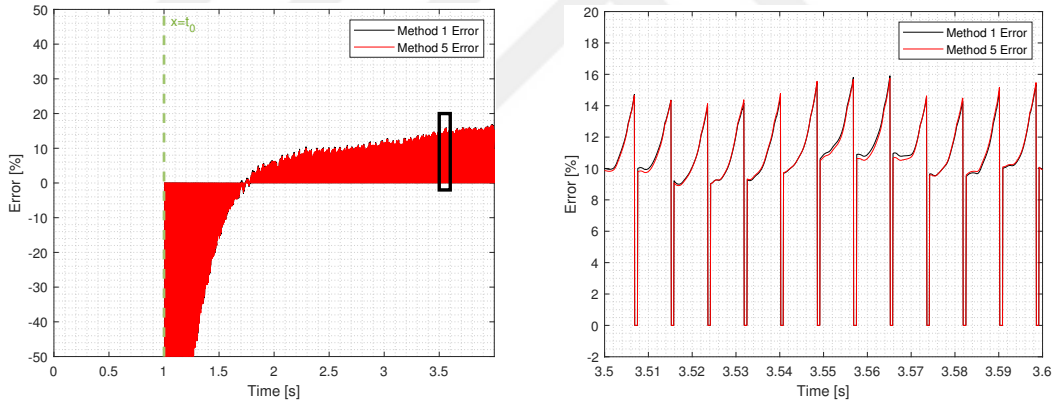
A closer inspection reveals that the outcomes from both methods are nearly indistinguishable.



(a) Comparison Between 0-3 Seconds (b) Zoomed Region

Figure 4.100: Comparison of T_c Estimation Among Different Estimation Methods

In Figure 4.101, the estimation error for T_c is shown for both methods. The errors from both methods follow a similar trend with nearly identical magnitudes, oscillating within a range of 0 to 15.



(a) Comparison Between 0-3 Seconds (b) Zoomed Region

Figure 4.101: Comparison of T_c Estimation Error Among Different Estimation Methods

4.2.3.7 Test 7

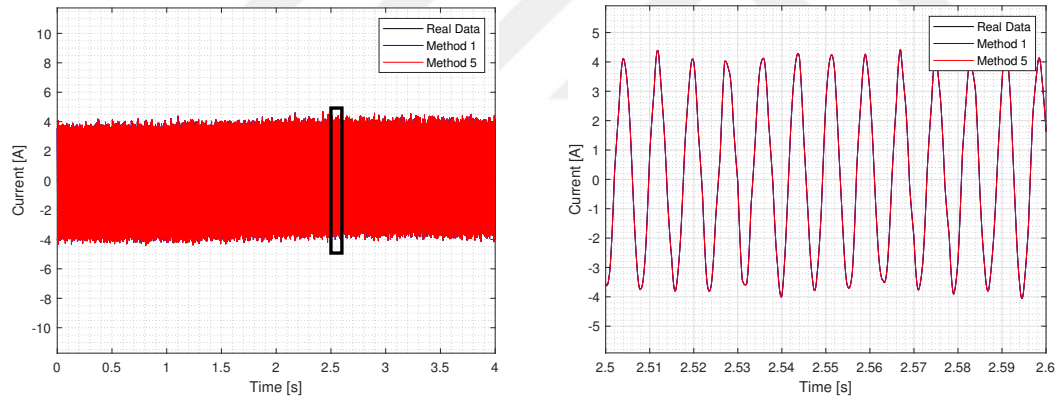
Table 4.12: Process Parameters of Cutting Test 2

No	D [mm]	N	ω_s [rpm]	F [mm/min]	a_p [mm]	a_e [mm]	β [deg]
7	16	4	3000	1500	1	8	45

The process parameters for Test 3, also referred to as the 'half-slot cutting,' are listed in Table 4.12. In this test, a different tool with 4 teeth and a 16 mm diameter is used.

In Figure 4.102, the estimation results for I_{dss} from both methods are compared with the collected data. Both methods provide similar estimations for this state, closely aligning with the real data.

A closer view of Figure 4.102b shows that both methods deliver nearly perfect estimation results.



(a) Comparison Between 0-3 Seconds

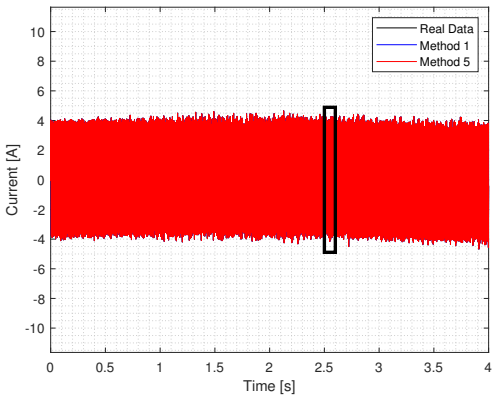
(b) Zoomed Region

Figure 4.102: Comparison of I_{dss} Estimation Among Different Estimation Methods

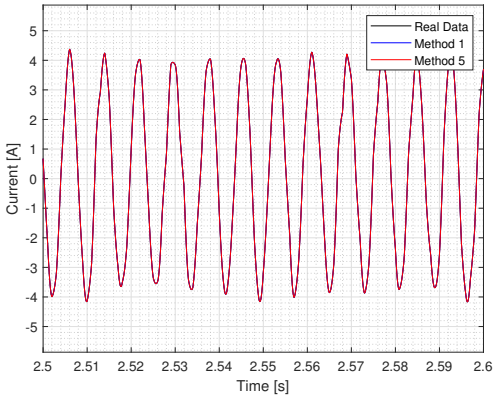
In Figure 4.103, the estimation results for I_{qss} from both methods are compared with the collected data. Both methods provide similar estimations for this state, closely aligning with the real data.

A closer look at Figure 4.103b reveals that both methods achieve nearly flawless

estimation results.



(a) Comparison Between 0-3 Seconds

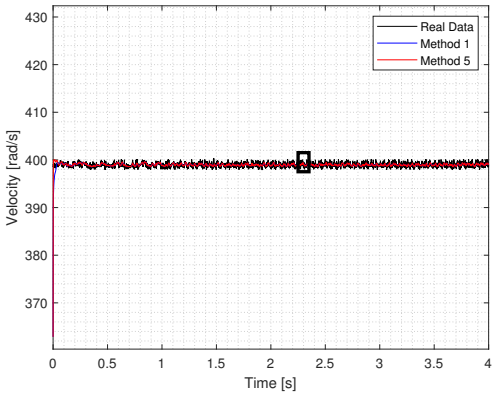


(b) Zoomed Region

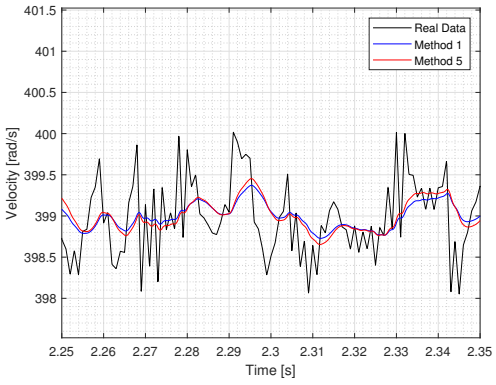
Figure 4.103: Comparison of I_{qss} Estimation Among Different Estimation Methods

In Figure 4.104, the estimation results for ω_m from both methods are compared with the collected data. Both methods produce similar estimations for this state, closely aligning with the actual data.

Figure 4.104b shows that both methods exhibit comparable trends that correspond well with the real data.



(a) Comparison Between 0-3 Seconds



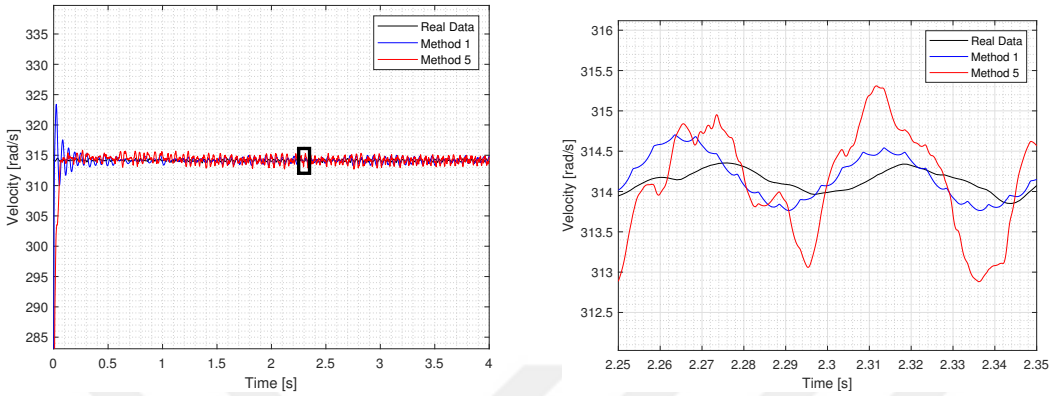
(b) Zoomed Region

Figure 4.104: Comparison of ω_m Estimation Among Different Estimation Methods

In Figure 4.105, the estimation results for ω_s from both methods are compared with

the collected data. Both methods provide estimations that are well-aligned with the real data for this state.

A closer look at Figure 4.105b shows that both methods exhibit trends that closely correlate with the actual data.



(a) Comparison Between 0-3 Seconds

(b) Zoomed Region

Figure 4.105: Comparison of ω_s Estimation Among Different Estimation Methods

In Figure 4.106, the estimation results for θ_T from both methods are compared with the collected data. A noticeable drift is evident in the real data, which is also reflected in the estimation results upon closer inspection.

Both methods attempt to counteract this drift by adjusting toward the model's expected values, using similar adjustments to the process noise and measurement noise parameters.

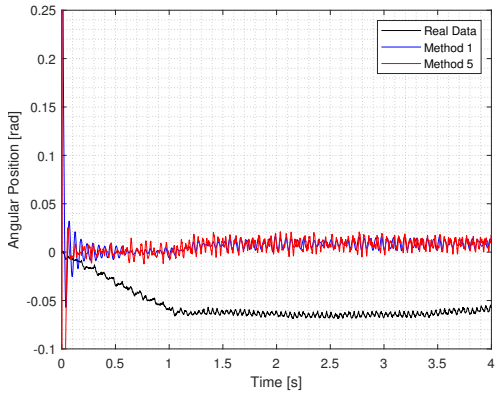


Figure 4.106: Comparison of θ_T Estimation Among Different Estimation Methods

In Figure 4.107, the estimation of the tangential cutting force coefficient K_{tc} from both methods is compared with the identified parameter. The results suggest that both methods estimate the parameter with a slight positive bias.

Both Method 1 and Method 5 produce nearly identical coefficient estimates. Despite Method 5 including an additional term to mitigate the drift in θ_t, the overall impact on the estimation of K_{tc} remains similar between the two methods.

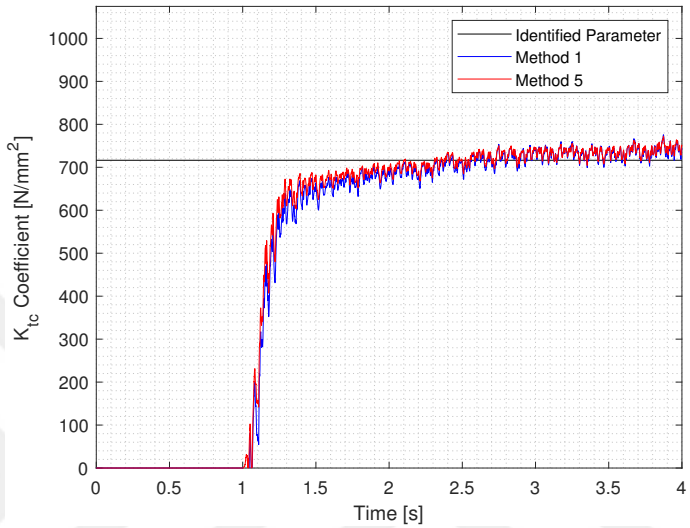
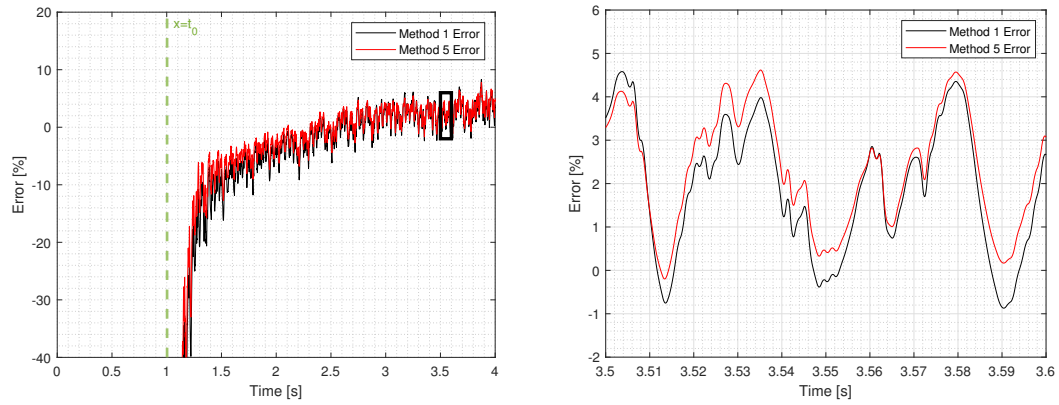


Figure 4.107: Comparison of K_{tc} Estimation Among Different Estimation Methods

A closer inspection of Figure 4.108b reveals that, in the region where the estimation methods stabilize, both methods exhibit an error margin between -1% and 5%.

As a result, compared to the simulation results, both Method 1 and Method 5 provide less accurate estimates, as shown in Figure 4.108b.



(a) Comparison Between 0-3.6 Seconds

(b) Zoomed Region

Figure 4.108: Comparison of Estimation Error for the K_{tc} Among Different Estimation Methods

In Figure 4.109, the estimation of the tangential cutting force coefficient K_{te} from both methods is compared with the identified parameter. The results show a negative bias in both methods. Both methods produce nearly identical estimation results.

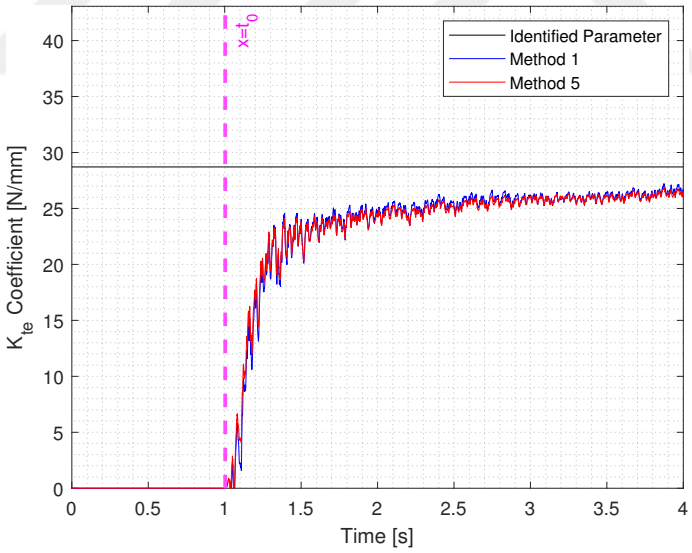
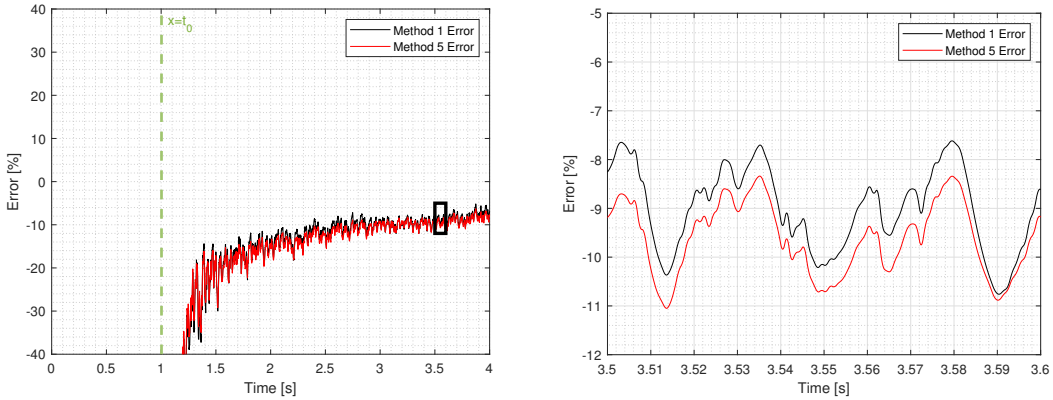


Figure 4.109: Comparison of K_{te} Estimation Among Different Estimation Methods

Figure 4.110 illustrates the estimation errors for the state K_{te}, comparing the two estimation methods. The green dashed line marks the point where the disturbance torque starts to impact the system.

A closer look at Figure 4.110 reveals that the estimation error for both methods ranges from -8% to 11%.



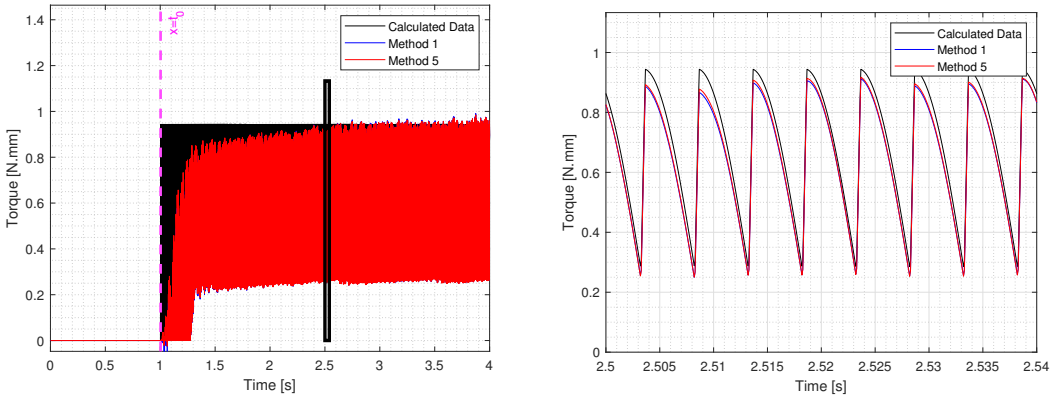
(a) Comparison Between 0-3.6 Seconds

(b) Zoomed Region

Figure 4.110: Comparison of Estimation Error for the K_{te} Among Different Estimation Methods

In Figure 4.111, the estimated tangential cutting torque T_c from both methods is compared with the calculated torque. Both methods produce similar results.

A closer inspection reveals that the outcomes from both methods are nearly indistinguishable.

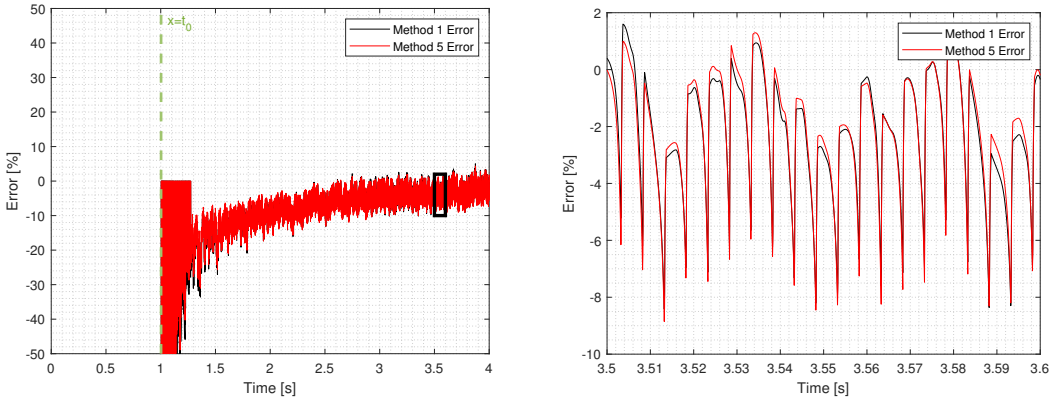


(a) Comparison Between 0-3 Seconds

(b) Zoomed Region

Figure 4.111: Comparison of T_c Estimation Among Different Estimation Methods

In Figure 4.112, the estimation error for T_c is displayed for both methods. The errors of both methods follow a similar trend with almost identical magnitudes, oscillating within a range of -8 to 2.



(a) Comparison Between 0-3 Seconds

(b) Zoomed Region

Figure 4.112: Comparison of T_c Estimation Error Among Different Estimation Methods

4.2.3.8 Results

Table 4.13 presents a comparative analysis of the two estimation methods across seven tests, detailing the root mean square error (RMSE) for the estimated tangential force coefficients K_{tc} and K_{te}. Additionally, the table provides the RMSE and peak-to-peak error (PPE) for the estimated tangential cutting torque T_c. This evaluation highlights each method's accuracy in estimating these critical parameters under varying conditions, contributing to a comprehensive assessment of their performance across all test scenarios.

It is important to note that both RMSE and PPE values were calculated after the estimation methods reached a stable result, ensuring a consistent basis for comparison.

Table 4.13: RMSE and PPE Comparison for K_{tc}, K_{te}, and T_c Across Seven Tests for Two Methods

Test	Method	RMSE of K_{tc} [%]	RMSE of K_{te} [%]	PPE of T_c [%]	RMSE of T_c [%]
1	Method 1	6.97	17.56	17.49	10.86
	Method 5	3.01	20.97	20.83	10.09
2	Method 1	8.50	9.20	4.00	2.79
	Method 5	4.47	6.2	2.00	1.31
3	Method 1	5.17	16.65	16.50	11.56
	Method 5	5.17	16.51	16.03	11.49
4	Method 1	1.19	4.37	1.88	1.05
	Method 5	1.12	4.01	1.51	0.89
5	Method 1	0.95	1.21	1.35	0.96
	Method 5	0.78	1.22	1.33	0.78
6	Method 1	6.02	14.18	13.70	10.23
	Method 5	5.89	14.35	13.60	10.22
7	Method 1	2.89	9.49	5.31	4.37
	Method 5	2.95	10.09	4.84	3.52

In Table 4.13, it is evident that the most accurate estimation results are associated with full slot tests. Additionally, increases in radial depth of cut, axial depth of cut, and tool diameter tend to reduce estimation errors. Although a higher axial depth generally improves accuracy, Test 6 presents a case where an excessive axial depth introduces vibrations, affecting estimation accuracy. This outcome can be attributed to the force model assumption that all cuts remain stable, which may not hold in cases with substantial vibration.

4.2.3.9 Discussion

In this verification process, the estimation methods are tested using real measurement data from cutting experiments. Two out of the five estimation methods are selected

for this verification due to their superior reliability and ability to handle data drift more effectively.

These two methods share many similarities, with the main difference being that Method 5 incorporates an auxiliary state to manage the drift of the transmission angle, θ_t.

Seven different tests are chosen to demonstrate the performance of the selected estimation methods under varying process parameters.

The first test involves a half-slot cutting experiment. For current estimation, Method 5 shows slightly better performance. In terms of velocity estimation, Method 5 provides results that are closer to the actual data, both in trend and magnitude.

When managing the drift in the transmission angle, both methods yield comparable results, aligning more closely with the process dynamics rather than direct measurements.

For the estimation of the tangential cutting coefficient, K_{tc}, Method 5 outperforms Method 1, although both provide reasonable estimates.

In the case of the tangential edge coefficient, K_{te}, Method 1 produces better results, though both methods provide acceptable estimates.

Regarding the estimation error for the tangential cutting torque, the results from both methods are quite similar.

The second test evaluates the methods under full-slot cutting conditions. Here, all system states, compared with real data, are well-estimated by both methods, and their estimations are quite similar.

For the estimation of K_{tc}, Method 5 again shows better results, while both methods perform reasonably well.

Similarly, for K_{te}, Method 5 provides better estimates, though both methods offer acceptable results.

Overall, considering the estimation error across the cutting tests, Method 5 consis-

tently provides better results.

In the third test, quarter-slot cutting data is used. As in the previous tests, all system states, compared with real data, are estimated similarly by both methods.

For the estimation of K_{tc}, both methods yield similar results.

For the estimation of K_{te}, both methods also provide comparable results.

In the fourth test, a half-slot test with similar process parameters, except for the axial depth of cut, is used to demonstrate the effect of depth of cut on the performance of the estimation methods.

In this test, all system states, compared with real data, are estimated similarly by both methods.

Compared to Test 2, the results of this test are slightly better for both methods, in terms of the estimated coefficients and the tangential cutting torque.

In the fifth test, a different diameter tool is used for a full-slot test. Overall, both methods produce similar and accurate results for this test.

In the sixth test, an up-milling test with a 2 mm radial depth of cut is performed. The results of this test are worse than those of the full-slot test in the fifth test, where the same tool was used.

In the seventh test, a tool with a different number of teeth is used for a half-slot test. The results of both methods are similar; however, due to the very small depth of cut, the results are not as good as those from the other tests.

When comparing estimation errors across tests, it is evident that error magnitudes increase as the radial depth of cut decreases. Additionally, while an increase in tool radius tends to decrease error, the number of teeth does not play a significant role. The axial depth of cut is a critical factor: increasing it generally enhances estimation accuracy, provided there is no tool vibration, as vibrations can introduce additional force components. Overall, both methods perform well, though radial depth of cut remains the primary process parameter influencing error magnitude.

CHAPTER 5

CONCLUSION

5.1 Summary and Conclusion

In this thesis, the estimation of the tangential cutting torque T_c using the spindle model is examined. The system is divided into two subsystems: the electric and mechanical subsystems.

The electric subsystem, modeled in the stationary reference frame, includes an AC induction motor. Its differential equations are structured so that only the stator and rotor currents serve as state variables.

The mechanical subsystem is represented as a two-inertia system, with motor and spindle inertias. A spring and damper connect the inertias to account for torsional and viscous friction effects on the spindle.

A force model, based on a mechanistic approach, is used to describe the interaction between the tool and the workpiece. This model numerically calculates the geometry between the tool and workpiece.

Once the complete system is mathematically modeled, unknown parameters in the equations are identified. Identification tests are carried out for both the mechanical and electric subsystems.

For the electric subsystem, traditional tests—DC, no-load, and blocked rotor tests—are performed. During these tests, current, voltage, and input power are recorded, and unknown parameters are identified using this data and basic electrical equations like Ohm's Law.

For the mechanical subsystem, a test is performed where a sinusoidal input signal of spindle velocity is applied, and currents, voltages, velocities, and positions are recorded. Symbolic transfer functions are derived from the block diagram, one between the electric torque and motor velocity, and another between motor and spindle velocities. Fast Fourier Transform (FFT) is then used to obtain the Bode plot of these transfer functions. MATLAB's transfer function fitting tool is applied to fit transfer functions to the Bode plots. Once the transfer functions are identified, unknown parameters are extracted by manipulating the symbolic transfer functions mathematically.

The identification of unknown force coefficients is necessary, as these are used to calculate the tangential cutting torque, which aids in verification since the torque cannot be directly measured. Therefore, using data from real cutting tests and process parameters, both the force model verification and the coefficient identification are conducted simultaneously. For identification, the calculated F_x and F_y, along with the recorded data of F_x and F_y, are input into MATLAB's 'Parameter Identification' tool, which utilizes the Nonlinear Least Squares method.

Using the identified coefficients, three selected tests are verified by applying the force model. These tests include all three distinct cutting tools used in the cutting experiments.

After identifying the unknown system parameters, verification of the system model is essential. For this reason, two open-loop verification tests are conducted. In the first test, no disturbance torque is applied, and the system is fed with recorded voltages from real tests. Outputs, including currents and velocities, are compared with actual test data to evaluate system performance under undisturbed conditions. In the second test, the system is subjected to a disturbance torque calculated by the force model, using the identified force coefficients and process parameters. This test checks the system's response to disturbances, ensuring robust performance.

The estimation methods are subsequently examined. The first method utilizes the complete system model to indirectly estimate the tangential cutting torque by estimating the tangential cutting force coefficients. To achieve this, an augmented state matrix is employed to estimate the coefficients, while a geometry matrix, based on

the force model, is used to update these coefficients at each sampling interval. Additionally, since the entire system model is considered nonlinear due to the interaction between the electrical and mechanical subsystems, an Extended Kalman Filter (EKF) is used as an observer.

In the second estimation method, the first approach is adapted to address the issue of asynchronous measurement data. To achieve this, an Asynchronous Extended Kalman Filter (AEKF) is employed.

In the third estimation method, a reduced system model is employed, which includes only the mechanical subsystem. However, the electrical torque is calculated from current measurements. Since only the mechanical subsystem is considered, the system model becomes linear, and therefore, a Kalman Filter is used to estimate the force coefficients, similar to the first method.

In the fourth estimation method, the entire system model is used, similar to the first method. However, instead of estimating the force coefficients, the tangential cutting torque is directly estimated by introducing it as a new state in the augmented state matrix. Since the system model is nonlinear, the Extended Kalman Filter (EKF) is used to estimate the tangential cutting torque.

In the fifth estimation method, the issue of drifting data in the transmission angle θ_T is addressed by introducing an auxiliary variable, δ_{n_g}, which is added to the augmented state matrix introduced in the first method. This method can also be considered a specialized version of the first method.

The test setup employed for the cutting experiments and data acquisition is also elaborated upon. Additionally, a brief explanation of the cutting tests conducted using this setup is provided.

The estimation methods are evaluated through verification tests. In the first verification method, simulated data is used to provide the measurements required by the estimation methods, while the second verification method employs actual data for these measurements. Both verification methods utilize real data for the input voltages and in the computation of the geometry matrix.

For the first verification method, three distinct tests are conducted using the same cutting tool but with different process parameters to compare all estimation methods against real data, aiming to demonstrate their performance under near-ideal conditions. Based on the results of these tests, the first and fifth methods are selected, as they are more effective in terms of both accuracy and precision.

For the second verification method, seven distinct tests are performed using real measurement data in the models. Only the two selected methods are used in this verification. In the first three tests, the same tests from the first verification method are repeated to compare the simulation results with real measurement data. The performance of estimation methods 1 and 5 is worse than in the first verification, which is expected due to the increased noise and other dynamics in the real data. However, the performance of the estimation methods in these three tests remains satisfactory. These tests also demonstrate that the radial depth of cut, a_e, is one of the most influential process parameters on the estimation methods' performance. When the radial depth of cut decreases, the estimation error increases.

The fourth test is a special case where all process parameters are the same as in the second cutting test, except for the axial depth of cut. This test shows that increasing the axial depth of cut improves the performance of the estimation methods. However, it should be noted that if the increase in axial depth of cut causes the cutting tool to oscillate, it can invalidate the assumptions of the force model, rendering the model inaccurate.

In the fifth and sixth tests, a different cutting tool with a different tool diameter is used to evaluate the estimation methods' performance with a different cutting tool. As expected, both estimation methods perform well in these tests. In the seventh test, a cutting tool with a 16 mm diameter and 4 flutes is used to assess the effect of the number of flutes on the performance of the estimation methods. It is found that the number of flutes is not as significant as the axial or radial depth of cut in affecting performance.

When comparing the performance across all tests, the fifth method generally produces slightly better estimations due to its specialization in addressing the issue of drifting in the transmission angular position. However, the difference between the two methods

is minimal, and the first method could also be selected as the estimation method.

In conclusion, the system has been modeled, and this model has been employed within the estimation methods. Although five different methods were examined, only two yielded satisfactory results given the circumstances. Notably, the fifth method was specifically developed for this application, whereas the first method was not. This suggests that the first method could reliably estimate tangential cutting torque in both ideal and suboptimal conditions, where measurement data may be less accurate.

5.2 Future Work

Although the current research provides a robust framework for estimating tangential cutting torque through advanced state estimation methods, several areas remain for future exploration to address the limitations and challenges encountered during this work.

One significant limitation is the sensitivity of the force model to measurement noise, which may affect the accuracy of the estimation methods. Future work could focus on developing more robust noise-handling techniques, such as advanced filtering algorithms or incorporating stochastic modeling, to enhance the reliability of the estimation process. In particular, exploring robust observers or noise-adaptive models could significantly improve the performance of the estimation methods, especially under highly variable or noisy data conditions.

Additionally, there is room for improvement in the computational efficiency of the estimation algorithms, particularly for real-time applications. By optimizing the computational aspects of the algorithms or exploring alternative methods, such as model reduction techniques, the framework could become more suitable for high-speed, real-time machining environments.

Another promising direction for future research is the adaptation of the proposed methods to different machining processes. While this work focuses on milling operations, the framework could be extended to other processes, such as turning or grinding, where tangential cutting torque estimation remains a challenge. Investigating the

applicability of the developed methods in these domains could further expand their usefulness and impact.

Future studies could also involve more extensive experimental validation, especially under a broader range of operational conditions. For instance, the current tests were conducted under controlled laboratory conditions; future experiments could be designed to include more realistic industrial environments, where factors such as tool wear, varying material properties, and machine vibrations might influence the results. Such experiments would provide valuable insights into the practical robustness of the estimation methods in real-world applications.

From a theoretical standpoint, future research could explore the use of alternative state estimation techniques, such as particle filters or machine learning-based approaches, which may offer improved performance in highly non-linear and time-varying systems. The integration of these advanced techniques could result in more accurate and adaptable models, especially in situations where the current methods struggle with non-linearities or unmodeled dynamics.

Additionally, addressing the issue of data drift in the transmission angle could be further refined. While the introduction of an auxiliary variable to handle this issue in the fifth estimation method has shown promising results, future work could focus on optimizing this approach and investigating other strategies to mitigate the impact of drifting data on the estimation accuracy.

Collaboration with researchers from related disciplines, such as materials science or electrical engineering, could lead to interdisciplinary advancements. For example, improving the understanding of material properties and their effects on cutting dynamics could enhance the accuracy of the force model, while insights from electrical engineering could improve the integration of the mechanical and electrical subsystems in the estimation framework.

Technological advancements, such as the development of high-speed sensors and more powerful data acquisition systems, also provide exciting opportunities for future research. Leveraging these technologies could enable more precise and faster data collection, allowing for real-time adjustments to the estimation methods and im-

proving overall system performance.

In conclusion, future research in this area should focus on refining the existing methods, exploring new applications, conducting more comprehensive experimental validations, and embracing technological advancements. These efforts have the potential to further improve the accuracy and applicability of tangential cutting torque estimation, ultimately contributing to more efficient and automated machining processes in industrial manufacturing.

REFERENCES

[1] F. W. Taylor, "On the art of cutting metals," *Transactions of the American Society of Mechanical Engineers*, vol. 28, pp. 31–248, 1907.

[2] M. Merchant, "Mechanics of the metal cutting process. i. orthogonal cutting and a type 2 chip," *Journal of Applied Physics*, vol. 16, no. 5, pp. 267–275, 1945.

[3] P. Rao and D. Rao, "Cutting forces in milling and their effect on surface quality of machined components," *Procedia Technology*, vol. 25, pp. 524–531, 2016.

[4] B. Powalka, J. S. Dhupia, A. G. Ulsoy, and R. Katz, "Identification of machining force model parameters from acceleration measurements," *International Journal of Manufacturing Research*, vol. 3, pp. 265–284, 2008.

[5] C. Wang, X. Zhang, B. Qiao, X. Chen, and H. Cao, "Milling force identification from acceleration signals using regularization method based on TSVD in peripheral milling," *Procedia CIRP*, vol. 77, pp. 18–21, 2018.

[6] M. Postel, D. Aslan, K. Wegener, and Y. Altintas, "Monitoring of vibrations and cutting forces with spindle mounted vibration sensors," *Cirp Annals*, vol. 68, no. 1, pp. 413–416, 2019.

[7] S. Auchet, P. Chevrier, M. Lacour, and P. Lipinski, "A new method of cutting force measurement based on command voltages of active electro-magnetic bearings," *International Journal of Machine Tools and Manufacture*, vol. 44, no. 14, pp. 1441–1449, 2004.

[8] M. Luo, H. Luo, D. Axinte, D. Liu, J. Mei, and Z. Liao, "A wireless instrumented milling cutter system with embedded PVDF sensors," *Mechanical Systems and Signal Processing*, vol. 110, pp. 556–568, 2018.

[9] H. Mostaghimi, C. I. Park, G. Kang, S. S. Park, and D. Y. Lee, "Reconstruction of cutting forces through fusion of accelerometer and spindle current signals," *Journal of manufacturing processes*, vol. 68, pp. 990–1003, 2021.

[10] B. Liu, C. Liu, X. Yu, Y. Zhou, and D. Wang, "Prediction , detection , and suppression of regenerative chatter in milling," *Advances in Mechanical Engineering*, vol. 14, pp. 1–26, 2022.

[11] Y. Yamada and Y. Kakinuma, "Sensorless cutting force estimation for full-closed controlled ball-screw-driven stage," *The International Journal of Advanced Manufacturing Technology*, vol. 87, pp. 3337–3348, 2016.

[12] K. Yamamoto, A. Kamba, K. Takeuchi, J. Fujita, Y. Fujimagari, and Y. Kakinuma, "Enhancing the multi-encoder-based cutting force estimation along the stationary axis of a machine tool with multiple inertia dynamics," *The International Journal of Advanced Manufacturing Technology*, vol. 123, pp. 1215–1229, 2022.

[13] S. J. Chapman, *Electric Machinery Fundamentals*. New York: McGraw-Hill Education, 5 ed., 2012.

[14] Y. Altintas, *Manufacturing Automation: Metal Cutting Mechanics, Machine Tool Vibrations, and CNC Design*. Cambridge University Press, 2012.

[15] R. G. Brown and P. Y. C. Hwang, *Introduction to random signals and applied kalman filtering: With MATLAB exercises*. John Willey, 2019.

[16] B. Automation, "Twincat 3 | Software For Automation," *Beckhoff Automation website*, 2024.

[17] B. Automation, "C6930 | Ultra-Compact Control Cabinet Industrial PC," *Beckhoff Automation website*, 2024.

[18] B. Automation, "Ax5125 | Digital Compact Servo Drive," *Beckhoff Automation website*, 2024.

[19] Heidenhain, "Rod 480 | Incremental Rotary Encoder," *Heidenhain website*, 2024.

[20] B. Automation, "Am8062 | Servomotor," *Beckhoff Automation website*, 2024.

[21] B. Automation, "Ax8640 | Power Supply Module For AX8000 Multi-Axis Servo System," *Beckhoff Automation website*, 2024.

[22] Heidenhain, “Ls403 | Linear Encoder,” *Heidenhain website*, 2024.

[23] K. Group, “9257b | Quartz 3-Component Dynamometer,” *Kistler Group website*, 2024.

[24] N. Instruments, “cdaq-9174 | CompactDAQ Chassis,” *National Instruments website*, 2024.

[25] N. Instruments, “Ni 9234 | Sound And Vibration Input Module,” *National Instruments website*, 2024.

APPENDICES

A Simulation Blocks for Milling Force Model

In this section, the simulation process for the cutting forces model is presented, detailing the model blocks used to accurately predict the forces generated during the machining process. Since the immersion angle (ϕ) is one of the inputs, its value is derived from the spindle position data provided by the driver. However, an offset correction is required to adjust the spindle angle, ensuring that the phase difference between the measured force data (F_x and F_y) and the calculated forces is eliminated.

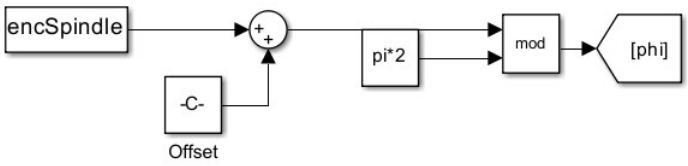


Figure A.1: Calculating Immersion Angle in Simulink ϕ

The following function block is used to calculate the starting (entry) ϕ_{st} and exit ϕ_{ex} angle in both transient and steady state. The model is shown in Figure A.2.

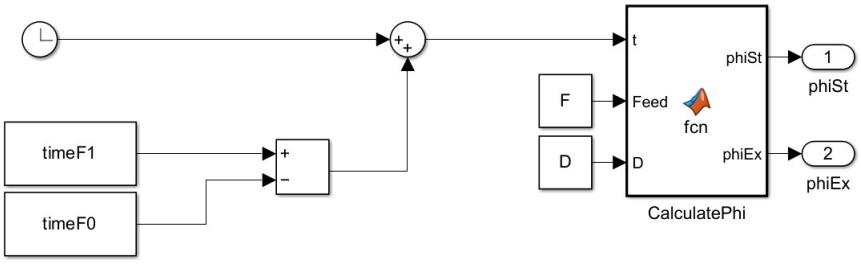


Figure A.2: Calculating ϕ_{st} and ϕ_{ex}

The algorithm behind the function called 'CalculatePhi' is shown in Algorithm 3.

1. Inputs:
    - t : Time, $[s]$ (The cutting process begins at time $t = 0$ seconds.)
    - F : Feedrate, mm/min
    - r : Radius of the cutter, mm
    - N : Number of teeth on the cutter
    - a_e : Radial depth of cut, mm
2. Outputs:
    - ϕ_{st} : Starting (entry) angle, rad
    - ϕ_{ex} : Exit angle, rad
3. Calculation Steps:
    - Initializing Starting (entry) angle, ϕ_{st}
    - Initializing Exit angle, ϕ_{ex}
    - Starting conditional statement to control whether cutting is started
    - Calculating the tool position relative to the workpiece in the direction of feed,x
    - Starting conditional statement to control check whether the radial depth of cut is less than or equal to the radius of the cutter.
    - Calculating entry angle based on the geometry between the relative position (x) and radius of the cutter, ϕ_{st}
    - Calculating exit angle based on the geometry using the radial depth of cut (a_e), ϕ_{ex}
    - Starting the else statement which accepts only when raidal depth of cut is greater than radius of the cutter
    - Calculating entry angle based on the geometry between the relative position (x) and radius of the cutter, ϕ_{st}
    - Calculating exit angle based on the geometry using the radial depth of cut (a_e), ϕ_{ex}

- Ending conditional statement
- Ending conditional statement

Algorithm 3 Calculation of ϕ_{st} and ϕ_{ex}

Require: t, F,D,a_e

Ensure: ϕ_{st},ϕ_{ex}

$\phi_{st} = 0$

$\phi_{ex} = 0$

if $t \geq 0$ **then**

$x = (F/60)t$

if $ae \leq r$ **then**

$\phi_{st} = arcsin(\frac{r-x}{r})$

$\phi_{ex} = arcsin(\frac{a_e-r}{r})$

else

$\phi_{st} = \arcsin(\frac{r-x}{r})$

$\phi_{ex} = \pi - \phi_{st}$

end if

end if

The force model is developed based on the procedure outlined in Algorithm 1, with its corresponding block diagram presented in Figure A.3.

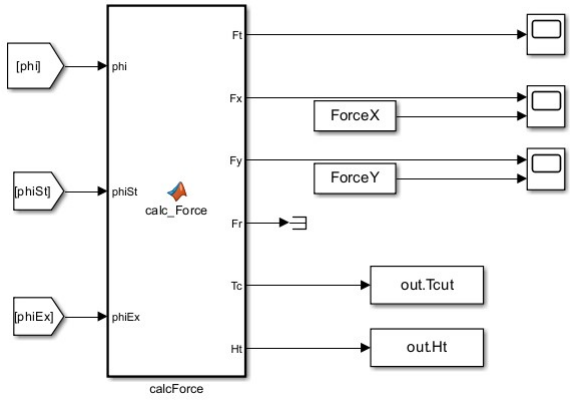


Figure A.3: Calculating Cutting Forces and Tangential Cutting Force

B AC Induction Motor Parameter Identification

In Figure B.1, the data sheet for the Franz Kessler DM 112/4L motor is presented.

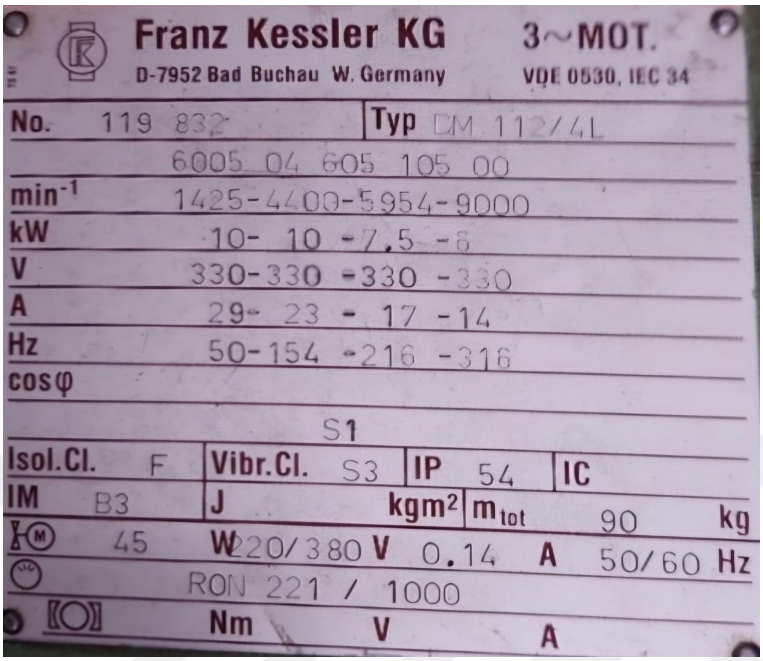


Figure B.1: AC Induction Motor Data Sheet

In Figure B.2, the setup for testing motor parameters is also illustrated. The following hardware components, listed from left to right, are utilized in this setup:

1. The Variac, an electrical transformer enabling adjustable voltage output, is employed for both the No-Load and Locked Rotor tests.
2. The DC power supply, which delivers a constant direct current (DC) output, is used during the DC test to measure the motor's phase resistance.
3. The AC induction motor serves as the actuator responsible for rotating the spindle system.

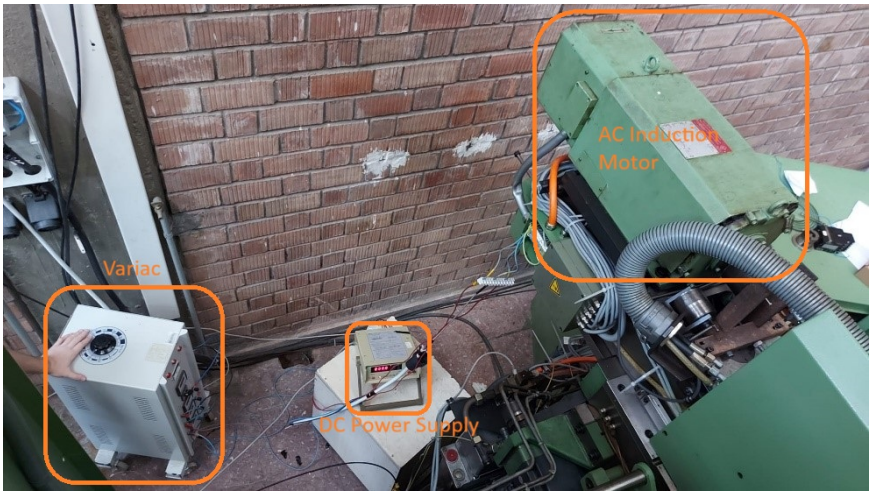


Figure B.2: Test Setup for Motor Parameter Identification

In Figure B.3, the setup for the Locked Rotor Test is also depicted. For this test, a mechanism is constructed around the motor's output shaft to immobilize it.

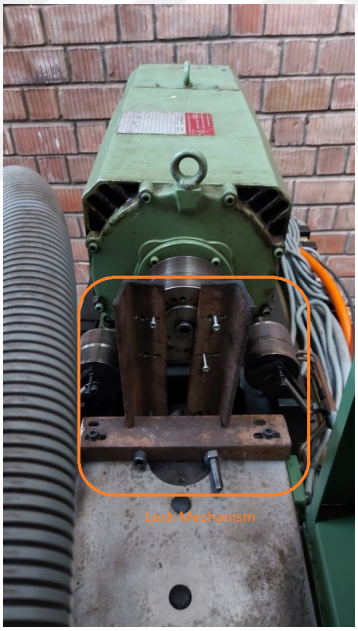


Figure B.3: Lock Mechanism for the Locked Rotor Test

C Control System

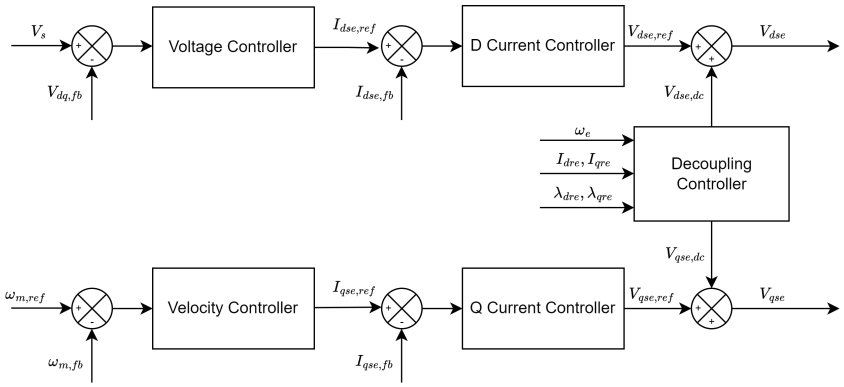


Figure C.1: General Control Block Diagram

Field-oriented control with feedback is also employed for controlling the spindle motor. This control system utilizes a cascaded structure, with two current controllers in the inner loop, corresponding to the direct and quadrature axes in the synchronous reference frame. The outer loop consists of voltage and speed controllers, which provide reference signals for the direct and quadrature axes current controllers. Additionally, a decoupling controller is incorporated to mitigate the coupling effects between the two axes.

C.1 Velocity Controller

The velocity controller, shown in Figure C.2, is also a PI controller that utilizes the back-calculation method as part of its anti-windup algorithm.

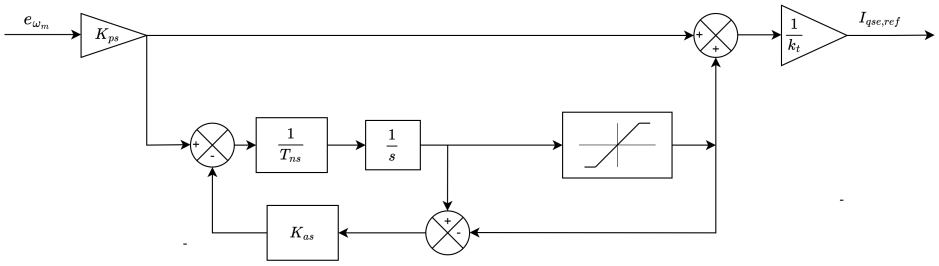


Figure C.2: Velocity Controller Block Diagram

C.2 Quadrature Axis Current Controller

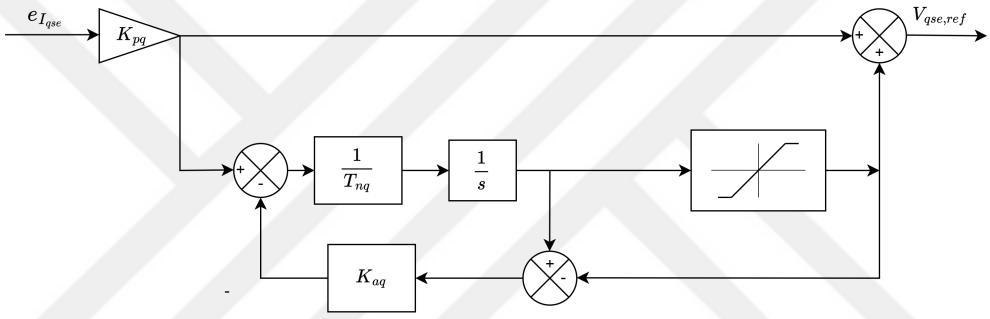


Figure C.3: Quadrature Axis Current Controller Block Diagram

The quadrature axis current controller, illustrated in Figure C.3, is also designed for the synchronous reference frame of the induction motor. This controller is a PI controller that employs the back-calculation method for its anti-windup algorithm.

C.3 Direct Axis Current Controller

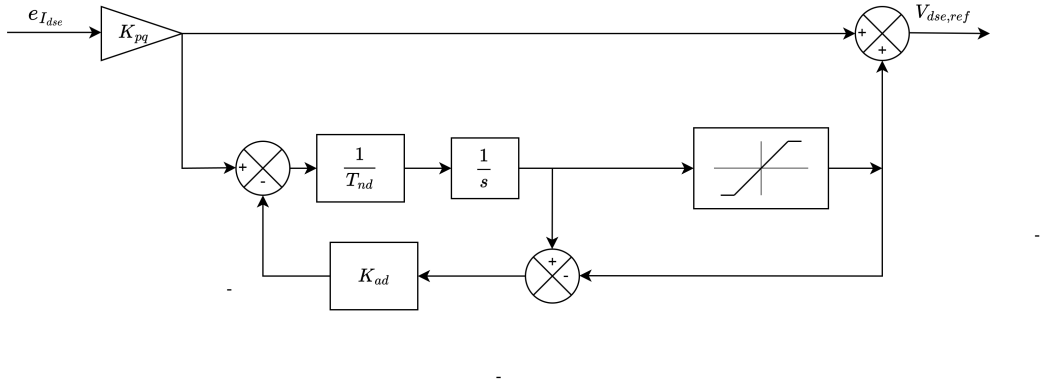


Figure C.4: Direct Axis Current Controller Block Diagram

The direct axis current controller, shown in Figure C.4, is also designed for the synchronous reference frame of the induction motor. This controller is a PI controller that utilizes the back-calculation method for its anti-windup algorithm.

C.4 Decoupling Controller

In the voltage equations of an induction motor expressed in the synchronous reference frame, there are also cross-coupling components between the axes, in addition to the back-EMF.

$$V_{dse} = RI_{dse} + L\frac{dI_{dse}}{dt} - LI_{qse}\omega + e_{dse} \tag{C.1}$$

$$V_{qse} = RI_{qse} + L\frac{dI_{qse}}{dt} + LI_{dse}\omega + e_{qse} \tag{C.2}$$

where R and L defined as:

$$R = R_s + R_r(\frac{L_m}{L_r})^2 \tag{C.3}$$

$$L = L_s\sigma \tag{C.4}$$

$$\sigma = 1 - \frac{L_m^2}{L_s L_r} \tag{C.5}$$

These voltage components can also adversely affect feedback current control, even with the use of a synchronous frame current regulator. At high operating frequencies, where these components become more pronounced, they may lead to an oscillatory current response. To mitigate the impact of these disturbance components and improve current control performance, a decoupling controller is typically employed alongside the current feedback controller.

$$V_{dse,dc} = -\omega_e L_s I_{qse} - R_r \frac{L_m}{L_r^2} \lambda_{dre} \tag{C.6}$$

$$V_{qse,dc} = \omega_e L_s I_{dse} + \omega_r \frac{L_m}{L_r} \lambda_{dre} \tag{C.7}$$

C.5 Transformation Between Stationary and Synchronous Frames

Since the motor is modeled in the stationary reference frame while the current controller operates in the synchronous reference frame, it is also necessary to transform the currents for compatibility. The voltage references generated by the respective current controllers are transformed using the angle derived from the reference motor velocity, as shown in Figure C.5. The required feedback for both the PI controllers and decoupling controllers, including the currents and fluxes of the motor in the stationary reference frame, is transformed into the synchronous reference frame using the angle obtained from the rotor fluxes of the motor, as illustrated in Figure C.6.

$$\begin{bmatrix} V_{dss} \\ V_{qss} \end{bmatrix} = \begin{bmatrix} \cos(\theta_{e,ref}) & -\sin(\theta_{e,ref}) \\ \sin(\theta_{e,ref}) & \cos(\theta_{e,ref}) \end{bmatrix} \begin{bmatrix} V_{dse} \\ V_{qse} \end{bmatrix} \tag{C.8}$$

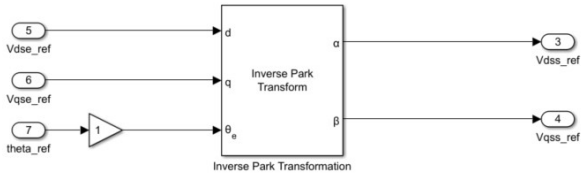


Figure C.5: Voltage Reference Frame Transformation Block Diagram

For the transformation of the feedback into the reference frame, the electrical angle is also derived from the rotor flux in the direct and quadrature axes using the following equation:

$$\theta_e = tan^{-1}(\frac{\lambda^s_{qr}}{\lambda^s_{dr}}) \tag{C.9}$$

I_{drs} and I_{qrs} are also transformed from the stationary to the synchronous reference frame using the following equation:

$$\begin{bmatrix} I_{dse} \\ I_{qse} \end{bmatrix} = \begin{bmatrix} \cos(\theta_e) & \sin(\theta_e) \\ sin(\theta_e) & \cos(\theta_e) \end{bmatrix} \begin{bmatrix} I_{dss} \\ I_{qss} \end{bmatrix} \tag{C.10}$$

λ_{drs} and λ_{qrs} are also transformed from the stationary to the synchronous reference frame using the following equation:

$$\begin{bmatrix} \lambda_{dre} \\ \lambda_{qre} \end{bmatrix} = \begin{bmatrix} \cos(\theta_e) & \sin(\theta_e) \\ sin(\theta_e) & \cos(\theta_e) \end{bmatrix} \begin{bmatrix} \lambda_{drs} \\ \lambda_{qrs} \end{bmatrix} \tag{C.11}$$

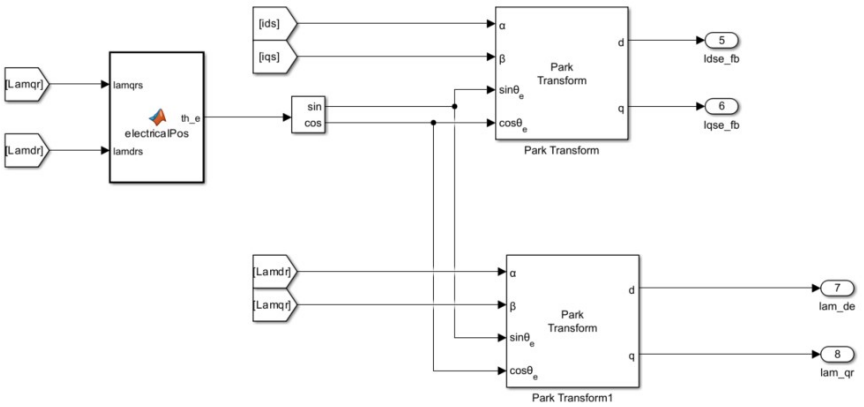


Figure C.6: Feedback Reference Frame Transformation Block Diagram

D Simulation Models for Estimation Methods

In this section, the simulation model which is used for the verification methods for the various estimation methods that are discussed in Section 4.1.

D.1 Common Blocks in Simulation

In this subsection, the simulation blocks used for the estimation methods, which are commonly shared across the different methods, are discussed.

The structure of the dynamic model simulation is common for all of the methods except the Method 3 which use only mechanical subsystem dynamics.

Recall that the electric subsystem is modeled in the stationary reference frame, as it simplifies the system compared to other reference frames. However, since the CNC driver only provides voltage measurements for V_{dse} and V_{qse}, these voltages are transformed into stationary reference frame voltages, V_{dss} and V_{qss}, in the simulation model. The 'Inverse Park Transform' requires a reference angle for the transformation, which is obtained from the motor position θ_m under the assumption that slip is nearly zero. This assumption is justified by the presence of the 'slip compensation' algorithm in the driver controller, which minimizes slip.

Using this assumption, the electric angle can be calculated from the motor position θ_m and the number of pole pairs p of the motor as follows:

$$\theta_e = p\theta_m \tag{D.1}$$

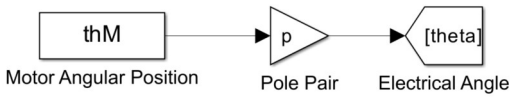


Figure D.1: Obtaining Electrical Angle θ_e from Motor Angular Position θ_m

Finally, the collected data for V_{dse} and V_{qse} is transformed using a preconfigured block for the 'Inverse Park Transform.'

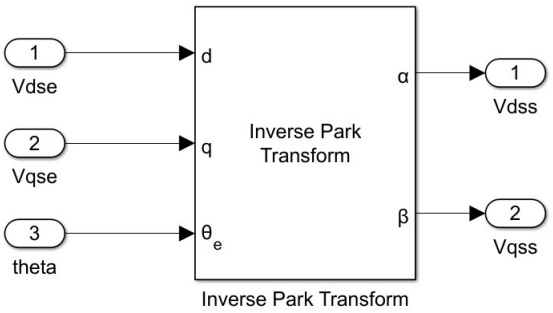


Figure D.2: Transformation of V_{dse}, V_{qse} to V_{dss}, V_{qss}

These voltage inputs are then applied to the electric subsystem, modeled in the simulation using the mathematical framework described in Section 2.2. The electric subsystem subsequently generates the electric torque T_e, which serves as the input for the mechanical subsystem, modeled according to the mathematical framework outlined in Section 2.3.

Figure D.3 illustrates the dynamic model, which integrates both the electrical and mechanical subsystems.

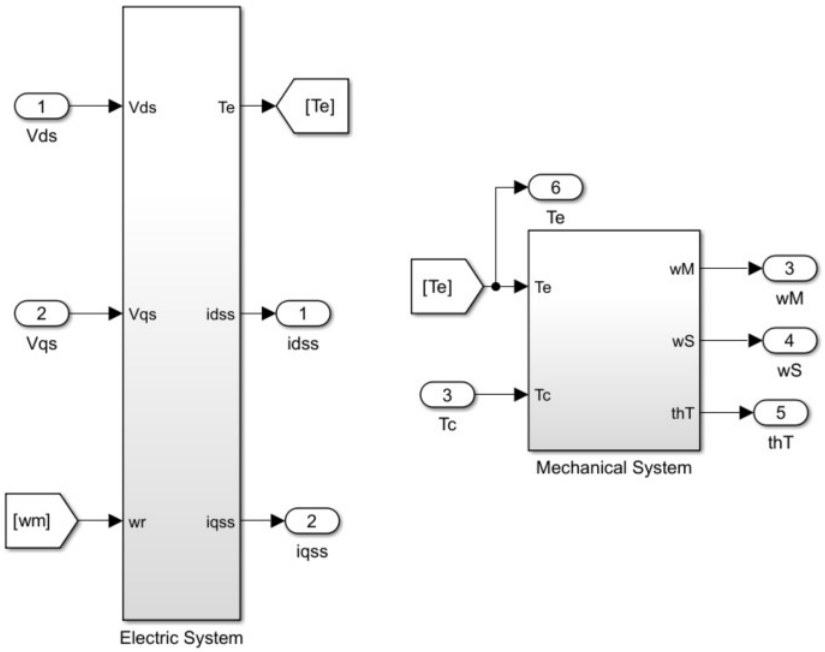


Figure D.3: Dynamic Model

However, the parameters identified in Chapter 3 are used with certain uncertainties to create a more realistic simulation model. These uncertainties are represented as follows:

$$f_{dm} = f_{nom}\psi \tag{D.2}$$

Here, f_{dm} represents the dynamic model parameters, while f_{nom} denotes the parameters identified in Sections 3.1.1 and 3.1.2. The term ψ is a gain used to account for uncertainties. Specifically, if $\psi = 1$, the uncertainty is considered to be zero.

To introduce measurement noise to the measurement vector $\mathbf{z}_k$ in the simulation, 'Band-Limited White Noise' blocks from Simulink are applied to each measurement. Five different seeds are used to generate random white noise, with the magnitude of the noise controlled by separate gains specific to each variable. The only gains that are set equal are those for the measured currents, I_{dss} and I_{qss}, to ensure consistent measurement noise for these variables.

Figure D.4 illustrates how the measurement vector with noise is obtained in Simulink for the estimation methods, excluding Method 3.

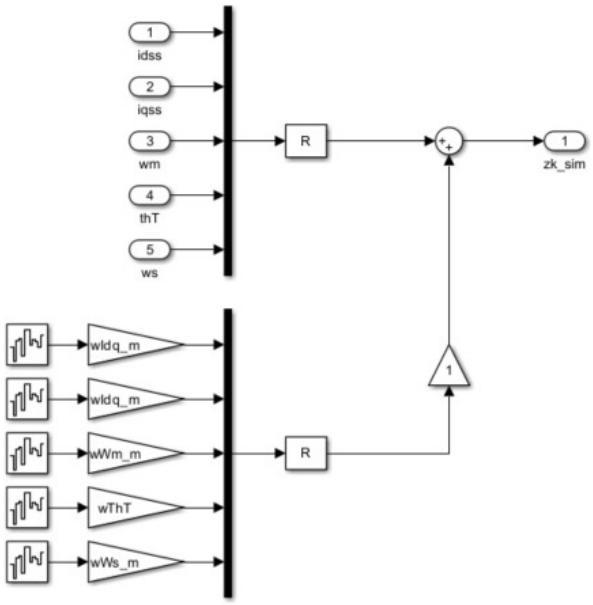


Figure D.4: Measurement Vector in Simulation

Since Method 3 only utilizes measurements from the mechanical subsystem, Figure D.5 illustrates how the measurement vector with noise is obtained in Simulink specifically for Method 3.

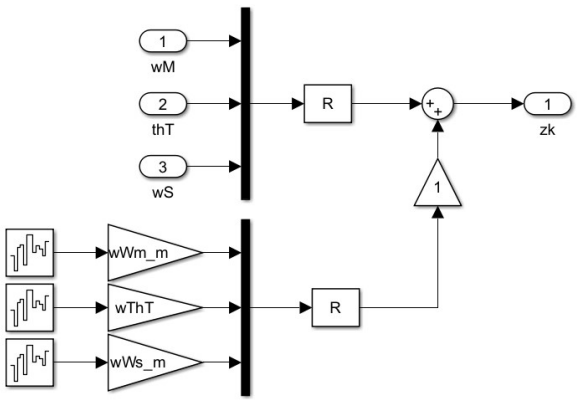


Figure D.5: Measurement Vector in Simulation

It should be noted, however, that for the measurements obtained from the mechanical subsystem, both Figures D.4 and D.5 utilize the same gain for the noise.

D.2 Blocks for Estimation Methods in Simulation

Each estimation method introduced and described in Section 4.1 has its own simulation block, designed according to its specific algorithm.

The simulation block constructed for Method 1 is illustrated in Figure D.6. The algorithm used in the block is presented in Algorithm 4.

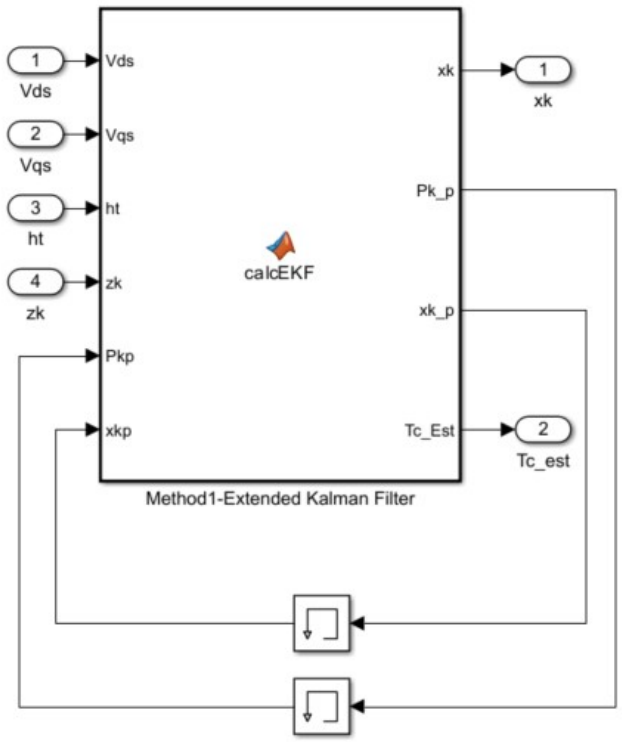


Figure D.6: Simulation Block for Method 1

Algorithm 4 Calculation of Extended Kalman Filter Equations for Method 1

/ Inputs ,which are time dependent, taken from Simulation */*

Require: V_{dss}, V_{qss},$\mathbf{h}_t$,$\mathbf{z}_k$,$\mathbf{P}_k^-$,$\mathbf{x}_k^-$

/ Inputs ,which are time independent, taken from Matlab Workspace */*

Require: $\mathbf{H}_k$,$\mathbf{Q}_k$,$\mathbf{R}_k$,$\mathbf{I}$,R_s,R_r,L_r,L_m,L_s,p,γ,J_m,J_s,b_m,b_s,b_t,k,n_g,r,t_s,K_t

/ inputs ,which are time independent, taken from Matlab Workspace and necessary matrix for calculation of the nonlinear Model */*

Require: $\mathbf{A}_2, \mathbf{B}_1, \mathbf{B}_2, \mathbf{I}_1, \mathbf{I}_2$

Ensure: $\hat{\mathbf{x}}_k$,$\mathbf{x}_k^-$,$\mathbf{P}_k^-$,T_c

$\mathbf{K}_k = \mathbf{P}_k^- \mathbf{H}_k^T (\mathbf{H}_k \mathbf{P}_k^- \mathbf{H}_k^T + \mathbf{R}_k)^{-1}$

$\hat{\mathbf{x}}_\mathbf{k} = \mathbf{x}_k^- + \mathbf{K}_k(\mathbf{z}_k - \mathbf{H}_k \mathbf{x}_k^-)$

$\mathbf{u} = [V_{dss}, V_{qss}]^T$

$\mathbf{P}_k = (\mathbf{I} - \mathbf{K}_k \mathbf{H}_k)\mathbf{P}_k^-$

$\mathbf{x}_k^- = nLModel(\mathbf{u}, t_s, \mathbf{x_k}, R_s, R_r, L_r, L_s, L_m, p, \gamma, K_t, \mathbf{h}_t, r, \mathbf{A}_2, \mathbf{B}_1, \mathbf{B}_2, \mathbf{I}_1, \mathbf{I}_2)$

$\mathbf{J}_k = calculateJ(\mathbf{x}_k, L_s, L_r, L_m, R_r, R_s, \gamma, p, n_g, J_m, J_s, k, b_t, b_m, b_s, t_s, \mathbf{h}_t, r)$

$\mathbf{P}_k^- = \mathbf{J}_k \mathbf{P_k} \mathbf{J}_k^T + \mathbf{Q}_k$

$\hat{T_c} = r(\mathbf{h}_t^T [\hat{\mathbf{x}}_k(8)\ \hat{\mathbf{x}}_k(9)]^T)$

An explanation of the algorithm is provided below:

1. Inputs from Simulation (Time-dependent):
   - V_{dss}, V_{qss}: Stator voltages represented in the stationary reference frame for the D-Q axis.
   - $\mathbf{h}_t$: Geometric matrix providing information on the geometry of the cutting process.
   - $\mathbf{z}_k$: Measurement vector at time step k.
   - $\mathbf{P}_k^-$: The prior estimate of the state covariance matrix.
   - $\mathbf{x}_k^-$: The prior estimate of the state vector.
2. Inputs from MATLAB Workspace (Time-independent):
   - $\mathbf{H}_k$: Observation (measurement) matrix, relating the state vector to the measurement vector.
   - $\mathbf{Q}_k$: Process noise covariance matrix.

- $\mathbf{R}_k$: Measurement noise covariance matrix.
- $\mathbf{I}$: Identity matrix (9x9).
- R_s, R_r: Stator and rotor resistances.
- L_s, L_r, L_m: Stator inductance, rotor inductance, and mutual inductance.
- p: Number of pole pairs.
- $\gamma = L_s L_r - L_m^2$.
- $K_t = 1.5 p L_m$.
- J_m, J_s: Motor and spindle inertias.
- b_m, b_s, b_t: Motor damping friction coefficient, spindle damping friction coefficient, and transmission friction coefficient.
- k: Torsional spring coefficients.
- n_g: Gear ratio of the transmission.
- r: Tool radius.
- t_s: Sampling time.

3. Inputs from MATLAB Workspace (Time-independent) for Nonlinear Model:
   - State matrix of the mechanical subsystem, $\mathbf{A}_2$
   - Input matrix of the electric subsystem, $\mathbf{B}_1$
   - Input matrix of the mechanical subsystem, $\mathbf{B}_2$
   - Identity matrix (4x4), $\mathbf{I}_1$
   - Identity matrix (3x3), $\mathbf{I}_2$
4. Output of the function:
   - $\hat{\mathbf{x}}_k$: Estimated state vector.
   - $\mathbf{x}_k^-$: Prior estimate of the state vector.
   - $\mathbf{P}_k^-$: Prior estimate of the state covariance matrix.
   - $\hat{T}_c$: Estimated cutting torque.
5. EKF Calculation Steps:
   - Calculation of Kalman gain, $\mathbf{K}_k$.

- Updating the estimation of the states, $\hat{\mathbf{x}}_k$.
- Covariance update, $\mathbf{P}_k$.
- Prediction of the next state (prior estimate) using the 'nLModel' function, $\mathbf{x}_k^-$.
- Calculation of the Jacobian matrix using the 'calculateJ' function, $\mathbf{J}_k$.
- Updating the prior covariance prediction, $\mathbf{P}_k^-$.
- Calculation of the estimated cutting torque from the estimated states, $\hat{T}_c$.

The algorithm that describes the nonlinear model of the system is presented in Algorithm 5.

Algorithm 5 Nonlinear Function for Method 1

Require: $(\mathbf{u}, t_s, \mathbf{x_k}, R_s, R_r, L_r, L_s, L_m, p, \gamma, K_t, \mathbf{h}_t, r, \mathbf{A}_2, \mathbf{B}_1, \mathbf{B}_2, \mathbf{I}_1, \mathbf{I}_2)$

Ensure: $\mathbf{x}_k$

$[I_{dss}, I_{qss}, I_{drs}, I_{qrs}, \omega_m, \theta_T, \omega_s, K_{tc}, K_{te}] = \mathbf{x}_k$

$\omega_r = \omega_m p$

$\mathbf{x}_{1,k} = [I_{dss}, I_{qss}, I_{drs}, I_{qrs}]^T$

$$A_1 = \begin{bmatrix} -\frac{L_r R_s}{\gamma} & \frac{L_m^2 \omega_e}{\gamma} & \frac{L_m R_r}{\gamma} & \frac{L_m L_r \omega_e}{\gamma} \\ -\frac{L_m^2 \omega_e}{\gamma} & -\frac{L_r R_s}{\gamma} & -\frac{L_m L_r \omega_e}{\gamma} & \frac{L_m R_r}{\gamma} \\ \frac{L_m R_s}{\gamma} & -\frac{L_s L_m \omega_e}{\gamma} & -\frac{R_r L_s}{\gamma} & -\frac{L_s L_r \omega_e}{\gamma} \\ \frac{L_s L_m \omega_e}{\gamma} & \frac{L_m R_s}{\gamma} & \frac{L_r L_s \omega_e}{\gamma} & -\frac{R_r L_s}{\gamma} \end{bmatrix}$$

$\mathbf{G}_1 = e^{\mathbf{A}_1 t_s}$

$\mathbf{H}_1 = \mathbf{A}_1^{-1}(\mathbf{G}_1 - \mathbf{I}_1)\mathbf{B_1}$

$\mathbf{x}_{1,kn} = \mathbf{G}_1 \mathbf{x}_{1,k} + \mathbf{G}_1 \mathbf{u}$

$T_e = K_t(\mathbf{x}_{1,kn}(2)\mathbf{x}_{1,kn}(3) - \mathbf{x}_{1,kn}(1)\mathbf{x}_{1,kn}(4))$

$T_c = r(K_{tc}\mathbf{h}_t(1) + K_{te}\mathbf{h}_t(2))$

$\mathbf{x}_{2,k} = [\omega_m\ \theta_T\ \omega_s]^T$

$\mathbf{u}_2 = [T_e\ T_c]$

$\mathbf{G}_2 = e^{\mathbf{A}_2 t_s}$

$\mathbf{H}_2 = \mathbf{A}_2^{-1}(\mathbf{G}_2 - \mathbf{I}_2)\mathbf{B_2}$

$\mathbf{x}_{2,kn} = \mathbf{G}_2 \mathbf{x}_{2,k} + \mathbf{G}_2 \mathbf{u}_2$

$\mathbf{x}_{k,n} = [\mathbf{x}_{1,kn}^T\ \mathbf{x}_{2,kn}^T\ K_{tc}\ K_{te}]^T$

Explanation of the steps in Algorithm 5:

1. Inputs from Algorithm 4:
    - Input vector containing the voltages, $\mathbf{u}$
    - Sampling time, t_s
    - State vector, $\mathbf{x}_k$
    - R_s, R_r: Stator and rotor resistances
    - L_s, L_r, L_m: Stator inductance, rotor inductance, and mutual inductance
    - p: Number of pole pairs
    - $\gamma = L_s L_r - L_m^2$
    - Geometric matrix providing information on the cutting geometry, $\mathbf{h}_t$
    - Cutting tool radius, r
    - State matrix of the mechanical subsystem, $\mathbf{A}_2$
    - Input matrix of the electric subsystem, $\mathbf{B}_1$
    - Input matrix of the mechanical subsystem, $\mathbf{B}_2$
    - Identity matrix (4x4), $\mathbf{I}_1$
    - Identity matrix (3x3), $\mathbf{I}_2$
2. Output of the function:
    - $\mathbf{x}_{k,n} = [I_{dss}, I_{dss}, I_{drs}, I_{qrs}, \omega_m, \theta_T, \omega_s]^T$: States of the entire system calculated by this algorithm.
3. Calculation steps:
    - Separate all states from $\mathbf{x}_k$
    - Calculate rotor velocity, ω_e, from motor velocity, ω_m
    - Create the state matrix for only the electric subsystem variables, $\mathbf{x}_{1,k}$
    - Calculate and update the state matrix, $\mathbf{A}_1$, used in the electric equations
    - Discretize $\mathbf{A}_1$ to obtain $\mathbf{G}_1$
    - Discretize $\mathbf{B}_1$ to obtain $\mathbf{H}_1$

- Calculate new states for electric subsystem variables at the next step, $\mathbf{x}_{1,kn}$
- Calculate the electric torque, T_e
- Calculate the cutting torque, T_c
- Create the state matrix for the mechanical subsystem variables, $\mathbf{x}_{1,k}$
- Create the input matrix for the mechanical subsystem, $\mathbf{u}_2$
- Discretize $\mathbf{A}_2$ to obtain $\mathbf{G}_2$
- Discretize $\mathbf{B}_2$ to obtain $\mathbf{H}_2$
- Calculate new states for the mechanical subsystem variables at the next step, $\mathbf{x}_{2,kn}$
- Create the state matrix that includes all variables for the entire system, $\mathbf{x}_{k,n}$

Algorithm that describes the calculation of the Jacobian Matrix can be seen from 6.

Algorithm 6 Calculation of the Jacobian Matrix

Require: $\mathbf{x}_k, L_s, L_r, L_m, R_r, R_s, \gamma, p, n_g, J_m, J_s, k, b_t, b_m, b_s, t_s, \mathbf{h}_t, K_t, r$

Ensure: $\mathbf{J}_k$

$I_{dss} = \mathbf{x}_k(1)$

$I_{qss} = \mathbf{x}_k(2)$

$I_{qrs} = \mathbf{x}_k(3)$

$I_{drs} = \mathbf{x}_k(4)$

$\omega_m = \mathbf{x}_k(5)$

$\mathbf{j}(1,5) = \frac{(I_{qss}L_m^2 + I_{qrs}L_mL_r)p}{\gamma}$

$\mathbf{j}(2,5) = -\frac{(I_{dss}L_m^2 + I_{drs}L_mL_r)p}{\gamma}$

$\mathbf{j}(3,5) = -\frac{(I_{qss}L_sL_m + I_{qrs}L_sL_r)p}{\gamma}$

$\mathbf{j}(4,5) = \frac{(I_{dss}L_sL_m + I_{drs}L_sL_r)p}{\gamma}$

$$\mathbf{j} = \begin{bmatrix} -\frac{L_rR_s}{\gamma} & \frac{L_m^2\omega_e}{\gamma} & \frac{L_mR_r}{\gamma} & \frac{L_mL_r\omega_e}{\gamma} & j_{1,5} & 0 & 0 \\ -\frac{L_m^2\omega_e}{\gamma} & -\frac{L_rR_s}{\gamma} & -\frac{L_mL_r\omega_e}{\gamma} & \frac{L_mR_r}{\gamma} & j_{2,5} & 0 & 0 \\ \frac{L_mR_s}{\gamma} & -\frac{L_sL_m\omega_e}{\gamma} & -\frac{R_rL_s}{\gamma} & -\frac{L_sL_r\omega_e}{\gamma} & j_{3,5} & 0 & 0 \\ \frac{L_sL_m\omega_e}{\gamma} & \frac{L_mR_s}{\gamma} & \frac{L_rL_s\omega_e}{\gamma} & -\frac{R_rL_s}{\gamma} & j_{4,5} & 0 & 0 \\ -\frac{K_tI_{qrs}}{J_m} & \frac{K_tI_{drs}}{J_m} & \frac{K_tI_{qss}}{J_m} & -\frac{K_tI_{dss}}{J_m} & -\frac{b_tn_g^2+b_m}{J_m} & -\frac{kn_g}{J_m} & \frac{b_tn_g}{J_m} \\ 0 & 0 & 0 & 0 & n_g & 0 & -1 \\ 0 & 0 & 0 & 0 & \frac{n_gb_t}{J_s} & \frac{k}{J_s} & -\frac{b_t+b_s}{J_s} \end{bmatrix}$$

$\mathbf{j}_k = e^{\mathbf{j}t_s}$

$\mathbf{J}_k(7,8) = -\frac{r\mathbf{h}_t(1)t_s}{J_s}$

$\mathbf{J}_k(7,9) = -\frac{r\mathbf{h}_t(2)t_s}{J_s}$

$J_k = augmenter(\mathbf{j}_k, \mathbf{J}_k(7,8), \mathbf{J}_k(7,9))$

1. Inputs from Algorithm 4:
    - State vector, $\mathbf{x}_k$
    - L_s, L_r, L_m: Stator inductance, rotor inductance, and mutual inductance
    - R_s, R_r: Stator and rotor resistances
    - $\gamma = L_sL_r - L_m^2$
    - p: Number of pole pairs
    - n_g: Gear ratio of the transmission
    - J_m, J_s: Motor and spindle inertia

- k: Torsional spring coefficients
- b_m, b_s, b_t: Motor damping friction coefficient, spindle damping friction coefficient, and transmission friction coefficient
- t_s: Sampling time
- $\mathbf{h}_t$: Geometric matrix providing information about the cutting geometry
- r: Cutting tool radius

2. Output of the function:
   - $\mathbf{J}_k$: Jacobian matrix in discrete time
3. Calculation Steps:
   - Separate the first five states from $\mathbf{x}_k$ and assign the related variables
   - Calculate specific elements of the matrix $\mathbf{j}$
   - Construct the matrix $\mathbf{j}$ as a (7x7) matrix
   - Discretize $\mathbf{j}$ to obtain $\mathbf{j}_k$
   - Create the elements to be included in the augmented matrix $\mathbf{J}_k$
   - Use the 'augmenter' function to obtain the augmented and discretized Jacobian matrix, $\mathbf{J}_k$

The algorithm for obtaining the augmented matrix for the Jacobian matrix, $\mathbf{J}_k$, is presented in Algorithm 7.

Algorithm 7 Augmentation of the Matrix

Require: $\mathbf{j}_k, \mathbf{J}_k(7,8), \mathbf{J}_k(7,9)$

Ensure: $\mathbf{J}_k$

$$\mathbf{j}_{k,2} = \begin{bmatrix} 0 & 0 \\ 0 & 0 \\ 0 & 0 \\ 0 & 0 \\ 0 & 0 \\ 0 & 0 \\ \mathbf{J}_k(7,8) & \mathbf{J}_k(7,9) \end{bmatrix}$$

$$\mathbf{Z} = \begin{bmatrix} 0 & 0 & 0 & 0 & 0 & 0 & 0 \\ 0 & 0 & 0 & 0 & 0 & 0 & 0 \end{bmatrix}$$

$$\mathbf{I} = \begin{bmatrix} 1 & 0 \\ 0 & 1 \end{bmatrix}$$

$$\mathbf{J}_k = \left[\begin{array}{c|c} \mathbf{j}_k \text{ (7x7)} & \mathbf{j}_{k,2}\text{(7x2)} \\ \hline \mathbf{Z}\text{(2x7)} & \mathbf{I}\text{(2x2)} \end{array}\right]$$

1. Inputs from Algorithm 7:
   - $\mathbf{j}_k$: Jacobian matrix of the seven states
   - $\mathbf{J}_k(7,8)$: Matrix elements associated with the tangential cutting force coefficient, K_{tc}
   - $\mathbf{J}_k(7,9)$: Matrix elements associated with the tangential cutting force coefficient, K_{te}
2. Output of the function:
   - $\mathbf{J}_k$: Jacobian matrix in discrete time
3. Calculation Steps:
   - Create a (7×2) matrix, $\mathbf{j}_{k,2}$
   - Create a zero matrix, $\mathbf{Z}$, of size (2×7)
   - Create an identity matrix, $\mathbf{I}$, of size (2×2)

- Combine $\mathbf{j}_k$, $\mathbf{j}_{k,2}$, $\mathbf{Z}$, and $\mathbf{I}$ to obtain $\mathbf{J}_k$

The simulation block constructed for Method 2 is illustrated in Figure D.7. In this block, there are two different measurement vectors, as previously explained, which differ from those used in Method 1. Additionally, there is an input called "tick", which is required to track the simulation steps within this block. The algorithm used in the block is presented in Algorithm 8.

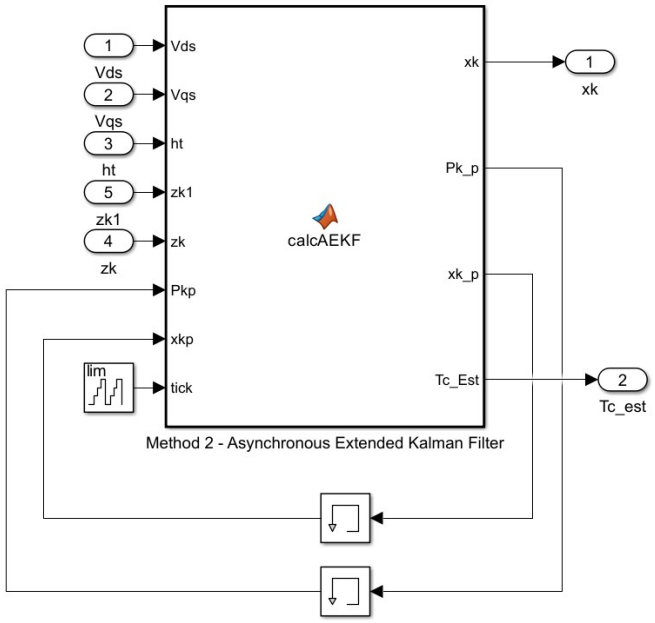


Figure D.7: Simulation Block for Method 2

Algorithm 8 Calculation of Asynchronous Extended Kalman Filter Equations for Method 2

/ Inputs ,which are time dependent, taken from Simulation */*

Require: V_{dss}, V_{qss},$\mathbf{h}_t$,$\mathbf{z}_{k,1}$,$\mathbf{z}_k$,$\mathbf{P}_k^-$,$\mathbf{x}_k^-$

/ Inputs ,which are time independent, taken from Matlab Workspace */*

Require: $\mathbf{H}_{k,1}$,$\mathbf{R}_{k,1}$,$\mathbf{H}_k$,$\mathbf{Q}_k$,$\mathbf{R}_k$,$\mathbf{I}$,R_s,R_r,L_r,L_m,L_s,p,γ,J_m,J_s,b_m,b_s,b_t,k,n_g,r,t_s,K_t

/ inputs ,which are time independent, taken from Matlab Workspace and necessary matrix for calculation of the nonlinear Model */*

Require: $\mathbf{A}_2, \mathbf{B}_1, \mathbf{B}_2, \mathbf{I}_1, \mathbf{I}_2$

Ensure: $\hat{\mathbf{x}}_k$,$\mathbf{x}_k^-$,$\mathbf{P}_k^-$,T_c

if then $(tick \equiv 0 \pmod 8) \; ! = 0$

$\mathbf{K}_{k,1} = \mathbf{P}_k^- \mathbf{H}_{k,1}^T (\mathbf{H}_{k,1} \mathbf{P}_k^- \mathbf{H}_{k,1}^T + \mathbf{R}_{k,1})^{-1}$

$\hat{\mathbf{x}}_\mathbf{k} = \mathbf{x}_k^- + \mathbf{K}_{k,1}(\mathbf{z}_{k,1} - \mathbf{H}_{k,1}\mathbf{x}_k^-)$

$\mathbf{P}_k = (\mathbf{I} - \mathbf{K}_{k,1}\mathbf{H}_{k,1})\mathbf{P}_k^-$

else

$\mathbf{K}_k = \mathbf{P}_k^- \mathbf{H}_k^T (\mathbf{H}_k \mathbf{P}_k^- \mathbf{H}_k^T + \mathbf{R}_k)^{-1}$

$\hat{\mathbf{x}}_\mathbf{k} = \mathbf{x}_k^- + \mathbf{K}_k(\mathbf{z}_k - \mathbf{H}_k\mathbf{x}_k^-)$

$\mathbf{P}_k = (\mathbf{I} - \mathbf{K}_k\mathbf{H}_k)\mathbf{P}_k^-$

end if

$\mathbf{u} = [V_{dss}, V_{qss}]^T$

$\mathbf{x}_k^- = nLModel(\mathbf{u}, t_s, \mathbf{x_k}, R_s, R_r, L_r, L_s, L_m, p, \gamma, K_t, \mathbf{h}_t, r, \mathbf{A}_2, \mathbf{B}_1, \mathbf{B}_2, \mathbf{I}_1, \mathbf{I}_2)$

$\mathbf{J}_k = calculateJ(\mathbf{x}_k, L_s, L_r, L_m, R_r, R_s, \gamma, p, n_g, J_m, J_s, k, b_t, b_m, b_s, t_s, \mathbf{h}_t, r)$

$\mathbf{P}_k^- = \mathbf{J}_k \mathbf{P_k} \mathbf{J}_k^T + \mathbf{Q}_k$

$\hat{T}_c = r(\mathbf{h}_t^T [\hat{\mathbf{x}}_k(8) \; \hat{\mathbf{x}}_k(9)]^T)$

An explanation of the algorithm is provided below:

1. Inputs from Simulation (Time-dependent):
   - V_{dss}, V_{qss}: Stator voltages represented in the stationary reference frame for the D-Q axis.
   - $\mathbf{h}_t$: Geometric matrix providing information on the geometry of the cutting process.
   - $\mathbf{z}_{k,1}$: Measurement vector for the faster measurement group.

- $\mathbf{z}_k$: Measurement vector for the entire measurement set at the time step corresponding to the slower measurement group.
- $\mathbf{P}_k^-$: The prior estimate of the state covariance matrix.
- $\mathbf{x}_k^-$: The prior estimate of the state vector.

2. Inputs from MATLAB Workspace (Time-independent):

- $\mathbf{H}_k$: Observation (measurement) matrix, relating the state vector to the measurement vector.
- $\mathbf{Q}_k$: Process noise covariance matrix.
- $\mathbf{R}_k$: Measurement noise covariance matrix.
- $\mathbf{I}$: Identity matrix (9x9).
- R_s, R_r: Stator and rotor resistances.
- L_s, L_r, L_m: Stator inductance, rotor inductance, and mutual inductance.
- p: Number of pole pairs.
- $\gamma = L_s L_r - L_m^2$.
- $K_t = 1.5pL_m$.
- J_m, J_s: Motor and spindle inertias.
- b_m, b_s, b_t: Motor damping friction coefficient, spindle damping friction coefficient, and transmission friction coefficient.
- k: Torsional spring coefficients.
- n_g: Gear ratio of the transmission.
- r: Tool radius.
- t_s: Sampling time.

3. Inputs from MATLAB Workspace (Time-independent) for Nonlinear Model:

- State matrix of the mechanical subsystem, $\mathbf{A}_2$
- Input matrix of the electric subsystem, $\mathbf{B}_1$
- Input matrix of the mechanical subsystem, $\mathbf{B}_2$
- Identity matrix (4x4), $\mathbf{I}_1$
- Identity matrix (3x3), $\mathbf{I}_2$

4. Output of the function:

   - $\hat{\mathbf{x}}_k$: Estimated state vector.
   - $\mathbf{x}_k^-$: Prior estimate of the state vector.
   - $\mathbf{P}_k^-$: Prior estimate of the state covariance matrix.
   - $\hat{T}_c$: Estimated cutting torque.

5. EKF Calculation Steps:

   - Check whether the tick is a multiple of 8.
   - If it is not, then:
     - Calculate the Kalman gain, $\mathbf{K}_{k,1}$, using $\mathbf{H}_{k,1}$ and $\mathbf{R}_{k,1}$.
     - Update the state estimation, $\hat{\mathbf{x}}_k$, using $\mathbf{K}_{k,1}$, $\mathbf{H}_{k,1}$, and $\mathbf{z}_{k,1}$.
     - Update the covariance, $\mathbf{P}_k$, using $\mathbf{K}_{k,1}$ and $\mathbf{z}_{k,1}$.
   - If it is, then:
     - Calculate the Kalman gain, $\mathbf{K}_k$, using $\mathbf{H}_k$ and $\mathbf{R}_k$.
     - Update the state estimation, $\hat{\mathbf{x}}_k$, using $\mathbf{K}_k$, $\mathbf{H}_k$, and $\mathbf{z}_k$.
     - Update the covariance, $\mathbf{P}_k$, using $\mathbf{K}_k$ and $\mathbf{z}_k$.
   - Predict the next state (prior estimate) using the 'nLModel' function, $\mathbf{x}_k^-$.
   - Calculate the Jacobian matrix using the 'calculateJ' function, $\mathbf{J}_k$.
   - Update the prior covariance prediction, $\mathbf{P}_k^-$.
   - Calculate the estimated cutting torque from the estimated states, $\hat{T}_c$.

This estimation method is applied in cases where the current measurements, I_{dss} and I_{qss}, have a sampling frequency of 8kHz, while the other measurements have a sampling frequency of 1kHz. In this scenario, the 'Counter Limited' block in Simulink is used to track the ticks, which count from 0 to 7 at 8kHz. A conditional statement is then used to check whether the count is 0.

If the count is not 0, only the current measurements are available, and the EKF performs an update based solely on these measurements. If the count is 0, all measurements are available, and the EKF uses the full set of measurements for the update, similar to the approach in Method 1.

Since the same nonlinear model is employed in this method, the functions 'nLModel', 'calculateJ', and 'augmenter' are used in the same manner as in Method 1.

The simulation block constructed for Method 3 is illustrated in Figure D.8. The algorithm used in the block is presented in Algorithm 9

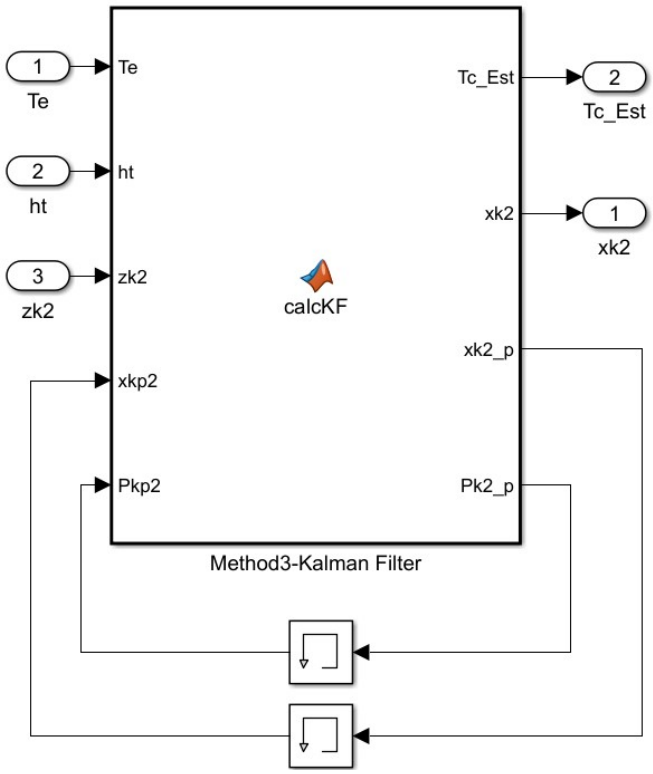


Figure D.8: Simulation Block for Method 3

Algorithm 9 Calculation of Kalman Filter Equations

/ Inputs ,which are time dependent, taken from Simulation */*

Require: T_e,$\mathbf{h}_t$,$\mathbf{z}_k$,$\mathbf{P}_k^-$,$\mathbf{x}_k^-$

/ Inputs ,which are time independent, taken from Matlab Workspace */*

Require: $\mathbf{A}$,$\mathbf{B}$,r,J_s,$\mathbf{R}_k$,$\mathbf{H}_k$,$\mathbf{Q}_k$,$\mathbf{I}$,t_s

Ensure: $\hat{\mathbf{x}}_k$,$\mathbf{x}_k^-$,$\mathbf{P}_k^-$,$\hat{T}_c$

$\mathbf{K}_k = \mathbf{P}_k^- \mathbf{H}_k^T (\mathbf{H}_k \mathbf{P}_k^- \mathbf{H}_k^T + \mathbf{R}_k)^{-1}$

$\hat{\mathbf{x}}_\mathbf{k} = \mathbf{x}_k^- + \mathbf{K}_k(\mathbf{z}_k - \mathbf{H}_k \mathbf{x}_k^-)$

$\mathbf{P}_k = (\mathbf{I} - \mathbf{K}_k \mathbf{H}_k)\mathbf{P}_k^-$

$u = T_e$

$[\mathbf{F}_k, \mathbf{G}_k] = StateMatrixAugmenter(t_s, \mathbf{A}, \mathbf{B}, r, \mathbf{h}_t, J_s)$

$\mathbf{x}_k^- = \mathbf{F}_k \mathbf{x}_k + \mathbf{G}_k u$

$\mathbf{P}_k^- = \mathbf{F}_k \mathbf{P}_\mathbf{k} \mathbf{F}_k^T + \mathbf{Q}_k$

$\hat{T}_c = r(\mathbf{h}_t^T [\hat{\mathbf{x}}_k(4); \hat{\mathbf{x}}_k(5)])$

Explanation of the steps in Algorithm 9:

1. Inputs from Simulation (Time-dependent):
   - T_e: Electric torque generated by the electric system
   - $\mathbf{h}_t$: Geometric matrix providing information on the geometry of the cutting
   - $\mathbf{z}_k$: Measurement vector at time step k
   - $\mathbf{P}_k^-$: Prior estimate of the state covariance matrix
   - $\mathbf{x}_k^-$: Prior estimate of the state vector
2. Inputs from MATLAB Workspace (Time-independent):
   - $\mathbf{A}$: State matrix in the continuous time domain
   - $\mathbf{B}$: Input matrix in the continuous time domain
   - r: Tool radius
   - $\mathbf{R}_k$: Measurement noise covariance matrix
   - $\mathbf{H}_k$: Observation (measurement) matrix relating the state vector to the measurement vector

- $\mathbf{Q}_k$: Process noise covariance matrix
- $\mathbf{I}$: Identity matrix (5x5)
- t_s: Sampling time

3. Output of the function:
   - $\hat{\mathbf{x}}_k$: Estimated state vector
   - $\mathbf{x}_k^-$: Prior estimate of the state vector
   - $\mathbf{P}_k^-$: Prior estimate of the state covariance matrix
   - $\hat{T}_c$: Estimated cutting torque
4. KF Calculation Steps:
   - Calculation of Kalman gain, $\mathbf{K}_k$
   - Update of the state estimation, $\hat{\mathbf{x}}_k$
   - Covariance update, $\mathbf{P}_k$
   - Assign T_e to the input u
   - Use 'StateMatrixAugmenter' to obtain the augmented discretized state matrix $\mathbf{F}_k$ and discretized reduced input matrix $\mathbf{G}_k$
   - Update the state prediction (priori), $\mathbf{x}_k^-$
   - Update the covariance prediction (priori), $\mathbf{P}_k^-$
   - Calculate the estimated cutting torque from the estimated states, $\hat{T}_c$

Algorithm for augmenting state matrix and input matrix is shown in Algorithm 10

Algorithm 10 Augmentation of the State Matrix

Require: t_s,$\mathbf{A}$,$\mathbf{B}$,r,$\mathbf{h}_t$,J_s

Ensure: $\mathbf{F}_k$,$\mathbf{G}_k$

$$\mathbf{A}_k = e^{t_s \mathbf{A}}$$

$$\mathbf{B}_k = \mathbf{A}^{-1}(\mathbf{A}_k - \mathbf{I})\mathbf{B}$$

$$\mathbf{Z} = \begin{bmatrix} 0 & 0 & 0 \\ 0 & 0 & 0 \end{bmatrix}$$

$$\mathbf{I} = \begin{bmatrix} 1 & 0 \\ 0 & 1 \end{bmatrix}$$

$$\mathbf{F}_{1,k} = \begin{bmatrix} 0 & 0 \\ 0 & 0 \\ -\frac{r\mathbf{h}_t(1)t_s}{J_s} & -\frac{r\mathbf{h}_t(2)t_s}{J_s} \end{bmatrix}$$

$$\mathbf{F}_k = \left[\begin{array}{c|c} \mathbf{A}_k \text{ (3x3)} & \mathbf{F}_{1,k}\text{(3x2)} \\ \hline \mathbf{Z}\text{(2x3)} & \mathbf{I}\text{(2x2)} \end{array}\right]$$

$$\mathbf{G}_k = \left[\begin{array}{c} \mathbf{B}_k \text{ (3x1)} \\ \hline 0 \\ 0 \end{array}\right]$$

1. Inputs from Algorithm 7:
   - t_s: Sampling time
   - $\mathbf{A}$: State matrix
   - $\mathbf{B}$: Input matrix
   - r: Tool radius
   - $\mathbf{h}_t$: Geometric matrix providing information about the cutting geometry
   - J_s: Spindle inertia
2. Output of the function:
   - $\mathbf{F}_k$: Discretized augmented state matrix
   - $\mathbf{G}_k$: Discretized augmented input matrix
3. Calculation Steps:

- Discretize $\mathbf{A}$ using the sampling time t_s to obtain $\mathbf{A}_k$
- Discretize $\mathbf{B}$ to obtain $\mathbf{B}_k$
- Create a zero matrix, $\mathbf{F}_{1,k}$, of size (2×3)
- Create an identity matrix, $\mathbf{I}$, of size (2×2)
- Construct the matrix for augmentation elements, $\mathbf{F}_{1,k}$
- Combine $\mathbf{A}_k$, $\mathbf{F}_{1,k}$, $\mathbf{F}_{1,k}$, and $\mathbf{I}$ to form $\mathbf{F}_k$
- Augment $\mathbf{B}_k$ by adding two zero elements to the last two rows to obtain $\mathbf{G}_k$

The simulation block created for Method 4 is illustrated in Figure D.9. The algorithm used in this block is presented in Algorithm 11.

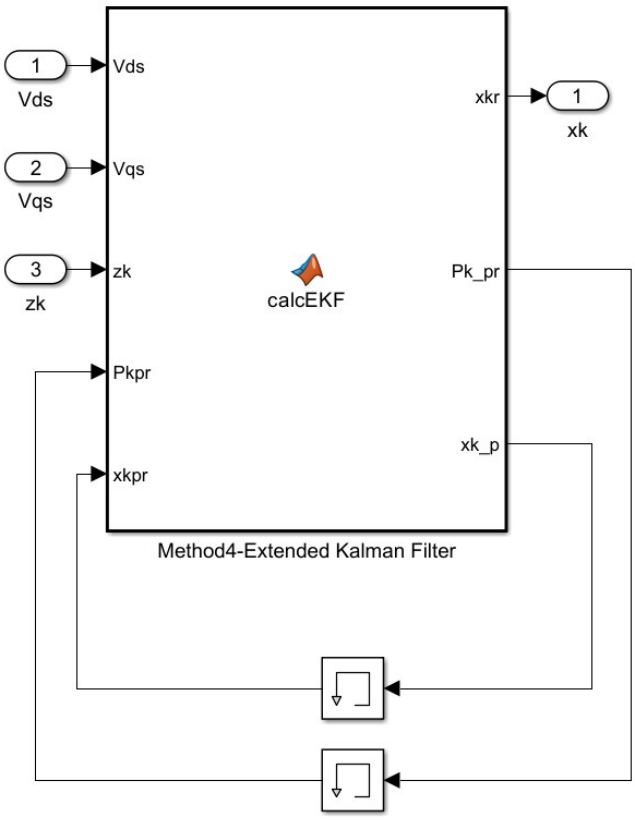


Figure D.9: Simulation Block for Method 4

The algorithm for Method 4 differs from the others, as the geometry matrix $\mathbf{h}_t$ is not provided in this method. Another key difference is that the tangential cutting

torque is directly estimated in this method, as it is included as one of the states in the augmented state matrix $\mathbf{x}_e$.

Algorithm 11 Calculation of Extended Kalman Filter Equations for Method 4

/ Inputs ,which are time dependent, taken from Simulation */*

Require: V_{dss}, V_{qss},$\mathbf{z}_k$,$\mathbf{P}_k^-$,$\mathbf{x}_k^-$

/ Inputs ,which are time independent, taken from Matlab Workspace */*

Require: $\mathbf{H}_k$,$\mathbf{Q}_k$,$\mathbf{R}_k$,$\mathbf{I}$,R_s,R_r,L_r,L_m,L_s,p,γ,J_m,J_s,b_m,b_s,b_t,k,n_g,,t_s,K_t

/ inputs ,which are time independent, taken from Matlab Workspace and necessary matrix for calculation of the nonlinear Model */*

Require: $\mathbf{A}_2, \mathbf{B}_1, \mathbf{B}_2, \mathbf{I}_1, \mathbf{I}_2$

Ensure: $\hat{\mathbf{x}}_k$,$\mathbf{x}_k^-$,$\mathbf{P}_k^-$

$\mathbf{K}_k = \mathbf{P}_k^- \mathbf{H}_k^T (\mathbf{H}_k \mathbf{P}_k^- \mathbf{H}_k^T + \mathbf{R}_k)^{-1}$

$\hat{\mathbf{x}}_\mathbf{k} = \mathbf{x}_k^- + \mathbf{K}_k(\mathbf{z}_k - \mathbf{H}_k \mathbf{x}_k^-)$

$\mathbf{u} = [V_{dss}, V_{qss}]^T$

$\mathbf{P}_k = (\mathbf{I} - \mathbf{K}_k \mathbf{H}_k)\mathbf{P}_k^-$

$\mathbf{x}_k^- = nLModel2(\mathbf{u}, t_s, \mathbf{x_k}, R_s, R_r, L_r, L_s, L_m, p, \gamma, K_t, r, \mathbf{A}_2, \mathbf{B}_1, \mathbf{B}_2, \mathbf{I}_1, \mathbf{I}_2)$

$\mathbf{J}_k = calculateJ2(\mathbf{x}_k, L_s, L_r, L_m, R_r, R_s, \gamma, p, n_g, J_m, J_s, k, b_t, b_m, b_s, t_s)$

$\mathbf{P}_k^- = \mathbf{J}_k \mathbf{P_k} \mathbf{J}_k^T + \mathbf{Q}_k$

An explanation of the algorithm is provided below:

1. Inputs from Simulation (Time-dependent):
   - V_{dss}, V_{qss}: Stator voltages represented in the stationary reference frame for the D-Q axis.
   - $\mathbf{z}_k$: Measurement vector at time step k.
   - $\mathbf{P}_k^-$: The prior estimate of the state covariance matrix.
   - $\mathbf{x}_k^-$: The prior estimate of the state vector.
2. Inputs from MATLAB Workspace (Time-independent):
   - $\mathbf{H}_k$: Observation (measurement) matrix, relating the state vector to the measurement vector.
   - $\mathbf{Q}_k$: Process noise covariance matrix.

- $\mathbf{R}_k$: Measurement noise covariance matrix.
- $\mathbf{I}$: Identity matrix (9x9).
- R_s, R_r: Stator and rotor resistances.
- L_s, L_r, L_m: Stator inductance, rotor inductance, and mutual inductance.
- p: Number of pole pairs.
- $\gamma = L_s L_r - L_m^2$.
- $K_t = 1.5 p L_m$.
- J_m, J_s: Motor and spindle inertias.
- b_m, b_s, b_t: Motor damping friction coefficient, spindle damping friction coefficient, and transmission friction coefficient.
- k: Torsional spring coefficients.
- n_g: Gear ratio of the transmission.
- t_s: Sampling time.

3. Inputs from MATLAB Workspace (Time-independent) for Nonlinear Model:
   - State matrix of the mechanical subsystem, $\mathbf{A}_2$
   - Input matrix of the electric subsystem, $\mathbf{B}_1$
   - Input matrix of the mechanical subsystem, $\mathbf{B}_2$
   - Identity matrix (4x4), $\mathbf{I}_1$
   - Identity matrix (3x3), $\mathbf{I}_2$
4. Output of the function:
   - $\hat{\mathbf{x}}_k$: Estimated state vector.
   - $\mathbf{x}_k^-$: Prior estimate of the state vector.
   - $\mathbf{P}_k^-$: Prior estimate of the state covariance matrix.
5. EKF Calculation Steps:
   - Calculation of Kalman gain, $\mathbf{K}_k$.
   - Updating the estimation of the states, $\hat{\mathbf{x}}_k$.
   - Covariance update, $\mathbf{P}_k$.

- Prediction of the next state (prior estimate) using the 'nLModel' function, $\mathbf{x}_k^-$.
- Calculation of the Jacobian matrix using the 'calculateJ' function, $\mathbf{J}_k$.
- Updating the prior covariance prediction, $\mathbf{P}_k^-$.
- Calculation of the estimated cutting torque from the estimated states, $\hat{T}_c$.

In this algorithm, since T_c is one of the states in the augmented state matrix and is already estimated as part of the state vector, it is not calculated separately in another step.

The algorithm that describes the nonlinear model of the system is presented in Algorithm 12.

Algorithm 12 Nonlinear Model for Method 4

Require: $(\mathbf{u}, t_s, \mathbf{x_k}, R_s, R_r, L_r, L_s, L_m, p, \gamma, K_t, \mathbf{h}_t, r, \mathbf{A}_2, \mathbf{B}_1, \mathbf{B}_2, \mathbf{I}_1, \mathbf{I}_2)$

Ensure: $\mathbf{x}_k$

$[I_{dss}, I_{qss}, I_{drs}, I_{qrs}, \omega_m, \theta_T, \omega_s, T_c] = \mathbf{x}_k$

$\omega_r = \omega_m p$

$\mathbf{x}_{1,k} = [I_{dss}, I_{qss}, I_{drs}, I_{qrs}]^T$

$$A_1 = \begin{bmatrix} -\frac{L_r R_s}{\gamma} & \frac{L_m^2 \omega_e}{\gamma} & \frac{L_m R_r}{\gamma} & \frac{L_m L_r \omega_e}{\gamma} \\ -\frac{L_m^2 \omega_e}{\gamma} & -\frac{L_r R_s}{\gamma} & -\frac{L_m L_r \omega_e}{\gamma} & \frac{L_m R_r}{\gamma} \\ \frac{L_m R_s}{\gamma} & -\frac{L_s L_m \omega_e}{\gamma} & -\frac{R_r L_s}{\gamma} & -\frac{L_s L_r \omega_e}{\gamma} \\ \frac{L_s L_m \omega_e}{\gamma} & \frac{L_m R_s}{\gamma} & \frac{L_r L_s \omega_e}{\gamma} & -\frac{R_r L_s}{\gamma} \end{bmatrix}$$

$\mathbf{G}_1 = e^{\mathbf{A}_1 t_s}$

$\mathbf{H}_1 = \mathbf{A}_1^{-1}(\mathbf{G}_1 - \mathbf{I}_1)\mathbf{B_1}$

$\mathbf{x}_{1,kn} = \mathbf{G}_1 \mathbf{x}_{1,k} + \mathbf{G}_1 \mathbf{u}$

$T_e = K_t(\mathbf{x}_{1,kn}(2)\mathbf{x}_{1,kn}(3) - \mathbf{x}_{1,kn}(1)\mathbf{x}_{1,kn}(4))$

$\mathbf{x}_{2,k} = [\omega_m \ \theta_T \ \omega_s]^T$

$\mathbf{u}_2 = [T_e \ T_c]$

$\mathbf{G}_2 = e^{\mathbf{A}_2 t_s}$

$\mathbf{H}_2 = \mathbf{A}_2^{-1}(\mathbf{G}_2 - \mathbf{I}_2)\mathbf{B_2}$

$\mathbf{x}_{2,kn} = \mathbf{G}_2 \mathbf{x}_{2,k} + \mathbf{G}_2 \mathbf{u}_2$

$\mathbf{x}_{k,n} = [\mathbf{x}_{1,kn}^T \ \mathbf{x}_{2,kn}^T \ T_c]^T$

Explanation of the steps in Algorithm 12:

1. Inputs from Algorithm 11:
    - Input vector containing the voltages, $\mathbf{u}$
    - Sampling time, t_s
    - State vector, $\mathbf{x}_k$
    - R_s, R_r: Stator and rotor resistances
    - L_s, L_r, L_m: Stator inductance, rotor inductance, and mutual inductance
    - p: Number of pole pairs
    - $\gamma = L_s L_r - L_m^2$
    - Cutting tool radius, r
    - State matrix of the mechanical subsystem, $\mathbf{A}_2$
    - Input matrix of the electric subsystem, $\mathbf{B}_1$
    - Input matrix of the mechanical subsystem, $\mathbf{B}_2$
    - Identity matrix (4x4), $\mathbf{I}_1$
    - Identity matrix (3x3), $\mathbf{I}_2$
2. Output of the function:
    - $\mathbf{x}_{k,n} = [I_{dss}, I_{dss}, I_{drs}, I_{qrs}, \omega_m, \theta_T, \omega_s]^T$: States of the entire system calculated by this algorithm.
3. Calculation steps:
    - Separate all states from $\mathbf{x}_k$
    - Calculate rotor velocity, ω_e, from motor velocity, ω_m
    - Create the state matrix for only the electric subsystem variables, $\mathbf{x}_{1,k}$
    - Calculate and update the state matrix, $\mathbf{A}_1$, used in the electric equations
    - Discretize $\mathbf{A}_1$ to obtain $\mathbf{G}_1$
    - Discretize $\mathbf{B}_1$ to obtain $\mathbf{H}_1$
    - Calculate new states for electric subsystem variables at the next step, $\mathbf{x}_{1,kn}$

- Calculate the electric torque, T_e
- Create the state matrix for the mechanical subsystem variables, $\mathbf{x}_{1,k}$
- Create the input matrix for the mechanical subsystem, $\mathbf{u}_2$
- Discretize $\mathbf{A}_2$ to obtain $\mathbf{G}_2$
- Discretize $\mathbf{B}_2$ to obtain $\mathbf{H}_2$
- Calculate new states for the mechanical subsystem variables at the next step, $\mathbf{x}_{2,kn}$
- Create the state matrix that includes all variables for the entire system, $\mathbf{x}_{k,n}$

Algorithm that describes the calculation of the Jacobian Matrix can be seen from 13.

Algorithm 13 calculate of the Jacobian Matrix for Method 4

Require: $\mathbf{x}_k, L_s, L_r, L_m, R_r, R_s, \gamma, p, n_g, J_m, J_s, k, b_t, b_m, b_s, t_s, \mathbf{h}_t, K_t$

Ensure: $\mathbf{J}_k$

$I_{dss} = \mathbf{x}_k(1)$

$I_{qss} = \mathbf{x}_k(2)$

$I_{qrs} = \mathbf{x}_k(3)$

$I_{drs} = \mathbf{x}_k(4)$

$\omega_m = \mathbf{x}_k(5)$

$\mathbf{j}(1,5) = \frac{(I_{qss}L_m^2 + I_{qrs}L_mL_r)p}{\gamma}$

$\mathbf{j}(2,5) = -\frac{(I_{dss}L_m^2 + I_{drs}L_mL_r)p}{\gamma}$

$\mathbf{j}(3,5) = -\frac{(I_{qss}L_sL_m + I_{qrs}L_sL_r)p}{\gamma}$

$\mathbf{j}(4,5) = \frac{(I_{dss}L_sL_m + I_{drs}L_sL_r)p}{\gamma}$

$$\mathbf{j} = \begin{bmatrix} -\frac{L_rR_s}{\gamma} & \frac{L_m^2\omega_e}{\gamma} & \frac{L_mR_r}{\gamma} & \frac{L_mL_r\omega_e}{\gamma} & j_{1,5} & 0 & 0 \\ -\frac{L_m^2\omega_e}{\gamma} & -\frac{L_rR_s}{\gamma} & -\frac{L_mL_r\omega_e}{\gamma} & \frac{L_mR_r}{\gamma} & j_{2,5} & 0 & 0 \\ \frac{L_mR_s}{\gamma} & -\frac{L_sL_m\omega_e}{\gamma} & -\frac{R_rL_s}{\gamma} & -\frac{L_sL_r\omega_e}{\gamma} & j_{3,5} & 0 & 0 \\ \frac{L_sL_m\omega_e}{\gamma} & \frac{L_mR_s}{\gamma} & \frac{L_rL_s\omega_e}{\gamma} & -\frac{R_rL_s}{\gamma} & j_{4,5} & 0 & 0 \\ -\frac{K_tI_{qrs}}{J_m} & \frac{K_tI_{drs}}{J_m} & \frac{K_tI_{qss}}{J_m} & -\frac{K_tI_{dss}}{J_m} & -\frac{b_tn_g^2+b_m}{J_m} & -\frac{kn_g}{J_m} & \frac{b_tn_g}{J_m} \\ 0 & 0 & 0 & 0 & n_g & 0 & -1 \\ 0 & 0 & 0 & 0 & \frac{n_gb_t}{J_s} & \frac{k}{J_s} & -\frac{b_t+b_s}{J_s} \end{bmatrix}$$

$\mathbf{j}_k = e^{\mathbf{j}t_s}$

$\mathbf{J}_k(7,8) = -\frac{t_s}{J_s}$

$J_k = augmenter2(\mathbf{j}_k, \mathbf{J}_k(7,8))$

1. Inputs from Algorithm 11:
    - State vector, $\mathbf{x}_k$
    - L_s, L_r, L_m: Stator inductance, rotor inductance, and mutual inductance
    - R_s, R_r: Stator and rotor resistances
    - $\gamma = L_sL_r - L_m^2$
    - p: Number of pole pairs
    - n_g: Gear ratio of the transmission
    - J_m, J_s: Motor and spindle inertia

- k: Torsional spring coefficients
- b_m, b_s, b_t: Motor damping friction coefficient, spindle damping friction coefficient, and transmission friction coefficient
- t_s: Sampling times

2. Output of the function:
   - $\mathbf{J}_k$: Jacobian matrix in discrete time
3. Calculation Steps:
   - Separate the first five states from $\mathbf{x}_k$ and assign the related variables
   - Calculate specific elements of the matrix **j**
   - Construct the matrix **j** as a (7x7) matrix
   - Discretize **j** to obtain $\mathbf{j}_k$
   - Create the elements to be included in the augmented matrix $\mathbf{J}_k$
   - Use the 'augmenter2' function to obtain the augmented and discretized Jacobian matrix, $\mathbf{J}_k$

The algorithm for obtaining the augmented matrix for the Jacobian matrix, $\mathbf{J}_k$, is presented in Algorithm 14.

Algorithm 14 Augmentation of the Jacobian Matrix

Require: $\mathbf{j}_k, \mathbf{J}_k(7,8)$

Ensure: $\mathbf{J}_k$

$$\mathbf{j}_{k,2} = \begin{bmatrix} 0 & 0 & 0 & 0 & 0 & 0 & \mathbf{J}_k(7,8) \end{bmatrix}$$

$$\mathbf{Z} = \begin{bmatrix} 0 & 0 & 0 & 0 & 0 & 0 & 0 \end{bmatrix}$$

$$\mathbf{J}_k = \left[\begin{array}{c|c} \mathbf{j}_k \text{ (7x7)} & \mathbf{j}_{k,2}\text{(7x1)} \\ \hline \mathbf{Z}\text{(1x7)} & 1 \end{array}\right]$$

1. Inputs from Algorithm 14:
   - $\mathbf{j}_k$: Jacobian matrix of the seven states
   - $\mathbf{J}_k(7,8)$: Matrix elements associated with the tangential cutting torque, T_c

2. Output of the function:
    - $\mathbf{J}_k$: Jacobian matrix in discrete time
3. Calculation Steps:
    - Create a (7×1) matrix, $\mathbf{j}_{k,2}$
    - Create a zero matrix, $\mathbf{Z}$, of size (1×7)
    - Combine $\mathbf{j}_k$, $\mathbf{j}_{k,2}$, $\mathbf{Z}$, and put 1 to obtain $\mathbf{J}_k$

The simulation block created for Method 5 is illustrated in Figure D.10.

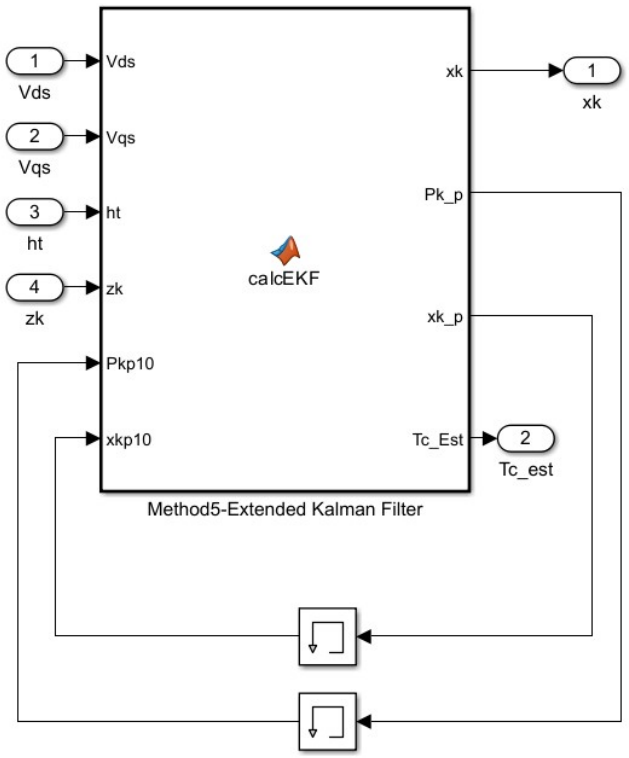


Figure D.10: Simulation Block for Method 5

The algorithm for Method 5 differs from the others as it is specifically developed for the special case where drifting occurs in the transition angle θ_T due to various factors.These factors can be listed as follows:

1. Minor errors in the motor encoder that cause small inaccuracies in the motor angular position, θ_m.

2. Minor errors in the spindle encoder that cause small inaccuracies in the spindle position, θ_s.

3. The driver might be missing readings while reading the encoder or encoders.

The algorithm developed to address this drifting issue is presented in Algorithm 15.

Algorithm 15 Calculation of Extended Kalman Filter Equations for Method 5

/ Inputs ,which are time dependent, taken from Simulation */*

Require: V_{dss}, V_{qss},$\mathbf{z}_k$,$\mathbf{P}_k^-$,$\mathbf{x}_k^-$

/ Inputs ,which are time independent, taken from Matlab Workspace */*

Require: $\mathbf{H}_k$,$\mathbf{Q}_k$,$\mathbf{R}_k$,$\mathbf{I}$,R_s,R_r,L_r,L_m,L_s,p,γ,J_m,J_s,b_m,b_s,b_t,k,n_g,r,t_s,K_t

/ inputs ,which are time independent, taken from Matlab Workspace and necessary matrix for calculation of the nonlinear Model */*

Require: $\mathbf{A}_2, \mathbf{B}_1, \mathbf{B}_2, \mathbf{I}_1$

Ensure: $\hat{\mathbf{x}}_k$,$\mathbf{x}_k^-$,$\mathbf{P}_k^-$,$\hat{T}_c$

$\mathbf{K}_k = \mathbf{P}_k^- \mathbf{H}_k^T (\mathbf{H}_k \mathbf{P}_k^- \mathbf{H}_k^T + \mathbf{R}_k)^{-1}$

$\hat{\mathbf{x}}_\mathbf{k} = \mathbf{x}_k^- + \mathbf{K}_k(\mathbf{z}_k - \mathbf{H}_k \mathbf{x}_k^-)$

$\mathbf{u} = [V_{dss}, V_{qss}]^T$

$\mathbf{P}_k = (\mathbf{I} - \mathbf{K}_k \mathbf{H}_k)\mathbf{P}_k^-$

$\mathbf{x}_k^- = nLModel3(\mathbf{u}, t_s, \mathbf{x}_\mathbf{k}, R_s, R_r, L_r, L_s, L_m, p, \gamma, K_t, r, \mathbf{A}_2, \mathbf{B}_1, \mathbf{B}_2, \mathbf{I}_1)$

$\mathbf{J}_k = calculateJ3(\mathbf{x}_k, L_s, L_r, L_m, R_r, R_s, \gamma, p, n_g, J_m, J_s, k, b_t, b_m, b_s, t_s)$

$\mathbf{P}_k^- = \mathbf{J}_k \mathbf{P}_\mathbf{k} \mathbf{J}_k^T + \mathbf{Q}_k$

An explanation of the algorithm is provided below:

1. Inputs from Simulation (Time-dependent):

   - V_{dss}, V_{qss}: Stator voltages represented in the stationary reference frame for the D-Q axis.
   - $\mathbf{z}_k$: Measurement vector at time step k.
   - $\mathbf{P}_k^-$: The prior estimate of the state covariance matrix.
   - $\mathbf{x}_k^-$: The prior estimate of the state vector.

2. Inputs from MATLAB Workspace (Time-independent):

- $\mathbf{H}_k$: Observation (measurement) matrix, relating the state vector to the measurement vector.
- $\mathbf{Q}_k$: Process noise covariance matrix.
- $\mathbf{R}_k$: Measurement noise covariance matrix.
- $\mathbf{I}$: Identity matrix (9x9).
- R_s, R_r: Stator and rotor resistances.
- L_s, L_r, L_m: Stator inductance, rotor inductance, and mutual inductance.
- p: Number of pole pairs.
- $\gamma = L_s L_r - L_m^2$.
- $K_t = 1.5pL_m$.
- J_m, J_s: Motor and spindle inertias.
- b_m, b_s, b_t: Motor damping friction coefficient, spindle damping friction coefficient, and transmission friction coefficient.
- k: Torsional spring coefficients.
- n_g: Gear ratio of the transmission.
- t_s: Sampling time.

3. Inputs from MATLAB Workspace (Time-independent) for Nonlinear Model:
   - State matrix of the mechanical subsystem, $\mathbf{A}_2$
   - Input matrix of the electric subsystem, $\mathbf{B}_1$
   - Input matrix of the mechanical subsystem, $\mathbf{B}_2$
   - Identity matrix (4x4), $\mathbf{I}_1$
4. Output of the function:
   - $\hat{\mathbf{x}}_k$: Estimated state vector.
   - $\mathbf{x}_k^-$: Prior estimate of the state vector.
   - $\mathbf{P}_k^-$: Prior estimate of the state covariance matrix.
5. EKF Calculation Steps:
   - Calculation of Kalman gain, $\mathbf{K}_k$.

- Updating the estimation of the states, $\hat{\mathbf{x}}_k$.
- Covariance update, $\mathbf{P}_k$.
- Prediction of the next state (prior estimate) using the 'nLModel' function, $\mathbf{x}_k^-$.
- Calculation of the Jacobian matrix using the 'calculateJ' function, $\mathbf{J}_k$.
- Updating the prior covariance prediction, $\mathbf{P}_k^-$.
- Calculation of the estimated cutting torque from the estimated states, $\hat{T}_c$.

The algorithm that describes the nonlinear model of the system is presented in Algorithm 16.

Algorithm 16 nLModel3

Require: $(\mathbf{u}, t_s, \mathbf{x_k}, R_s, R_r, L_r, L_s, L_m, p, \gamma, K_t, \mathbf{h}_t, r, \mathbf{A}_2, \mathbf{B}_1, \mathbf{B}_2, \mathbf{I}_1)$

Ensure: $\mathbf{x}_k$

$[I_{dss}, I_{qss}, I_{drs}, I_{qrs}, \omega_m, \theta_T, \omega_s, \delta_{n_g}, K_{tc}, K_{te}] = \mathbf{x}_k$

$\omega_r = \omega_m p$

$\mathbf{x}_{1,k} = [I_{dss}, I_{qss}, I_{drs}, I_{qrs}]^T$

$$A_1 = \begin{bmatrix} -\frac{L_r R_s}{\gamma} & \frac{L_m^2 \omega_e}{\gamma} & \frac{L_m R_r}{\gamma} & \frac{L_m L_r \omega_e}{\gamma} \\ -\frac{L_m^2 \omega_e}{\gamma} & -\frac{L_r R_s}{\gamma} & -\frac{L_m L_r \omega_e}{\gamma} & \frac{L_m R_r}{\gamma} \\ \frac{L_m R_s}{\gamma} & -\frac{L_s L_m \omega_e}{\gamma} & -\frac{R_r L_s}{\gamma} & -\frac{L_s L_r \omega_e}{\gamma} \\ \frac{L_s L_m \omega_e}{\gamma} & \frac{L_m R_s}{\gamma} & \frac{L_r L_s \omega_e}{\gamma} & -\frac{R_r L_s}{\gamma} \end{bmatrix}$$

$\mathbf{G}_1 = e^{\mathbf{A}_1 t_s}$

$\mathbf{H}_1 = \mathbf{A}_1^{-1}(\mathbf{G}_1 - \mathbf{I}_1)\mathbf{B_1}$

$\mathbf{x}_{1,kn} = \mathbf{G}_1 \mathbf{x}_{1,k} + \mathbf{G}_1 \mathbf{u}$

$T_e = K_t(\mathbf{x}_{1,kn}(2)\mathbf{x}_{1,kn}(3) - \mathbf{x}_{1,kn}(1)\mathbf{x}_{1,kn}(4))$

$T_c = r(K_{tc}\mathbf{h}_t(1) + K_{te}\mathbf{h}_t(2))$

$\mathbf{x}_{2,k} = [\omega_m\ \theta_T\ \omega_s\ \delta_{n_g}]^T$

$\mathbf{u}_2 = [T_e\ T_c]$

$\mathbf{G}_2 = e^{\mathbf{A}_2 t_s}$

$\mathbf{H}_2 = \mathbf{A}_2^{-1}(\mathbf{G}_2 - \mathbf{I}_1)\mathbf{B_2}$

$\mathbf{x}_{2,kn} = \mathbf{G}_2 \mathbf{x}_{2,k} + \mathbf{G}_2 \mathbf{u}_2$

$\mathbf{x}_{k,n} = [\mathbf{x}_{1,kn}^T\ \mathbf{x}_{2,kn}^T\ K_{tc}\ K_{te}]^T$

Explanation of the steps in Algorithm 16:

1. Inputs from Algorithm 15:
    - Input vector containing the voltages, $\mathbf{u}$
    - Sampling time, t_s
    - State vector, $\mathbf{x}_k$
    - R_s, R_r: Stator and rotor resistances
    - L_s, L_r, L_m: Stator inductance, rotor inductance, and mutual inductance
    - p: Number of pole pairs
    - $\gamma = L_s L_r - L_m^2$
    - Cutting tool radius, r
    - State matrix of the mechanical subsystem, $\mathbf{A}_2$
    - Input matrix of the electric subsystem, $\mathbf{B}_1$
    - Input matrix of the mechanical subsystem, $\mathbf{B}_2$
    - Identity matrix (4x4), $\mathbf{I}_1$
2. Output of the function:
    - $\mathbf{x}_{k,n} = [I_{dss}, I_{dss}, I_{drs}, I_{qrs}, \omega_m, \theta_T, \omega_s, \delta_{n_g}, K_{tc}, K_{te}]^T$: States of the entire system calculated by this algorithm.
3. Calculation steps:
    - Separate all states from $\mathbf{x}_k$
    - Calculate rotor velocity, ω_e, from motor velocity, ω_m
    - Create the state matrix for only the electric subsystem variables, $\mathbf{x}_{1,k}$
    - Calculate and update the state matrix, $\mathbf{A}_1$, used in the electric equations
    - Discretize $\mathbf{A}_1$ to obtain $\mathbf{G}_1$
    - Discretize $\mathbf{B}_1$ to obtain $\mathbf{H}_1$
    - Calculate new states for electric subsystem variables at the next step, $\mathbf{x}_{1,kn}$
    - Calculate the electric torque, T_e

- Create the state matrix for the mechanical subsystem variables, $\mathbf{x}_{1,k}$
- Create the input matrix for the mechanical subsystem, $\mathbf{u}_2$
- Discretize $\mathbf{A}_2$ to obtain $\mathbf{G}_2$
- Discretize $\mathbf{B}_2$ to obtain $\mathbf{H}_2$
- Calculate new states for the mechanical subsystem variables at the next step, $\mathbf{x}_{2,kn}$
- Create the state matrix that includes all variables for the entire system, $\mathbf{x}_{k,n}$

Algorithm that describes the calculation of the Jacobian Matrix can be seen from 17.

Algorithm 17 Calculation of the Jacobian Matrix for Method 5

Require: $\mathbf{x}_k, L_s, L_r, L_m, R_r, R_s, \gamma, p, n_g, J_m, J_s, k, b_t, b_m, b_s, t_s, \mathbf{h}_t, K_t$

Ensure: $\mathbf{J}_k$

$I_{dss} = \mathbf{x}_k(1)$

$I_{qss} = \mathbf{x}_k(2)$

$I_{qrs} = \mathbf{x}_k(3)$

$I_{drs} = \mathbf{x}_k(4)$

$\omega_m = \mathbf{x}_k(5)$

$\mathbf{j}(1,5) = \frac{(I_{qss}L_m^2 + I_{qrs}L_mL_r)p}{\gamma}$

$\mathbf{j}(2,5) = -\frac{(I_{dss}L_m^2 + I_{drs}L_mL_r)p}{\gamma}$

$\mathbf{j}(3,5) = -\frac{(I_{qss}L_sL_m + I_{qrs}L_sL_r)p}{\gamma}$

$\mathbf{j}(4,5) = \frac{(I_{dss}L_sL_m + I_{drs}L_sL_r)p}{\gamma}$

$$\mathbf{j} = \begin{bmatrix} -\frac{L_rR_s}{\gamma} & \frac{L_m^2\omega_e}{\gamma} & \frac{L_mR_r}{\gamma} & \frac{L_mL_r\omega_e}{\gamma} & j_{1,5} & 0 & 0 & 0 \\ -\frac{L_m^2\omega_e}{\gamma} & -\frac{L_rR_s}{\gamma} & -\frac{L_mL_r\omega_e}{\gamma} & \frac{L_mR_r}{\gamma} & j_{2,5} & 0 & 0 & 0 \\ \frac{L_mR_s}{\gamma} & -\frac{L_sL_m\omega_e}{\gamma} & -\frac{R_rL_s}{\gamma} & -\frac{L_sL_r\omega_e}{\gamma} & j_{3,5} & 0 & 0 & 0 \\ \frac{L_sL_m\omega_e}{\gamma} & \frac{L_mR_s}{\gamma} & \frac{L_rL_s\omega_e}{\gamma} & -\frac{R_rL_s}{\gamma} & j_{4,5} & 0 & 0 & 0 \\ -\frac{K_tI_{qrs}}{J_m} & \frac{K_tI_{drs}}{J_m} & \frac{K_tI_{qss}}{J_m} & -\frac{K_tI_{dss}}{J_m} & -\frac{b_tn_g^2+b_m}{J_m} & -\frac{kn_g}{J_m} & \frac{b_tn_g}{J_m} & 0 \\ 0 & 0 & 0 & 0 & (n_g + \delta_{n_g} & 0 & -1 & \omega_m \\ 0 & 0 & 0 & 0 & \frac{n_gb_t}{J_s} & \frac{k}{J_s} & -\frac{b_t+b_s}{J_s} & 0 \\ 0 & 0 & 0 & 0 & 0 & 0 & 0 & 1 \end{bmatrix}$$

$\mathbf{j}_k = e^{\mathbf{j}t_s}$

$\mathbf{J}_k(7,9) = -\frac{r\mathbf{h}_t(1)t_s}{J_s}$

$\mathbf{J}_k(7,10) = -\frac{r\mathbf{h}_t(2)t_s}{J_s}$

$J_k = augmenter3(\mathbf{j}_k, \mathbf{J}_k(7,9), \mathbf{J}_k(7,10))$

1. Inputs from Algorithm 15:

   - State vector, $\mathbf{x}_k$
   - L_s, L_r, L_m: Stator inductance, rotor inductance, and mutual inductance
   - R_s, R_r: Stator and rotor resistances
   - $\gamma = L_sL_r - L_m^2$
   - p: Number of pole pairs
   - n_g: Gear ratio of the transmission

- J_m, J_s: Motor and spindle inertia
- k: Torsional spring coefficients
- b_m, b_s, b_t: Motor damping friction coefficient, spindle damping friction coefficient, and transmission friction coefficient
- t_s: Sampling time
- $\mathbf{h}_t$: Geometric matrix providing information about the cutting geometry
- r: Cutting tool radius

2. Output of the function:
   - $\mathbf{J}_k$: Jacobian matrix in discrete time
3. Calculation Steps:
   - Separate the first five states from $\mathbf{x}_k$ and assign the related variables
   - Calculate specific elements of the matrix **j**
   - Construct the matrix **j** as a (8x8) matrix
   - Discretize **j** to obtain $\mathbf{j}_k$
   - Create the elements to be included in the augmented matrix $\mathbf{J}_k$
   - Use the 'augmenter' function to obtain the augmented and discretized Jacobian matrix, $\mathbf{J}_k$

The algorithm for obtaining the augmented matrix for the Jacobian matrix, $\mathbf{J}_k$, is presented in Algorithm 18.

Algorithm 18 augmenter3

Require: $\mathbf{j}_k, \mathbf{J}_k(7,9), \mathbf{J}_k(7,10)$

Ensure: $\mathbf{J}_k$

$$\mathbf{j}_{k,2} = \begin{bmatrix} 0 & 0 \\ 0 & 0 \\ 0 & 0 \\ 0 & 0 \\ 0 & 0 \\ 0 & 0 \\ 0 & 0 \\ \mathbf{J}_k(7,8) & \mathbf{J}_k(7,9) \end{bmatrix}$$

$$\mathbf{Z} = \begin{bmatrix} 0 & 0 & 0 & 0 & 0 & 0 & 0 & 0 \\ 0 & 0 & 0 & 0 & 0 & 0 & 0 & 0 \end{bmatrix}$$

$$\mathbf{I} = \begin{bmatrix} 1 & 0 \\ 0 & 1 \end{bmatrix}$$

$$\mathbf{J}_k = \left[\begin{array}{c|c} \mathbf{j}_k \text{ (8x8)} & \mathbf{j}_{k,2}\text{(8x2)} \\ \hline \mathbf{Z}\text{(2x8)} & \mathbf{I}\text{(2x2)} \end{array}\right]$$

1. Inputs from Algorithm 18:
   - $\mathbf{j}_k$: Jacobian matrix of the seven states
   - $\mathbf{J}_k(7,9)$: Matrix elements associated with the tangential cutting force coefficient, K_{tc}
   - $\mathbf{J}_k(7,10)$: Matrix elements associated with the tangential cutting force coefficient, K_{te}
2. Output of the function:
   - $\mathbf{J}_k$: Jacobian matrix in discrete time
3. Calculation Steps:
   - Create a (8×2) matrix, $\mathbf{j}_{k,2}$
   - Create a zero matrix, $\mathbf{Z}$, of size (2×8)

- Create an identity matrix, $\mathbf{I}$, of size (2×2)
- Combine $\mathbf{j}_k$, $\mathbf{j}_{k,2}$, $\mathbf{Z}$, and $\mathbf{I}$ to obtain $\mathbf{J}_k$

E Verification Test Setup

In this appendix, the hardware and software utilized in the test setup is discussed in greater detail.

TwinCAT 3, developed by Beckhoff, turns standard PCs into real-time controllers for industrial automation. It features a modular architecture, integrates with Microsoft Visual Studio, and supports IEC 61131-3 and high-level languages like C/C++. The platform is scalable, supports various communication protocols, and includes safety features compliant with SIL 3 [16].

The Beckhoff C6930 is a compact and high-performance Industrial PC (IPC) for demanding applications [17]. Key specifications include:

- **Processor:** Intel® Core™ i5.
- **Memory:** 16 GB DDR4 RAM.
- **Storage:** 256 GB SSD.
- **Cooling:** Fanless design for low maintenance.
- **Operating System:** Windows and TwinCAT 3.
- **Interfaces:** Ethernet, USB 3.0, and PCIe slots.
- **Power Supply:** 24 V DC.
- **Mounting:** Space-saving, control cabinet installation.
- **Temperature Range:** 0 to 55°C.

The Beckhoff C6930 is shown in Figure E.1.



Figure E.1: Beckhoff C6930

The spindle motor is a Franz Kessler DM 112/4L AC induction motor, with its datasheet shown in Figure B.1 and its picture in Figure E.2.



Figure E.2: Franz Kessler DM112/4L AC Induction Motor

The Beckhoff AX5125 is a high-performance servo drive designed for precise and dynamic motion control [18]. Key specifications are:

- **Rated Current:** 25 A.
- **Power Supply:** 3-phase, 400...480 V AC.
- **Output Power:** Up to 12 kW.
- **Control Features:** Supports EtherCAT for high-speed communication and seamless integration with Beckhoff control systems.
- **Feedback Interfaces:** EnDat, BiSS, Resolver, and incremental encoders for precise positioning.

- **Safety:** Integrated STO (Safe Torque Off) functionality according to IEC 61800-5-2.
- **Cooling:** Fan-cooled design for efficient thermal management.
- **Mounting:** Compact design suitable for control cabinet installation.

The Heidenhain ROD 480 1800 is a high-resolution incremental rotary encoder commonly used in precision motion control applications [19], and its picture is presented in Figure E.3. Key specifications are:

- **Resolution:** 1,800 lines per revolution.
- **Output Signal:** Incremental, with sine/cosine 1 V_{PP} interface.
- **Shaft Type:** Solid shaft, 10 mm diameter.
- **Maximum Speed:** 12,000 rpm.
- **Accuracy:** Angular accuracy up to ±20 arc seconds.
- **Operating Temperature:** -20°C to +100°C.
- **Protection Class:** IP64, ensuring protection against dust and splashes.
- **Mounting:** Suitable for applications requiring high precision and dynamic performance.



Figure E.3: Heidenhain ROD 480 1800

The Beckhoff AM8062 is a high-performance servomotor designed for industrial applications [20]. Key specifications include:

- **Standstill Torque:** 21.1 Nm to 29.9 Nm, depending on the winding.
- **Rated Speed:** 1,400 min^{-1}, 3,000 min^{-1}, and 5,000 min^{-1} options available.
- **Cooling Method:** Convection cooling, with an option for forced cooling.
- **Feedback System:** OCT feedback system (absolute encoder) for precise control.
- **Shaft Dimensions:** Shaft diameter of 32 k6 and a free shaft end of 58 mm.
- **Rotor Moment of Inertia:** 20.0 $\text{kg}\cdot\text{cm}^2$, contributing to high dynamic response.
- **Protection Class:** IP54, with an IP65 option with shaft seal for enhanced durability.
- **Ambient Temperature Range:** Operational range from +5°C to +40°C.

The Beckhoff AX8640 is a power supply module within the AX8000 multi-axis servo system, designed to convert mains voltage into DC link voltage for axis and option modules [21]. Key specifications include:

- **Function:** Power supply module.
- **Rated Supply Voltage:** 3-phase, 200–480 V AC.
- **DC Link Voltage:** Up to 848 V DC.
- **DC Link Output Current:** 40.0 A DC.
- **System Bus:** EtherCAT.
- **Drive Profile:** CiA402 according to IEC 61800-7-201 (CoE).
- **Ambient Operating Temperature:** 0°C to +40°C; up to +55°C with power reduction.
- **Approvals/Markings:** CE, cULus, EAC.
- **Protection Rating:** IP20.

- **Dimensions (H x W x D):** 230 mm x 90 mm x 192 mm (without connectors).

The Heidenhain LS403 is a sealed linear encoder designed for precise position measurement in industrial applications [22]. Key specifications are:

- **Measuring Standard:** DIADUR glass scale.
- **Output Signals:** 11 µApp, with a signal period of 20 µm.
- **Accuracy Grades:** ±5 µm and ±3 µm, depending on configuration.
- **Measuring Lengths:** Available in lengths from 70 mm to 2040 mm.
- **Recommended Measuring Steps:** 1 µm and 0.5 µm options.
- **Reference Marks:** One or two reference marks for position referencing.

The Kistler 9257B is shown in Figure E.4.



Figure E.4: Kistler 9257B Dynamometer

The Kistler 9257B is a quartz three-component dynamometer for measuring force in three orthogonal directions [23]. Key specifications are:

- **Measuring Range:** F_x, F_y: $\pm 5\,\text{kN}$; F_z: $\pm 10\,\text{kN}$
- **Calibrated Partial Ranges:** F_x, F_y: 0 to 500 N and 50 N; F_z: 0 to 1,000 N and 100 N
- **Overload Capacity:** F_x, F_y, F_z: $\pm 7.5\,\text{kN}$; F_z (if $F_x, F_y \leq 0.5 \times F_z$): $\pm 15\,\text{kN}$
- **Threshold:** $< 0.01\,\text{N}$; **Sensitivity:** F_x, F_y: $\approx -7.5\,\text{pC/N}$; F_z: $\approx -3.7\,\text{pC/N}$

- **Linearity/Hysteresis:** $\leq \pm 1\%$ FSO / $\leq 0.5\%$ FSO
- **Cross Talk:** $\leq \pm 2\%$
- **Rigidity:** c_x, c_y: > 1 kN/μm; c_z: > 2 kN/μm
- **Natural Frequency:** $f_n(x, y, z)$: ≈ 3.5 kHz (unmounted), $f_n(x, y)$: ≈ 2.3 kHz, $f_n(z)$: ≈ 3.5 kHz (mounted)
- **Operating Temp.:** 0°C to 70°C
- **Capacitance:** ≈ 220 pF; **Insulation:** $> 10^{13}\,\Omega$ (at 20°C)
- **Protection:** IP67; **Weight:** 7.3 kg; **Clamping Area:** 100 mm $\times$ 170 mm

The Kistler LabAmp 5167A is shown in Figure E.5.



Figure E.5: The Kistler LabAmp 5167A

The Kistler LabAmp 5167A is a laboratory charge amplifier with integrated data acquisition for piezoelectric sensors [**?**]. Key specifications include:

- **Channels:** 4 or 8, with BNC connectors for input and analog output.
- **Measuring Range:** ±100 to ±1,000,000 pC.
- **Frequency Range (-3 dB):** Up to 45,000 Hz.
- **Input Noise (typical):** As low as 0.007 pC_{rms} (1 Hz to 10 kHz).
- **Drift (DC Mode):** < ±0.03 pC/s at 25°C and 60% RH.
- **Data Acquisition:** 24-bit, up to 100 kSps per channel.
- **Filters:** Flexible low-pass, high-pass, and notch filters.

- **Synchronization:** PTP option for multi-device data acquisition.
- **Control:** Web-browser interface or KiStudio Lab Software.

The NI cDAQ-9174 is a 4-slot USB CompactDAQ chassis for sensor measurement systems [24]. Key specifications include:

- **Slots:** 4
- **Connectivity:** USB 2.0
- **Analog Input FIFO:** 127 samples per slot
- **Sample Rate:** Dependent on installed C Series modules
- **Timing Accuracy:** 50 ppm; **Resolution:** 12.5 ns
- **Operating Temp.:** -20°C to 55°C
- **Shock/Vibration:** 30 g peak (shock), 0.3 g rms (operating vibration)
- **Dimensions:** 88.1 mm x 180.0 mm x 180.3 mm
- **Weight:** Approx. 1.27 kg

The NI 9234 is a 4-channel, 24-bit C Series module designed for sound and vibration measurements [25]. Key specifications include:

- **Channels:** 4 analog inputs
- **ADC Resolution:** 24 bits
- **Sampling Rate:** Up to 51.2 kS/s per channel
- **Input Range:** ±5 V
- **Input Coupling:** Software-selectable AC/DC
- **IEPE Excitation:** 2.1 mA per channel, software-selectable
- **Connectivity:** BNC connectors

- **Compatibility:** CompactDAQ and CompactRIO systems
- **Operating Temperature:** -40°C to 70°C
- **Dimensions:** 88.1 mm x 88.1 mm x 25.4 mm
- **Weight:** Approximately 150 g